UNIVERSITY OF SOUTHAMPTON

FINITE ELEMENT DYNAMIC ANALYSIS OF ROTATING TAPERED THREE DIMENSIONAL TIMOSHENKO BEAMS

By

Abdelaziz BAZOUNE

A thesis submitted for the degree of

Doctor of Philosophy

in the

SCHOOL OF ENGINEERING SCIENCES

MECHANICAL ENGINEERING

November 2002

UNIVERSITY OF SOUTHAMPTON

ABSTRACT

SCHOOL OF ENGINEERING SCIENCES
MECHANICAL ENGINEERING

Doctor of Philosophy

FINITE ELEMENT DYNAMIC ANALYSIS OF ROTATING TAPERED THREE DIMENSIONAL BEAMS

by A. BAZOUNE

The equations of motion are derived for the three dimensional rotating tapered Timoshenko beam using a Lagrangian formulation in conjunction with the finite element technique. These equations include the effects of Coriolis forces, shear deformation and rotary inertia, hub radius, taper ratios and pre-cone and setting angle. A mixed set of generalized co-ordinates that accounts for inertia coupling between reference motions and local elastic deformations is employed. The shape functions of the three dimensional beam element are derived using Timoshenko beam theory. Explicit expressions of the element mass, stiffness, Coriolis and inertia terms matrices are derived in parametric form thus avoiding extensive numerical computations. The generalized eigenvalue problem is defined and cast into state space form using explicit expressions for the mass, stiffness and Coriolis matrices.

Modal transformations from the space of nodal co-ordinates to the space of modal co-ordinates are invoked to alleviate the problem of large dimensionality resulting from the finite element discretization. Both planar and complex modal transformations are presented and implemented to obtain a reduced order model. The reduced order model form of equations of motion is computer generated, integrated forward in time and the system dynamic response is evaluated for different types of external loading conditions.

Explicit expressions for Southwell coefficients for rotating tapered Timoshenko beams are obtained as a function of all parameter variations.

The frequency spectrum of the forced time signal response is computed and plotted along with the response profiles for a wide range of parameter variation using the FFT algorithm.

Acknowledgment

I would like to express my sincere and deep gratitude to my supervisor Dr. N. G. Stephen, Senior Lecturer of Mechanical Engineering at the University of Southampton for his excellent guidance and immeasurable support and encouragement at every stage of this work.

I wish to thank Dr. Y. A. Khulief, Professor of Mechanical Engineering at King Fahd University of Petroleum and Minerals, Dhahran, Saudi Arabia for introducing me to this fascinating subject, his advice and patience were limitless.

I am indebted to King Fahd University of Petroleum and Minerals for the facilities and support during this work .

I wish to thank my parents for the unconditional support they have provided throughout my life, I could not have asked for more. Special thanks to my parents who left us forever. They did not live to witness this particular event of my life. May God reward them.

I thank my family members for their many sacrifices and great deal of moral support as well as a sense of purpose during this work.

Finally, very special thanks go to my wife for her indispensable patience and love. She was asking me every day: Is it done yet? Yes, it's finally done!

Nomenclature

Unless otherwise stated, the following notation is used

$[\mathcal{A}]$	rotational transformation matrix
$[\mathcal{A}_\psi]$	constant setting angle transformation
$[\mathcal{A}_\phi]$	constant pre-cone angle transformation
$[\mathcal{A}_\circ]$	$= [\mathcal{A}_\phi]\,[\mathcal{A}_\psi]$
$[\mathcal{A}_\varphi]$	partial derivative of $[\mathcal{A}]$ with respect to φ
$\left[\widetilde{\mathcal{A}}_I\right]$	skew symmetric matrix
A^i	cross-sectional area of the i^{th} beam element
A_o	cross-sectional area of the beam at the root
$[B^i_j]$	elemental strain displacement matrix
b^i	breadth of the cross-section of the beam at an arbitrary location x^i
b_o	breadth of the cross-section of the beam at the root
$\left[\widetilde{C}^i\right]$	element Coriolis matrix
$\{d^i\}$	elastic deformation vector
$\{e^i\}$, $\{\overline{e}^i\}$	generalized nodal displacement vectors defined with respect to $(x^i\ y^i\ z^i)$ and $(\overline{x}\ \overline{y}\ \overline{z})$ co-ordinate axes
E	modulus of elasticity
F^i_P	centrifugal force
F^i_x, F^i_y, F^i_z	x, y, and z-components of the centrifugal force
f	frequency, Hz
G	modulus of rigidity
h^i	depth of the cross-section of the beam at an arbitrary location x^i
h_o	depth of the cross-section of the beam at the root
$[I]$	identity matrix
I^i_{yy}	second moment of area of the cross-section about the y-axis
I^i_{yz}	product moment of area of the cross-section about the yz-axes
I^i_{zz}	second moment of area of the cross-section about the z-axis
I_o	second moment of area of the cross-section at the root of the beam
i	refers to the i^{th} element
$\left[\overline{k}^i_{b,v}\right]$	elemental bending stiffness matrix in the (xy)-plane
$\left[\overline{k}^i_{b,w}\right]$	elemental bending stiffness matrix in the (xz)-plane
$\left[\overline{k}^i_a\right]$	elemental axial stiffness matrix

$\left[\overline{k}^i_{ee}\right]$	composite elemental elastic stiffness matrix
$\left[\overline{k}^i_{b,vw}\right]$	elemental stiffness matrix due to coupling in bending
$[\overline{k}^i_{\theta_x}]$	elemental torsional stiffness matrix
$\left[\overline{k}^i_{s,v}\right]$	elemental shear stiffness matrix in the (xy)-plane
$\left[\overline{k}^i_{s,w}\right]$	elemental shear stiffness matrix in the (xz)-plane
$\left[\overline{k}^i_{c,v}\right]$	elemental centrifugal stiffness matrix in the (xy)-plane
$\left[\overline{k}^i_{c,w}\right]$	elemental centrifugal stiffness matrix in the (xz)-plane
$\mathcal{L}^i$	$= \mathcal{T}^i - \mathcal{U}^i - \mathcal{V}^i$, Lagrangian
$[\mathbb{L}]$	left complex modal matrix
L	truncated length of the beam
L^i	outboard length of the beam from element under consideration
L_{oy}	untruncated length of the beam in the (xy)-plane
L_{oz}	untruncated length of the beam in the (xz)-plane
l^i	element length
$[M^i]$	composite elemental mass matrix
$[m^i_{rr}]$	element mass matrix associated with reference motion
$[m^i_{re}]$	element mass matrix representing the coupling between reference motion and elastic deformations
$[m^i_{ee}]$	composite element elastic mass matrix
$[m^i_a]$	element axial mass matrix
$[m^i_{\theta_x}]$	element torsional mass matrix
$[m^i_{t,v}]$	element translational mass matrix in the (xy)-plane
$[m^i_{t,w}]$	element translational mass matrix in the (xz)-plane
$[m^i_{\theta_z,v}]$	element rotary inertia mass matrix in the (xy)-plane
$[m^i_{\theta_y,w}]$	element rotary inertia mass matrix in the (xz)-plane
$[m^i_{\theta,vw}]$	elemental rotary inertia mass matrix due to coupling in bending
$[M]$	global mass matrix of the beam
M^i_y, M^i_z	bending moments
$[\mathcal{N}^i]$	modified shape functions of the i^{th} beam element
n	total number of elements
$P^i_\circ$, P^i_1	points in the undeformed state of the i^{th} beam element before and after setting angles are made
$[\mathbb{P}]$	modal planar transformation matrix
P^i	point in the deformed state of the i^{th} beam element

Q_y^i, Q_z^i	shear forces
$\mathcal{R}_\circ$	hub radius
$\mathcal{R}_P^i$	global position vector of point P^i
R	$= \mathcal{R}_\circ/L$, non-dimensional hub radius
$\left[\Re^i\right]$	transformation matrix from elemental co-ordinates to body co-ordinates
$\left[\overline{\Re}^i\right]$	diagonal transformation matrix built up of $\left[\Re^i\right]$ matrices
$[\mathbb{R}]$	right complex modal matrix
r_{gy}	$= \sqrt{I_{o_{yy}}/A_o}$, radius of gyration of the cross-section of the beam about the y-axis
r_{gz}	$= \sqrt{I_{o_{zz}}/A_o}$, radius of gyration of the cross-section of the beam about the z-axis
$r_{P_\circ}^i$, $r_{P_1}^i$	position vectors of point $P_\circ^i$ and P_1^i, respectively
S_i	Southwell coefficient corresponding to the i^{th} mode
$\mathcal{S}^i$	element shape functions
$\mathcal{T}^i$	kinetic energy of the i^{th} beam element
$\mathcal{U}^i$	strain energy of the i^{th} beam element
u^i	axial nodal displacement
V^i	element volume
$\mathcal{V}^i$	potential energy of the i^{th} beam element
v^i	elemental translational nodal displacement in the y-direction
v_b^i	bending nodal displacement in the y-direction
v_s^i	shear nodal displacement in the y-direction
w^i	elemental translational nodal displacement in the z-direction
w_b^i	bending nodal displacement in the z-direction
w_s^i	shear nodal displacement in the z-direction
x^i	elemental co-ordinate in the x-direction
y^i	elemental co-ordinate in the y-direction
z^i	elemental co-ordinate in the z-direction
(xyz)	local co-ordinate system
$(x'y'z')$	co-ordinate system obtained by rotating the (xyz) co-ordinate system about the x-axis by a setting angle ψ
$(x''y''z'')$	co-ordinate system obtained by rotating the $(x'y'z')$ co-ordinate system about the y'-axis by a pre-cone angle ϕ
$\left(x^iy^iz^i\right)$	element co-ordinate system
$(\overline{x}\ \overline{y}\ \overline{z})$	element co-ordinate system initially parallel to $\left(x^iy^iz^i\right)$ system
(XYZ)	global co-ordinate system

α_{yi}, α_{zi}	constants defined by equations (3.21)-(3.28), $(i = 0, 1, ..., 3)$
β_i	constants defined by equations (3.89)-(3.93), $(i = 0, 1, ..., 4)$
γ^i	angle of distortion due to shear deformation
ϵ^i	element strain
ζ^i	$= z^i/l^i$, non-dimensional elemental co-ordinates in the z-direction
η^i	$= y^i/l^i$, non-dimensional elemental co-ordinates in the y-direction
θ_x^i	element torsional displacement
θ_y^i	element bending rotation about the z-axis
θ_z^i	element bending rotation about the y-axis
κ_y, κ_z	shear correction factors in the y- and z-directions, respectively
μ_i	constants defined by equations (3.13)-(3.14), $(i = 1, 2)$
ν	Poisson's ratio
ν_y	$= L/L_{oy}$, taper ratio in the y-direction
ν_z	$= L/L_{oz}$, taper ratio in the z-direction
ξ^i	$= x^i/l^i$, non-dimensional elemental coordinates in the x-direction
ρ	mass density
σ^i	element normal stress
τ^i	element shear stress
Φ_y, Φ_z	shear deformation parameters
ϕ	pre-cone angle
φ	$= \Omega t$
ψ	setting angle
Ω	rate of spin of the hub
$\overline{\Omega}$	$= \Omega L^2/\sqrt{EI_{o_{yy}}/\rho A_o}$, spin parameter
ω	natural frequency of the beam, (rad/s)
λ	$= \omega L^2\sqrt{\rho A_o/EI_{o_{yy}}}$, frequency parameter
$[\ ]^T$	transpose of $[\ ]$
$[\ ]_E$, $[\ ]_T$	Euler-Bernoulli or Timoshenko quantities

In loving memory of
my parents

Contents

List of Tables

List of Figures

Chapter 1

Literature Review

1.1 Introduction

Rotating tapered beams[1] represent a good model for many engineering structures and find practical applications in aircraft propellers, helicopter blading, high speed flexible mechanisms, robot manipulators and spinning space structures. Taper is desired for optimum distribution of weight and strength and is often motivated by special structural and functional requirements such as changing the bending stiffnesses along the beam in order to satisfy certain constraints that arise from other aspects of the blade design, such as power control or forced response characteristics.

The problem of determining the dynamic modal characteristics (natural frequencies and associated mode shapes) of rotating beams is of paramount importance to the design and performance evaluation, and has been the subject of interest to many investigators. Accurate prediction of the dynamic characteristics of such structures is necessary in the early stages of the design process in order to avoid any possible conditions susceptible to resonance within the range of operating speed, and to prevent any failure that may occur as a result of sustained vibration at or near the resonant frequency range.

Rotating structural components have traditionally been modelled as beams vibrating in flexure. While developing these models, various parameters pertinent to the functional requirements have been added in order to cope with aerodynamic reasons in addition to other technical and economical issues. These parameters include variable and non-symmetrical cross-sections[2],

[1] A beam can be defined as a structure having one of its dimensions (the span) much larger than the other two which define the cross-section. The axis of the beam is defined along the span, and a cross-section normal to this axis is assumed to smoothly vary along the span of the beam.

[2] In such irregular cross-sections the elastic axis does not necessarily coincide with the mass axis of the beam.

pre-twist, pre-cone, pre-lag, setting angle, root offset, taper, rotary inertia, shear deformation. Attached masses, shrouds and springs were also included and various end conditions were considered. In addition, the high speed of rotation generates sizable centrifugal and Coriolis forces that should not be overlooked. Such parameters are crucial to the design evaluation and dynamic performance of rotating structures that comprise basic components in many engineering applications. As a result, these parameters contribute to additional complicated effects[3] that are usually not taken into account in elementary beam theory.

With all parameters present in the model, solving the problem becomes extremely complicated. An exact solution is almost impossible and many simplified mathematical models with a variety of geometries and properties have been developed to investigate the dynamic characteristics of such rotating beams using a variety of methods, for example, the Myklestad method [5, 39], the method of integral equations [12], the power series solution method [16, 20], the Southwell method, the Rayleigh Ritz method [17, 36], the perturbation technique, the transfer matrix approach [35, 37], the Galerkin method [21, 24], the wave propagation method, the dynamic stiffness matrix method [30], the finite difference method [43] and the finite element technique [13, 19, 22, 24, 25, 27].

While the derivations of the equations of motion underlying the aforementioned methods differ from each other in many details, they all rely on a common approach to characterize small deformations in flexible beams.

The numerical accuracy and feasibility of solutions obtained by the different methods remain major issues of interest to researchers in this area. With the recent development of computer hardware and software, the powerful Finite Element Method (FEM) has proved itself capable of formulating complicated structural systems and obtaining accurate results, and has therefore attracted a great deal of attention over the past few decades.

1.2 Literature Survey

Most of the published work devoted to the field of rotating structural components dealing with analytical and numerical methods employed beam models. Many references related to beam vibration problems can be found in the ample literature and the number is increasing rapidly. Because of the voluminous body of the existing literature, the scope of the present review has

[3]Such effects include coupled bending-bending, bending-torsion, extension -torsion, stretching and bending and warping of the cross-section during torsion. Other effects related to aerodynamic forces, buckling and thermal stresses have also been reported in the literature. In addition, inertia or dynamic coupling effects that result from the reference motion and the elastic deformations have become major issues of concern to some researchers.

been directed to the relevant issues of primary concern, that deal only with rotating beams. The majority of the published models deals with two-dimensional formulations[4]. Three dimensional models[5], however, have not yet received similar attention. Compared to rotating uniform and tapered Euler-Bernoulli beams [6-19], the problem of rotating tapered Timoshenko beams has received less attention inspite of its importance in many engineering systems. Moreover, solutions reported in the current literature are less than adequate when compared to the simpler case of the rotating uniform Euler-Bernoulli beams.

1.2.1 History of Bending Vibration

The theory of bending vibration of beams goes back to the eighteenth century when Daniel Bernoulli and Leonhard Euler first derived the differential equation for the lateral vibration of a slender beam. Since then, this theory has been known as the classical[6] Euler-Bernoulli Beam Theory (EBT) in which it is assumed that plane cross-sections initially perpendicular to the neutral axis of the beam remain planar and perpendicular to the neutral axis after deformation. The equation of motion for such a beam is a fourth-order differential equation with constant coefficients and its solution is well established in the literature. This theory predicts the frequencies of the flexural vibrations of the lower modes of slender beams with adequate accuracy. For higher modes, however, it is known to give higher frequency values than those obtained by experiment. This theory represents a simplified engineering approximation to the bending vibration of beams.

Almost a century later, Rayleigh [1] modified the classical theory of beams to include the effect of rotary inertia[7]. However, the improved version did not adequately explain the higher modes until 1921, when Timoshenko [2] introduced an additional correction for the transverse shear deformation which was known later as Timoshenko Beam Theory (TBT)[8]. In this refined

[4]In two-dimensional formulation, it is assumed that the flexural vibrations of beams occur in one plane only.

[5]If bending deformations occur in two perpendicular planes, the flexural vibration is said to be of a three dimensional type.

[6]It is also referred to as the Elementary Beam Theory (EBT) or the thin beam theory by many authors.

[7]Rotatory inertia is also used in some references. This effect includes inertia due to the rotation of the beam cross-section during flexural vibration. Rotary inertia is equivalent to an increase in mass and therefore will cause a decrease in natural frequency.

[8]This theory is also referred to as Thick Beam Theory (TBT) by many authors. TBT is applied when the cross-sectional dimensions of the beam are not small compared to its length and/or when higher modes are required; i.e; the effect of shear deformation and rotary inertia is function of the wavelength of vibration. It is more pronounced as the mode order increases.

With reference to TBT, there is a footnote in: E. B. Magrab, "*Vibration of Elastic Structural Members*", Sijthoff & Noordhoff, 1979, p. 171, which states that: *Although Rayleigh is credited with developing the rotary inertia correction and Timoshenko with the shear correction, a footnote in: S. Timoshenko: Vibration Problems in Engineering, (Van Nostrand, New York), 2nd Edn., 1937, p. 338, states that both these corrections are given by M. Bresses in his cours de Mécanique Appliquée, (Mallet-Bachelier, Paris), 1859, p.126.*

theory, which is less restrictive than the EBT, it is assumed that plane cross-sections, initially perpendicular to the neutral axis of the beam, remain plane but no longer perpendicular to the neutral axis after deformation[9]. Moreover, the effect of shear is insignificant in the lower modes but increases in the higher modes and causes a significant decrease in the frequency value. The governing equations are two coupled partial differential equations expressed in terms of two dependent variables: the flexural displacement and the angle of rotation due to bending. For a uniform beam, the two coupled partial differential equations can be re-expressed as one fourth-order partial differential equation in terms of the flexural displacement or the angle of rotation due to bending. However, this is not the case for non-uniform beams. Solving the equation for a non-rotating uniform rectangular section beam with simple supports, Timoshenko [2] showed that the correction due to shear is approximately four times larger than the correction due to rotary inertia.

Among the several values of the shear correction factor[10] that have been suggested in the literature [2, 77, 78], those proposed by Cowper [78] appear to be widely accepted and are therefore frequently used. The shear deformation parameter[11] which represents the ratio between the bending and shear stiffnesses has also been introduced in TBT and has been taken as a constant or averaged within the element as reported in [24]. The most widely encountered expression for the shear deformation parameter is the one given by Przemeniecki [92].

1.2.2 Stiffening Effect of Rotation

In the 1920's the power generation industry designed turbo-machines to operate at substantial loads and speeds above the lowest critical speed. The stiffening effect of rotation was first acknowledged in 1920 by Lamb and Southwell [3]. In their attempt to predict the fundamental frequency for rotating components, Lamb and Southwell introduced the effect of stiffening caused by the spin of a disc through a general approximate relation of a lower bound form

$$\lambda_{Ri}^2 = \lambda_{Ni}^2 + \overline{\Omega}^2 \tag{1.1}$$

[9]The material here exhibits great flexibility in transverse shear contradicting the usual assumption of inifinite rigidity in transverse shear postulated by the EBT. In TBT, the slope of the deflection curve consists of two components, one caused by bending and one by shear.

[10]Since the shear is not uniformly distributed over the cross-section of the beam, a shear correction factor κ that depends on the shape of the cross-section is introduced in TBT.

[11]The shear deformation parameter Φ is defined by the relation $\Phi = 12EI \;/\; \kappa GAl^2$ where E is the Young's modulus of elasticity, G is the shear modulus of rigidity, κ is the shear correction factor, A is the cross-section area, I is the second moment of area and l is the element length. A detailed proof for the expression of Φ can be found in reference [75].

where $\overline{\Omega}$ represents the rotational speed parameter[12] and λ_{Ni} and λ_{Ri} are the non-dimensional natural frequencies[13] of the i^{th} mode of the non-rotating and rotating disc, respectively[14].

In a subsequent paper, Southwell and Gough [4] extended the previous work to include many blade shapes such as the uniform cantilever and the knife-edged wedge. They used Rayleigh's quotient[15] in order to estimate the fundamental natural frequency and established an upper bound relation of the form

$$\lambda_{Ri}^2 = \lambda_{Ni}^2 + S_i \overline{\Omega}^2 \tag{1.2}$$

where S_i is a constant that corresponds to the i^{th} mode. This is referred to as the Southwell's coefficient (SC)[16] and depends on the form of the blade. Thus, the value of λ_{Ri} may be determined within upper and lower limits of error. Solving the problem for the rotating uniform cantilevered blade, the authors found $S_1 = 1.193$. For the knife-edged wedge problem, they found $S_1 = 1.455$ and $S_1 = 1.524$ using a graphical and a tabular method, respectively. From these predictions, it can be concluded that the two methods are in close agreement for the evaluation of the SC corresponding to the fundamental mode. Furthermore, these results show the dependence of the SC on the different shapes of the blade. The upper bound relationship proposed by Southwell and Gough [4] is very practical since prediction of the frequency of the rotating beam may be found from knowledge of the corresponding spin parameter and the natural frequency of the non-rotating beam. Moreover, it represents a very economical and concise way of displaying and interpreting data for rotating beams.

While several attempts have been made in the literature to extend the Southwell relation to rotating structures with different material and geometrical properties [9, 10, 23, 24, 29, 79], focus has been made on the refinement of the expression of S_i and its dependence on the different

[12]Spin parameter and non-dimensional speed of rotation are sometimes used instead. In this relation, and in what follows, the rotational speed parameter is assumed to be constant, that is there is no angular acceleration.

[13]Frequency parameter is also used instead of non-dimensional natural frequency.

[14]The above relation is the non-dimensional version of the Southwell relation. The dimensionalized form is $\omega_{Ri}^2 = \omega_{Ni}^2 + \Omega^2$, where Ω represents the speed of rotation and ω_{Ni} and ω_{Ri} are the natural frequencies of the i^{th} mode of the non-rotating and rotating disc, respectively. Here, the quantities Ω, ω_{Ni} and ω_{Ri} are expressed in (rad/sec).

[15]Rayleigh's quotient known as Rayleigh's energy method is an approximate method for estimating the lower frequencies of vibrating bodies. It is defined as the ratio of the maxima of the potential energy to the kinetic energy by the following relation

$$\overline{\omega}_{Ri}^2 = \frac{V_{\max}}{T_{\max}}$$

where $V_{\max}$ and $T_{\max}$ are respectively the maximum potential and kinetic energy. For rotating beams, however, the potential energy includes a part associated with the centrifugal- force field in addition to the strain energy.

[16]Southwell's coefficient and Southwell's relation are often referred to as Southwell's method, since he first noticed the important property that the frequency prediction is a lower bound.

parameters included in the formulation of the beam model.

Most of the investigations encountered in the literature used SC corresponding to the fundamental mode based on two dimensional EBT and neglected the effect of taper. One of the objectives of this thesis is to find SC's corresponding to the lowest four bending frequencies of a rotating three dimensional beam including pre-cone, setting angle, rotary inertia and shear deformations in addition to taper in two directions.

1.2.3 Planar Rotating Beams

Euler-Bernoulli Beam

The inclusion of a setting angle[17] ψ, in beam vibration problems was originated by the work of Lo and Renbarger [6] in 1951. They derived a non-linear differential equation for bending vibration of a rotating uniform Euler-Bernoulli beam clamped to a rigid hub and vibrating in a plane making an angle $\left(\frac{\pi}{2} - \psi\right)$ with the plane of rotation. For $\psi = 0°$ the motion is known to be out-of the plane of rotation and for $\psi = 90°$ the motion is in the plane of rotation[18]. In this formulation, the non-linear term which appears as a function of ψ arises from the Coriolis acceleration due to the precession of the hub. For zero setting angle, the effect of Coriolis forces vanishes while for low rotational speed it becomes small and therefore can been neglected as in [6]. Lo and Renbarger [6] showed that the frequency parameters at any arbitrary setting angle ψ are related to the frequencies at $\psi = 0°$, by the non-dimensional relation

$$\lambda_{Ri}^2 = \lambda_{Ri0}^2 - \overline{\Omega}^2 \sin^2 \psi \tag{1.3}$$

where λ_{Ri0} and λ_{Ri} represent respectively, the frequency parameter of the i^{th} mode at zero and at an arbitrary setting angle[19]. In the above, the term $\overline{\Omega}^2 \sin^2 \psi$ is a softening effect which opposes the stiffening effect of rotation shown in the Southwell's equation. For $\psi = 0°$, this term

[17]Some authors used stagger angle, pitch angle and blade angle instead. The angle by which the beam is mounted embedded (*encastré*) at the root on the periphery of the hub with the plane of rotation is called the setting angle ψ. Usually this angle is positive counterclockwise. Few investigators considered ψ in the clockwise direction or the setting angle to be $\left(\frac{\pi}{2} - \psi\right)$. The setting angle in the helicopter area is analogous to the pitch angle of the blade, which must be adjusted in order to control the thrust and force distribution over the rotor disk.

[18]Sometimes, these are called flapping and lead-lag motions, respectively. Flapping is the up-and-down (vertical) movement of the beam with respect to the plane of rotation. Lead-lag or leading and lagging is the horizontal movement that occurs in the plane of rotation.

In this research, it is presumed that the setting angle is taken in the counter-clockwise direction and the width of the cross-section is larger than its depth.

[19]The dimensionalized form of this formula can be written as $\omega_{Ri}^2 = \omega_{Ri0}^2 - \Omega^2 \sin^2 \psi$, where Ω represents the speed of rotation and ω_{Ri0} and ω_{Ri} are the natural frequencies of the i^{th} mode at zero and at an arbitrary setting angle, respectively.

vanishes and for $\psi = 90°$ it is maximum and dominates in certain cases the stiffening effect. Lo and Renbarger [6] concluded that when the Coriolis effect is neglected, the modes of vibration become independent of the setting angle ψ since the term $\overline{\Omega}^2 \sin^2 \psi$ does not vary with the mode number. With knowledge of the spin and the out-of-plane or in-plane frequency parameters along with this relationship in hand, the in-plane or out-of-plane frequency parameter is easily investigated without recourse to further extensive calculations.

In connection with the above Southwell relation, it can be easily shown that if the relationship given by Lo and Renbarger [6] is substituted into the Southwell relation, the resulting out-of-plane and in-plane Southwell coefficients differ by unity, regardless of the mode considered. This is true provided that the beam is slender and has constant stiffness and inertia properties. This characteristic was shown by Naguleswaran [83] and has also been shown to be the case for rotating tapered Timoshenko beams as reported by Bazoune *et al.* [29]. This formula along with the Southwell relation provides a well suited tool for frequency estimates at a preliminary stage design.

Later, Lo [7] simplified the previous problem by assuming the blade to be rigid everywhere except at the root where it is connected to the rotating shaft by means of a torsional spring. In an attempt to obtain a correlation with the above formulae, Lo found that $S_i = \cos^2 \psi$. This means that the SC is the same for all modes which is contradictory to the Southwell relation where S_i varies from one mode to another. In addition to the setting angle, there are however, as found in the literature, other factors that have a strong effect on SC such as the hub radius parameter[20] R. In solving the problem of the rigid blade, Lo [7] neglected the Coriolis acceleration and presented a solution in a phase plane. Compared to the case when the Coriolis acceleration was included, the discrepancy in the frequency estimate was found to be of the order of 0.7%. Lo [7] concluded that the percentage error in frequency is a function of the frequency ratio $\lambda_{Ni}/\overline{\Omega}$, the setting angle ψ, and the ratio of the amplitude of vibration to the length L of the beam.

Sutherland [5] developed a method based on a Myklestad type method by a suitable modification of the shear and moment equations at consecutive stations of the beam. The effect of the centrifugal forces for the uncoupled bending vibrations of a rotating blade that is vibrating in the plane of rotation was taken into account. In this method, the elastic beam is divided into a number of sections. Each section consists of a weightless span and a concentrated mass. Calculations are performed in a tabular form based on an assumed frequency estimate and proceed through sets of relations to a final expression which determines an approximate value of the fre-

[20]The hub radius parameter, a non-dimensional quantity, is defined as $R = \mathcal{R}_o/L$, where $\mathcal{R}_o$ is the hub radius (root offset) and L is the length of the beam.

quency. A new frequency is then assumed, and the calculations are repeated until a convergent frequency corresponding to zero or a small error is obtained. Calculations of the frequencies were performed through a numerical example by considering a wedge beam tapered in the thickness direction and rotating at 400 rad/s for a 2 in. (5.080 cm) hub radius. The out-of-plane and in-plane frequencies were found to be 941.6 rad/s and 853 rad/s, respectively. For a larger hub of 38 in. (96.520 cm) offset and rotating at a speed of 200 rad/s, the predicted out-of-plane and in-plane frequencies were 916.5 rad/s and 894.4 rad/s, respectively. The formula proposed by Lo and Renbarger [6] can be easily used to check the accuracy of the in-plane frequencies manifested in this investigation. For this particular example and for the given out-of plane frequencies, the in-plane frequencies were found to be 852.41 rad/s and 893.89 rad/s for small and large hub radii, respectively. It is clear that for both hub radii and speeds, the results of Sutherland [5] are in good agreement with the previous formula. On the other hand, it was concluded that the in-plane and out-of-plane frequencies differ by an amount depending upon the hub radius. This is not true. It was proved by Lo and Renbarger [6] and later by many others, that in the absence of Coriolis forces, the difference between the out-of-plane and in-plane frequencies depends on the quantity $\overline{\Omega}^2 \sin^2 \psi$. In terms of SC, this difference is equal to unity as stated previously. Although the procedure presented by Sutherland [5] is straightforward, even with few degrees of flexural freedom, it is cumbersome and impractical.

Carnegie [8] derived an expression for the potential energy increase due to centrifugal effects of a straight uniform symmetrical cross-section blade mounted at the root on the periphery of a rotating rigid hub and making a setting angle $-\psi$ with the plane of rotation[21]. The derivation was based on small deformations and neglected the effect of shear distortion and rotary inertia. The Coriolis effect, being small, was also neglected. In his investigation, Carnegie [8] established an approach to the calculation of the frequency problem utilizing Rayleigh's quotient. Based on this formulation, the author established an upper bound estimate for the non-rotating fundamental frequency parameter of a straight uniform symmetrical cross-section blade. Numerical prediction for the non-rotating fundamental frequency parameter was found to be 3.53 which represents an error estimate of 0.4% when compared to the exact[22] value 3.51602. In a second example, Carnegie found that when a steel blade of 9 in. length is rotating at 1000 rad/s, the fundamental flapping and lead-lag frequencies were, respectively, 11.3 and 13.1 times

[21] According to the previous definition, the negative sign here indicates that the setting angle is taken in the clockwise direction.

[22] In the context of beam theory, analytical solution is often referred to as exact solution by many authors. It is not, of course, exact in the continuum sense since the beam theory itself is only an approximation method.

greater than the non-rotating frequency. Thus, owing to the change in setting angle from 0 to 90° the increase in frequency is 16%.

Based on the geometric properties[23] provided in reference [8], the flapping and lead-lag frequencies were reproduced and found to be 16.9 and 15.6 times greater than the non-rotating frequency. Consequently, the flapping frequency represents an increase of 8.33% when compared to the lead-lag one.

In order to check how the predictions presented by Carnegie stand up with the above formula[24] proposed by Lo and Renbarger [6], it was found that the lead-lag frequency is 12.98 greater than the non-rotating frequency which is in excellent agreement with the results provided by Carnegie [8].

Using a successive iteration procedure, Schilhansl [9] investigated the stiffening effect of the centrifugal force caused by small rotational speed and obtained an upper bound estimate for the fundamental bending frequency by means of an explicit expression of the Southwell coefficient for a rotating beam with a clamped root and a setting angle. The relation derived by Schilhansl [9] shows that the SC varies linearly with the hub radius parameter R, and depends upon the setting angle ψ. This relationship, plotted for setting angles of $\psi = 0°$ and $90°$, shows that SC for flapping and lead-lag modes are parallel. The former is higher than the latter, and the difference between them is independent of R and is equal to unity as mentioned above.

Pnueli [10] extended the work of Schilhansl [9] to account for high rotational speed and provided a lower bound estimate for the Southwell coefficient corresponding to the fundamental bending mode. However, the work described in references [9] and [10] is limited to the fundamental bending mode of a slender beam with constant mass and stiffness properties.

In accordance with Lo and Renbarger [6], Rao and Carnegie [11] reported that if the flexural vibration of a rotating cantilever beam occurs in a plane other than perpendicular to the plane of rotation then the bending problem is a nonlinear one because of the presence of Coriolis forces. They used the Ritz energy method in conjunction with the appropriate Lagrangian function to solve the problem of the free and forced vibrations with a harmonic exciting force of known frequency, acting at the free end of the cantilever beam. They assumed cubic polynomial shape functions for the first two harmonics and obtained a solution in a parametric form for the fundamental frequency of the non-rotating beam. The frequency value obtained was higher than

[23]The material properties were not provided by Carnegie [8]. Therefore, it has been assumed that the elastic modulus of elasticity $E = 200$ GPa, the density $\rho = 7850$ kg/m^3 for steel.

[24]For this setting angle configuration, the above formula has been modified to read $\lambda_{Ri0}^2 = \lambda_{Ri}^2 - \overline{\Omega}^2 \sin^2 \psi$ in order to compare results provided by Carnegie [8]. Note that $\overline{\Omega} = 22.6$, $\lambda_{Ri} = 46.243$ and $\lambda_{Ri0} = 39.889$.

the analytical one by an amount of 0.6%. In addition, they arrived at the same formula derived by Schilhansl [9] for the SC corresponding to the fundamental flexural mode. The authors concluded that the non-linear term becomes more influential as the speed of rotation increases.

Jones [12] reduced the problem of determining the natural frequencies of the transverse vibration of a rotating uniform Euler-Bernoulli beam carrying a tip mass[25] to the study of an eigenvalue problem for variable ratio of the tip mass to the beam mass. She used the method of integral equations to calculate lower bound estimates for the eigenvalue problem. This method is based on an asymmetric decomposition of a Green's function which leads to a Volterra integral equation. Lower bound predictions for the first two lowest modes were shown to increase as the square of the ratio of the tip to the beam mass increases. However, neither the physical interpretation of the different parameters in the formulation of the problem was given, nor were the results explained. In addition, the solution involved such complicated mathematics that, from an engineering point of view, it has little practical value.

Hoa [13] presented a finite element analysis for rotating prismatic[26] beams. The effect of hub radius, setting angle, and tip mass were incorporated into the finite element model. In this analysis, the displacement field is approximated by a third order polynomial and is restricted to the classical Euler-Bernoulli beam theory with equal-length elements. Explicit expressions for the elemental mass and stiffness matrices were derived. The effect of tip mass was added into the mass and the centrifugal stiffness matrices[27], resulting in an increase of both the stiffness and mass matrix of the model. The numerical predictions show that the non-dimensional frequencies are affected by the different parameters incorporated into the model. These include the evidence of a stiffening effect that is produced by the increase in rotational speed and/or hub radius and the influence of the setting angle which is significant on the fundamental mode and is negligible on higher ones. The reason for this is attributed to the fact that the softening term $\Omega^2 \sin^2 \psi$ is constant regardless of the mode considered; therefore it has more influence on modes with small frequency parameters. On the other hand, results show that for a fixed rotational speed, the fundamental frequency increases as the tip mass decreases. The relationship between the fundamental frequency and the rotational speed parameter shows a linear behavior for high tip mass value[28] and passes through the origin (starting at zero for zero rotational speed parameter)

[25]The addition of a tip mass is known to increase both the airflow as in a wind turbine and the flexing motion as in flexible blade autocooling fans.

[26]Some authors used prismatic beam instead of uniform beam.

[27]The tip mass has an effect on the mass matrix of the last element only since it is associated with the tip of the beam.

[28]The author assigned a value of ∞ to high tip mass value.

with a slope of unity showing a lower bound estimate for infinite tip mass. For low tip mass value, however, including zero tip mass, this relationship is no longer linear and exhibits nearly a concave parabolic shape. Furthermore, the case of zero tip mass shows an upper bound estimate for the predictions of the fundamental frequency. Moreover, increasing the tip mass is shown to lower the second and third frequency parameters at low rotational speed and to increase them at high rotational speed. The justification for this is since for low rotational speed, the effect of tip mass on the mass matrix is dominant and tends to lower the frequencies, whilst as the rotational speed increases the stiffness matrix of the system increases which in turn increases the frequencies as reported by Hoa [13]. Other results show the variation of frequency parameters of the fundamental mode for different values of setting angle[29]. The case for which the motion is neither in-plane nor out-of plane represents a three dimensional vibration since the motion has two components: one in the flapwise direction, the second in the edgewise direction. Therefore, it is necessary in such cases to specify which component has been taken into consideration[30]. However, the author considered only the case of the flapwise component and has neglected the Coriolis effect.

Later, Hoa *et al.* [14] indicated a sign error in the middle term of the element of the centrifugal stiffness matrix in reference [13] which led to eigenvalues that are too high. Consequently, some results were reproduced and compared with the exact solution for the case of a rotating beam with zero tip mass and different hub radius including 0 and 1. As a result, a good agreement was found between the new predictions and the exact values.

Hodges and Rutkowski [15] presented Legendre polynomial shape functions in conjunction with the FEM to study the frequencies of free vibration rotating beams. In this method, the displacement function is expressed in terms of a complete[31] set of shifted Legendre polynomials. The degree of accuracy depends on the number of elements i used and the number of terms chosen in the series, i.e., the highest degree n of the series. As a special case for this procedure, the authors reported that for $n = 3$, this will yield the standard beam finite element shape functions given in reference [92]. The lowest three frequency parameters were presented for rotating uniform and tapered cantilever beams at different values of i and n. Results corresponding

[29] If the setting angle differs from 0° or 90°, the vibrational motion occurs in a two perpendicular planes different from the out-of-plane and the in-plane, respectively. The bending modes of vibration in such cases are referred to as flapwise bending and chordwise (edgewise) bending.

[30] If the cross-section of the beam is set with a setting angle ψ, this will cause the second moments of area and the product moment of area of the beam to be functions of the setting angle. The presence of the product moment of area in the strain and kinetic energy expressions, will cause the flapwise bending and edgewise bending to couple, thus resulting in a bending-bending vibration type. For $\psi = 0°$ or $\psi = 90°$, this coupling term vanishes.

[31] In the FEM context, this means that all the terms are present in the series.

to $i = 1$ and $n = 15$ converged to the analytical solution. Other non-dimensional frequency predictions were shown for a non-uniform beam that is linearly tapered in the depth direction only. The fundamental frequency for a tapered beam was shown to be higher than that of a prismatic beam whilst the second and third frequencies are lower than those of the uniform beam. A careful examination of these predictions for the rotating tapered beam revealed a small discrepancy in all the frequencies when compared to the present investigation. This issue has been raised in reference [43]. The reason for this discrepancy, as addressed in [43], may be due to either an error in reporting the results in reference [15] or an inadequacy of the polynomial/element chosen to represent the vibration characteristics. Though this method is seen to give accurate results for the flapping motion of rotating uniform beams with simple geometries, it is claimed that it can be extended to incorporate coupled bending bending torsion type and extension with geometric nonlinearity[32]. However, the effect of the setting angle was neglected in all the predictions shown. The investigation presented by Hodges and Rutkowski [15] is limited to the flapping motion of slender beams and did not include the Coriolis effect.

Wright *et al.* [16] utilized Hamilton's principle in the formulation of the problem of a rotating beam with a finite hub radius where both flexural rigidity and mass distribution varied in a prescribed manner. A power series solution in the form of the method of Frobenius was employed to obtain estimates for the frequencies and mode shapes. This procedure leads to a characteristic equation for which the characteristic determinant must vanish. The square root of the characteristic values (eigenvalues), for which the determinant is zero, represent the natural frequencies of the beam. These frequencies can be found using any available root-finding routine. Numerical predictions were provided for a wide range of boundary conditions including a hinged root which allows a rigid body flapping mode[33] whose fundamental frequency is equal to the speed of hub rotation. Although the method of solution presents results with high accuracy when compared to the exact solution, it cannot be applied to complicated structures. It depends on how many terms are retained in the series solution. Moreover, it involves an extensive use of algebra in addition to computer use for finding the root of the characteristic equation.

The problem tackled by Hoa [13] was extended by Bhat [17] who included the rotary inertia effect of the tip mass. He used orthogonal polynomials in the Rayleigh Ritz method to solve for the natural frequencies of flexural vibrations. He obtained a standard eigenvalue problem of the

[32]Geometric nonlinearity is considered when large deformations and large rotations with finite strains can be accomodated. Consequently, the structure deforms to such an extent that the original geometry and/or position and direction of the loads significantly affect the structural behaviour.

[33]In rigid body mode the elastic element undergoes no elastic deformation. For non-rotating beam the fundamental frequency is equal to zero.

form $\left(\lambda^2 [\mathbf{A}] + [\mathbf{B}]\right) \{\mathbf{v}\} = \{\mathbf{0}\}$. Eigenvalues λ^2 and eigenvectors $\{\mathbf{v}\}$ were obtained by solving this equation. Bhat described this method as advantageous for the deflection shapes because the matrix $[\mathbf{A}]$ becomes diagonal. Despite the method of solution, there are many differences in the formulation of this problem when compared to the work of Hoa [13]. For instance, while Hoa incorporated the effect of stiffening due to rotation into the strain energy expression, Bhat included it into the kinetic energy expression[34]. On the other hand, while Hoa added the effect of tip mass into both the stiffness and mass matrices, Bhat included its effect into the kinetic energy expression only. Nevertheless, the final equations of motion and the associated eigenvalue problem are similar in both formulations[35].

Natural frequencies and mode shapes were presented for different rotational speed and parameter combinations such as tip mass, hub radius and setting angle. Predictions of the natural frequencies versus rotational speed for different tip masses were in good agreement with those presented by Hoa. The results are, in general, similar to those of Hoa except that these predictions show that as the setting angle increases from 0° to 90° the frequency parameters increase[36]. A quick visualisation reveals that when the setting angle is 0°, the beam becomes weak in bending in the plane of rotation and hence the bending frequency is less. On the other hand, only the second moment of area I_{xx} is used, and in the transverse direction, the second moment of area is infinite. Hence as the setting angle is increased from 0° to 90° the beam becomes stiffer in the plane of rotation. The effect of moment of inertia on the tip mass was seen to depress the frequency values as the moment of inertia increases with increasing speed of rotation for both flapping and lead-lag motion.

Later, Kim and Dickinson [18] clarified that the $[\mathbf{A}]$ matrix in the work of Bhat can be diagonal only if the rotary inertia of the concentrated mass and of the beam cross-section are negligible (treated as zero) and if both the distributed and concentrated masses are included in the construction of the orthogonality conditions used to generate the set of admissible functions.

Khulief [19] used the FEM to extend the work of Hoa [13] and Bhat [17] to linearly tapered beams and derived explicit expressions for the finite element mass and stiffness matrices using consistent[37] mass formulation. Unlike Hoa [13] and Bhat [17], Khulief [19] neglected the effect

[34]Since the stiffening effect due to rotation involves the rotational speed Ω^2, most of the investigators include this effect into the strain enegy expression. In addition, the stiffness matrix of the rotating beam includes the centrifugal stiffness matrix, a part associated with the centrifugal-force field.

[35]In the abscence of Coriolis forces, the Ω terms in the standard eigenvalue problem $\left(\overline{\omega}^2 [\mathbf{A}] + [\mathbf{B}]\right) \{\mathbf{v}\} = \{\mathbf{0}\}$, are in the matrix $[\mathbf{B}]$ which constitutes the stiffness term.

[36]At first glance, this looks contradictory to the previous investigations. This is because the setting angle here is taken as the angle between the Y- and x- axis. The description of the coordinate systems is not consistent with the figure shown. For more details, refer to reference [17].

[37]When the element mass matrix is formulated from the same shape function used for the element stiffness

of hub radius and assumed that the tip mass has negligible rotary inertia effect. The first and second bending frequencies were shown to exhibit a stiffening effect for different taper ratios including beams with fixed and hinged-free end conditions. A crossover between the frequencies of the beam was also noticed at different taper ratios.

Timoshenko Beam

Several attempts have been made by many investigators to include the effect of shear deformation and rotary inertia on the frequencies of vibration of rotating uniform beams. The inclusion of these parameters is necessary when accurate higher bending modes are desired.

Du *et al.* [20] used a Newtonian approach to the formulation of the equations for the free vibration of a rotating uniform beam. They extended the Frobenius series solution developed in [16] to include the effect of shear deformation, rotary inertia and a tip mass. Dimensionless frequencies were presented in both graphical and tabular forms. Except for only one table, results reported in tabular form were for the case of rotating Euler-Bernoulli beam for a wide range of boundary conditions including a hinged root. Again the effect of tip mass for a cantilever Euler-Bernoulli beam indicates that the fundamental frequency decreases as the tip mass increases which is in agreement with Hoa [13] and Bhat [17]. For higher modes however, it was noted that for rotational speed parameters greater than unity, the frequencies increase as the tip mass increases, while for rotational speeds equal to 0 and 1, the frequencies exhibit a reverse trend. Other results (graphical form) show the relationship between the reciprocal of the slenderness ratio[38] (r_{gy}/L) versus the ratio between Timoshenko and Euler-Bernoulli frequency parameters. In these figures it was shown that for $(r_{gy}/L) = 0$, the ratio of the frequency parameters was equal to unity showing that TBT converges to EBT. As (r_{gy}/L) increases, this ratio was shown to decrease which indicates that as the thickness of the beam increases, Timoshenko beam frequencies decrease.

Wang *et al.* [21] extended the use of shifted Legendre polynomials as shape functions in conjunction with the extended Galerkin's method for the prediction of natural frequencies of a uniform Timoshenko beam that is mounted on the periphery of a finite rigid hub and making a setting angle with the plane of rotation. The results of simulation show evidence of the stiffening effect to rotating Timoshenko beams. Shear deformation and rotary inertia effects on

matrix, the mass matrix is said to be consistent mass matrix.

[38]The slenderness ratio is defined as (L/r_{gy}), where L is the length of the beam and $r_{gy} = \sqrt{\frac{I_{oyy}}{A_o}}$ is the radius of gyration with respect to the y-axis in which I_{oyy} is the root second moment of area with respect to the y-axis and A_o is the root cross-section.

natural frequencies increase appreciably with the mode number. It was also noticed that as the slenderness ratio increases, the ratio between Timoshenko and Euler-Bernoulli frequency tends to unity showing that TBT merges to EBT which is in agreement with Du *et al.* [20]. Moreover, it was concluded that the effect of shear deformation is generally larger than that of rotary inertia for the non-rotating beam but their relative effects may be reversed for higher mode frequencies of the rotating beams owing to centrifugal stiffening effects. On the other hand, it was shown that for Timoshenko beams, the effect of setting angle is more pronounced on lower mode frequencies and is insignificant on higher ones as discussed earlier for Euler-Bernoulli beams.

Yokoyama [22] developed a finite element procedure in conjunction with the Lagrangian function to determine free vibration modal characteristics for the beam discussed in [21]. Explicit expressions for the elemental stiffness and mass matrices were presented including shear deformation and rotary inertia effects. Despite the method by which the problem is formulated and solved, reference [22] did not address any extension of the work developed in [21]. Results presented in reference [21] were reproduced by Yokoyama [22] who used 16 finite beam elements of equal length. A perfect agreement was found between the two methods of solution. Similar conclusions to the ones drawn by Wang *et al.* [21] were reported.

Lee and Kuo [23] extended the work of Wright *et al.* [16] and Schilhansl [9] to account for shear deformation and rotary inertia effects using the Rayleigh quotient to derive an upper bound estimate for the SC for the fundamental bending frequency of a rotating uniform beam with a general elastically restrained root for which translational and rotational flexibility were considered. The upper bound estimate was found to contain corrections depending on the shear deformation parameter Φ and the inverse of the slenderness ratio (r_{gy}/L). When these effects were ignored, the SC for a cantilever beam was found to be in agreement with the one provided in [9]. The upper bound estimate for the fundamental mode was also shown to be in good agreement with the numerical predictions obtained by Wang *et al.* [21] for Euler-Bernoulli beam. However, the fundamental bending mode was seen to be sensitive to the elastic end restraint. The authors concluded that the effect of translational flexibility at the root is greater than that of rotational flexibility.

Putter and Manor [24] used the FEM for predictions of frequencies of a Timoshenko beam that is clamped at the periphery of a rotating finite rigid hub at 90° setting angle. The analysis was based on a fifth-order-polynomial displacement field in which the deflection and slope at the ends were taken as common nodal degrees of freedom along with two integrals within the

element as nodeless additional degrees of freedom. Results for uniform Euler-Bernoulli beam were presented and compared to those of Dokainish and Rawtani [80] who used a plate element, and to the formula presented by Schilhansl [9]. Comparison between these investigations shows good agreement for low rotational speed parameters and for small values of the nondimensional hub radius R, but for high rotational speed and large values of R, these results were not close to each other. The reason for this discrepancy could be attributed to two facts; the first one because the stiffening effect manifested by the upper bound estimate of SC reported in [9] is no longer linear with R for high rotational speeds. The second one because the comparison was made between two different structures, namely, a plate which has a low aspect ratio[39] and a beam which has a large aspect ratio. In a second example, the authors considered a Timoshenko beam for which (r_{gy}/L) was between 0.025 and 0.05. The stiffening effect was manifested for both cases for the first two lowest modes. However, it was seen that for low values of R, increasing (r_{gy}/L) reduces the frequencies while for larger values of R, its effect was negligible. The effect of (r_{gy}/L) was seen to be more influential on higher modes. In the last example, the authors neglected the effect of shear deformation and rotary inertia in considering a turbine blade with shrouded mass which was assumed to be a concentrated mass attached to the node. Again, the predictions show a stiffening effect for the first two lowest modes, and as the shroud to beam mass ratio increases, the frequencies increase. Based on these numerical predictions, the authors provided two Southwell coefficients for the first and second mode for the range $0 \leq \Omega \leq 10$ in which the effect of the shroud mass was manifested. The suggested Southwell coefficients were shown to vary linearly with R and with the shroud to beam mass ratio.

Few attempts have been made to further extend the analysis of the vibration of rotating Timoshenko beams to include the effect of taper on the dynamic characteristics of such structures. Recently, Bazoune and Khulief [27] first developed a new finite beam element for the free vibration analysis of a rotating doubly tapered Timoshenko beam. The formulation permits any combination of taper ratios as well as unequal element lengths. Explicit expressions for the finite element mass and stiffness matrices were derived using the consistent mass approach, while accounting for centrifugal stiffening effects. The results of simulation were generated for a wide range of rotational speed, width and depth taper ratios including the first ten vibrational modes for both fixed and hinged end conditions. Evidence of new knowledge, due to the effect of tapering, was shown in the reported results of simulation. It was shown that the natural frequencies increase as the rotational speed increases, while they decrease as the taper ratio

[39] Aspect ratio is the ratio of the length of the beam to its width.

increases. However, it was observed that a critical taper ratio exists, after which the frequencies of a rotating tapered beam reverse their trend of change. It is apparent that the stiffening effect due to rotation dominates the softening effect resulting from the decrease of the cross-sectional area due to taper, thus rendering the beam stiffer. Khulief and Bazoune [28] extended the work of [27] to account for different combinations of fixed, hinged and free end conditions. The simulation results presented in [27] and [28] are only for the out-of-plane vibration of rotating tapered Timoshenko beams where the effect of hub radius and setting angle were not considered. Later Bazoune *et al.* [29] further extended the work of [27] to include the effect of hub radius and in-plane vibration by introducing a setting angle ψ into the previous formulation. The in-plane and out-of-plane vibrations were manifested in the predicted results. It was clearly shown that the in-plane frequencies are always lower than the out-of-plane frequencies. This fact is in agreement with the above formula provided by Lo and Renbarger [6] and can be easily verified. On the other hand, explicit expressions for the Southwell coefficient corresponding to the fundamental flapping and lead-lag frequencies were reported for different taper ratios including rotary inertia and shear deformation effects. Comparison has been made for the case of uniform Euler-Bernoulli beam and has been found to be in excellent agreement with the work of Schilhansl [9]. Further, it has also been shown that the relationship between SC and R is linear for uniform and tapered Timoshenko beams and depends on the setting angle. Moreover, the SC for both flapping and lead-lag mode are parallel and the difference between them is always unity regardless of the hub radius parameter R as stated earlier.

Mulmule *et al.* [25] extended the work of Yokoyama [22] to include depth taper and claimed that their results compared favorably with results attributed to Hodges and Rutkowski [15]. This was disputed by Naguleswaran [26] who pointed out that the method used in reference [15] yields more accurate frequencies than those obtained in this investigation. The results presented for the case of uniform Timoshenko beam agree with those of Yokoyama [22], which is evident because the methods used in references [22] and [25] are very similar as addressed by Naguleswaran [26]. In addition, the authors reported that the shear correction factor taken in their investigation was $\kappa = 5/6$ which cannot produce the same results presented by Yokoyama [22] who used a value of $\kappa = 0.85$. Numerical predictions reveal evidence of a stiffening effect as the hub radius and/or the speed of rotation increase, which is a common behavior of rotating uniform beams. The lead-lag frequency parameters are lower than those of the flapping motion. This trend is also common to rotating prismatic beams. The new knowledge is manifested on some graphical predictions that show the variation of the lowest two lead-lag and flapping frequency parameters as a function

of the taper ratio, rotational speed and hub radius parameters[40]. These results show that the fundamental frequency parameter increases as the taper ratio increases which is in agreement with the conclusion drawn in reference [27]. On the other hand, the authors concluded that as the taper ratio increases, the frequency parameter of the second mode decreases. This is not consistent with the trend shown by the results. The predictions show that, when neglecting the hub radius, the second frequency parameter for uniform beams (zero taper) are higher than those of tapered beams. Those corresponding to a taper ratio of 0.5 are lower than those of uniform beams and higher than those corresponding to a taper ratio of 0.1. For a hub radius parameter of 2, the labeling corresponding to a taper ratio of 0.1 was missing while the one corresponding to 0.0 was duplicated. This was misleading in connection with the conclusion drawn by Mulmule *et al.*

1.2.4 Spatial Rotating Beams

Euler-Bernoulli beam

In real life problems, bending deformations occur simultaneously in two different perpendicular planes. The vibrational motion in this case is said to be of a three dimensional type. These flexural motions are usually referred to as flapwise (flatwise) bending and chordwise (edgewise) bending.

Three dimensional structures include helicopter blading, long flexible rotating space booms and aircraft propellers. They are of considerable interest and technological importance in many engineering applications. Three dimensional prismatic and tapered beams represent a more realistic model for such structures. Therefore, an effective and accurate three dimensional beam element formulation is needed.

References [30, 33] contain thorough reviews of several approximate methods used in the bending vibrations of rotating beams or blades.

As reported in reference [32], if the centre of flexure coincides with the centre of mass, as for blade cross-section having a two-fold symmetry, then three possible types[41] of free vibration modes occur independently: axial, bending in the two perpendicular principal planes and torsion. Axial modes are generally at higher frequencies and therefore are not considered by most investigators. If the cross-section has only one axis of symmetry, then bending vibrations in the

[40]Values of taper ratio were taken to be 0.0, 0.1 and 0.5, while values for hub radius parameters were 0.0 and 2.0. The range of the rotational speed parameter was from 0 to 10.

[41]By types it is meant the nature or sort of vibration: axial, bending or torsion. Regardless of the bending if it is flapwise or chordwise, it is considered as one type. Thus, three types of vibrations exist.

plane of symmetry are uncoupled but the transverse bending and torsional modes are coupled. With no symmetry, as in an airfoil cross-section, all three types of modes are coupled.

Some investigations were devoted to the formulation and derivation of equations of motion of pre-twisted blades using beam theory [34, 38]. Further, coupling is introduced into the problem if the blade has an initial pre-twist. The most important effect of pre-twist is to couple extension[42] with torsion. The coupling of flexure with torsion and extension with torsion is a rather complex problem that merits much further study. For instance, pre-twist of rectangular cross-section beams causes coupling between the two bending modes while torsional modes couple with extension. With only one axis of symmetry, pre-twist causes all three modes to couple resulting in a coupled vibration of the bending-bending-torsion type.

The inclusion of the effect of torsion was first introduced in the pioneering formulation of elastic rotor blade modeling developed by Houbolt and Brooks [35]. They assumed linear strains and small deformations and derived the equations of motion for combined flapwise bending, chordwise bending and torsion of pre-twisted beams with asymmetrical airfoil cross-section. The equations of motion allowed for variable mass per unit length and stiffness and included many second order terms. A possible solution by the Rayleigh-Ritz method was suggested but no attempt at a solution was made for a practical case because the equations of motion in the general form are too complex to be solved exactly. The authors in [35] concluded that coupling effects due to centrifugal forces may be as important as the inertia coupling effects in the case of asymmetrical non-rotating blades. The equations of motion of Houbolt and Brooks [35] have been widely accepted and are frequently used as the basis for linear rotor blade analysis. Few attempts have been made to obtain solutions for some special cases of reference [35].

Murthy [36] used a transmission matrix method which is basically a transfer matrix method to determine the dynamic characteristics of rotor blades described by Houbolt and Brooks [35]. In order to determine the transmission matrix, the equations of motion must be reduced to a set of first order differential equations. A state vector was chosen to include deflections, slopes, moments and shears. For this purpose, the differential equations were first written in a non-dimensional form and then re-expressed in state form. Once the transmission matrices have been determined, the frequency determinants and the modal functions can be obtained in terms of the elements of the transmission matrix for a given set of boundary conditions. The author treated the problem of combined flapwise bending, chordwise bending, and torsion of pre-twisted blades. Secondary effects such as shear deformation, rotary inertia and non-linear terms were

[42]Extension is used instead of axial deformation by some researchers.

not included. Results were presented for some particular cases of rotating and non-rotating blades. The lowest five frequencies for the combined flapwise bending and torsion of the non-rotating fixed-free end were presented and compared to the integrating matrix method. The agreement between the two different methods was good. Other predictions, including the lowest three natural frequencies of the combined flapwise and chordwise bending were also presented for the case of a rotating fixed-free beam. Again, the stiffening effect was clearly shown for the case of pre-twisted beams.

Swaminathan and Rao [37] modelled a turbomachinery blade as a rotating Euler-Bernoulli beam of rectangular cross-section pre-twisted about its centroidal axis and uniformly tapered in width based on a suitable Lagrangian approach. The solution was tackled by the Rayleigh-Ritz method in which they assumed five term approximate shape functions to satisfy the boundary conditions. The resulting eigenvalue problem was defined and solved for certain special cases. Results of simulation covered a range for which the pre-twist angle was between 0° and 60°. The predictions show that as the pre-twist increases, the fundamental and the third mode increases while the second one decreases. When compared to experimental results, these predictions show a close agreement. On the other hand, it was found that the pre-twist and the width taper effects were opposing each other for the fundamental and third mode, but for the second mode, their contributions were reversed. The speed of rotation in such a tapered and pre-twisted blade is also seen to stiffen the frequencies of vibration. However, Swaminathan and Rao [37] ignored the Coriolis effect.

By means of a transfer matrix technique, Isakson and Eisley [38] studied the effect of pre-twist on the natural frequencies of uniform and tapered non-rotating blades and the effect of pre-twist and setting angle on the natural frequencies of rotating uniform articulated blades and offset of the root support from the axis of rotation. Only bending was considered. In this investigation, the authors' main purpose was to establish a simplified procedure to predict the effect of rotational speed on the natural frequencies. Consequently, they established a relationship to calculate SC by using Rayleigh's quotient and arrived at the same formula proposed by Southwell and Gough [4]. As a result, the authors extended the effect of stiffening introduced by Southwell [4] to pre-twisted rotating blades where the Southwell approximation was again shown to be of a linear relationship with the nondimensioal hub radius R. However, no attempt has been made to derive an explicit expression for the SC and its dependence on taper and pre-twist. In addition, they used the relation developed by Lo and Renbarger [6] for a quick prediction of frequencies at several setting angles. Graphical representation of the numerical predictions of

the lowest four frequencies were presented at different parameter changes and compared to the above two relations. It was found that the simplified approach yields very poor results except at small values of rotational speed. The authors concluded that the fundamental frequency of a rotating pre-twisted cantilever blade depends primarily upon the setting angle and only secondarily on the pre-twist and is less well represented by the Rayleigh-Southwell approximation when pre-twist and setting angle are introduced. On the other hand, the accuracy of the approximation in determining the fundamental frequency of an articulated blade is relatively insensitive to pre-twist and setting angle. Furthermore, the authors found that the relation developed by Lo and Renbarger [6] is useful in determining the fundamental frequency of a pre-twisted cantilever blade when the setting angle is measured at the root and the fundamental mode is not substantially coupled with other modes.

Hodges and Dowell [39] derived nonlinear equations of motion for rotating tapered beams where the centroidal axes offset from the elastic axis with an eccentricity[43]. The equations of motion were derived by means of two complementary methods, Hamilton's principle and the Newtonian approach, and included a variable pre-twist and small pre-cone angle. Many different nonlinear terms in the resulting system of equations were identified namely, the Coriolis contribution terms, the bending-torsion terms and the centrifugal coupling terms that produce nonlinear flap-lag inertial terms. In order to simplify the equations of motion, they used an ordering scheme which is based on the restriction that squares of the bending slopes, the torsion deformation and the chord/radius and thickness/radius ratios are negligible with respect to unity. All remaining nonlinear terms were retained. No attempt was made to produce numerical results from the investigation.

In 1977, Rao and Banerjee [40] considered a cantilever blade with an asymmetric cross-section mounted on a rotating disc where the blade was assumed as a discrete system. By a suitable modification of the Myklestad method, they obtained a frequency equation by deriving generalized polynomial expressions for the slope and deflections. Thus, the frequency equation derived was of an order of 26 and consisted of coefficients of the polynomial varying from the order of 10^{-6} to the order of 10^{-262} for $n = 9$, where n is the number of segments. The accuracy of this method is doubtful since at that time, it was difficult to handle the above mentioned order to obtain an exponent range suitable for the compiler. Numerical predictions were shown for both bending and torsional modes. Frequencies corresponding to bending modes were shown to increase as the speed of rotation increases. When compared to other techniques, a good

[43]For more details of the co-ordinate systems used in this investigation, refer to reference [39].

agreement was noticed between the actual results, the experimental ones and those obtained by using the Galerkin method. However, the authors concluded that the results obtained by this procedure were considered as lower bound estimates because of the discretization of the beam. Better accuracy could be achieved if the beam was divided into shorter sections.

Laurenson [41] presented a very general study for the modal analysis of rotating flexible structures that can be modelled by beams. Only uncoupled bending modes were considered. An eight node finite element discretization was utilized. The study was illustrated by considering a slender prismatic beam with rectangular cross-section and offsets from the axis of rotation by a hub radius $\mathcal{R}_o$. A set of Cartesian co-ordinate systems along with transformation matrices were defined in order to introduce the orientation and angular setting of the beam. For instance, the (XYZ) axes represent a global co-ordinate system with origin on the hub spin axis such that the Z-axis corresponds to the spin axis which rotates with constant angular speed. The X- and Y-axes lie along the principal axes of the cross-section of the beam and the Y-axis being coincident with the undeformed beam centerline. Two consecutive rotations of the beam cross-section were considered in the counterclockwise direction; the first one about the X-axis with an angle θ called a pre-cone, while the second one about the Z-axis with an angle ϕ called a pre-lag. Predictions in graphical forms for the first two lowest modes were manifested for both the (XY)-plane and the (YZ)-plane and covered a wide range of parameter changes of θ and ϕ. The author neglected the Coriolis effect for the configuration corresponding to $\theta = \phi = 0°$. However, the stiffening effect was clearly manifested in both planes and dominated the softening one. For the case when $\theta = 90°$ and $\phi = 0°$, the stiffening effect was seen to have no influence on the beam modal characteristics while the softening term tended to dominate the system in both planes. Laurenson [41] provided a SC for the fundamental flapping mode in which a refinement due to the inclusion of the pre-lag and pre-cone angles was included. When the effect of these angles is ignored, the proposed SC is seen to be in a very good agreement with the one presented by Schilhansl [9] for zero setting angle.

Yoo and Shin [42] derived equations of motions for a rotating uniform cantilever Euler-Bernoulli beam and considered the coupling effect between stretching and bending motions. The Rayleigh-Ritz assumed mode method was used. The lowest two frequencies were presented using ten assumed modes for the uncoupled flapwise and chordwise bending modes. These results were in good agreement with the results of Wright *et al.* [16] and the formula of Lo and Renbarger [6]. On the other hand, the authors obtained SC for the first three lowest modes at a wide range of R. When plotting these values together with R, it was shown that SC is

in linear relationship with R which is in agreement with previous works. Compared to other investigations [9, 10, 23, 24, 29, 40], it was found that predictions reported by Yoo and Shin [42] give the lowest estimates.

Subrahmanyam and Kaza [43] used a refined version of the finite difference method based on a second order central difference to predict the natural frequencies of rotating blades having an unsymmetrical airfoil section where lead-lag, flapping and coupled bending-torsional vibration cases of untwisted blades were considered. The coupling in bending-torsional vibrations is due to the fact that the shear center does not coincide with the centroid of the blade. Lead-lag frequencies including the first two lowest modes were tabulated for a rotating prismatic slender beam having 30 segments ($n = 30$) at a wide range of R. Comparison of these results to those presented by Putter and Manor [24] who used the FEM in their investigation, reveals good agreement between the two methods of solution. Frequencies of the lowest three modes for a rotating Euler-Bernoulli beam tapered in the depth direction were also presented. A large discrepancy was noticed when comparing these predictions to those obtained by Hodges and Rutkowski [15]. As a result, it was argued that the predictions of Hodges and Rutkowski [15] are all in error for the rotating tapered beam case as was mentioned earlier. Moreover, the coupled bending-torsional frequencies were also determined and compared to those of Rao and Banerjee [40] on one hand, and to the experimental values on the other hand, showing a fair agreement among the different methods. However, the authors in [43] indicated that their results were more accurate than those in [40] whilst they were found to be higher than the experimental values. The discrepancy found between the theoretical and experimental results as reported by Subrahmanyam and Kaza [43] was mainly due to the fact that the air surrounding the experiment may depress the frequencies by an amount of 0.5%, and further, the theoretical solution needs to be corrected for shear and rotary inertia effects.

Subrahmanyam and Kaza [44] extended the work in [43] to include the effect of buckling, linear pre-twist, pre-cone and Coriolis forces on bending modes for a slender beam of a rectangular cross-section. Root clamping on the axis and out of the axis of rotation were considered. Two methods of solution for studying blade vibration and stability were used, namely, a finite difference method based upon second-order central differences that gives lower bound estimates, and the potential energy method that produces upper bound estimates. From the equations of motion, the pre-cone was shown to have a softening effect. It was manifested that as the pre-cone increases the frequencies of all modes decrease. This characteristic was also confirmed in tabulated predictions at different parameter variations. The predictions show that for small

pre-cone and pre-twist, the frequencies increase as the rotational speed parameter increases, thus exhibiting a stiffening effect. For large pre-cone angles however, the frequencies of pre-twisted or untwisted blade were shown to increase in a non-linear manner up to a certain value of the rotational speed parameter after which a reversed trend was observed until the fundamental bending frequency becomes zero, indicating static instability. This phenomenon could be attributed to the fact that for large pre-cone angles and rotational speed parameters the softening effect dominates the stiffening one, thus depressing the frequencies to zero. Based on the predictions of the simulation, it was concluded that the inclusion of the Coriolis effect is necessary for blades of moderate-to-large thickness ratios while it is unimportant for blades with small thickness ratios. On the other hand, it was also concluded that for a beam mounted off the axis of rotation, the pre-twist and setting angle have a significant influence on rotation-induced buckling instability. However, this influence depends markedly on the blade thickness ratio.

Subrahmanyam and Kaza [45] further extended the work in [44] to include the effect of second order geometric nonlinearities. Their derivations included large pre-cone angles, Coriolis effects, and second order geometric nonlinearities. The Galerkin method was employed in the solution of the problem by assuming the bending and extensional deflections in terms of a series of generalized co-ordinates and mode shape functions. However, large pre-cone angle is known to have a destabilization effect on the rotor blade in helicopters.

Later Subrahmanyam *et al.* [46] extended the work in [44] to investigate further the stability of rotating linearly pre-twisted blades including torsion. The coupled bending-bending-torsion equations of dynamic motion of rotating linearly pre-twisted and large pre-coned blades of symmetric cross-section including second-degree geometric nonlinearities and Coriolis effects were derived. These equations were solved by using the Galerkin method and a linear perturbation procedure. The authors concluded that the effect of linear and nonlinear Coriolis forces on the coupled frequencies of thin blades is found to be negligible. However, the Coriolis effect must be retained in analyzing thick blades.

Timoshenko beam

None of the previous investigations on three dimensional beams treated the effect of rotary inertia and shear deformation. Further, rotating three dimensional Timoshenko beams have received less attention and the survey of the current literature reveals a shortage in solution results pertinent to this type of structure.

Stafford and Giurgiutiu [47] developed equations of motion for the uncoupled in-plane (lead-

lag) and out-of-plane (flapping) vibrations of a uniform Timoshenko beam rotating at constant angular velocity in a fixed plane. Although the effects of the centrifugal and Coriolis forces induced by the rotational speed were included in the formulation of the model, the latter has been ignored in the solution. The authors assumed a power series solution in the form of Frobenius with the transfer matrix technique in order to compute the eigenvalues of the resultant system. Predictions of the lowest six modes versus rotational speed were plotted. Consequently, it was found that the relation between the fundamental frequencies (flapping and lead-lag) and the rotational speed is linear. However, the second mode and higher, exhibits a non-linear relationship at low speeds and a linear one at high speeds. It was also shown that when the frequency is much greater than the rotational speed, the lead-lag and flapping curves cannot be distinguished. Moreover, the effect of rotary inertia and shear deformation was more pronounced at higher modes and high rotational speeds. In the second example, which is an application to helicopter blades, the authors found that resonance occurs in the lead-lag mode at an operation speed of 40 rad/s. It was concluded that corrections due to rotary inertia and shear deformations are quite accurate, therefore their inclusion for helicopter rotors and other relatively slow blades where the frequencies exceed the rotational speeds is justified.

Ansari [48] extended the vibration of pre-twisted blades to include the effects of shear deformations, rotary inertia and Coriolis forces. The results of simulation indicate that the effect of nonlinear coupling due to Coriolis forces is of significance at high rotational speeds and therefore cannot be ignored in many applications.

Krupka and Baumanis [49] presented a rotating tapered and pre-twisted Timoshenko beam utilizing Carnegie's formulation of the Lagrange equations of motions [8]. They solved the set of field equations using Myklestad's adaptation of the Holzer method based on lumped parameter formulation. They found that the effect of shear deformation and rotary inertia decreased the natural frequency by 4% for the first mode and by 8% for the second mode. They stated, without proof, that the effects of these corrections may be of greater importance than the centrifugal effects. However, reference [49] lacks necessary information concerning the shear deformation parameter and slenderness ratio values in order to reproduce and/or validate its results.

Studies of rotating beams with other complicating effects such as warping and thermal effects were reported by Subrahmanyam *et al.* [50] using both the finite difference and the Ritz method.

1.2.5 Dynamic Time Response Analysis

All the above contributions dealt with modal analysis[44] of rotating elastic structures using beam models. Often, researchers are concerned with how their models respond with time to prescribed loadings. Forced vibration responses of such models have been investigated much less frequently. These loads may cause stresses and deformations that affect the model performance or may cause stresses resulting in failures or unacceptable vibrations. Time history analysis, which is often called Dynamic Time Response Analysis (DTRA) can be effectively simulated to predict the dynamic behaviors of such finite element models in early design stages in order to properly control the structure or take corrective measures to alleviate any possible failures. Various examples of vibrational loads that may be represented are harmonic loads (e.g. rotating imbalances), random loads (e.g. rocket engines, airborne transportation), and transient loads.

Euler Bernoulli beam

Some investigations were dedicated to study the dynamic behavior of robot manipulators with a time-varying prescribed base motion $\Omega(t)$ using rotating uniform or tapered Euler-Bernoulli beams [50 - 54]. Du *et al.* [50 - 51] presented a three dimensional general lumped mass finite element structural dynamic model developed for the study of a robot manipulator with a time varying prescribed base motion. Links of the robot manipulator were connected together by revolute joints while the first one was rigidly attached to a base having six degrees of freedom and allowing arbitrary and large motions. The equations of motion were derived using the principle of virtual work allowing for large elastic deformations and small strains in order to include geometric nonlinearities. Pre-twist was included in the formulation of the problem. The developed model was utilized to solve the eigenvalue problem of a spinning beam as well as to predict the dynamic response simulation of a robotic manipulator with a time-varying base motion similar to that suggested by Kane[45] *et al.* [56]. The simulation results were shown for eight uniform beam elements and included the first five frequencies of a rotating beam with fixed and hinged-free end conditions. Although the Coriolis effect was included in the formulation of the problem; it was ignored in the examples shown. Compared to the exact results, these predictions show a percentage error of 0.2% for the first mode and 7% for the fifth mode for a rotating uniform cantilevered beam at which the rotating speed parameter $\overline{\Omega} = 6$. In the second

[44] In modal analysis, natural frequencies (eigenvalues) and associated mode shapes (eigenvectors) are examined. These quantities describe the only possible vibrational modes with which a structure will respond to vibrational input. Therefore, natural frequencies are useful quantities in developing an acceptable design.

[45] Kane's driver is a spin up manoeuver of a long slender beam of 10 m length.

part of the simulation, the tip deflections in the flapping, lead-lag and torsional direction of the deployment of a robotic manipulator were shown. These deflections, being much larger than those predicted in the work of Kane *et al.* [56], may cause significant failure or damage to the beam. The authors attributed this difference to the exclusion of the warping effect on the beam torsion stiffness in their computation. However, effects due to shear deformation and rotary inertia that were neglected could greatly contribute to these differences.

Yoo *et al.* [53] presented a linear modelling method for a flexible slender beam having homogeneous and isotropic material properties. The beam was assumed to undergo large overall motion and concomitant with small linear elastic deformation. The only contribution of the present modelling method was the introduction of a stretch deformation variable by which the strain energy function may be expressed in another quadratic form. This study was illustrated by two examples. In the first one, a cantilever beam of 30.5 m length was attached to a rigid base that performs an abrupt prescribed planar rotational motion around the vertical axis for a time interval of 30 seconds. The resulting axial and transverse tip deflections were shown to be quite large when compared to the length of the beam. Moreover, a deflection of this order may cause a drastic failure of the beam. In the second attempt, the material and geometric properties of the beam were modified while the length of the beam was shortened to 10 m. The base performed a different prescribed planar rotational motion of sinusoidal type for a period of 120 seconds. The maximum lateral tip deflection was 7 cm which is acceptable when compared to length of the beam. In addition, this result is in agreement with the small linear elastic deformation assumption that underlines the formulation of the model.

Pedersen and Pedersen [54] derived equations of motion for a general multibody system using the principle of virtual work including centrifugal and Coriolis forces. The formulation was restricted to simple shape functions for a beam with equal-length elements, constant mass and stiffness properties in which the rotary inertia and shear deformation effects were ignored. The computation was verified by the well-known example 'Kane's driver' of reference [56]. In this example, the beam was divided into five equal finite elements. The maximum tip displacements in the lateral and axial directions were respectively, -0.592 m and -0.019 m. For unequal element lengths however, the maximum deflection in the lateral direction was found to be -0.5875 m. Nevertheless, this little improvement can be attributed to the fact that the curvature is largest close to the root of the beam.

Yigit *et al.* [55] tackled the problem of predicting the motion of an elastic beam that undergoes bending in one plane only and is rigidly attached to a shaft. The rigid body was driven

by a prescribed torque $M(t)$. Differential equations of motion were derived using the extended Hamilton's principle and taking into account the coupling between the rigid body motion and elastic deformations. The results show that the coupling may radically alter the nature of the response. A linearized analysis of the coupled equations of motion and the numerical solution of the fully coupled non-linear equations show that the uncoupled equations may lead to substantially incorrect results, particularly with regard to frequencies. There are two significant effects to be noted: (i) the response frequencies increase with a decreasing ratio of the flexible beam and rigid shaft inertia, (ii) the effect of elastic motion on the rigid body motion becomes more significant by decreasing the ratio of the flexible beam and rigid shaft inertia.

Timoshenko beam

Few investigators have tackled the problem of Dynamic Analysis for rotating beams including rotary inertia and shear deformation effects, inspite of its importance in many engineering and technological applications to rotating structures using beam models. Kane *et al.* [56] presented a cantilever beam model that is built into a rigid base and performing a specified motion of rotation and translation as a model for a robot manipulator. This formulation extended the previous ones[46] to account for shear deformation and rotary inertia effects as well as warping, centrifugal stiffening and Coriolis forces. A step-by-step outline procedure algorithm for solving the equations of motion was presented for the implementation of that formulation. The simulation algorithm was illustrated by considering a space-based robotic manipulator which consists of three links L_1, L_2 and L_3, connected by revolute joints[47]. The outboard link L_3 of the manipulator consisted of a base A and two distinct segments B_1 and B_2. The behavior of L_3 which is 8 m long during deployment of the manipulator from a stowed configuration to a fully operational configuration was examined. The deployment process was presumed to last for 15 seconds. As a result, tip torsional, lead-lag and flapping flexural deformations of L_3 were shown graphically for a time of 30 seconds which is twice the deployment time. The maximum deflections were depicted to be 8°, 9 cm and 15 cm, respectively. After the end of the deployment time, the above amplitude deflections became of no-significance. The response of the tip B_2 was also examined for which the angular speed increased from 0 to 6 rad/s in the time interval of 15 seconds, and remains constant thereafter. The results show a disagreement with other investigators' results.

[46]The author called the previous investigations as the conventional approach.

[47]The link L_1 makes an angle φ_1 with the base, while the intermediate link L_2 makes an angle φ_2 with L_1 and φ_3 with the outboard link L_3. During the deployment time the angles φ_1, φ_2 and φ_3 were respectively varying from 180° to 90°, 180° to 45° and 180° to 90°.

Kane *et al.* [56] attributed this disagreement to the fact that all previous investigations did not take into account the fact that *every transverse displacement of a point on the neutral axis of a beam (that is, a nonzero value of either v or w) gives rise to axial displacement*[48] u. On the other hand, the effects of shear deformation and rotary inertia were neglected in the examples shown.

Boutaghou and Erdman [57] derived equations of motion for rotating elastic structures using Hamilton's principle including the centrifugal stiffening effect arising in fast rotating structures. As a result of large rotation and elastic deformations, they included the nonlinear geometric stiffening effect. Equations of motion were derived for the case of uniform Euler-Bernoulli and Timoshenko beams. The time history of the tip transverse displacement, bending rotation and axial displacement for a two-noded beam element were shown graphically for thin and thick beams using the spin-up maneuver suggested by Kane *et al.* [56]. Various beam examples with different geometrical properties were taken for the case of a Timoshenko beam. For Timoshenko beams, it was shown that the tip axial deflections were not influenced by the out-of-plane inertial forces for the case of spin-up maneuver problems. An increase in the inertia proportionally affects the amplitude of the in-plane and out-of-plane elastic deformations.

Lai [58] presented a nonlinear finite element modeling procedure that takes into account the effect of shear deformation, gyroscopic inertia, and geometric stiffness. To build up confidence and validate their model, the authors selected Kane's rotating beam as a typical model for such structures [56]. The numerical predictions show that the gyroscopic inertia affects the maximum tip displacements by approximately 3%, 9% and 18% for a beam rotating at 300, 500 and 700 rpm, respectively. This shows the importance of these terms for high-speed machinery. On the other hand, the geometric stiffening was shown to inhibit the maximum tip displacement for approximately 35% for a beam rotating at 1200 rpm. In addition, it is shown that if the rotating speed exceeds 1200 rpm the tip displacement of the steel beam becomes excessive. Moreover, at a speed of 1250 rpm the structure goes through a large deformation. The linear elastic model becomes inadequate and the system response becomes dynamically unstable. However, the contribution of shear deformation was not shown in the results.

Using the rotating beam problem of Kane *et al.*[56], Fallahi *et al.* [59] conducted a comparative study in formulating the elastic displacement field for Timoshenko beams with tip mass

[48]It is clearly understood that u is the axial displacement in the x-direction, and v and w the transverse displacements in the y- and z-directions, respectively

and geometric stiffening effect. The effect of speed and tip mass on the contribution of the Coriolis acceleration were investigated. The tip mass was reported as a percentage of the mass of the beam. The predictions show that at 500 rpm and for 10% and 20% tip mass increase, the tip transverse deflections were respectively 1.4 and 1.7 times greater than those where there is no tip mass. It was also shown that the tip transverse deflection increases as the speed of rotation increases. On the other hand, the numerical simulations show that correction terms due to Coriolis, tangential and normal accelerations increase with both speed and tip mass.

Bakr and Shabana [60] investigated the behavior of rotating Timoshenko beams with constant properties in multibody systems consisting of interconnected rigid and deformable bodies each of which may undergo finite rotations. Flexible components in the system were discretized by using the FEM. The formulation presented in this paper was exemplified by two dimensional flexible multibody aircraft. The aircraft model consisted of seven bodies and two identical gears. The two wings of the aircraft were considered to be flexible while all other components were treated as rigid. Each flexible wing was discretized into ten equal Timoshenko beam elements. The two flexible wings were rigidly attached to the fuselage while the wheels of the aircraft were assumed to be attached to the carrier. The model was excited by a sinusoidal rotation of the aircraft carrier about the axis of rotation with a frequency of 15 rad/s. Bending tip deflection of one of the two wings was shown for three cases for a period of 1.5 s. In the first case, rotary inertia and shear deformation were neglected, in the second case the rotary inertia only was taken into consideration while in the third case, both rotary inertia and shear deformation were accounted for. Predictions show that the effect of these factors is insignificant in lower modes of bending frequencies and is highly pronounced in higher modes. On the other hand, it was shown that the tip deflection[49] is not greatly affected by the inclusion or removal of these effects. The authors concluded that the inclusion of rotary inertia and shear deformation has a significant effect on the dynamic response of flexible multibody systems with large angular rotations and in which the reference motion and the elastic deformation are coupled.

Oguamanam and Heppler [61] derived equations of motion of a prismatic isotropic Timoshenko beam with a tip mass attached to a rotating hub taking into account the effects of centrifugal forces that appear in the equations of motion as nonlinear functions of the angular speed. The system was simulated via a time response analysis with and without the effects of the nonlinearities that arise due to centripetal acceleration being considered and these results were

[49]The unit of the tip deflection in the various figures was shown in mm, while in the text, the authors referred to a dimensionless tip deflection without mentioning the normalization that has been done with respect to which variable. This point is somehow misleading in this paper.

compared to the corresponding results for an Euler-Bernoulli beam model. It was observed that there is a threshold hub angular speed below which the centrifugal stiffening effects are negligible not only in terms of the natural frequencies of the system as had previously been established but also in terms of displacement trajectories. The authors found that the Timoshenko beam predicts larger deflections at high angular speeds than does the Euler-Bernoulli model. However, the authors did not include the nonlinear terms arising from the Coriolis forces.

1.3 Modal Reduction Schemes

The Finite Element Method (FEM) is one of the most powerful numerical technique and has great potential and flexibility in modeling large complex structures. However, utilizing nodal co-ordinates in the discretization process leads to a large number of degrees of freedom of the model and consequently, results in a large number of dynamic equations for which a solution becomes impracticable. Moreover, the use of nodal co-ordinates results in a dynamic model of widely spread eigen-spectrum that includes many insignificant modes and consequently, a numerically stiff system is often created that causes the numerical integration scheme to search inefficiently for a solution or may even fail to find one.

Using modal co-ordinates alleviates the problem of large dimensionality incurred by using nodal co-ordinates, and avoids the inclusion of higher insignificant modes when they do not share an appreciable amount of the system's kinetic energy [62]. In general, a subset of eigenvectors that spans the frequency spectrum of the forcing function are retained as significant modes.

The distinction between significant and insignificant modal co-ordinates leads to a convenient formulation of the reduced order model by means of a reduction technique referred to as mass condensation [63], in which it is assumed that the mass of the structure can be lumped at only specific degrees of freedom. The disadvantage of this technique is that the banded nature of the original system may be destroyed and may lead to a much more expensive eigensolution. In addition, the inertia matrix is sometimes singular because of the presence of a massless degree of freedom that may cause the eigensolver to fail. Several investigations related to mass condensation have been reported in the literature [62, 64].

Hurty [66], Craig and Bampton [67] and Benfield and Hruda [68] used the component modes to analyze complex structural systems. Based on substructuring, this approach couples various components of a structure to predict the dynamic behavior of the entire structure. Ojalvo and Newman [69] presented a matrix-reduction method to predict the frequencies of vibration of large structures by solving an eigenvalue problem of a size smaller than the original one.

Laurenson [41] addressed the issue of reduction techniques and indicated the revisions that should be considered when the FEM is used in dynamic analysis of flexible structures that include the effect of spinning. In [70], Likins developed a general study in which he provided the governing equations for flexible appendages and outlined the steps that should be followed in conjunction with the FE formulation in order to reduce the size of the original structure by means of a modal transformation. Shabana and Wehage [71] extended the co-ordinate reduction technique to spatial substructures with large angular rotations. Kane and Torby [72] applied the extended modal reduction method to solve the eigenvalue problem of a simple rotor problem using state space formulation to allow for non-symmetric matrices such that damping, and gyroscopic effects may be treated. However, the authors in [72] did not perform any dynamic analysis.

In the previously cited investigations, there is a strong view in support of using complex modes in modal transformations of systems with gyroscopic (Coriolis) matrices. However, the associated numerical complexities are acknowledged. To avoid such numerical difficulties, another view suggested the use of planar modes obtained after modifying the mass matrix to include gyroscopic effects. Nevertheless, other investigators, especially those concerned with dynamic response analysis, have consistently employed planar modal transformations. It is noteworthy to mention that no dynamic response analysis study that invoked complex modal transformations was reported in the available literature except the one presented by Khulief and Mohiuddin [73].

The truncation operation aims at eliminating the insignificant modes that are, in general, higher modes that do not contain an appreciable amount of the system's kinetic energy. In general, a subset of eigenvectors that spans the frequency spectrum of the forcing function are retained as significant modes. Moreover the retained modes must include the first few lower ones in terms of which the characteristics of the system must be preserved.

Two modal reduction schemes are established. The first scheme utilizes planar modes obtained by solving the self-adjoint eigenvalue problem[50], while the second scheme invokes the complex modes of the non-self-adjoint eigenvalue. In each case, a reduced order modal form of the equations of motion is obtained.

[50] An $n \times n$ complex matrix $[\mathbf{A}]$ is called Hermitian (or self-adjoint) if $[\mathbf{A}]^T = [\mathbf{A}]$. Here $[\mathbf{A}]^T$ designates the conjugate of the transpose of $[\mathbf{A}]$. Hermitian matrices are the analogues of real symmetric matrices. As a result, the eigenvalues of an Hermitian matrix are all real. In addition, any two eigenvectors associated with distinct eigenvalues are orthogonal. Further, an Hermitian matrix $[\mathbf{A}]$ is always diagonalizable.

1.4 Damping

In most of the above contributions damping[51] was neglected because its influence on the dynamic response was minor. However, the effect of damping cannot be ignored if the response of a system is required for a long period of time. Rao [90] reported that if the frequency of excitation (in the case of a periodic force) is at or near one of the natural frequencies of the system, damping is of primary importance and must be taken into account.

In addition to inertial (mass) and stiffness properties, most structural systems have damping properties; these are material and system damping. Material damping is the damping inherent in the material while system or structural damping includes the damping at the supports, boundaries, joints, etc. in addition to material damping. Since utilizing damping materials is the most common way to reduce resonance responses, accurate measurements of damping are crucial to the proper design,optimization, and modeling of systems from a vibration reduction standpoint. In general, since damping effects are not known in advance, they must be considered in the vibration analysis of any system. However, for rotating structural components these effects are minor when compared to others such as the stiffening one that is due to rotation and therefore can be ignored.

1.5 Objectives

A survey of the current literature reveals a shortage of solution results pertinent to rotating three dimensional doubly tapered Timoshenko beams. Since rotating blades in real life have angular settings in addition to being stubby and tapered, it is the purpose of this investigation to address this important class of problems that arise in many practical engineering applications and to generate a realistic means of obtaining a complete dynamic analysis (modal analysis and time response analysis) of a rotating tapered three dimensional Timoshenko beam experiencing axial, flexural and torsional vibrations by employing a discrete mathematical model in conjunction with the FEM.

In this thesis, a three dimensional dynamic analysis is considered to include both formulation, and solution of the generalized eigenvalue problem as well as solutions of equations of motion that are used to predict the time histories of positions of the system. In the course of the analysis the followings are considered:

- introducing a new 3-D doubly tapered finite beam element.

[51] Damping serves to control the steady-state resonant response and to attenuate traveling waves in the structure.

- the beam element will account for shear deformation and rotary inertia.
- the beam setting angle as well as the beam pre-cone angle are also taken into consideration in the finite element formulation.
- the stiffening effect due to a centrifugal force field will be accounted for.
- the Coriolis effect will be represented in the dynamic model.
- the torsion-coupling bending resulting from the Coriolis effect is accounted for.
- the generalized eigenvalue problem will be defined and solved to obtain, in general, a complex set of eigenvalues and their corresponding eigenvectors.
- explicit expressions for Southwell coefficients (SC) for the first four frequencies are obtained taking into account all the parameter changes.
- to alleviate the problem of large dimensionality, the modal transformation method will be formulated for such systems with complex mode shapes, and a reduced order model will be defined.
- the modal form of equations of motion will be integrated forward in time to predict the system histories of elastic deformations due to different types of excitation such as impulse, sinusoidal and prescribed loadings.
- the forced frequencies along with their spectral magnitudes of the time response signals are obtained using Fast Fourier Transform (FFT) algorithm.

1.6 Overview

In the course of the analysis, the following will be covered:

Chapter 2 includes necessary assumptions that underline the derivations of equations of motion. A set of transformation matrices is introduced to explain the orientation of the beam (setting angle and pre-cone angle). A multibody system may be represented by a mathematical model that consists of two collections of bodies. One collection includes the rigid hub while the other one includes the elastic beam. In order to perform the dynamic analysis of such a structure two sets of generalized co-ordinates are identified and employed. The first one is the rigid body degree of freedom described by the rotational motion of the reference frame while

the second one is the elastic degrees of freedom that characterizes the elastic deformations of the beam.

The equations of motion are defined using a suitable Lagrangian approach thus utilizing the kinetic and strain energy of the model. To develop the kinetic energy equation, an arbitrary rotating vector within the beam element is considered and the velocity vector is expressed accordingly, thus, taking into account the effect of the rigid hub rotation and the coupling that exists between the reference motion and the elastic deformations.

Chapter 3 develops key concepts of the tapered beam element. The beam's geometric properties are defined. The beam element model is discretized and the shape functions are developed. Elemental inertia, stiffness, Coriolis and centrifugal inertia matrices are derived and evaluated in a symbolic form in which the spin rate, the shear deformation parameters, the setting angle, the pre-cone angle and taper ratios appear as parameters. The explicit expressions of these matrices have the computational advantage of eliminating the loss of computer time and round-off errors associated with extensive matrix operations required for their numerical evaluation. The standard finite element assembly procedure is invoked to obtain the equations of motion for the entire beam.

The general form of the generalized eigenvalue problem is derived in Chapter 4. A suitable state space form representation of the problem is established and the generalized eigenvalue problem is given in terms of the state matrices [**A**] and [**B**]. Two modal reduction schemes are employed: the planar and the complex modal transformations. The former ignores the Coriolis effect where the mode shapes are planar, while the later includes the Coriolis effect where the mode shapes are complex, i.e., have real and imaginary parts.

In Chapter 5, results of the simulation are presented and discussed. It starts with an overview of the computer scheme in which several parts of the computer program are illustrated in flowchart form including: input data, system matrices, eigenvalue solution, modal reduction schemes and numerical integration. Many degenerate cases along with various comparisons with previous investigators are reproduced to show and validate the accuracy and fidelity of the present model. In the second part, the modal characteristics of the rotating beam are calculated and compared to those available in the literature. Natural frequencies are shown in tabular and graphical forms, consisting of two and three dimensional plots. The effects of taper ratios and pre-cone and setting angle as well as other effects are highlighted and discussed in these plots. Explicit expressions for Southwell coefficients for the first four frequencies are obtained taking into account all the parameter changes.

Both Planar Reduction Order Model (PROM) and Complex Reduction Order Model (CROM) are invoked in the calculations of the frequencies of the rotating beam and compared to the Full Order Model (FOM). In the last part, a dynamic analysis of the beam is performed in which the beam is excited by different types of external loadings and the response is plotted for a wide range of parameter variations.

The forced frequencies along with their spectral magnitudes of the time response signals are obtained using Fast Fourier Transform (FFT) algorithm.

Chapter 6 includes conclusions and recommendations for future studies.

Chapter 2

The Elastodynamic Formulation

The modelling and formulation of the equations of motion of a dynamic system is the most important and difficult step of the entire analysis procedure. In this chapter, the dynamic model of a three dimensional spinning tapered Timoshenko beam is developed using the energy method in conjunction with the appropriate Lagrangian function to derive the equations of motion of the beam. A new set of time invariant element inertia matrices that describe the coupling between the reference motion and elastic deformations is developed and expressed in terms of a set of time invariant quantities (scalars and matrices) that depend on the assumed displacement field, rotary inertia, shear deformation, setting angle, hub radius and tapering in the (xy)- and (xz)-planes. This formulation permits easy inclusion of the effects that are usually not taken into account in standard beam theory such as inclusion of setting angle, pre-cone angle, tapering in the (xy)- and (xz)-planes, inertia coupling between the reference motion and the elastic deformations of the beam, and centrifugal and Coriolis forces resulting from the precession of reference axes.

2.1 General Assumptions

The assumptions that underline the present formulation are as follows:

(1) The material of the beam is homogeneous, isotropic and linearly elastic, and the deformations (displacements) are small.

(2) The deflection of the beam is produced by the displacement of points of its centreline.

(3) The plane cross-sections initially perpendicular to the neutral axis of the beam remain plane but no longer perpendicular to the neutral axis after deformation.

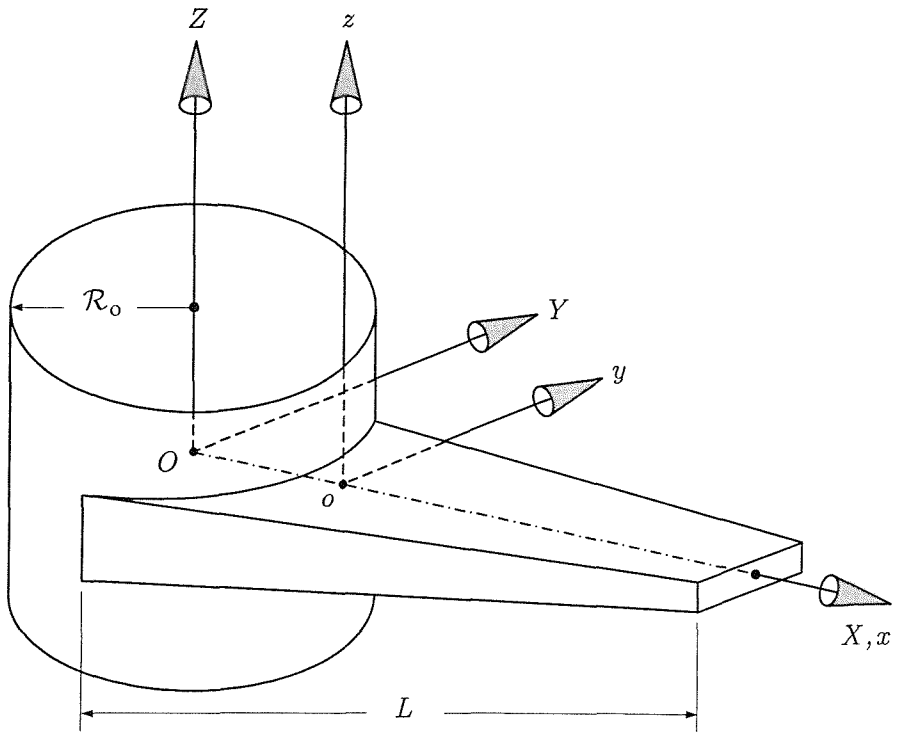

Figure 2-1: Undeformed state of the tapered beam before any angular settings.

(4) Damping, aerodynamic forces as well as the thermal stresses and the warping of the cross-section of the beam are neglected.

(5) The hub is assumed to be rigid.

2.2 Description of the Model

The tapered beam considered in this investigation is shown by the model of Figure 2-1, mounted on the periphery of a rotating rigid hub of radius $\mathcal{R}_o$. A preliminary setting such that the setting angle and the pre-cone is first described before deformations take place. Consequently, the orientations and rotations of the different co-ordinate axes are also described.

The (XYZ) axes represent a global Cartesian co-ordinate system with origin on the hub spin axis such that the Z-axis corresponds to the spin axis which rotates with an angular speed $\Omega_Z = \dot{\varphi}$. The (xyz) system is defined as a Cartesian system of local co-ordinates whose components are parallel to the global (XYZ) co-ordinate system and rigidly attached to the root of the beam with its origin shifted by a distance $\mathcal{R}_o$ in the radial X-direction from the global (XYZ) co-ordinate system. The x- and X-axes are collinear and coincident with the undeformed beam centreline.

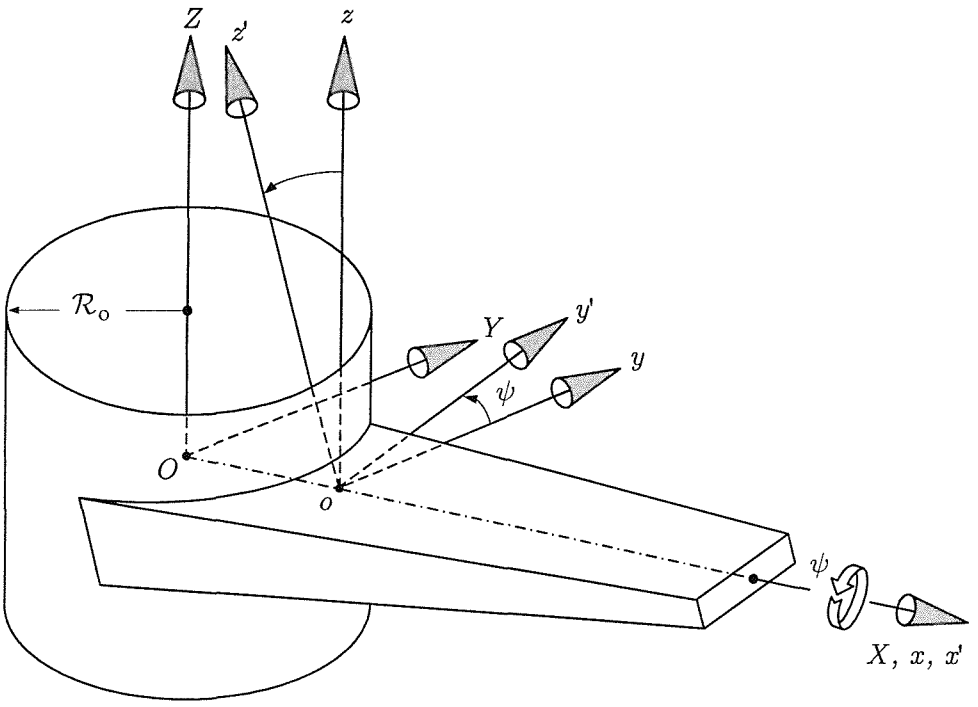

Figure 2-2: Undeformed state of the tapered beam after the setting angle ψ is made.

The Cartesian co-ordinate system $(x'y'z')$ is obtained by rotating the (xyz) co-ordinate system about the x-axis by an angle ψ, termed the setting angle, as shown in Figure 2-2, so that the y'- and z'-axes align with the cross-section principal axes while the $(x''y''z'')$ Cartesian co-ordinate system is obtained by rotating the $(x'y'z')$ co-ordinate system about y'-axis by an angle ϕ, termed the pre-cone, as shown in Figure 2-3.

Figure 2-4 shows the deformed state of the three dimensional spinning tapered Timoshenko beam model.

2.3 Transformation Matrices

2.3.1 Setting Angle

The orientation of any cross-section of the beam is achieved by a sequence of two consecutive transformations allowing for angular settings before any elastic deformation. In the first one, the $(x'y'z')$ co-ordinate system is obtained by rotating the (xyz) co-ordinate system by an angle ψ called a setting angle about the x-axis as shown in Figure 2-2. Since this is a constant transformation that corresponds to a single axis rotation about the x-axis, one may write

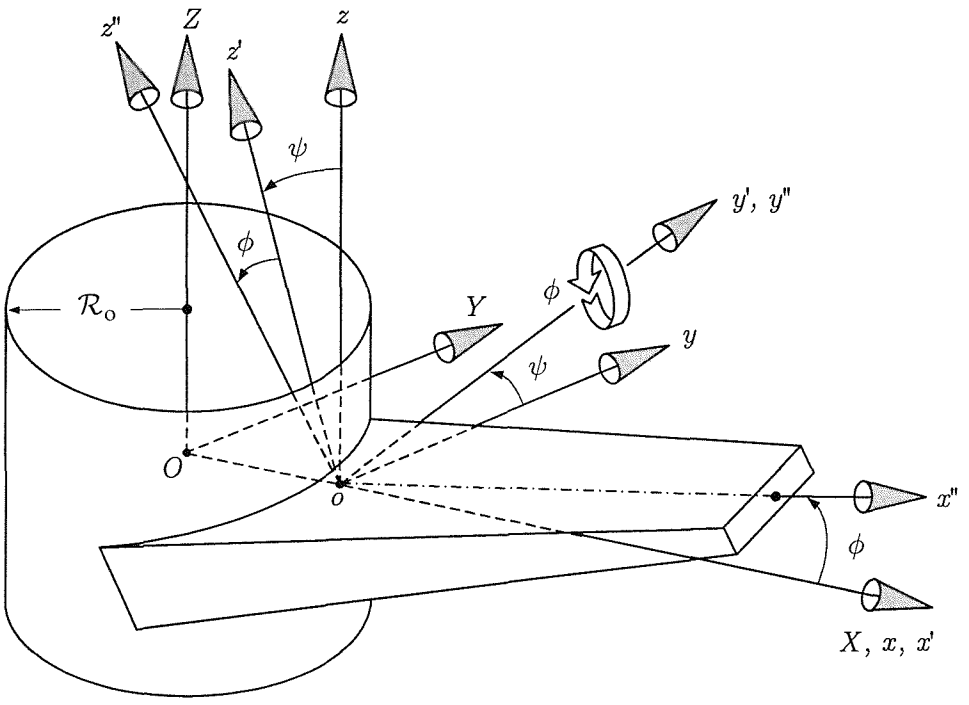

Figure 2-3: Undeformed state of the tapered beam after the pre-cone angle ϕ is made.

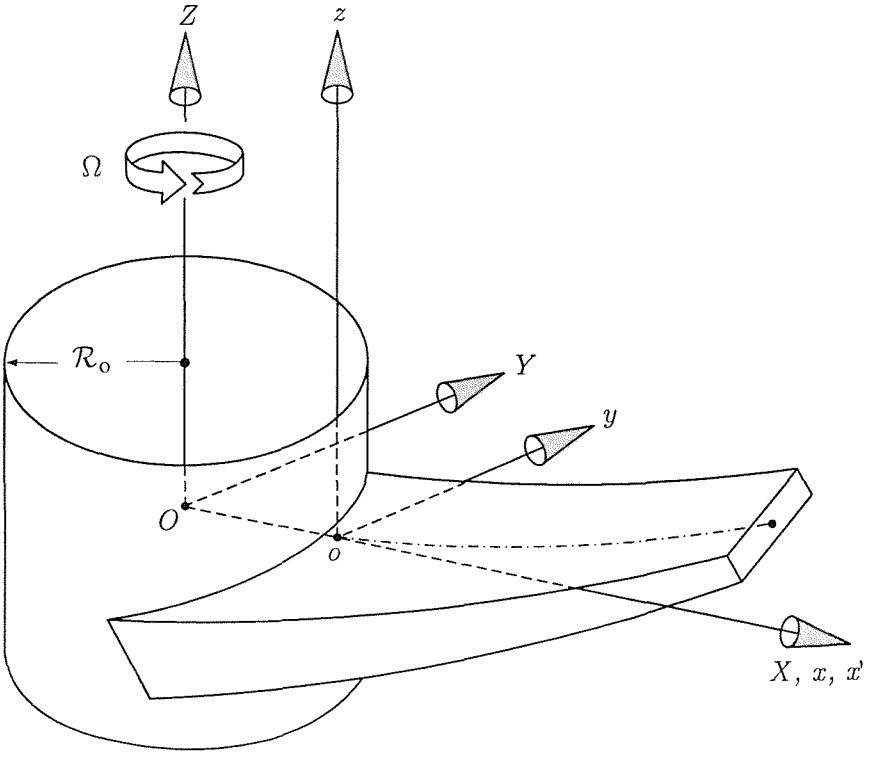

Figure 2-4: Deformed state of the rotating tapered Timoshenko beam.

$$\begin{Bmatrix} x' \\ y' \\ z' \end{Bmatrix} = [\mathcal{A}_\psi] \begin{Bmatrix} x \\ y \\ z \end{Bmatrix} \tag{2.1}$$

where $[\mathcal{A}_\psi]$ denotes the rotational transformation with an angle ψ about the x-axis. The expression of $[\mathcal{A}_\psi]$ is given by

$$[\mathcal{A}_\psi] = \begin{bmatrix} 1 & 0 & 0 \\ 0 & \cos\psi & \sin\psi \\ 0 & -\sin\psi & \cos\psi \end{bmatrix} \tag{2.2}$$

2.3.2 Pre-cone Angle

In the second transformation, the $(x''y''z'')$ co-ordinate system is obtained by rotating the $(x'y'z')$ co-ordinate system by an angle ϕ called the pre-cone angle or simply pre-cone about the y'-axis as shown in Figure 2-3. Since this is a constant transformation which corresponds to a single axis rotation about the y'-axis, one may write

$$\begin{Bmatrix} x'' \\ y'' \\ z'' \end{Bmatrix} = [\mathcal{A}_\phi] \begin{Bmatrix} x' \\ y' \\ z' \end{Bmatrix} \tag{2.3}$$

where $[\mathcal{A}_\phi]$ denotes the rotational transformation with an angle ϕ about the y'-axis. The expression of $[\mathcal{A}_\phi]$ is given by

$$[\mathcal{A}_\phi] = \begin{bmatrix} \cos\phi & 0 & -\sin\phi \\ 0 & 1 & 0 \\ \sin\phi & 0 & \cos\phi \end{bmatrix} \tag{2.4}$$

The relationship between the co-ordinate systems $(x''y''z'')$ and (xyz) can be established by substituting equation (2.1) into (2.3)

$$\begin{Bmatrix} x'' \\ y'' \\ z'' \end{Bmatrix} = [\mathcal{A}_\phi]\,[\mathcal{A}_\psi] \begin{Bmatrix} x \\ y \\ z \end{Bmatrix} = [\mathcal{A}_o] \begin{Bmatrix} x \\ y \\ z \end{Bmatrix} \tag{2.5}$$

resulting in a transformation that is composed of the two rotations $[\mathcal{A}_\phi]$ and $[\mathcal{A}_\psi]$ given by

$$[\mathcal{A}_\circ] = [\mathcal{A}_\phi]\,[\mathcal{A}_\psi] = \begin{bmatrix} \cos\phi & \sin\phi\sin\psi & -\sin\phi\cos\psi \\ 0 & \cos\psi & \sin\psi \\ \sin\phi & -\cos\phi\sin\psi & \cos\phi\cos\psi \end{bmatrix} \tag{2.6}$$

2.3.3 Transformation due to Rotation

The location of an arbitrary infinitesimal volume at point P^i of the i^{th} beam element can be determined globally by specifying the position of the body-fixed (xyz) co-ordinate system of the body and the location of point P^i with respect to the (xyz) co-ordinate system. Let $\mathcal{R}_\circ$ and φ represent, respectively, the translational and rotational orientation of the body co-ordinate system (xyz) with respect to the global co-ordinate system (XYZ). The rotational transformation matrix $[\mathcal{A}]$ relates the body co-ordinate system (xyz) to the global co-ordinate system (XYZ) by the following relation

$$\begin{Bmatrix} X \\ Y \\ Z \end{Bmatrix} = \{\mathcal{R}_\circ\} + [\mathcal{A}] \begin{Bmatrix} x \\ y \\ z \end{Bmatrix} \tag{2.7}$$

where $\{\mathcal{R}_\circ\} = \begin{bmatrix} X_\circ & 0 & 0 \end{bmatrix}^T$ is the location of the origin of the body co-ordinate system relative to the global co-ordinate system. Notice that $[\mathcal{A}]$ is implicitly time dependent in which $\dot{\varphi} = \Omega_Z$ represents the angular velocity of the hub. The expression of $[\mathcal{A}]$ is given by

$$[\mathcal{A}] = \begin{bmatrix} \cos\varphi & -\sin\varphi & 0 \\ \sin\varphi & \cos\varphi & 0 \\ 0 & 0 & 1 \end{bmatrix} \tag{2.8}$$

2.4 Generalized Co-ordinates

To specify the position of any point in the model, it is necessary to define a set of generalized co-ordinates, in terms of which the global position of any infinitesimal volume on the body is determined.

For the system under consideration, the location of an arbitrary infinitesimal volume on the i^{th} beam element is defined in terms of two sets of generalized co-ordinates. The first one is the rigid body degree of freedom described by the rotational motion of the reference frame while

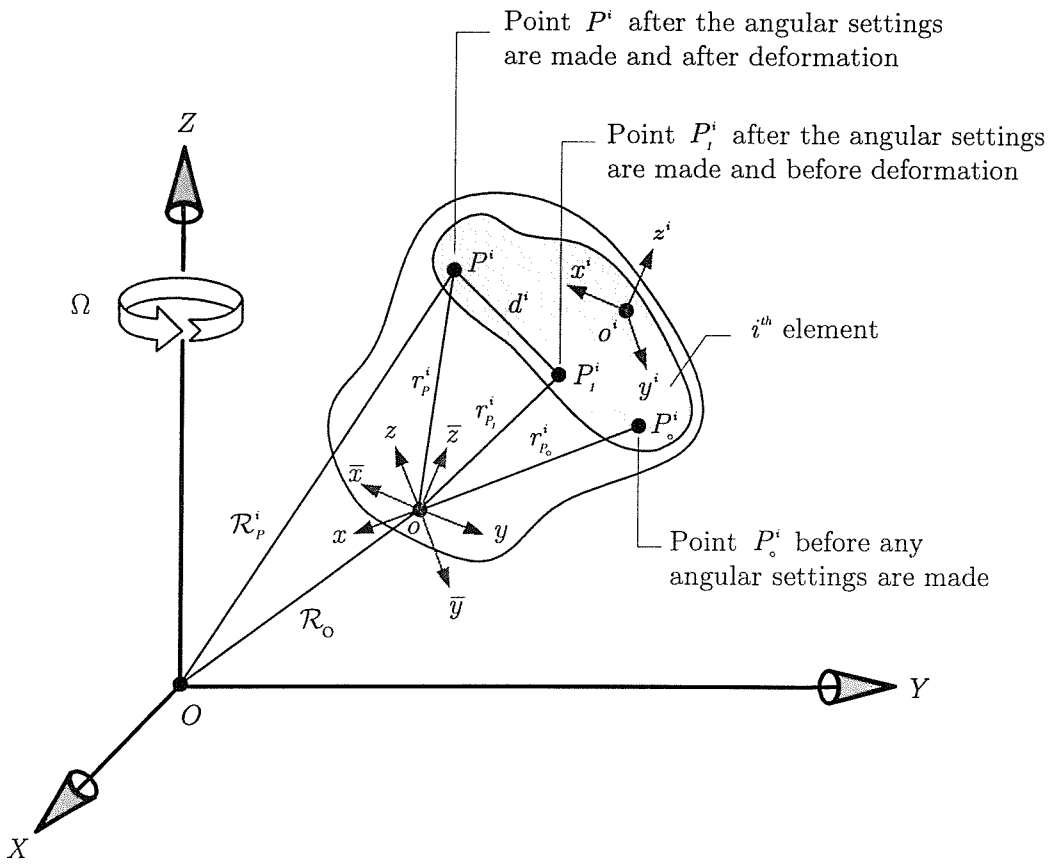

Figure 2-5: Arbitrary point of the i^{th} beam element before and after deformation.

the second one is the elastic degrees of freedom that characterizes the elastic deformations of the beam. The elastic degrees of freedom usually represent the relative translations and angular displacements (rotations) of infinitesimal volumes at nodal points on the element. Using the FEM, the location and angular orientation of any infinitesimal volume on the i^{th} beam element can be approximated in terms of elastic degrees of freedom associated with this element and a shape function employed to describe the elastic degrees of freedom.

2.5 The Displacement Field and Shape Functions

Referring to Figure 2-5, the $(x^i y^i z^i)$ system represents a beam element co-ordinate axes with its origin affixed to an infinitesimal volume at some point on the body, while the $(\overline{x}\ \overline{y}\ \overline{z})$ is a system of co-ordinate axes parallel to the $(x^i y^i z^i)$ but with its origin coincident with the origin of the body-fixed axes (xyz). Let P_o^i be any point in the undeformed state of the i^{th} beam element and before any angular setting is made. Point P_o^i is defined by the position vector

$\{r^i_{P_\circ}\} = \begin{bmatrix} x_\circ & 0 & 0 \end{bmatrix}^T$ in the body co-ordinate system (xyz). Let P^i_1 be the undeformed state of point $P^i_\circ$ after the setting angles are made, such that the position vector $\left\{r^i_{P_1}\right\}$ of point P^i_1 in the local co-ordinate system (xyz) is given by

$$\left\{r^i_{P_1}\right\} = [\mathcal{A}_\circ]\{r^i_{P_\circ}\} \tag{2.9}$$

where the superscript i refers to the i^{th} beam element and $[\mathcal{A}_\circ]$ is the constant transformation matrix defined earlier by equation (2.6). Let P^i be the position of point P^i_1 after deformation. The local position $\{r^i_P\}$ of point P^i of the i^{th} beam element can be written as

$$\{r^i_P\} = \left\{r^i_{P_1}\right\} + \{d^i\} \tag{2.10}$$

where $\{r^i_P\}$ and $\left\{r^i_{P_1}\right\}$ are respectively vectors from the origin of the body co-ordinate system to point P^i and P^i_1 in the deformed and undeformed states. The vector $\{d^i\}$ is the elastic deformation vector which gives the difference between the deformed and undeformed vectors $\{r^i_P\}$ and $\left\{r^i_{P_1}\right\}$, respectively. In order to represent the deformation vector $\{d^i\}$ in a finite dimensional space, the finite element approach can be used. A finite element discretization of the continuum is obtained by a finite set of nodal points. If $\{\overline{e}^i\}$ represents the nodal elastic co-ordinates of the i^{th} element with respect to $(\overline{x}\ \overline{y}\ \overline{z})$ co-ordinate system, elastic deformations of an arbitrary point P^i of the i^{th} element can be described using shape functions $[\mathcal{S}^i]$ and a set of nodal co-ordinates $\{\overline{e}^i\}$ as [77]:

$$\{d^i\} = [\mathcal{S}^i]\{\overline{e}^i\} \tag{2.11}$$

where $[\mathcal{S}^i]$ is the elemental shape function matrix that must satisfy the completeness and differentiability requirements [94]. The explicit expression of the matrix of shape functions $[\mathcal{S}^i]$ will be given in the next chapter.

A transformation $[\Re^i]$ is employed to define $\{d^i\}$ with respect to the (xyz) system such that

$$\{d^i\} = [\Re^i][\mathcal{S}^i]\{\overline{e}^i\} \tag{2.12}$$

where $[\Re^i]$ is a 3×3 transformation matrix from the element co-ordinate system to the body fixed co-ordinate system, [77]. Compatibility conditions between elements on a given body are simpler if generalized elastic co-ordinates are defined with respect to the body-fixed (xyz)

co-ordinate system [77]. This can be accomplished by the transformation

$$\{\overline{e}^i\} = \left[\overline{\Re}^i\right] \{e^i\} \tag{2.13}$$

in which the nodal displacement vector $\{e^i\}$ represents a set of generalized co-ordinates of the i^{th} element defined relative to the body fixed co-ordinate system and $\left[\overline{\Re}^i\right]$ is a diagonal matrix built up of $[\Re^i]$ matrices and has a dimension that is equal to the number of nodal co-ordinates of the element. Substitution of equation (2.13) into (2.12), yields

$$\{d^i\} = [\Re^i] [\mathcal{S}^i] \left[\overline{\Re}^i\right] \{e^i\} = [\mathcal{N}^i] \{e^i\} \tag{2.14}$$

where

$$[\mathcal{N}^i] = [\Re^i] [\mathcal{S}^i] \left[\overline{\Re}^i\right] \tag{2.15}$$

is the associated modified shape function of the i^{th} element that accounts for transformation from the element co-ordinate system to the body co-ordinate system. The nodal displacement vector $\{e^i\}$, has a dimension of $(n_{dof} \times 1)$ where n_{dof} is the total number of elastic degrees of freedom of the i^{th} element. Notice that $\{e^i\}$ is time dependent while $[\mathcal{N}^i]$ is space dependent. If the rotation of the element co-ordinate system with respect to the body co-ordinate system is small, which is true for small elastic deformations, the matrices $[\Re^i]$ and $\left[\overline{\Re}^i\right]$ are considered constant. The respective expressions of $[\Re^i]$ and $\left[\overline{\Re}^i\right]$ are given in Appendix A.

Figure 2-6 shows a typical two-node three dimensional beam element of length l^i, where each node has six degrees of freedom. The vector $\{e^i\}$ defined with respect to the element axes is denoted by

$$\{e^i\}_{12\times1} = \begin{bmatrix} u_1^i & v_1^i & w_1^i & \theta_{x1}^i & \theta_{y1}^i & \theta_{z1}^i & u_2^i & v_2^i & w_2^i & \theta_{x2}^i & \theta_{y2}^i & \theta_{z2}^i \end{bmatrix}^T \tag{2.16}$$

where $(u_1^i,\ u_2^i)$ are the nodal axial displacements, and $(v_1^i,\ v_2^i)$ and $(w_1^i,\ w_2^i)$ are the nodal translational displacements in the y- and z-directions, respectively; $(\theta_{x1}^i,\ \theta_{x2}^i)$ are the nodal torsional displacements about the x-axis, and $(\theta_{y1}^i,\ \theta_{y2}^i)$ and $(\theta_{z1}^i,\ \theta_{z2}^i)$ are the nodal rotational displacements in the (xz)- and (xy)-planes, respectively.

The global position of point P^i of the i^{th} beam element is given by

$$\{\mathcal{R}_P^i\} = \{\mathcal{R}_o\} + [\mathcal{A}] \{r_P^i\} \tag{2.17}$$

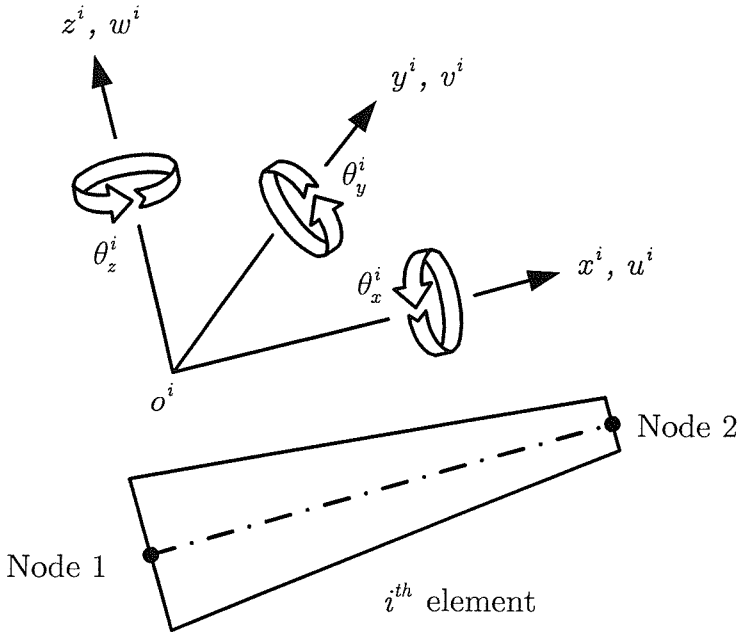

Figure 2-6: Generalized co-ordinates of the three dimensional i^{th} beam element.

Substitution of equations (2.10) and (2.14) into (2.17) yields

$$\{\mathcal{R}_P^i\} = \{\mathcal{R}_o\} + [\mathcal{A}]\left(\left\{r_{P_1}^i\right\} + [\mathcal{N}^i]\{e^i\}\right) \tag{2.18}$$

2.6 Velocity Expression of the Model

To evaluate the kinetic energy of the i^{th} element, it is necessary to derive an expression of the velocity vector of the infinitesimal volume at point P^i of the i^{th} element. Differentiate the position vector $\{\mathcal{R}_P^i\}$ with respect to time yields the velocity vector of point P^i

$$\left\{\dot{\mathcal{R}}_P^i\right\} = \left\{\dot{\mathcal{R}}_o\right\} + [\dot{\mathcal{A}}]\left(\left\{r_{P_1}^i\right\} + [\mathcal{N}^i]\{e^i\}\right) + [\mathcal{A}]\left(\left\{\dot{r}_{P_1}^i\right\} + [\mathcal{N}^i]\{\dot{e}^i\}\right) \tag{2.19}$$

simplifying this equation to get

$$\left\{\dot{\mathcal{R}}_P^i\right\} = \left\{\dot{\mathcal{R}}_o\right\} + [\dot{\mathcal{A}}]\left\{r_{P_1}^i\right\} + [\dot{\mathcal{A}}][\mathcal{N}^i]\{e^i\} + [\mathcal{A}][\mathcal{N}^i]\{\dot{e}^i\} \tag{2.20}$$

where the time derivative of the vector $\left\{r_{P_1}^i\right\}$ has been taken to be zero provided it has a constant magnitude. The transformation $[\mathcal{A}]$ takes care of the direction of that vector. Apply the differential operator

$$\frac{\mathrm{d}(\ \ )}{\mathrm{d}t} = \frac{\partial(\ \ )}{\partial t} + \{\Omega\} \times (\ \ ) \tag{2.21}$$

for the vector $\{\mathcal{R}_o\}$, one can write

$$\frac{\mathrm{d}\{\mathcal{R}_o\}}{\mathrm{d}t} = \frac{\partial\{\mathcal{R}_o\}}{\partial t} + \{\Omega\} \times \{\mathcal{R}_o\} = \{\Omega\} \times \{\mathcal{R}_o\} = \left[\widetilde{\Omega}\right]\{\mathcal{R}_o\} \tag{2.22}$$

where in general, the tilde placed over a matrix $\left[\widetilde{\Omega}\right]$ indicates that the components of a vector $\{\Omega\}$ are used to generate a skew symmetric matrix $\left[\widetilde{\Omega}\right]$ as [95]

$$\{\Omega\} = \begin{Bmatrix} \Omega_x \\ \Omega_y \\ \Omega_z \end{Bmatrix}, \qquad \left[\widetilde{\Omega}\right] = \begin{bmatrix} 0 & -\Omega_z & \Omega_y \\ \Omega_z & 0 & -\Omega_x \\ -\Omega_y & \Omega_x & 0 \end{bmatrix} \tag{2.23}$$

For the case under study, the vector $\{\Omega\}$ and the skew symmetric matrix $\left[\widetilde{\Omega}\right]$ are, respectively, given by

$$\{\Omega\} = \begin{Bmatrix} 0 \\ 0 \\ \Omega_Z \end{Bmatrix}, \qquad \left[\widetilde{\Omega}\right] = \begin{bmatrix} 0 & -\Omega_Z & 0 \\ \Omega_Z & 0 & 0 \\ 0 & 0 & 0 \end{bmatrix} \tag{2.24}$$

The skew symmetric matrix $\left[\widetilde{\Omega}\right]$ can be written in the form

$$\left[\widetilde{\Omega}\right] = \Omega \begin{bmatrix} 0 & -1 & 0 \\ 1 & 0 & 0 \\ 0 & 0 & 0 \end{bmatrix} = \dot{\varphi}\left[\widetilde{\mathcal{A}_I}\right] \tag{2.25}$$

where the subscript z is dropped from Ω_Z and $\left[\widetilde{\mathcal{A}_I}\right]$ is a skew symmetric matrix given by

$$\left[\widetilde{\mathcal{A}_I}\right] = \begin{bmatrix} 0 & -1 & 0 \\ 1 & 0 & 0 \\ 0 & 0 & 0 \end{bmatrix} \tag{2.26}$$

Differentiating the matrix $[\mathcal{A}]$ with respect to time yields

$$[\dot{\mathcal{A}}] = \dot{\varphi}\,[\mathcal{A}_\varphi] \tag{2.27}$$

where the expression of $[\mathcal{A}_\varphi]$ is given by

$$[\mathcal{A}_\varphi] = \begin{bmatrix} -\sin\varphi & -\cos\varphi & 0 \\ \cos\varphi & -\sin\varphi & 0 \\ 0 & 0 & 0 \end{bmatrix} \tag{2.28}$$

Substitute equations (2.9), (2.22), (2.25) and (2.27) into equation (2.20) and using matrix-vectorial notation, one can write

$$\left\{\dot{\mathcal{R}}_P^i\right\} = \left[\left[\widetilde{\mathcal{A}_I}\right]\{\mathcal{R}_\circ\} + [\mathcal{A}_\varphi]\,[\mathcal{A}_\circ]\left\{r_{P_\circ}^i\right\} + [\mathcal{A}_\varphi]\,[N^i]\{e^i\} \qquad [\mathcal{A}][N^i]\right] \begin{Bmatrix} \dot{\varphi} \\ \dot{e}^i \end{Bmatrix} \tag{2.29}$$

in order to isolate the velocity terms. The above expression can be written in compact form as

$$\left\{\dot{\mathcal{R}}_{P^i}^i\right\} = \left[[\mathcal{D}^i] \qquad [\mathcal{A}][N^i]\right] \begin{Bmatrix} \dot{\varphi} \\ \dot{e}^i \end{Bmatrix} \tag{2.30}$$

where

$$[\mathcal{D}^i] = \left[\widetilde{\mathcal{A}_I}\right]\{\mathcal{R}_\circ\} + [\mathcal{A}_\varphi]\,[\mathcal{A}_\circ]\left\{r_{P_\circ}^i\right\} + [\mathcal{A}_\varphi]\,[N^i]\{e^i\} \tag{2.31}$$

2.7 Kinetic Energy

The kinetic energy expression of the i^{th} element is obtained by integrating the kinetic energy of the infinitesimal volume at point P^i over the volume V^i, that is

$$\mathcal{T}^i = \frac{1}{2}\int_{V^i} \rho \left\{\dot{\mathcal{R}}_P^i\right\}^T \left\{\dot{\mathcal{R}}_P^i\right\} \mathrm{d}V^i \tag{2.32}$$

where ρ is the mass density of the i^{th} element. Utilizing the velocity equation (2.30), the expression of $\mathcal{T}^i$ can be written in vector-matrix form as

$$\mathcal{T}^i = \frac{1}{2}\begin{Bmatrix} \dot{\varphi} \\ \dot{e}^i \end{Bmatrix}^T \left(\int_{V^i} \rho \begin{bmatrix} [\mathcal{D}^i]^T[\mathcal{D}^i] & [\mathcal{D}^i]^T[\mathcal{A}][\mathcal{N}^i] \\ [\mathcal{N}^i]^T[\mathcal{A}]^T[\mathcal{D}^i] & [\mathcal{N}^i]^T[\mathcal{N}^i] \end{bmatrix} \mathrm{d}V^i\right) \begin{Bmatrix} \dot{\varphi} \\ \dot{e}^i \end{Bmatrix} \tag{2.33}$$

where the orthonormality of the matrix $[\mathcal{A}]$, i.e., $[\mathcal{A}]^T[\mathcal{A}] = [\,\mathbf{I}\,]$ is utilized to simplify the lower right submatrix of equation (2.33). The above equation can be written in more compact form as

$$\mathcal{T}^i = \frac{1}{2}\left\{\dot{q}^i\right\}^T \left[M^i\right] \left\{\dot{q}^i\right\} \tag{2.34}$$

where $\left\{q^i\right\}$ is the vector of generalized co-ordinates given by $\left\{q^i\right\} = \left[\varphi^T \quad \left\{e^i\right\}^T\right]^T$ in which φ represents the reference co-ordinates while $\left\{e^i\right\}$ is the elastic nodal displacement vector of the i^{th} element. The matrix $\left[M^i\right]$ is the elemental mass matrix that can be written in a symbolic form as

$$\left[M^i\right] = \begin{bmatrix} \left[m^i_{rr}\right] & \left[m^i_{re}\right] \\ \left[m^i_{er}\right] & \left[m^i_{ee}\right] \end{bmatrix} \tag{2.35}$$

where $\left[m^i_{re}\right] = \left[m^i_{er}\right]^T$. The subscripts r and e refer to reference and elastic co-ordinates, respectively. The submatrix $\left[m^i_{rr}\right]$ is the mass matrix associated with the reference co-ordinate system, usually referred to as the mass matrix due to rigid body rotation, while the submatrix $\left[m^i_{re}\right]$ represents the inertia coupling between the reference motion and the elastic deformations of the i^{th} element. The submatrix $\left[m^i_{ee}\right]$ associated with the elastic co-ordinates is of the kind usually occurring in linear structural dynamics problems and comprises all the matrices associated with the elastic generalized co-ordinates. This submatrix is invariant and can be evaluated once in advance in dynamic analysis. The elastic and reference co-ordinates can be dynamically decoupled by neglecting these two submatrices. Using equations (2.33) and (2.35), the elements of the mass matrix $\left[M^i\right]$ are represented as follows

$$\left[m^i_{rr}\right] = \int_{V^i} \rho \left[\mathcal{D}^i\right]^T \left[\mathcal{D}^i\right] \mathrm{d}V^i \tag{2.36}$$

$$\left[m^i_{re}\right] = \left[m^i_{er}\right]^T = \int_{V^i} \rho \left[\mathcal{D}^i\right]^T [\mathcal{A}][\mathcal{N}^i]\mathrm{d}V^i \tag{2.37}$$

$$\left[m^i_{ee}\right] = \int_{V^i} \rho[\mathcal{N}^i]^T[\mathcal{N}^i]\mathrm{d}V^i \tag{2.38}$$

Unlike $\left[m^i_{ee}\right]$, the submatrices $\left[m^i_{rr}\right]$ and $\left[m^i_{re}\right]$ are implicitly time dependent since they are function of the generalized co-ordinates thus resulting in an inertia variant model. Expanding equations (2.36) and (2.37) using (2.31) results in the following:

$$[m^i_{rr}] = \int_{V^i} \rho \begin{pmatrix} \{\mathcal{R}_\circ\}^T [\mathcal{I}_\circ] \{\mathcal{R}_\circ\} + 2\{\mathcal{R}_\circ\}^T \left[\widetilde{\mathcal{A}_I}\right]^T [\mathcal{A}_\varphi] [\mathcal{N}^i] \{e^i\} \\ +2\{\mathcal{R}_\circ\}^T \left[\widetilde{\mathcal{A}_I}\right]^T [\mathcal{A}_\varphi] [\mathcal{A}_\circ] \{r^i_{P_\circ}\} + \{e^i\}^T [\mathcal{N}^i]^T [\mathcal{I}_\circ] [\mathcal{N}^i] \{e^i\} \\ +2\{e^i\}^T [\mathcal{N}^i]^T [\mathcal{I}_\circ] [\mathcal{A}_\circ] \{r^i_{P_\circ}\} + \{r^i_{P_\circ}\}^T [\mathcal{A}_\circ]^T [\mathcal{I}_\circ] [\mathcal{A}_\circ] \{r^i_{P_\circ}\} \end{pmatrix} \mathrm{d}V^i \quad (2.39)$$

$$[m^i_{re}] = \int_{V^i} \rho \begin{pmatrix} \{\mathcal{R}_\circ\}^T \left[\widetilde{\mathcal{A}_I}\right]^T [\mathcal{A}] [\mathcal{N}^i] + \{e^i\}^T [\mathcal{N}^i]^T \left[\widetilde{\mathcal{A}_I}\right]^T [\mathcal{N}^i] \\ + \{r^i_{P_\circ}\}^T [\mathcal{A}_\circ]^T \left[\widetilde{\mathcal{A}_I}\right]^T [\mathcal{N}^i] \end{pmatrix} \mathrm{d}V^i \quad (2.40)$$

where

$$[\mathcal{I}_\circ] = [\mathcal{A}_\varphi]^T [\mathcal{A}_\varphi] = \left[\widetilde{\mathcal{A}_I}\right]^T \left[\widetilde{\mathcal{A}_I}\right] = \begin{bmatrix} 1 & 0 & 0 \\ 0 & 1 & 0 \\ 0 & 0 & 0 \end{bmatrix} \quad (2.41)$$

and

$$\left[\widetilde{\mathcal{A}_I}\right]^T = [\mathcal{A}_\varphi]^T [\mathcal{A}] \quad (2.42)$$

where the expressions of $\left[\widetilde{\mathcal{A}_I}\right]$ and $[\mathcal{A}_\varphi]$ are given previously by equations (2.26) and (2.28), respectively. The expressions of $[m^i_{rr}]$, $[m^i_{re}]$ can be written in compact form as

$$[m^i_{rr}] = [\mathbf{I}^i_{\mathcal{R}_\circ \mathcal{R}_\circ}] + 2[m^i_{\mathcal{R}_\circ e}] \{e^i\} + 2\left[\mathbf{I}^i_{\mathcal{R}_\circ r_{P_\circ}}\right] + \{e^i\}^T [m^i_t] \{e^i\} + 2\{e^i\}^T \left[m^i_{r_{P_\circ e}}\right] + \left[\mathbf{I}^i_{r_{P_\circ} r_{P_\circ}}\right] \quad (2.43)$$

and

$$[m^i_{re}] = [m^i_{\mathcal{R}_\circ}] + \{e^i\}^T \left[\widetilde{C^i}\right] + \left[m^i_{r_{P_\circ}}\right] \quad (2.44)$$

where

$$[\mathbf{I}^i_{\mathcal{R}_\circ \mathcal{R}_\circ}] = \int_{V^i} \rho \{\mathcal{R}_\circ\}^T [\mathcal{I}_\circ] \{\mathcal{R}_\circ\} \mathrm{d}V^i \quad (2.45)$$

$$[m^i_{\mathcal{R}_\circ e}] = \int_{V^i} \rho \{\mathcal{R}_\circ\}^T \left[\widetilde{\mathcal{A}_I}\right]^T [\mathcal{A}_\varphi] [\mathcal{N}^i] \mathrm{d}V^i \quad (2.46)$$

$$\left[\mathbf{I}^i_{\mathcal{R}_\circ r_{P_\circ}}\right] = \int_{V^i} \rho \{\mathcal{R}_\circ\}^T \left[\widetilde{\mathcal{A}_I}\right]^T [\mathcal{A}_\varphi] [\mathcal{A}_\circ] \{r^i_{P_\circ}\} \mathrm{d}V^i \quad (2.47)$$

$$\left[m_t^i\right] = \int_{V^i} \rho[\mathcal{N}^i]^T[\mathcal{I}_o][\mathcal{N}^i]\mathrm{d}V^i \tag{2.48}$$

$$\left[m^i_{r_{P_o}e}\right] = \int_{V^i} \rho[\mathcal{N}^i]^T\left[\mathcal{I}_o\right]\left[\mathcal{A}_o\right]\left\{r^i_{P_o}\right\}\mathrm{d}V^i \tag{2.49}$$

$$\left[\mathbf{I}^i_{r_{P_o}r_{P_o}}\right] = \int_{V^i} \rho\left\{r^i_{P_o}\right\}^T\left[\mathcal{A}_o\right]^T\left[\mathcal{I}_o\right]\left[\mathcal{A}_o\right]\left\{r^i_{P_o}\right\}\mathrm{d}V^i \tag{2.50}$$

$$\left[m^i_{\mathcal{R}_o}\right] = \int_{V^i} \rho\left\{\mathcal{R}_o\right\}^T\left[\widetilde{\mathcal{A}_I}\right]^T[\mathcal{A}][\mathcal{N}^i]\mathrm{d}V^i \tag{2.51}$$

$$\left[\widetilde{C^i}\right] = \int_{V^i} \rho[\mathcal{N}^i]^T\left[\widetilde{\mathcal{A}_I}\right][\mathcal{N}^i]\mathrm{d}V^i \tag{2.52}$$

$$\left[m^i_{r_{P_o}}\right] = \int_{V^i} \rho\left\{r^i_{P_o}\right\}^T\left[\mathcal{A}_o\right]^T\left[\widetilde{\mathcal{A}_I}\right]^T[\mathcal{N}^i]\mathrm{d}V^i \tag{2.53}$$

$$\left[m^i_{ee}\right] = \int_{V^i} \rho[\mathcal{N}^i]^T[\mathcal{N}^i]\mathrm{d}V^i \tag{2.54}$$

By using equation (2.15), one can write

$$\left[m^i_{\mathcal{R}_o e}\right] = \int_{V^i} \rho\left\{\mathcal{R}_o\right\}^T\left[\widetilde{\mathcal{A}_I}\right]^T\left[\mathcal{A}_\varphi\right]\left[\Re^i\right]\left[\mathcal{S}^i\right]\left[\overline{\Re}^i\right]\mathrm{d}V^i \tag{2.55}$$

$$\left[m_t^i\right] = \left[\overline{\Re}^i\right]^T\left(\int_{V^i} \rho\left[\mathcal{S}^i\right]^T\left[\Re^i\right]^T\left[\mathcal{I}_o\right]\left[\Re^i\right]\left[\mathcal{S}^i\right]\mathrm{d}V^i\right)\left[\overline{\Re}^i\right] \tag{2.56}$$

$$\left[m^i_{r_{P_o}e}\right] = \int_{V^i} \rho\left[\overline{\Re}^i\right]^T\left[\mathcal{S}^i\right]^T\left[\Re^i\right]^T\left[\mathcal{I}_o\right]\left[\mathcal{A}_o\right]\left\{r^i_{P_o}\right\}\mathrm{d}V^i \tag{2.57}$$

$$\left[m^i_{\mathcal{R}_o}\right] = \int_{V^i} \rho\left\{\mathcal{R}_o\right\}^T\left[\widetilde{\mathcal{A}_I}\right]^T[\mathcal{A}]\left[\Re^i\right]\left[\mathcal{S}^i\right]\left[\overline{\Re}^i\right]\mathrm{d}V^i \tag{2.58}$$

$$\left[\widetilde{C^i}\right] = \left[\overline{\Re}^i\right]^T\left(\int_{V^i} \rho\left[\mathcal{S}^i\right]^T\left[\Re^i\right]^T\left[\widetilde{\mathcal{A}_I}\right]\left[\Re^i\right]\left[\mathcal{S}^i\right]\mathrm{d}V^i\right)\left[\overline{\Re}^i\right] \tag{2.59}$$

$$\left[m^i_{r_{P_o}}\right] = \int_{V^i} \rho\left\{r^i_{P_o}\right\}^T\left[\mathcal{A}_o\right]^T\left[\widetilde{\mathcal{A}_I}\right]^T\left[\Re^i\right]\left[\mathcal{S}^i\right]\left[\overline{\Re}^i\right]\mathrm{d}V^i \tag{2.60}$$

$$\left[m^i_{ee}\right] = \left[\overline{\Re}^i\right]^T\left(\int_{V^i} \rho\left[\mathcal{S}^i\right]^T\left[\mathcal{S}^i\right]\mathrm{d}V^i\right)\left[\overline{\Re}^i\right] \tag{2.61}$$

defined with respect to the body co-ordinate axes. The orthonormality of the matrix $\left[\Re^i\right]$, i.e., $\left[\Re^i\right]^T\left[\Re^i\right] = [\,\mathbf{I}\,]$ is utilized to simplify the expression of $\left[m^i_{ee}\right]$. Expressions of $\left[\widetilde{C^i}\right]$ and $\left[m^i_{ee}\right]$ can be written in more compact form as

$$\left[\widetilde{C^i}\right] = \left[\overline{\Re}^i\right]^T \left[\widetilde{\overline{C}^i}\right] \left[\overline{\Re}^i\right] \tag{2.62}$$

$$\left[m^i_{ee}\right] = \left[\overline{\Re}^i\right]^T \left[\overline{m}^i_{ee}\right] \left[\overline{\Re}^i\right] \tag{2.63}$$

where $\left[\widetilde{\overline{C}^i}\right]$ and $\left[\overline{m}^i_{ee}\right]$ are given by

$$\left[\widetilde{\overline{C}^i}\right] = \int_{V^i} \rho \left[\mathcal{S}^i\right]^T \left[\Re^i\right]^T \left[\widetilde{\mathcal{A}_I}\right] \left[\Re^i\right] \left[\mathcal{S}^i\right] \mathrm{d}V^i \tag{2.64}$$

$$\left[\overline{m}^i_{ee}\right] = \int_{V^i} \rho \left[\mathcal{S}^i\right]^T \left[\mathcal{S}^i\right] \mathrm{d}V^i \tag{2.65}$$

The submatrix $\left[\overline{m}^i_{ee}\right]$, is the composite mass matrix that can be written as:

$$\left[\overline{m}^i_{ee}\right] = \left[\overline{m}^i_a\right] + \left[\overline{m}^i_{\theta_x}\right] + \left[\overline{m}^i_{t,v}\right] + \left[\overline{m}^i_{t,w}\right] + \left[\overline{m}^i_{\theta_z,v}\right] + \left[\overline{m}^i_{\theta_y,w}\right] + \left[\overline{m}^i_{\theta,vw}\right] \tag{2.66}$$

defined with respect to the element co-ordinate axes. Notice that the constituents of $\left[\overline{m}^i_{ee}\right]$ are time invariant and defined as

$\left[\overline{m}^i_a\right]$ $\equiv$ elemental axial mass matrix

$\left[\overline{m}^i_{\theta_x}\right]$ $\equiv$ elemental torsional mass matrix

$\left[\overline{m}^i_{t,v}\right]$ $\equiv$ elemental translational mass matrix in the (xy)-plane

$\left[\overline{m}^i_{t,w}\right]$ $\equiv$ elemental translational mass matrix in the (xz)-plane

$\left[\overline{m}^i_{\theta_z,v}\right]$ $\equiv$ elemental rotary inertia mass matrix in the (xy)-plane

$\left[\overline{m}^i_{\theta_y,w}\right]$ $\equiv$ elemental rotary inertia mass matrix in the (xz)-plane

$\left[\overline{m}^i_{\theta,vw}\right]$ $\equiv$ elemental rotary inertia mass matrix due to coupling in bending

The explicit expressions of the above matrices will be given in the next chapter. Notice that the elemental rotary inertia mass matrices $\left[\overline{m}^i_{\theta_z,v}\right]$, $\left[\overline{m}^i_{\theta_y,w}\right]$ and $\left[\overline{m}^i_{\theta,vw}\right]$ being dependent on the second moments of areas I^i_{yy} and I^i_{zz} and the product second moment of area I^i_{yz}, respectively, are functions of the setting angle ψ.

The expression for $\mathcal{T}^i$ can be written in abbreviated form as

$$\mathcal{T}^i = \frac{1}{2}\dot{\varphi}^T \left[m^i_{rr}\right] \dot{\varphi} + \dot{\varphi}^T \left[m^i_{re}\right] \left\{\dot{e}^i\right\} + \frac{1}{2} \left\{\dot{e}^i\right\}^T \left[m^i_{ee}\right] \left\{\dot{e}^i\right\} \tag{2.67}$$

The kinetic energy $\mathcal{T}$ of the entire beam is obtained by summing the kinetic energy of each of its individual element. Denoting by n the total number of elements of the beam, the kinetic energy $\mathcal{T}$ of the beam is given by

$$\mathcal{T} = \sum_{j=1}^{n} \mathcal{T}^i = \frac{1}{2} \{\dot{q}\}^T [M] \{\dot{q}\} \tag{2.68}$$

where $\{q\}$ is the vector of generalized co-ordinates of the beam given by $\{q\} = \begin{bmatrix} \varphi^T & \{e\}^T \end{bmatrix}^T$ in which φ represents the reference co-ordinate while $\{e\}$ is the elastic nodal displacements vector of all elements of the beam and $[M]$ is the mass matrix of the beam. The matrix $[M]$ can be written as

$$[M] = \begin{bmatrix} [M_{rr}] & [M_{re}] \\ [M_{er}] & [M_{ee}] \end{bmatrix} \tag{2.69}$$

where the entries of the mass $[M]$ are given by

$$[M_{rr}] = \sum_{i=1}^{n} \left(\int_{V^i} \rho \left[\mathcal{D}^i\right]^T \left[\mathcal{D}^i\right] \mathrm{d}V^i \right) \tag{2.70}$$

$$[M_{re}] = [M_{er}]^T = \sum_{i=1}^{n} \left(\int_{V^i} \rho \left[\mathcal{D}^i\right]^T [\mathcal{A}][\mathcal{N}^i] \mathrm{d}V^i \right) \tag{2.71}$$

$$[M_{ee}] = \sum_{i=1}^{n} \left(\int_{V^i} \rho [\mathcal{N}^i]^T [\mathcal{N}^i] \mathrm{d}V^i \right) \tag{2.72}$$

2.8 Strain Energy

The development of the strain energy expression of the spinning tapered Timoshenko beam will not differ from the one used in linear structural analysis. This is basically due to the fact that elastic co-ordinates are defined locally and accordingly, there will be no stiffness coupling between the reference motion and elastic deformations. However, there is a stiffness coupling in the elastic co-ordinates resulting from the orientation of the cross-section by a setting angle ψ.

Consider a point P^i in a deformed state of the i^{th} element, located at a distance x^i from the left end and denote the components of displacements along the x-, y-, and z-axes by U^i, V^i, and W^i respectively. When the i^{th} element deforms the displacements of its cross-section can be described by the translations u^i, v^i and w^i in the x-, y- and z-directions as well as the small rotations θ_x^i, θ_y^i and θ_z^i about x-, z-, and y-axes, respectively.

For linear small elastic deformations of an isotropic body, the strain energy of the i^{th} element can be given by

$$\mathcal{U}^i = \frac{1}{2}\int_{V^i} \left(\sigma^i_{xx}\varepsilon^i_{xx} + \sigma^i_{yy}\varepsilon^i_{yy} + \sigma^i_{zz}\varepsilon^i_{zz} + \tau^i_{xy}\gamma^i_{xy} + \tau^i_{yz}\gamma^i_{yz} + \tau^i_{xz}\gamma^i_{xz}\right) \mathrm{d}V^i \tag{2.73}$$

where ε^i, γ^i and σ^i, τ^i are strain and associated stress components at point P^i of the i^{th} element of the infinitesimal volume V^i. The generalized Hooke's law for an isotropic homogeneous material is

$$\begin{aligned}
\sigma^i_{xx} &= \tfrac{E}{(1+\nu)(1-2\nu)}\left[(1-\nu)\,\varepsilon^i_{xx} + \nu\left(\varepsilon^i_{yy} + \varepsilon^i_{zz}\right)\right] \\
\sigma^i_{yy} &= \tfrac{E}{(1+\nu)(1-2\nu)}\left[(1-\nu)\,\varepsilon^i_{yy} + \nu\left(\varepsilon^i_{zz} + \varepsilon^i_{xx}\right)\right] \\
\sigma^i_{zz} &= \tfrac{E}{(1+\nu)(1-2\nu)}\left[(1-\nu)\,\varepsilon^i_{zz} + \nu\left(\varepsilon^i_{xx} + \varepsilon^i_{yy}\right)\right] \\
\tau^i_{xy} &= G\gamma^i_{xy} \\
\tau^i_{yz} &= G\gamma^i_{yz} \\
\tau^i_{xz} &= G\gamma^i_{xz}
\end{aligned} \tag{2.74}$$

where ν is Poisson's ratio, E is the Young's modulus of elasticity, and G is the shear modulus of rigidity of the material. For an isotropic material, these quantities are related by

$$E = 2G(1+\nu) \tag{2.75}$$

Substitution of equations (2.74) and (2.75) into (2.73) yields

$$\mathcal{U}^i = \frac{1}{2}\int_{V^i} \left(\frac{1}{E}\left[\sigma^{i^2}_{xx} + \sigma^{i^2}_{yy} + \sigma^{i^2}_{zz} - 2\nu\left(\sigma^i_{xx}\sigma^i_{yy} + \sigma^i_{xx}\sigma^i_{zz} + \sigma^i_{yy}\sigma^i_{zz}\right)\right] + \frac{1}{G}\left(\tau^{i^2}_{xy} + \tau^{i^2}_{yz} + \tau^{i^2}_{yz}\right)\right) \mathrm{d}V^i \tag{2.76}$$

On the other hand, equation (2.76) can be written as

$$\mathcal{U}^i = \frac{1}{2}\left\{e^i\right\}^T \left[k^i_{ee}\right] \left\{e^i\right\} \tag{2.77}$$

where $\left[k^i_{ee}\right]$ is the elemental elastic stiffness matrix defined with respect to the body co-ordinate system and can be evaluated once prior to the dynamic analysis. By using equation (2.15), one can write

$$\mathcal{U}^i = \frac{1}{2}\left\{e^i\right\}^T \left(\left[\overline{\Re}^i\right]^T \left[\overline{k}^i_{ee}\right] \left[\overline{\Re}^i\right]\right) \left\{e^i\right\} \tag{2.78}$$

where $\left[\overline{k}_{ee}^{i}\right]$ is the elemental elastic stiffness matrix defined with respect to the element co-ordinate system. The relationship between $\left[\overline{k}_{ee}^{i}\right]$ and $\left[k_{ee}^{i}\right]$ is given by

$$\left[k_{ee}^{i}\right] = \left[\overline{\Re}^{i}\right]^{T} \left[\overline{k}_{ee}^{i}\right] \left[\overline{\Re}^{i}\right] \tag{2.79}$$

The strain energy expression is independent of the reference co-ordinates, because the elastic generalized co-ordinates are defined with respect to the body-fixed (xyz) co-ordinate system. Equations (2.73) through (2.79) are derived in general form and are valid for any elastic structure that undergoes small deformations in space. Equation (2.77) can be written in a more general form as

$$\mathcal{U}^{i} = \frac{1}{2} \left\{ \begin{array}{c} \varphi \\ e^{i} \end{array} \right\}^{T} \left[\begin{array}{cc} 0 & 0 \\ 0 & \left[k_{ee}^{i}\right] \end{array} \right] \left\{ \begin{array}{c} \varphi \\ e^{i} \end{array} \right\} \tag{2.80}$$

Since the bending planes (xy) and (xz) are assumed to coincide with the principal axes of the cross-section of the beam while the x-axis is assumed to coincide with the centroidal axis of the beam, all deformations caused by the different stresses can be separated into six groups. These groups will now be considered independently and the strain energy for each of these groups will be derived separately according to the procedure prescribed by Przemeniecki [92].

2.8.1 Strain Energy due to Axial Deformation

The kinematic displacement of the i^{th} element that is subjected to small axial deformation can be written in terms of its non-zero component as

$$U^{i} = u^{i} \tag{2.81}$$

and the associated strain component as

$$\varepsilon_{xx}^{i} = \frac{\partial u^{i}}{\partial x^{i}} \tag{2.82}$$

The corresponding strain energy expression is then given by

$$\mathcal{U}_{a}^{i} = \frac{1}{2} \int_{V^{i}} \left\{\varepsilon_{xx}^{i}\right\}^{T} \left\{\sigma_{xx}^{i}\right\} \mathrm{d}V^{i} \tag{2.83}$$

Substitution of equation (2.74) into (2.83) yields

$$\mathcal{U}_a^i = \frac{1}{2}\int_0^{l^i} \left(\frac{\partial u^i}{\partial x^i}\right)^T EA^i \left(\frac{\partial u^i}{\partial x^i}\right) \mathrm{d}x^i \tag{2.84}$$

where A^i is the cross-sectional area of the i^{th} element. Notice that $\dfrac{\partial u^i}{\partial x^i}$ can be expressed as

$$\frac{\partial u^i}{\partial x^i} = \frac{\partial}{\partial x^i}\left(\left[\mathcal{N}_a^i\right]\left\{e^i\right\}\right) = \left[\Re^i\right]\left[B_a^i\right]\left[\overline{\Re}^i\right]\left\{e^i\right\} \tag{2.85}$$

where $\left[B_a^i\right]$ is a differential operator associated with axial deformations and given by

$$\left[B_a^i\right] = \frac{\partial}{\partial x^i}\left[\mathcal{S}_a^i\right] \tag{2.86}$$

where $\left[\mathcal{S}_a^i\right]$ is the element axial shape function. Substitute equation (2.85) into (2.84) to get

$$\mathcal{U}_a^i = \frac{1}{2}\left\{e^i\right\}^T \left[\overline{\Re}^i\right]^T \left(\int_0^{l^i} \left[B_a^i\right]^T EA^i \left[B_a^i\right] \mathrm{d}x^i\right) \left[\overline{\Re}^i\right]\left\{e^i\right\} \tag{2.87}$$

or

$$\mathcal{U}_a^i = \frac{1}{2}\left\{e^i\right\}^T \left(\left[\overline{\Re}^i\right]^T \left[\overline{k}_a^i\right] \left[\overline{\Re}^i\right]\right)\left\{e^i\right\} \tag{2.88}$$

where $\left[\overline{k}_a^i\right]$ is the elemental axial stiffness matrix defined with respect to the element co-ordinate axes and given by

$$\left[\overline{k}_a^i\right] = \int_0^{l^i} \left[B_a^i\right]^T EA^i \left[B_a^i\right] \mathrm{d}x^i \tag{2.89}$$

In more compact form, equation (2.88) can be written as

$$\mathcal{U}_a^i = \frac{1}{2}\left\{e^i\right\}^T \left[k_a^i\right]\left\{e^i\right\} \tag{2.90}$$

where

$$\left[k_a^i\right] = \left[\overline{\Re}^i\right]^T \left[\overline{k}_a^i\right] \left[\overline{\Re}^i\right] \tag{2.91}$$

is defined with respect to the body co-ordinate axes.

2.8.2 Strain Energy due to Torsion

Neglecting the warping due to torsional deformation of the cross-section, the i^{th} element is assumed to undergo torsional deformation about the x-axis only. Figure 2-7 shows the partial end view of the i^{th} element (and could represent any section). An arbitrary point on the cross-

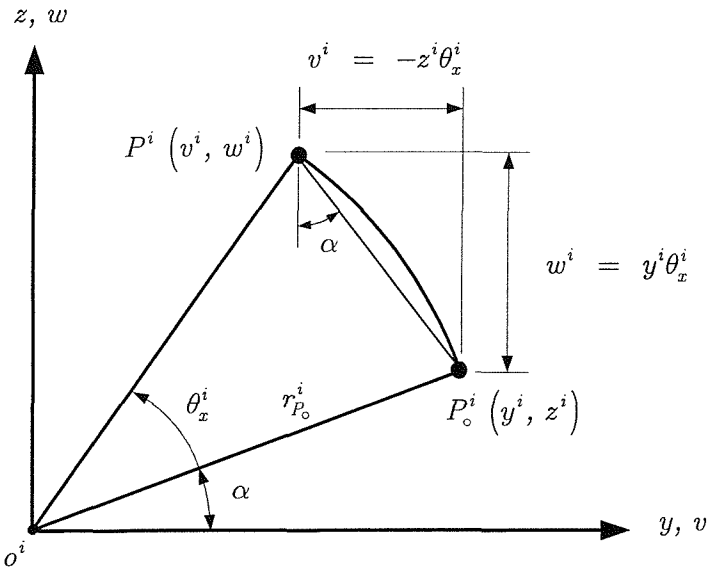

Figure 2-7: Displacement components in the plane of the cross-section.

section, point P_o^i located at a distance $r_{P_o}^i$ from the center of twist o^i, has moved to point P^i as a result of twist deformation. Assuming the angle of twist, θ_x^i to be small, the resulting kinematic displacement components U^i, V^i, and W^i are given by

$$\begin{aligned} U^i &= 0 \\ V^i &= -r_{P_o}^i\ \theta_x^i\ \sin\alpha = -z^i\ \theta_x^i \\ W^i &= r_{P_o}^i\ \theta_x^i\ \cos\alpha = y^i\ \theta_x^i \end{aligned} \tag{2.92}$$

while the associated non-zero strain components are given by

$$\gamma_{xy}^i = -z^i\ \frac{\partial\theta_x^i}{\partial x^i} \tag{2.93}$$

$$\gamma_{xz}^i = y^i\ \frac{\partial\theta_x^i}{\partial x^i} \tag{2.94}$$

and the corresponding shear stresses can be obtained from equation (2.75) as

$$\tau_{xy}^i = G\gamma_{xy}^i \tag{2.95}$$

and

$$\tau_{xz}^{i} = G\gamma_{xz}^{i} \tag{2.96}$$

The strain energy expression due to torsional deformation of the i^{th} element is expressed as

$$\mathcal{U}_{\theta_x}^{i} = \frac{1}{2}\int_{V^i} \left(\tau_{xy}^{i}\gamma_{xy}^{i} + \tau_{xz}^{i}\gamma_{xz}^{i}\right) \mathrm{d}V^{i} \tag{2.97}$$

Substitution of equations (2.95) and (2.96) into (2.97) yields

$$\mathcal{U}_{\theta_x}^{i} = \frac{1}{2}\int_{0}^{l^i} \left(\frac{\partial\theta_x^i}{\partial x^i}\right)^{T} G\, J^{i} \left(\frac{\partial\theta_x^i}{\partial x^i}\right) \mathrm{d}x^{i} \tag{2.98}$$

where J^i is the torsion constant. Notice that $\dfrac{\partial\theta_x^i}{\partial x^i}$ can be expressed as

$$\frac{\partial\theta_x^i}{\partial x^i} = \frac{\partial}{\partial x^i}\left(\left[\mathcal{N}_{\theta_x}^{i}\right]\left\{e^{i}\right\}\right) = \left[\Re^{i}\right]\left[B_{\theta_x}^{i}\right]\left[\overline{\Re}^{i}\right]\left\{e^{i}\right\} \tag{2.99}$$

where $\left[B_{\theta_x}^{i}\right]$ is a differential operator associated with twist deformation given by

$$\left[B_{\theta_x}^{i}\right] = \frac{\partial}{\partial x^i}\left[\mathcal{S}_{\theta_x}^{i}\right] \tag{2.100}$$

and $\left[\mathcal{S}_{\theta_x}^{i}\right]$ is the elemental shape function due to torsional deformation. Substitution of equation (2.99) into (2.98) yields

$$\mathcal{U}_{\theta_x}^{i} = \frac{1}{2}\left\{e^{i}\right\}^{T}\left[\overline{\Re}^{i}\right]^{T}\left(\int_{0}^{l^i}\left[B_{\theta_x}^{i}\right]^{T} GJ^{i}\left[B_{\theta_x}^{i}\right]\mathrm{d}x^{i}\right)\left[\overline{\Re}^{i}\right]\left\{e^{i}\right\}^{T} \tag{2.101}$$

or

$$\mathcal{U}_{\theta_x}^{i} = \frac{1}{2}\left\{e^{i}\right\}^{T}\left(\left[\overline{\Re}^{i}\right]^{T}\left[\overline{k}_{\theta_x}^{i}\right]\left[\overline{\Re}^{i}\right]\right)\left\{e^{i}\right\} \tag{2.102}$$

where $\left[\overline{k}_{\theta_x}^{i}\right]$ is the elemental torsional stiffness matrix of the i^{th} element given by

$$\left[\overline{k}_{\theta_x}^{i}\right] = \int_{0}^{l^i}\left[B_{\theta_x}^{i}\right]^{T} GJ^{i}\left[B_{\theta_x}^{i}\right]\mathrm{d}x^{i} \tag{2.103}$$

In more compact form, equation (2.98) can be written as

$$\mathcal{U}^i_{\theta_x} = \frac{1}{2}\left\{e^i\right\}^T \left[k^i_{\theta_x}\right] \left\{e^i\right\} \tag{2.104}$$

where

$$\left[k^i_{\theta_x}\right] = \left[\overline{\Re}^i\right]^T \left[\overline{k}^i_{\theta_x}\right] \left[\overline{\Re}^i\right] \tag{2.105}$$

is defined with respect to the body co-ordinate axes.

2.8.3 Bending Strain Energy in Deep Beams

If the cross-sectional dimensions of the beam are not small compared to its length or higher bending modes are required, one needs to consider the effects of rotary inertia and shear deformation according to Timoshenko Beam Theory (TBT). Figure 2-8 shows bending deformation of the i^{th} element in the (xy)- and (xz)-plane, respectively. The corresponding kinematic relations of the i^{th} element are expressed as

$$\begin{aligned} U^i &= -y^i \left(\frac{\partial v^i}{\partial x^i}\right) - z^i \left(\frac{\partial w^i}{\partial x^i}\right) \\ V^i &= v^i \\ W^i &= w^i \end{aligned} \tag{2.106}$$

where the two translations $(v^i,\ w^i)$ consist of a contribution $(v^i_b,\ w^i_b)$ due to bending and a contribution $(v^i_s,\ w^i_s)$ due to shear deformation, that is

$$v^i = v^i_b + v^i_s \tag{2.107}$$

$$w^i = w^i_b + w^i_s \tag{2.108}$$

Taking derivatives of the previous relations with respect to the element co-ordinate x^i gives

$$\frac{\partial v^i}{\partial x^i} = \frac{\partial v^i_b}{\partial x^i} + \frac{\partial v^i_s}{\partial x^i} = \theta^i_z + \gamma^i_{xy} \tag{2.109}$$

$$\frac{\partial w^i}{\partial x^i} = \frac{\partial w^i_b}{\partial x^i} + \frac{\partial w^i_s}{\partial x^i} = -\theta^i_y + \gamma^i_{xz} \tag{2.110}$$

where

$$\theta^i_z = \frac{\partial v^i_b}{\partial x^i} \tag{2.111}$$

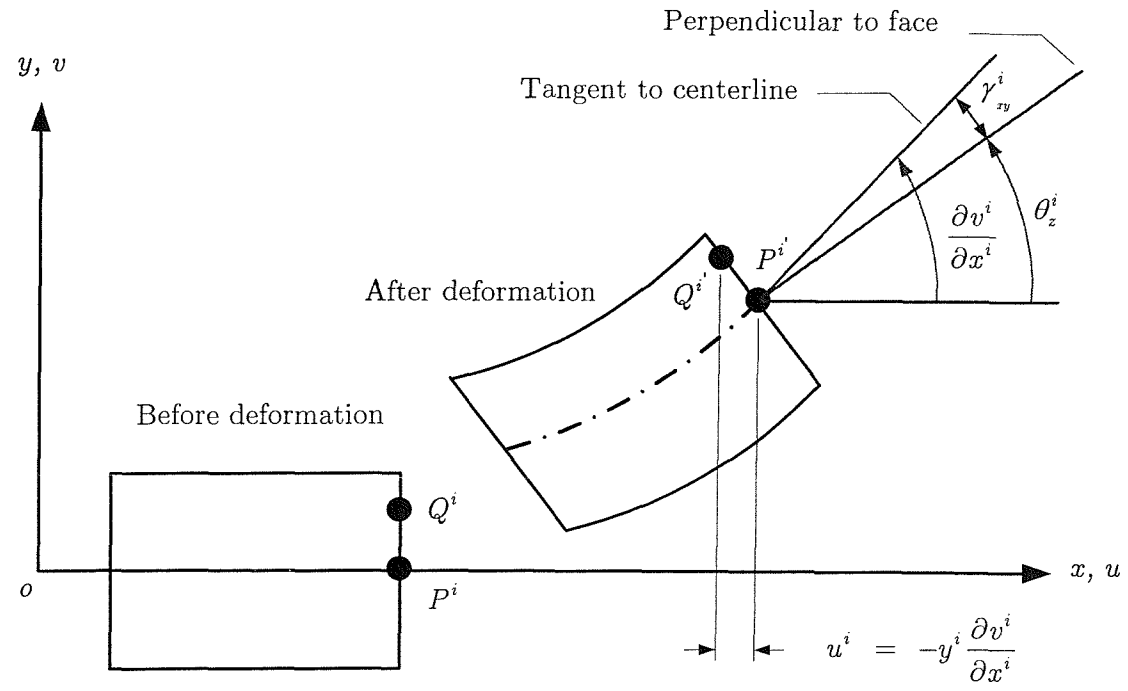

a) Planar deformation in the (xy)-plane

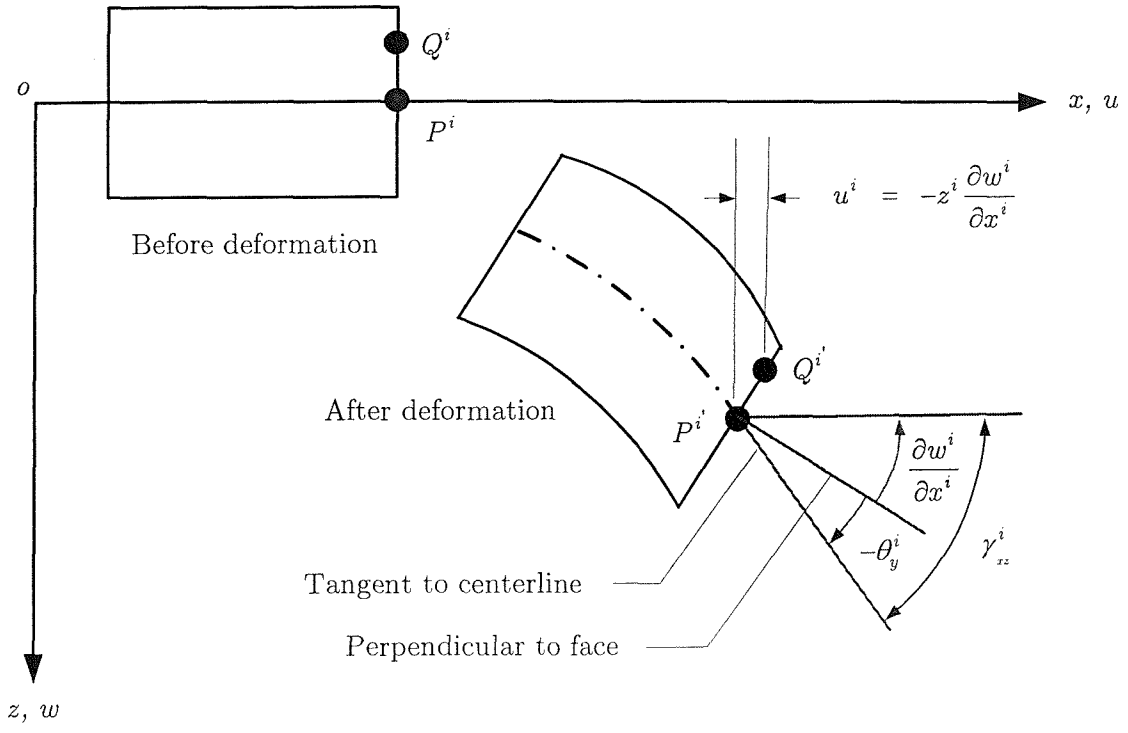

b) Planar deformation in the (xz)-plane

Figure 2-8: Bending deformations in deep beams.

$$\theta_y^i = -\frac{\partial w_b^i}{\partial x^i} \tag{2.112}$$

and the right hand corkscrew convention has been employed. The resultant shearing angle is always measured as the angle between the tangent to the deformed axis and the normal to the cross-section while the rotation angle is always measured relative to the undeformed axis of the beam. The non-zero strain component corresponding to bending deformation is thus given by

$$\varepsilon_{xx}^i = \frac{\partial U^i}{\partial x^i} = -y^i \frac{\partial^2 v_b^i}{\partial {x^i}^2} - z^i \frac{\partial^2 w_b^i}{\partial {x^i}^2} \tag{2.113}$$

The strain energy due to bending deformation is then given by

$$\mathcal{U}_b^i = \frac{1}{2} \int_{V^i} \left\{\varepsilon_{xx}^i\right\}^T \left\{\sigma_{xx}^i\right\} \mathrm{d}V^i \tag{2.114}$$

by using equation (2.74), the previous equation can be written as

$$\mathcal{U}_b^i = \frac{E}{2} \int_{V^i} \left\{\varepsilon_{xx}^i\right\}^T \left\{\varepsilon_{xx}^i\right\} \mathrm{d}V^i \tag{2.115}$$

substitution of equation (2.113) into (2.115) yields

$$\mathcal{U}_b^i = \frac{E}{2} \int_0^{l^i} \int_{A^i} \left(y^{i^2} \left(\frac{\partial^2 v_b^i}{\partial {x^i}^2} \right)^2 + 2 y^i z^i \left(\frac{\partial^2 v_b^i}{\partial {x^i}^2} \right) \left(\frac{\partial^2 w_b^i}{\partial {x^i}^2} \right) + z^{i^2} \left(\frac{\partial^2 w_b^i}{\partial {x^i}^2} \right)^2 \right) \mathrm{d}A^i \mathrm{d}x^i \tag{2.116}$$

or

$$\mathcal{U}_b^i = \frac{E}{2} \int_0^{l^i} \int_{A^i} \left(y^{i^2} \left(\frac{\partial \theta_z^i}{\partial x^i} \right)^2 + 2 y^i z^i \left(\frac{\partial \theta_z^i}{\partial x^i} \right) \left(\frac{\partial \theta_y^i}{\partial x^i} \right) + z^{i^2} \left(\frac{\partial \theta_y^i}{\partial x^i} \right)^2 \right) \mathrm{d}A^i \mathrm{d}x^i \tag{2.117}$$

Noting

$$I_{zz}^i = \int_{A^i} y^{i^2} \mathrm{d}A^i \equiv \text{second moment of area about the } z\text{-axis} \tag{2.118}$$

$$I_{yz}^i = \int_{A^i} y^i z^i \mathrm{d}A^i \equiv \text{product second moment of area} \tag{2.119}$$

$$I_{yy}^i = \int_{A^i} z^{i^2} \mathrm{d}A^i \equiv \text{second moment of area about the } y\text{-axis} \tag{2.120}$$

the strain energy due to bending deformation can be expressed as

$$\mathcal{U}_b^i = \frac{E}{2}\int_0^{l^i}\left(I_{zz}^i\left(\frac{\partial\theta_z^i}{\partial x^i}\right)^2 + 2I_{yz}^i\left(\frac{\partial\theta_z^i}{\partial x^i}\right)\left(\frac{\partial\theta_y^i}{\partial x^i}\right) + I_{yy}^i\left(\frac{\partial\theta_y^i}{\partial x^i}\right)^2\right)\mathrm{d}x^i \tag{2.121}$$

where $\frac{\partial\theta_z^i}{\partial x^i}$, $\frac{\partial\theta_y^i}{\partial x^i}$ and $\frac{\partial\theta_z^i}{\partial x^i}\frac{\partial\theta_y^i}{\partial x^i}$ can be expressed in terms of the generalized co-ordinates $\{e^i\}$ as

$$\frac{\partial\theta_z^i}{\partial x^i} = \frac{\partial}{\partial x^i}\left(\left[\mathcal{N}_{\theta_z}^i\right]\{e^i\}\right) = \left[\Re^i\right]\left[B_{\theta_z}^i\right]\left[\overline{\Re}^i\right]\{e^i\} \tag{2.122}$$

$$\frac{\partial\theta_y^i}{\partial x^i} = \frac{\partial}{\partial x^i}\left(\left[\mathcal{N}_{\theta_y}^i\right]\{e^i\}\right) = \left[\Re^i\right]\left[B_{\theta_y}^i\right]\left[\overline{\Re}^i\right]\{e^i\} \tag{2.123}$$

$$\frac{\partial\theta_z^i}{\partial x^i}\frac{\partial\theta_y^i}{\partial x^i} = \left[\Re^i\right]\left[B_{\theta_{yz}}^i\right]\left[\overline{\Re}^i\right]\{e^i\} \tag{2.124}$$

where $\left[B_{\theta_z}^i\right]$, $\left[B_{\theta_y}^i\right]$ and $\left[B_{\theta_{yz}}^i\right]$ are differential operators associated with bending deformations and given by

$$\left[B_{\theta_z}^i\right] = \frac{\partial}{\partial x^i}\left(\left[\mathcal{S}_{\theta_z}^i\right]\right) \tag{2.125}$$

$$\left[B_{\theta_y}^i\right] = \frac{\partial}{\partial x^i}\left(\left[\mathcal{S}_{\theta_y}^i\right]\right) \tag{2.126}$$

$$\left[B_{\theta_{yz}}^i\right] = \left[B_{\theta_z}^i\right]\left[B_{\theta_y}^i\right] \tag{2.127}$$

and $\left[\mathcal{S}_{\theta_z}^i\right]$ and $\left[\mathcal{S}_{\theta_y}^i\right]$ are the elemental shape functions due to bending deformations in the (xy)- and (xz)-planes, respectively.

The strain energy expression of equation (2.121) can be written as

$$\mathcal{U}_b^i = \frac{1}{2}\{e^i\}^T\left[\overline{\Re}^i\right]^T\left(\int_0^{l^i}\begin{pmatrix}\left[B_{\theta_z}^i\right]^T E\, I_{zz}^i\left[B_{\theta_z}^i\right] \\ +\left[B_{\theta_{yz}}^i\right]^T E\, I_{yz}^i\left[B_{\theta_{yz}}^i\right] \\ +\left[B_{\theta_y}^i\right]^T E\, I_{yy}^i\left[B_{\theta_y}^i\right]\end{pmatrix}\mathrm{d}x^i\right)\left[\overline{\Re}^i\right]\{e^i\} \tag{2.128}$$

in compact form, the previous expression can be written as

$$\mathcal{U}_b^i = \frac{1}{2}\{e^i\}^T\left(\left[\overline{\Re}^i\right]^T\left[\overline{k}_b^i\right]\left[\overline{\Re}^i\right]\right)\{e^i\} \tag{2.129}$$

where

$$\left[\overline{k}_b^i\right] = \left[\overline{k}_{b,v}^i\right] + \left[\overline{k}_{b,vw}^i\right] + \left[\overline{k}_{b,w}^i\right] \tag{2.130}$$

in which $\left[\overline{k}^i_{b,v}\right]$, and $\left[\overline{k}^i_{b,w}\right]$ represent the elemental bending stiffness matrices due to bending deformations in the (xy)- and (xz)-plane, respectively, while $\left[\overline{k}^i_{b,vw}\right]$ represents the stiffness matrix due to coupling in bending. Notice that the matrices $\left[\overline{k}^i_{b,v}\right]$, $\left[\overline{k}^i_{b,vw}\right]$ and $\left[\overline{k}^i_{b,w}\right]$ are functions of the setting angle ψ as a result of the orientation of the cross-sectional area of the beam. The expressions of $\left[\overline{k}^i_{b,v}\right]$, $\left[\overline{k}^i_{b,vw}\right]$ and $\left[\overline{k}^i_{b,w}\right]$ are respectively, given by

$$\left[\overline{k}^i_{b,v}\right] = \int_0^{l^i} \left[B^i_{\theta_z}\right]^T E\, I^i_{zz} \left[B^i_{\theta_z}\right] \mathrm{d}x^i \tag{2.131}$$

$$\left[\overline{k}^i_{b,vw}\right] = \int_0^{l^i} \left[B^i_{\theta_{yz}}\right]^T E\, I^i_{yz} \left[B^i_{\theta_{yz}}\right] \mathrm{d}x^i \tag{2.132}$$

$$\left[\overline{k}^i_{b,w}\right] = \int_0^{l^i} \left[B^i_{\theta_y}\right]^T E\, I^i_{yy} \left[B^i_{\theta_y}\right] \mathrm{d}x^i \tag{2.133}$$

In more compact form, equation (2.129) can be written as

$$\mathcal{U}^i_b = \frac{1}{2} \left\{e^i\right\}^T \left[k^i_b\right] \left\{e^i\right\} \tag{2.134}$$

where

$$\left[k^i_b\right] = \left[\overline{\Re}^i\right]^T \left[\overline{k}^i_b\right] \left[\overline{\Re}^i\right] \tag{2.135}$$

is defined with respect to the body co-ordinate axes.

2.8.4 Strain Energy due to Shear Deformation

The shear strains in the (xy)- and (xz)-planes are, respectively, given by

$$\gamma^i_{xy} = \frac{\partial v^i}{\partial x^i} - \theta^i_z \tag{2.136}$$

$$\gamma^i_{xz} = \frac{\partial w^i}{\partial x^i} + \theta^i_y \tag{2.137}$$

and the corresponding strain energy is given by

$$\mathcal{U}^i_s = \frac{1}{2} \int_{V^i} \left(\tau^i_{xy}\gamma^i_{xy} + \tau^i_{xz}\gamma^i_{xz}\right) dV^i \tag{2.138}$$

where the shear stress τ^i_{pq} corresponds to a given shear force over the cross section area. Since

the shear stress is not uniformly distributed over the cross-section, dimensionless shear correction factors κ_y and κ_z are introduced to account for this nonuniform distribution of the shear such that

$$\tau^i_{xy} = \kappa_y \, G\gamma^i_{xy} \,, \tag{2.139}$$

$$\tau^i_{xz} = \kappa_z \, G\gamma^i_{xz} \tag{2.140}$$

The shear correction factors κ_y and κ_z depend on the shape of the cross section. For compact cross-sections, however $\kappa_y \approx \kappa_z \approx \kappa$. Several values of the shear correction factor κ are derived for various cross-sectional shapes in the literature. Cowper [78] proposed the formulae

$$\kappa = \frac{6(1+\nu)}{7+6\nu}, \text{ for solid circular cross-section} \tag{2.141}$$

$$\kappa = \frac{10(1+\nu)}{(12+11\nu)}, \text{ for solid rectangular cross-section} \tag{2.142}$$

while Stephen and Levinson [79] suggested the formulae

$$\kappa = \frac{6(1+\nu)^2}{(7+12\nu+4\nu^2)}, \text{ for solid circular cross-section} \tag{2.143}$$

$$\kappa = \frac{5(1+\nu)}{(6+5\nu)}, \text{ for solid rectangular cross-section} \tag{2.144}$$

The strain energy $\mathcal{U}^i_s$ can be rewritten in the form

$$\mathcal{U}^i_s = \frac{1}{2}\int_{V^i} G\left(\kappa_y \gamma^{i^2}_{xy} + \kappa_z \gamma^{i^2}_{xz}\right) \mathrm{d}V^i \tag{2.145}$$

which can be written as

$$\mathcal{U}^i_s = \frac{1}{2}\int_0^{l^i} \left(\left(\frac{\partial v^i}{\partial x^i} - \theta^i_z\right)^T \kappa_y G A^i \left(\frac{\partial v^i}{\partial x^i} - \theta^i_z\right) + \left(\frac{\partial w^i}{\partial x^i} + \theta^i_y\right)^T \kappa_z G A^i \left(\frac{\partial w^i}{\partial x^i} + \theta^i_y\right) \right) \mathrm{d}x^i \tag{2.146}$$

Let

$$\frac{\partial v^i}{\partial x^i} - \theta^i_z = \left(\frac{\partial}{\partial x^i}\left[\mathcal{N}^i_v\right] - \left[\mathcal{N}^i_{\theta_z}\right]\right)\{e^i\} = \left[\Re^i\right]\left(\left[B^i_v\right] - \left[\mathcal{S}^i_{\theta_z}\right]\right)\left[\overline{\Re}^i\right]\{e^i\} \tag{2.147}$$

$$\frac{\partial w^i}{\partial x^i} + \theta^i_y = \left(\frac{\partial}{\partial x^i}\left[\mathcal{N}^i_w\right] + \left[\mathcal{N}^i_{\theta_y}\right]\right)\{e^i\} = \left[\Re^i\right]\left(\left[B^i_w\right] + \left[\mathcal{S}^i_{\theta_y}\right]\right)\left[\overline{\Re}^i\right]\{e^i\} \tag{2.148}$$

where $\left[B_v^i\right]$, and $\left[B_w^i\right]$ are differential operators associated with translational deformations in the y- and z-directions, respectively, given by

$$\left[B_v^i\right] = \frac{\partial}{\partial x^i}\left[\mathcal{S}_v^i\right] \tag{2.149}$$

$$\left[B_w^i\right] = \frac{\partial}{\partial x^i}\left[\mathcal{S}_w^i\right] \tag{2.150}$$

and $\left[\mathcal{S}_v^i\right]$ and $\left[\mathcal{S}_w^i\right]$ are the elemental shape functions due translational deformations in the y- and z-directions, respectively. Substitution of equations (2.147) and (2.148) into (2.145) yields

$$\mathcal{U}_s^i = \frac{1}{2}\left\{e^i\right\}^T\left[\overline{\Re}^i\right]^T\left(\int_0^{l^i}\left(\begin{array}{c}\left(\left[B_v^i\right]-\left[\mathcal{S}_{\theta_z}^i\right]\right)^T\kappa_y GA^i\left(\left[B_v^i\right]-\left[\mathcal{S}_{\theta_z}^i\right]\right)\\ +\left(\left[B_w^i\right]+\left[\mathcal{S}_{\theta_y}^i\right]\right)^T\kappa_z GA^i\left(\left[B_w^i\right]+\left[\mathcal{S}_{\theta_y}^i\right]\right)\end{array}\right)\mathrm{d}x^i\right)\left[\overline{\Re}^i\right]\left\{e^i\right\} \tag{2.151}$$

or in compact form this can be written as

$$\mathcal{U}_s^i = \frac{1}{2}\left\{e^i\right\}^T\left(\left[\overline{\Re}^i\right]^T\left[\overline{k}_s^i\right]\left[\overline{\Re}^i\right]\right)\left\{e^i\right\} \tag{2.152}$$

in which

$$\left[\overline{k}_s^i\right] = \left[\overline{k}_{s,v}^i\right] + \left[\overline{k}_{s,w}^i\right] \tag{2.153}$$

where

$$\left[\overline{k}_{s,v}^i\right] = \int_0^{l^i}\left(\left[B_v^i\right]-\left[\mathcal{S}_{\theta_z}^i\right]\right)^T\kappa_y GA^i\left(\left[B_v^i\right]-\left[\mathcal{S}_{\theta_z}^i\right]\right)\mathrm{d}x^i \tag{2.154}$$

$$\left[\overline{k}_{s,w}^i\right] = \int_0^{l^i}\left(\left[B_w^i\right]+\left[\mathcal{S}_{\theta_y}^i\right]\right)^T\kappa_z GA^i\left(\left[B_w^i\right]+\left[\mathcal{S}_{\theta_y}^i\right]\right)\mathrm{d}x^i \tag{2.155}$$

In more compact form, equation (2.152) can be written as

$$\mathcal{U}_s^i = \frac{1}{2}\left\{e^i\right\}^T\left[k_s^i\right]\left\{e^i\right\} \tag{2.156}$$

where

$$\left[k_s^i\right] = \left[\overline{\Re}^i\right]^T\left[\overline{k}_s^i\right]\left[\overline{\Re}^i\right] \tag{2.157}$$

The elemental elastic stiffness matrix is the composite matrix that comprises the contribution of each of the elastic previous stiffness matrices; that is

$$\left[\overline{k}^i_{ee}\right] = \left[\overline{k}^i_a\right] + \left[\overline{k}^i_{b,v}\right] + \left[\overline{k}^i_{b,vw}\right] + \left[\overline{k}^i_{b,w}\right] + [\overline{k}^i_{\theta_x}] + [\overline{k}^i_{s,v}] + [\overline{k}^i_{s,w}] \tag{2.158}$$

where

$$\begin{aligned}
\left[\overline{k}^i_a\right] &\equiv \text{elemental axial stiffness matrix} \\
\left[\overline{k}^i_{b,v}\right] &\equiv \text{elemental bending stiffness matrix in the } (xy)\text{-plane} \\
\left[\overline{k}^i_{b,w}\right] &\equiv \text{elemental bending stiffness matrix in the } (xz)\text{-plane} \\
\left[\overline{k}^i_{b,vw}\right] &\equiv \text{elemental stiffness matrix due to coupling in bending} \\
[\overline{k}^i_{\theta_x}] &\equiv \text{elemental torsional stiffness matrix} \\
[\overline{k}^i_{s,v}] &\equiv \text{elemental shear stiffness matrix in the } (xy)\text{-plane} \\
[\overline{k}^i_{s,w}] &\equiv \text{elemental shear stiffness matrix in the } (xz)\text{-plane}
\end{aligned}$$

with respect to body co-ordinate axes, equation (2.158) can be written as

$$\left[k^i_{ee}\right] = \left[\overline{\Re}^i\right]^T \left[\overline{k}^i_{ee}\right] \left[\overline{\Re}^i\right] \tag{2.159}$$

2.9 Strain Energy Increase due to Rotation

The rotation of the hub induces an axial force F^i_P in the beam due to the centrifugal effect. If the beam bends in the (xz)-plane as shown in Figure 2-9, the change in the horizontal projection of the i^{th} element of length $\mathrm{d}s^i$ is given by

$$\mathrm{d}s^i - \mathrm{d}x^i = \sqrt{(\mathrm{d}x^i)^2 + \left(\frac{\partial w^i}{\partial x^i}\right)^2 \mathrm{d}x^i} - \mathrm{d}x^i \approx \frac{1}{2}\left(\frac{\partial w^i}{\partial x^i}\right)^2 \mathrm{d}x^i \tag{2.160}$$

assuming small displacements so that higher order terms of the change in the axial direction of the i^{th} element can be neglected.The strain energy increase due to the centrifugal force F^i_P acting on a point P^i of the infinitesimal volume V^i at a distance x^i from the left end of the i^{th} element is thus given by

$$\mathcal{U}^i_{c,w} = \frac{1}{2}\int_0^{l^i} \left(\frac{\partial w^i}{\partial x^i}\right)^T F^i_P \left(\frac{\partial w^i}{\partial x^i}\right) \mathrm{d}x^i \tag{2.161}$$

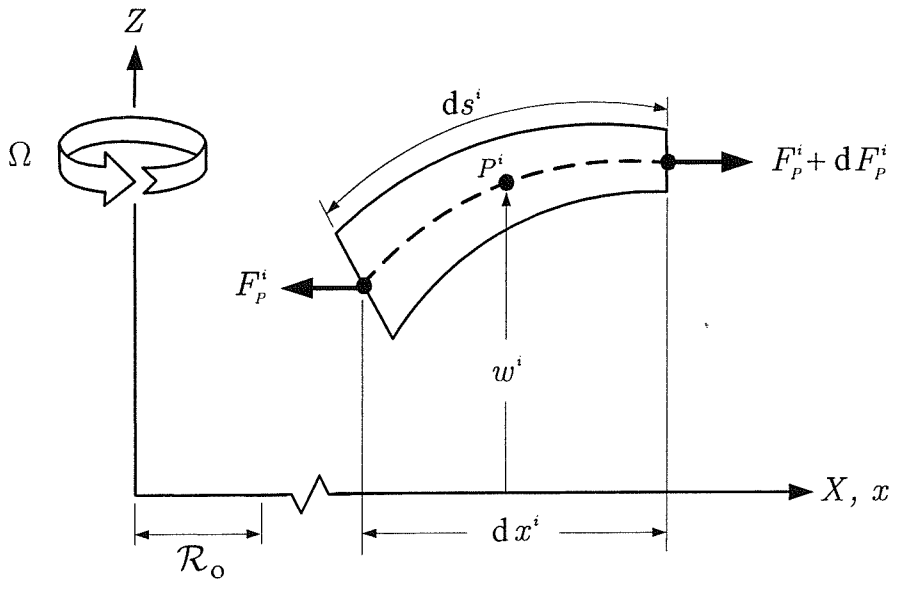

Figure 2-9: Deflection due to rotation in the (xz)-plane.

Similarly, for the (xy)-plane, one can write

$$\mathcal{U}^i_{c,v} = \frac{1}{2}\int_0^{l^i} \left(\frac{\partial v^i}{\partial x^i}\right)^T F^i_P \left(\frac{\partial v^i}{\partial x^i}\right) \mathrm{d}x^i \tag{2.162}$$

and the total strain energy of the i^{th} element due to rotation is thus given by

$$\mathcal{U}^i_c = \frac{1}{2}\int_0^{l^i} \left(\left(\frac{\partial v^i}{\partial x^i}\right)^T F^i_P \left(\frac{\partial v^i}{\partial x^i}\right) + \left(\frac{\partial w^i}{\partial x^i}\right)^T F^i_P \left(\frac{\partial w^i}{\partial x^i}\right)\right) \mathrm{d}x^i \tag{2.163}$$

where $\dfrac{\partial v^i}{\partial x^i}$ and $\dfrac{\partial w^i}{\partial x^i}$ can be expressed in terms of the elastic generalized co-ordinates $\{e^i\}$ as

$$\frac{\partial v^i}{\partial x^i} = \frac{\partial}{\partial x^i}\left(\left[\mathcal{N}^i_v\right]\{e^i\}\right) = \left[\Re^i\right]\left[B^i_v\right]\left[\overline{\Re}^i\right]\{e^i\} \tag{2.164}$$

$$\frac{\partial w^i}{\partial x^i} = \frac{\partial}{\partial x^i}\left(\left[\mathcal{N}^i_w\right]\{e^i\}\right) = \left[\Re^i\right]\left[B^i_w\right]\left[\overline{\Re}^i\right]\{e^i\} \tag{2.165}$$

Substitution of equations (2.164) and (2.165) into (2.163) gives

$$\mathcal{U}^i_c = \frac{1}{2}\{e^i\}^T\left[\overline{\Re}^i\right]^T\left(\int_0^{l^i}\left(\left[B^i_v\right]^T F^i_P\left[B^i_v\right] + \left[B^i_w\right]^T F^i_P\left[B^i_w\right]\right)\mathrm{d}x^i\right)\left[\overline{\Re}^i\right]\{e^i\} \tag{2.166}$$

in compact form, this can be written as

$$\mathcal{U}_c^i = \frac{1}{2}\{e^i\}^T \left(\left[\overline{\Re}^i\right]^T \left[\overline{k}_c^i\right] \left[\overline{\Re}^i\right] \right) \{e^i\} \tag{2.167}$$

where

$$\left[\overline{k}_c^i\right] = \left[\overline{k}_{c,v}^i\right] + \left[\overline{k}_{c,w}^i\right] \tag{2.168}$$

in which

$$\begin{aligned} \left[\overline{k}_{c,v}^i\right] &\equiv \text{elemental centrifugal stiffness matrix in the } (xy)\text{-plane} \\ \left[\overline{k}_{c,w}^i\right] &\equiv \text{elemental centrifugal stiffness matrix in the } (xz)\text{-plane} \end{aligned}$$

The respective expressions of $\left[\overline{k}_{c,v}^i\right]$ and $\left[\overline{k}_{c,w}^i\right]$ are given by

$$\left[\overline{k}_{c,v}^i\right] = \int_0^{l^i} \left[B_v^i\right]^T F_P^i \left[B_v^i\right] \mathrm{d}x^i \tag{2.169}$$

$$\left[\overline{k}_{c,w}^i\right] = \int_0^{l^i} \left[B_w^i\right]^T F_P^i \left[B_w^i\right] \mathrm{d}x^i \tag{2.170}$$

Notice that F_P^i is a function of the pre-cone angle ϕ. The explicit expression of F_P^i will be given in the next chapter. In more compact form, equation (2.167) can be written as

$$\mathcal{U}_c^i = \frac{1}{2}\{e^i\}^T \left[k_c^i\right] \{e^i\} \tag{2.171}$$

where

$$\left[k_c^i\right] = \left[\overline{\Re}^i\right]^T \left[\overline{k}_c^i\right] \left[\overline{\Re}^i\right] \tag{2.172}$$

The matrices $\left[\overline{k}_c^i\right]$ and $\left[k_c^i\right]$ can be written in the form (see reference [29] for proof)

$$\left[k_c^i\right] = \Omega^2 \left[\mathbb{k}_c^i\right] \tag{2.173}$$

in order to isolate Ω^2. The matrices $\left[\overline{\mathbb{k}}_c^i\right]$ and $\left[\mathbb{k}_c^i\right]$ are related by

$$\left[\mathbb{k}_c^i\right] = \left[\overline{\Re}^i\right]^T \left[\overline{\mathbb{k}}_c^i\right] \left[\overline{\Re}^i\right] \tag{2.174}$$

The elemental stiffness matrix $\left[k^i\right]$ is the composite stiffness matrix that comprises the elemental elastic stiffness matrix $\left[k_{ee}^i\right]$ and the elemental stiffness matrix due to centrifugal force field $\left[k_c^i\right]$, that is

$$\left[k^i\right] = \left[k_{ee}^i\right] + \left[k_c^i\right] \tag{2.175}$$

or

$$\left[k^i\right] = \left[k_{ee}^i\right] + \Omega^2 \left[\mathbb{k}_c^i\right] \tag{2.176}$$

The elemental strain energy $\mathcal{U}^i$ can be given by

$$\mathcal{U}^i = \mathcal{U}_e^i + \mathcal{U}_c^i \tag{2.177}$$

where $\mathcal{U}_e^i$ is the elastic strain energy due to all elastic deformations and $\mathcal{U}_c^i$ is the strain energy increase due to rotation. The strain energy $\mathcal{U}^i$ can be expressed as

$$\mathcal{U}^i = \frac{1}{2} \begin{Bmatrix} \varphi \\ e^i \end{Bmatrix}^T \begin{bmatrix} 0 & 0 \\ 0 & \left[k^i\right] \end{bmatrix} \begin{Bmatrix} \varphi \\ e^i \end{Bmatrix} \tag{2.178}$$

where

$$\left[k^i\right] = \left[\overline{\Re}^i\right]^T \left[\overline{k}^i\right] \left[\overline{\Re}^i\right] \tag{2.179}$$

The strain energy $\mathcal{U}$ of the beam can be obtained by summing the strain energy of each of its elements. Denoting the number of elements by n, the total strain energy can be given by

$$\mathcal{U} = \sum_{j=1}^{n} \mathcal{U}^i = \frac{1}{2} \{q\}^T [K] \{q\} \tag{2.180}$$

where

$$[K] = [K_{ee}] + \Omega^2 [\mathbb{K}] \tag{2.181}$$

where $[K_{ee}]$ and $[\mathbb{K}]$ are the assembled elastic stiffness matrices and the assembled modified centrifugal stiffness matrix.

2.10 Equations of Motion

The Lagrangian approach is used in deriving the equations of motion at the element level, which can be written mathematically as

$$\frac{\mathrm{d}}{\mathrm{d}t}\left(\frac{\partial \mathcal{L}^i}{\partial \{\dot{q}^i\}}\right) - \frac{\partial \mathcal{L}^i}{\partial \{q^i\}} = \{Q^i\} \tag{2.182}$$

where $\mathcal{L}^i$ is the Lagrangian function, $\{q^i\}$ is the generalized co-ordinate vector defined previously and $\{Q^i\}$ is the associated vector of generalized forces. The Lagrangian function at the element level can be written as

$$\mathcal{L}^i = \mathcal{T}^i - \mathcal{U}^i - \mathcal{V}^i \tag{2.183}$$

where $\mathcal{V}^i$ is the elemental potential energy[1] that has been ignored so far. Substituting the kinetic and strain energy expressions of equations (2.67), and (2.178) into Lagrangian function, and performing the required differentiations and algebraic manipulations, one can write

$$\mathcal{L}^i = \frac{1}{2}\dot{\varphi}^T \left[m^i_{rr}\right] \dot{\varphi} + \dot{\varphi}^T \left[m^i_{re}\right] \{\dot{e}^i\} + \frac{1}{2}\{\dot{e}^i\}^T \left[m^i_{ee}\right] \{\dot{e}^i\} - \frac{1}{2}\{e^i\}^T \left[k^i\right] \{e^i\} \tag{2.184}$$

2.10.1 Equations of Motion Associated with Reference Motion

The equation of motion associated with the generalized co-ordinate φ (reference motion) may be written as

$$\frac{\mathrm{d}}{\mathrm{d}t}\left(\frac{\partial \mathcal{L}^i}{\partial \dot{\varphi}}\right) - \frac{\partial \mathcal{L}^i}{\partial \varphi} = \{Q^i_\varphi\} \tag{2.185}$$

Performing the necessary algebraic manipulations and differentiations with respect to time and generalized co-ordinates φ and arranging terms, one arrives at

$$\begin{aligned} \frac{\mathrm{d}}{\mathrm{d}t}\left(\frac{\partial \mathcal{L}^i}{\partial \dot{\varphi}}\right) &= \left[m^i_{rr}\right] \ddot{\varphi} + 2\left(\left[m^i_{\mathcal{R}_o e}\right] \{\dot{e}^i\} + \{\dot{e}^i\}^T \left[m^i_t\right] \{e^i\} + \{\dot{e}^i\}^T \left[m^i_{r_{P_o e}}\right]\right) \dot{\varphi} \\ &+ \left(\left[m^i_{\mathcal{R}_o}\right] + \{e^i\}^T \left[\widetilde{C^i}\right] + \left[m^i_{r_{P_o}}\right]\right) \{\ddot{e}^i\} + \{\dot{e}^i\}^T \left[\widetilde{C^i}\right] \{\dot{e}^i\} \end{aligned} \tag{2.186}$$

[1] Potential energy is the stored energy possessed by a system as a result of the relative positions of the components of that system.

and

$$\frac{\partial \mathcal{L}^i}{\partial \varphi} = \dot{\varphi}^T \left(\left[\mathbf{I}^{i*}_{\mathcal{R}_o e} \right] \{e^i\} + \left[\mathbf{I}^{i*}_{\mathcal{R}_o r_{P_o}} \right] \right) \dot{\varphi} + \left[m^i_{\mathcal{R}_o e} \right] \{\dot{e}^i\} \dot{\varphi} \tag{2.187}$$

where $*$ within a matrix denotes differentiation with respect to φ. The expressions of $\left[m^{i*}_{\mathcal{R}_o e} \right]$ and $\left[\mathbf{I}^{i*}_{\mathcal{R}_o r_{P_o}} \right]$ are given by

$$\left[m^{i*}_{\mathcal{R}_o e} \right] = \int_{V^i} \rho \{\mathcal{R}_o\}^T [\mathcal{A}_\varphi] [\Re^i] [\mathcal{S}^i] \left[\overline{\Re}^i \right] dV^i \tag{2.188}$$

$$\left[\mathbf{I}^{i*}_{\mathcal{R}_o r_{P_o}} \right] = \int_{V^i} \rho \{\mathcal{R}_o\}^T [\mathcal{A}_\varphi] [\mathcal{A}_o] \left\{ r^i_{P_o} \right\} dV^i \tag{2.189}$$

Substitution of equations (2.186) and (2.187) into (2.185) gives the equation of motion of the hub-beam associated with the generalized co-ordinate φ. Thus one can write

$$\left[m^i_{rr} \right] \ddot{\varphi} + \left[m^i_{re} \right] \{\ddot{e}^i\} = \{Q^i_{ext}\}_\varphi + \{f^i_\varphi\} \tag{2.190}$$

where $\{Q^i_{ext}\}$ and $\{f^i_\varphi\}$ are, respectively, the vector of the external applied forces and the vector associated with quadratic velocity terms that accounts for Coriolis and centripetal effects. The later is obtained by differentiating the Lagrangian function with respect to the generalized co-ordinate φ and time. The vector $\{f^i_\varphi\}$ is given by

$$\begin{aligned} \{f^i_\varphi\} &= -\left(\left[m^i_{\mathcal{R}_o e} \right] \{\dot{e}^i\} + 2 \{\dot{e}^i\}^T \left[m^i_t \right] \{e^i\} + 2 \{\dot{e}^i\}^T \left[m^i_{r_{P_o e}} \right] \right) \Omega \\ &+ \left(\left[m^{i*}_{\mathcal{R}_o e} \right] \{e^i\} + \left[\mathbf{I}^{i*}_{\mathcal{R}_o r_{P_o}} \right] \right) \Omega^2 - \{\dot{e}^i\}^T \left[\widetilde{C^i} \right] \{\dot{e}^i\} \end{aligned} \tag{2.191}$$

2.10.2 Equations of Motion Associated with Elastic Co-ordinates

Similarly, the equations of motion of the i^{th} spinning tapered Timoshenko beam associated with the generalized co-ordinates $\{e^i\}$ may be written as

$$\frac{\mathrm{d}}{\mathrm{d}t} \left(\frac{\partial \mathcal{L}^i}{\partial \{\dot{e}^i\}} \right) - \frac{\partial \mathcal{L}^i}{\partial \{e^i\}} = \{Q^i_e\} \tag{2.192}$$

Performing the necessary algebraic manipulations and differentiation with respect to time and generalized co-ordinates $\{e^i\}$ and arranging terms, one arrives at

$$\frac{\mathrm{d}}{\mathrm{d}t} \left(\frac{\partial \mathcal{L}^i}{\partial \{\dot{e}^i\}} \right) = \left[m^i_{re} \right]^T \ddot{\varphi} + \Omega \left[\widetilde{C^i} \right]^T \{\dot{e}^i\} + \left[m^i_{ee} \right] \{\ddot{e}^i\} \tag{2.193}$$

and

$$\frac{\partial \mathcal{L}^i}{\partial \{e^i\}} = \left(\left[m^i_{\mathcal{R}_o e}\right]^T + \left[m^i_t\right]^T \{e^i\} + \left[m^i_{r_{P_o e}}\right] \right) \Omega^2 + \Omega \left[\widetilde{C^i}\right] \{\dot{e}^i\} - \left[k^i\right] \{e^i\} \tag{2.194}$$

Substitution of equations (2.193) and (2.194) into (2.192) gives

$$\left[m^i_{re}\right]^T \ddot{\varphi} + \left[m^i_{ee}\right] \{\ddot{e}^i\} + \left[k^i\right] \{e^i\} = \{Q^i_{ext}\}_e + \{f^i_e\} \tag{2.195}$$

where $\{Q^i_{ext}\}_e$ and $\{f^i_e\}$ are, respectively, the vector of the external applied forces and the elastic force vector of quadratic velocity terms that accounts for Coriolis and centripetal effects associated with elastic co-ordinates. The later is obtained by differentiating the Lagrangian function with respect to the elastic co-ordinate $\{e^i\}$ and time. The expression of $\{f^i_e\}$ is given by

$$\{f^i_e\} = \left(\left[m^i_{\mathcal{R}_o e}\right]^T + \left[m^i_t\right] \{e^i\} + \left[m^i_{r_{P_o e}}\right] \right) \Omega^2 - 2\Omega \left[\widetilde{C^i}\right] \{\dot{e}^i\} \tag{2.196}$$

Equations (2.190) and (2.195) can be combined into a single equation using vector matrix notation as

$$\begin{bmatrix} \left[m^i_{rr}\right] & \left[m^i_{re}\right] \\ \left[m^i_{re}\right]^T & \left[m^i_{ee}\right] \end{bmatrix} \begin{Bmatrix} \ddot{\varphi} \\ \{\ddot{e}^i\} \end{Bmatrix} + \begin{bmatrix} 0 & 0 \\ 0 & \left[k^i\right] \end{bmatrix} \begin{Bmatrix} \varphi \\ \{e^i\} \end{Bmatrix} = \begin{Bmatrix} \{Q^i_{ext}\}_\varphi + f^i_\varphi \\ \{Q^i_{ext}\}_e + f^i_e \end{Bmatrix} \tag{2.197}$$

Equations (2.197) represent the governing system (rigid hub-elastic beam element) differential equations based on the multibody elastodynamic formulation. The system unknowns are the generalized co-ordinates φ and $\{e^i\}$. The former refers to the reference generalized co-ordinate of the rigid hub while the latter refers to the elastic generalized co-ordinates of the beam element. The quantities $\ddot{\varphi}$ and $\{\ddot{e}^i\}$ refer to the acceleration of the reference and elastic motions of the beam, respectively.

The submatrices $\left[m^i_{rr}\right]$ and $\left[m^i_{ee}\right]$ represent respectively the inertia of the reference motion and the mass matrix of the elastic generalized co-ordinates while the submatrix $\left[m^i_{re}\right]$ represents the coupling inertia between the reference motion and elastic deformations.

The submatrix $\left[k^i\right]$ given by equation (2.175) is the modified stiffness matrix of the beam element due to elastic deformations and incorporates the effects of rotation. In addition, it includes a stiffness coupling term in bending known as the bending-bending term which is caused by the orientation of the cross-section of the beam by a setting angle ψ.

2.10.3 Equations of Motion for Constant Hub Speed

For constant angular velocity of the hub, the angular acceleration $\ddot{\varphi}$ vanishes, and the previous equations of motion will be expressed in terms of the elastic co-ordinates $\{e^i\}$ as

$$\left[m_{ee}^i\right]\{\ddot{e}^i\} + 2\Omega\left[\widetilde{C^i}\right]\{\dot{e}^i\} + \left(\left[k^i\right] - \Omega^2\left[m_l^i\right]\right)\{e^i\} = \{Q_{ext}^i\}_e + \{f_e^{i*}\} \tag{2.198}$$

or

$$\left[m_{ee}^i\right]\{\ddot{e}^i\} + 2\Omega\left[\widetilde{C^i}\right]\{\dot{e}^i\} + \left(\left[k_{ee}^i\right] + \Omega^2\left(\left[\mathbb{k}_c^i\right] - \left[m_t^i\right]\right)\right)\{e^i\} = \{Q_{ext}^i\}_e + \{f_e^{i*}\} \tag{2.199}$$

where

$$\{f_e^{i*}\} = \left(\left[m_{\mathcal{R}_o e}^i\right]^T + \left[m_{r_{P_o e}}^i\right]\right)\Omega^2 \tag{2.200}$$

is referred to as centrifugal inertia force that result from differentiating the Lagrangian with respect to the generalized co-ordinate $\{e^i\}$ and time. The expressions of $\left[m_{\mathcal{R}_o e}^i\right]$ and $\left[m_{r_{P_o e}}^i\right]$ are respectively given by equations (2.55) and (2.57). Notice that $\left[m_{r_{P_o e}}^i\right]$ is invariant while $\left[m_{\mathcal{R}_o e}^i\right]$ is implicit function of time since it is function of φ. Its entries will be iteratively updated as the integration algorithm proceeds forward in time during the solution of the system equations of motion.

The sum of the individual element energies over the entire beam may be utilized, by using equations (2.68) and (2.180) to establish the Lagrangian function for the beam. Substitution of the expression of the obtained Lagrangian function into Lagrange's equation yields the governing differential equation of the entire beam

$$[M_{ee}]\{\ddot{e}\} + 2\Omega\left[\widetilde{C}\right]\{\dot{e}\} + \left([K_{ee}] + \Omega^2\left([\mathbb{K}] - [M_t]\right)\right)\{e\} = \{Q_{ext}\}_e + \{f_e^*\} \tag{2.201}$$

where

$$\{Q_{ext}\}_e = \sum_{i=1}^{n}\{Q_{ext}^i\}_e, \tag{2.202}$$

$$\{f_e^*\} = \sum_{i=1}^{n}\{f_e^{i*}\} \tag{2.203}$$

The vector $\{Q_{ext}\}_e$ represents the external generalized forces applied to the beam and $\{f_e^*\}$ is a force vector of quadratic velocity terms. The nonlinear term $2\Omega\left[\widetilde{C}\right]\{\dot{e}\}$ accounts for Coriolis

effects, while the term $-\Omega^2 [M_t] \{e\}$ represents the centripetal acceleration contribution. Equation (2.201) represents the forced vibration of the lead-lag motion. The out-of-plane vibrational motion can be obtained from equation (2.201) by dropping the term $\Omega^2 [M_t] \{e\}$ resulting in

$$[M_{ee}] \{\ddot{e}\} + 2\Omega \left[\widetilde{C}\right] \{\dot{e}\} + \left([K_{ee}] + \Omega^2 [\mathbb{K}]\right) \{e\} = \{Q_{ext}\}_e + \{f_e^*\} \tag{2.204}$$

For any general orientation of the cross-section of the beam, the beam lies in a plane that makes a setting angle ψ and a pre-cone angle ϕ with the plane of rotation. The equations of motion for this case need to be modified to include the effect of these angular settings (setting angle and pre-cone). This can be done by introducing the potential energy of the beam to account for the pre-cone and setting angle as well as the speed of rotation.

2.11 Potential Energy

The potential energy of the transverse deformation of the i^{th} element depends on its lateral deflection w^i only and is given by the integral

$$\mathcal{V}^i = -\frac{1}{2} \int_0^{l^i} F_z^i \, w^i \mathrm{d}x^i \tag{2.205}$$

where w^i is the nodal displacement in the z-direction. The force F_z^i is the z-component of the force F_P^i. The expression of F_z^i needs to be evaluated with respect to the global reference Z-axis. Referring to Figure 2-10, the radial component of the centrifugal force per unit volume of the i^{th} element of the beam acting at a distance x^i is given by

$$F_r^i = \rho \, A^i \Omega^2 \left(\mathcal{R}_\circ + r_P^i \cos\phi\right) \tag{2.206}$$

A component of w^i along the z-axis would result in two components; $w^i \cos(\psi + \phi)$ along the global Z-axis, and $-w^i \sin(\psi + \phi)$ along the global Y-axis.

The force F_r^i can be resolved in two components

$$F_X^i \approx F_r^i \approx \rho \, A^i \, \Omega^2 \left(\mathcal{R}_\circ + r_P^i \cos\phi\right), \tag{2.207}$$

$$F_Y^i = F_X^i \left[-w^i \sin(\psi + \phi) \; / \; \left(\mathcal{R}_\circ + r_P^i \cos\phi\right)\right] = -w^i \, \rho \, A^i \, \Omega^2 \sin\left(\psi + \phi\right) \tag{2.208}$$

Moreover, the force F_Y^i can be resolved into two components along the elemental y- and z-axes.

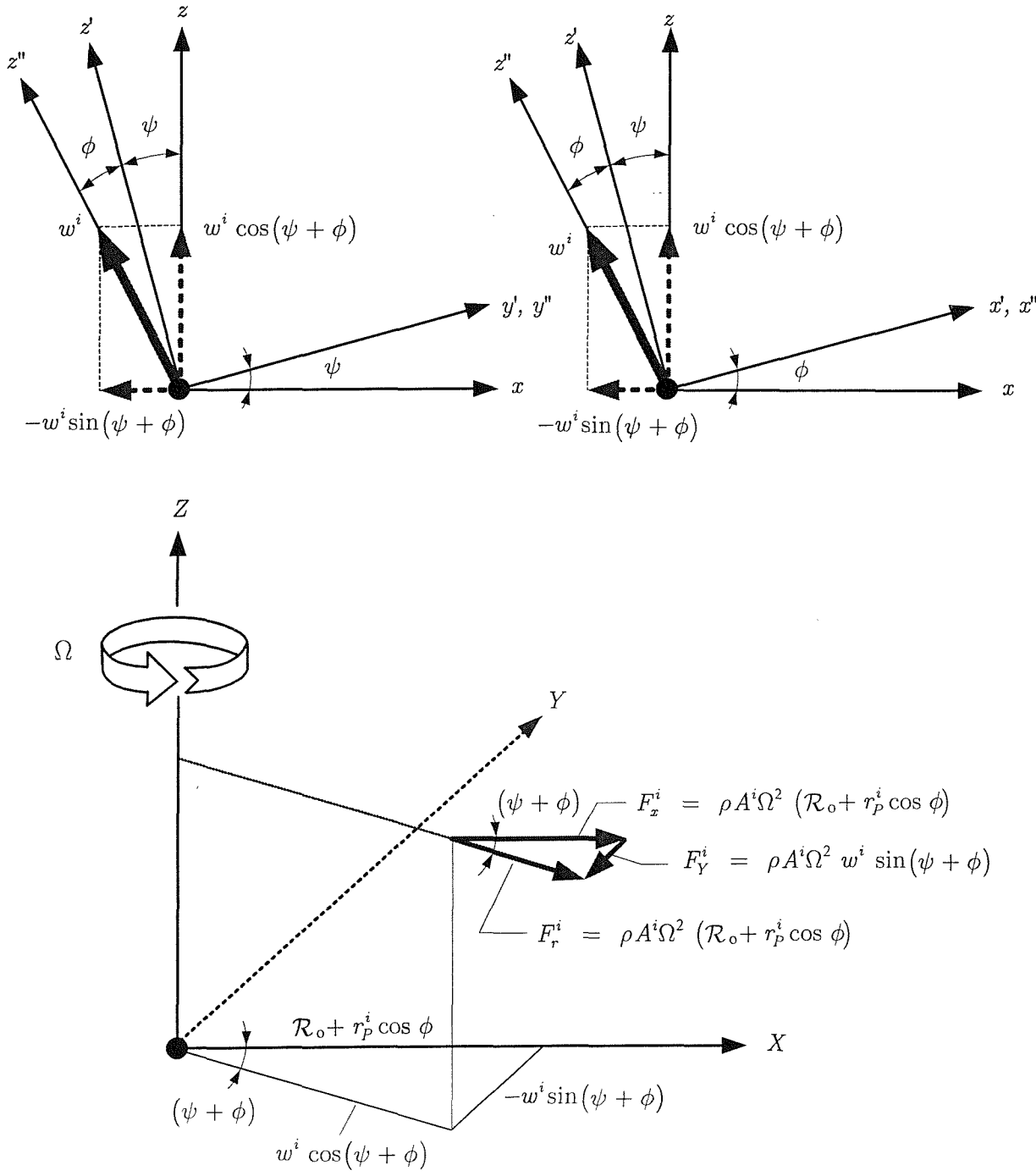

Figure 2-10: Displacements and force components.

The components of F_Y^i along these respective directions are then given by

$$F_y^i = F_Y^i \cos\psi = -w^i \rho A^i \Omega^2 \sin(\psi+\phi)\cos\psi, \tag{2.209}$$

$$F_z^i = -F_Y^i \sin\psi\cos\phi = w^i \rho A^i \Omega^2 \sin\psi\cos\phi\sin(\psi+\phi) \tag{2.210}$$

Substitution of equation (2.210) into (2.205) yields

$$\mathcal{V}^i = -\frac{1}{2}\{e^i\}^T \left(\int_0^{l^i} [\mathcal{N}^i]^T \rho A^i \Omega^2 \sin\psi\cos\phi\sin(\psi+\phi) [\mathcal{N}^i] \, dx^i \right) \{e^i\} \tag{2.211}$$

or

$$\mathcal{V}^i = -\frac{1}{2}\{e^i\}^T \left[\overline{\Re}^i\right]^T \left([\overline{m}_{t,w}^i] \Omega^2 \sin\psi\cos\phi\sin(\psi+\phi) \right) \left[\overline{\Re}^i\right] \{e^i\} \tag{2.212}$$

where $[\overline{m}_{t,w}^i]$ is the elemental translational mass matrix in the z-direction. The expression of $[\overline{m}_{t,w}^i]$ can be given by

$$[\overline{m}_{t,w}^i] = \int_0^{l^i} \rho A^i [\mathcal{S}_w^i]^T [\mathcal{S}_w^i] \, dx^i \tag{2.213}$$

$[\mathcal{S}_w^i]$ is the shape function matrix that is used to model the elastic deformations of the beam in the z-direction. In more compact form equation (2.212) can be written as

$$\mathcal{V}^i = -\frac{1}{2}\{e^i\}^T \left([m_{t,w}^i] \Omega^2 \sin\psi\cos\phi\sin(\psi+\phi) \right) \{e^i\} \tag{2.214}$$

where

$$[m_{t,w}^i] = \left[\overline{\Re}^i\right]^T [\overline{m}_{t,w}^i] \left[\overline{\Re}^i\right] \tag{2.215}$$

is defined with respect to the body co-ordinate axes.

2.12 Governing Equations of Motion

Utilizing the kinetic energy and strain and potential energy expressions of equations (2.68), (2.178) and (2.214) into Lagrange's equation, and performing the required differentiation and algebraic manipulations, the Lagrangian function at the element level can be written in compact

form using equation (2.183). For constant hub speed, the equation of motion of the entire elastic beam can be established using the standard finite element assembling procedure according to the node numbering on the beam, and can be written as

$$[M_{ee}]\{\ddot{e}\} + 2\Omega\left[\widetilde{C}\right]\{\dot{e}\} + \left([K_{ee}] + \Omega^2\left([\mathbb{K}] - [M_{t,w}]\sin\psi\cos\phi\sin\left(\psi+\phi\right)\right)\right)\{e\} = \{Q_{ext}\}_e + \{f_e^*\} \tag{2.216}$$

Equation (2.216) represents the matrix form of the governing differential equations of the spinning tapered three dimensional Timoshenko beam. In compact form, the above equation can be written as

$$[M_{ee}]\{\ddot{e}\} + 2\Omega\left[\widetilde{C}\right]\{\dot{e}\} + [K^*]\{e\} = \{Q\} \tag{2.217}$$

where

$$[K^*] = [K_{ee}] + \Omega^2\left([\mathbb{K}] - [M_{t,w}]\sin\psi\cos\phi\sin\left(\psi+\phi\right)\right) \tag{2.218}$$

and

$$\{Q\} = \{Q_{ext}\}_e + \{f_e^*\} \tag{2.219}$$

Chapter 3

The Finite Element Formulation

The mathematical modeling is the most critical step in any dynamic analysis, because the validity of the simulation results depends directly on how well the model can represent the behavior of the real physical system. The Finite Element Method (FEM) has been recognized to have great potential and flexibility in modeling complex and large structures, and obtaining accurate results. Therefore it is used to discretize the elastic tapered Timoshenko beam.

The development of the three-dimensional elastic beam model follows closely that of its planar equivalent developed in [27]. The present beam model is discretized as an assemblage of finite elements in which the translations and rotations of the interconnected nodes represent the degrees of freedom of the model. In this formulation, beam elements are linearly tapered in two planes while allowing for unequal breadth and depth taper ratios as well as unequal element lengths. Each element has a length l^i such that the length of the entire beam is the summation of its individual element lengths. The root cross-section of the beam is rigidly attached to the periphery of the hub and decreases along the span while the tip cross-section is located at the free end of the beam. The beam element is assumed to be a straight bar of symmetric cross-section capable of resisting axial forces, bending moments about its principal axes, and twisting moments about its centroidal axis. Effects of shear deformation, rotary inertia, hub radius, setting angle, pre-cone angle, tapering in the (xy)- and (xz)-planes and spinning of the hub are considered in this model.

Since the elemental mass, stiffness, Coriolis and inertia force matrices of the rotating tapered Timoshenko beam depend on the geometrical properties of the present model, it is first necessary to develop explicit expressions for the variable cross-section area of the beam as well as the second moments of area and the product moment of area of the cross-section of the beam in terms of an arbitrary elemental co-ordinates x^i, y^i, and z^i of the i^{th} beam element and other parameters

that define the beam geometry.

In addition, the shape functions for the three dimensional Timoshenko beam element undergoing axial, torsional and bending deformations are also derived and presented explicitly in matrix form. Using these shape functions, and the variable geometric properties of the beam element[1], exact expressions of the element mass, stiffness, Coriolis and inertia terms matrices are derived and expressed in symbolic form where all the parameter changes are accounted for. The explicit expressions of these matrices have the computational advantage of eliminating the loss of computer time and round-off errors associated with extensive matrix operations required for their numerical evaluation.

3.1 Geometric Properties of the Model

In order to define the geometric properties of the rotating tapered Timoshenko beam shown by the model of Figure 3-1, one needs to introduce the following notation

$$L = \sum_{i=1}^{n} l^i \tag{3.1}$$

$$L_{iy} = L_{oy} - L^i \tag{3.2}$$

$$L_{iz} = L_{oz} - L^i \tag{3.3}$$

$$\nu_y = L/L_{oy} \tag{3.4}$$

$$\nu_z = L/L_{oz} \tag{3.5}$$

where the superscript i stands for the i^{th} element, l^i is the element length, n is the total number of elements, L is the entire beam length and L^i is the outboard length of the beam from the element under consideration. The quantities L_{oy} and L_{oz} are the untruncated lengths of the beam in the (xy)- and (xz)-planes, respectively while ν_y and ν_z represent the depth and breadth taper ratios in the (xy)- and (xz)-planes, respectively. Notice that this type of beam is linearly tapered in both planes and is called a double-tapered beam. The case of uniform beam (constant cross-section) corresponds to $\nu_y = \nu_z = 0.0$ (i.e., when $L_{oy} \longrightarrow \infty$ and $L_{oz} \longrightarrow \infty$), while $\nu_y = \nu_z = 1.0$ define a wedge (or a cone for a circular cross-section).

At any position $P^i\left(x^i, y^i, z^i\right)$ of the i^{th} beam element, the following geometrical relations

[1]By geometric properties of the beam it is the variable cross-section area of the beam as well as the second moments of area and the product moment of area of the cross-section of the beam in terms of an arbitrary elemental coordinates x^i, y^i, and z^i of the i^{th} beam element and other parameters that define the beam geometry.

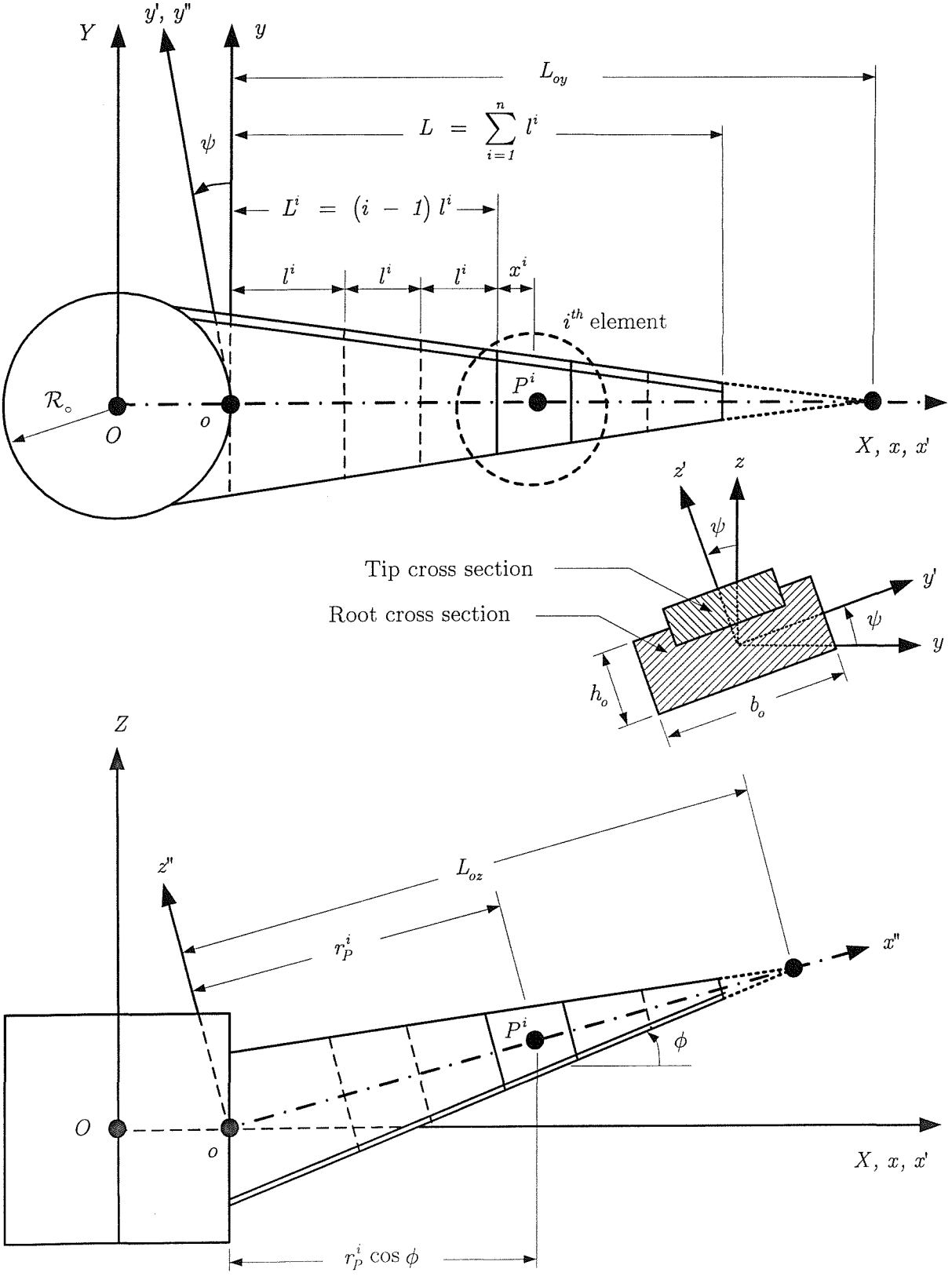

Figure 3-1: Timoshenko beam linearly tapered in two planes.

can be obtained

$$\frac{b^i}{b_o} = \frac{L_{oy} - \left(x^i + (i-1)l^i\right)}{L_{oy}} \tag{3.6}$$

$$\frac{h^i}{h_o} = \frac{L_{oz} - \left(x^i + (i-1)l^i\right)}{L_{oz}} \tag{3.7}$$

where b_o and h_o are the breadth and depth of the root cross-section of the beam while b^i and h^i represent the breadth and depth of the i^{th} beam element at an arbitrary location x^i. If one lets

$$L^i = (i-1)l^i \tag{3.8}$$

substitution of equation (3.8) into (3.6) and (3.7) yields

$$\frac{b^i}{b_o} = \frac{L_{oy} - x^i - L^i}{L_{oy}} \tag{3.9}$$

$$\frac{h^i}{h_o} = \frac{L_{oz} - x^i - L^i}{L_{oz}} \tag{3.10}$$

The cross-section area of the i^{th} beam element at an arbitrary location x^i can be given by

$$A^i = b^i h^i \tag{3.11}$$

Substitution of equations (3.9) and (3.10) into (3.11) yields the variable cross-section area

$$A^i = \frac{A_o}{L_{oy}L_{oz}}\left(\mu_1 - 2\mu_2 x^i + x^{i^2}\right) \tag{3.12}$$

where A_o is the root cross-section area of the beam and μ_1 and μ_2 are constants given by

$$\mu_1 = L_{iy}L_{iz} \tag{3.13}$$

$$\mu_2 = \frac{1}{2}(L_{iy} + L_{iz}) \tag{3.14}$$

Expressions for the second moments of area of the i^{th} beam element about its principal axes are

$$I^i_{yy} = \frac{1}{12}\, b^i\, h^{i^3} \tag{3.15}$$

$$I^i_{zz} = \frac{1}{12}\, h^i\, b^{i^3} \tag{3.16}$$

Substitution of equations (3.9) and (3.10) into (3.15) and (3.16) yields

$$I^i_{yy} = \Gamma_{yy}\left(\alpha_{z0} - \alpha_{z1}x^i + \alpha_{z2}x^{i^2} - \alpha_{z3}x^{i^3} + x^{i^4}\right) \tag{3.17}$$

$$I^i_{zz} = \Gamma_{zz}\left(\alpha_{y0} - \alpha_{y1}x^i + \alpha_{y2}x^{i^2} - \alpha_{y3}x^{i^3} + x^{i^4}\right) \tag{3.18}$$

where

$$\Gamma_{yy} = I_{o_{yy}}/L_{oy}L^3_{oz} \tag{3.19}$$

$$\Gamma_{zz} = I_{o_{zz}}/L_{oz}L^3_{oy} \tag{3.20}$$

$$\alpha_{y0} = \mu_1 L^2_{iy} \tag{3.21}$$

$$\alpha_{y1} = \left(L^3_{iy} + 3\mu_1 L_{iy}\right) \tag{3.22}$$

$$\alpha_{y2} = 6\mu_2 L_{iy} \tag{3.23}$$

$$\alpha_{y3} = 2\left(\mu_2 + L_{iy}\right) \tag{3.24}$$

$$\alpha_{z0} = \mu_1 L^2_{iz} \tag{3.25}$$

$$\alpha_{z1} = \left(L^3_{iz} + 3\mu_1 L_{iz}\right) \tag{3.26}$$

$$\alpha_{z2} = 6\mu_2 L_{iz} \tag{3.27}$$

$$\alpha_{z3} = 2\left(\mu_2 + L_{iz}\right) \tag{3.28}$$

where $I_{o_{yy}}$ and $I_{o_{zz}}$ represent the second moments of area of the root cross-section of the beam about its principal axes.

3.2 Co-ordinate Transformation

The rotation of the cross-section area of the beam about its centroidal axis in the (yz)-plane with a setting angle ψ, see Figure 3-1, results in a relationship defined by the following co-ordinate transformation

$$\begin{Bmatrix} y^i \\ z^i \end{Bmatrix} = \begin{bmatrix} \cos\psi & \sin\psi \\ -\sin\psi & \cos\psi \end{bmatrix} \begin{Bmatrix} y' \\ z' \end{Bmatrix} \tag{3.29}$$

Consequently, substitution of equation (3.29) into equations (2.117)-(2.119) yields

$$I^i_{yy} = I^i_{y'y'}\cos^2\psi + I^i_{z'z'}\sin^2\psi - I^i_{y'z'}\sin 2\psi \tag{3.30}$$

$$I^i_{yz} = \left(I^i_{y'y'} - I^i_{z'z'}\right)\sin\psi\cos\psi + I^i_{y'z'}\cos 2\psi \tag{3.31}$$

$$I^i_{zz} = I^i_{y'y'} \sin^2\psi + I^i_{z'z'} \cos^2\psi + I^i_{y'z'} \sin 2\psi \tag{3.32}$$

where for symmetrical cross-sections, the product second moment of area $I^i_{y'z'}$ vanishes.

3.3 The Beam Element Model

Figure 2.6 shows a typical three dimensional beam element which consists of two nodes and each node has six degrees of freedom; three nodal translations u^i_i, v^i_i and w^i_i and three nodal rotations θ^i_{xi}, θ^i_{yi} and θ^i_{zi}. The nodal displacement vector $\{\overline{e}^i\}$ defined with respect to the element axes is denoted by

$$\{\overline{e}^i\}_{12\times1} = \begin{bmatrix} u^i_1 & v^i_1 & w^i_1 & \theta^i_{x1} & \theta^i_{y1} & \theta^i_{z1} & u^i_2 & v^i_2 & w^i_2 & \theta^i_{x2} & \theta^i_{y2} & \theta^i_{z2} \end{bmatrix}^T \tag{3.33}$$

where subscripts 1 and 2 denote the translation and rotation of the i^{th} beam element at nodal points 1 and 2. In the above $(u^i_1,\ u^i_2)$ are the nodal axial displacements in the x-direction, and $(v^i_1,\ v^i_2)$ and $(w^i_1,\ w^i_2)$ are the nodal translational displacements in the y- and z-directions, respectively; $(\theta^i_{x1},\ \theta^i_{x2})$ are the nodal torsional displacements about the x-axis, and $(\theta^i_{y1},\ \theta^i_{y2})$ and $(\theta^i_{z1},\ \theta^i_{z2})$ are the nodal rotational displacements in the (xy)- and (xz)-planes, respectively.

According to the standard finite element procedure, the elastic deformations of an arbitrary point P^i of the i^{th} beam element can be expressed as

$$\{d^i\}_{3\times1} = [S^i]_{3\times12}\,\{\overline{e}^i\}_{12\times1} \tag{3.34}$$

where $\{d^i\}$ represents the elastic deformation vector of the i^{th} beam element and $[S^i]$ is the matrix of shape functions that are used to describe its deformations. Note that the shape functions are spatially dependent while the vector of nodal displacements is time dependent. Equation (3.34) is a general equation and is valid for any type of shape functions $[S^i]$ used to model structural elements. However, the shape functions adopted in this work are of linear relationship for torsional and axial deformations and can be easily derived. The shape functions used for translation and rotational bending deformations are the conventional cubic Hermitian polynomials and incorporate a shear deformation parameter, in accordance with the Timoshenko model. The shape functions for torsional and axial deformation are linear, and are included for completeness.

3.4 Kinematic Relations

The kinematic relations for the three dimensional Timoshenko beam element undergoing axial, torsional and bending deformations in the (xy)- and (xz)-plane can be expressed by combining equations (2.81), (2.92) and (2.106), that is

$$\begin{aligned} U^i &= u^i - y^i\left(\frac{\partial v^i}{\partial x^i}\right) - z^i\left(\frac{\partial w^i}{\partial x^i}\right) \\ V^i &= -z^i\theta_x^i + v^i \\ W^i &= y^i\theta_x^i + w^i \end{aligned} \tag{3.35}$$

3.5 Derivation of Shape Functions

3.5.1 Axial and Torsional Deformation

Shape functions for axial and torsional deformations $\left[\mathcal{S}_a^i\right]$ and $\left[\mathcal{S}_{\theta x}^i\right]$ can be found in any elementary text, and are given by

$$\left[\mathcal{S}_a^i\right] = \left[\mathcal{S}_{\theta x}^i\right] = \left[1 - \frac{x^i}{l^i} \qquad \frac{x^i}{l^i}\right] = \left[1 - \xi^i \qquad \xi^i\right] \tag{3.36}$$

where $\xi^i = x^i/l^i$ is the dimensionless axial co-ordinate.

3.5.2 Bending Deformation

Shape functions for bending deformations in the (xy)-plane are derived by considering the i^{th} finite beam element shown in Figure 3-2. By analogy, one can obtain the shape functions for bending in the (xz)-plane. The translational deformation $v^i(x^i)$ at an arbitrary point $P^i\left(x^i, y^i, z^i\right)$ is expressed as

$$v^i(x^i) = a_0 + a_1 x^i + a_2 x^{i^2} + a_3 x^{i^3} \tag{3.37}$$

or in matrix form

$$v^i(x^i) = \left[\chi^i\right]\{a_j\} \tag{3.38}$$

where

$$\left[\chi^i\right] = \left[1 \quad x^i \quad x^{i^2} \quad x^{i^3}\right] \tag{3.39}$$

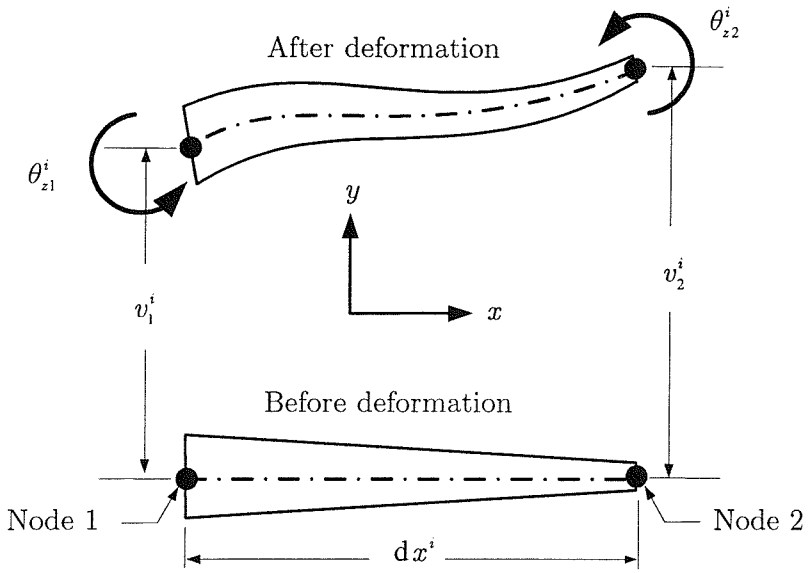

Figure 3-2: Planar bending deformation of the i^{th} beam element in the (xy)-plane.

and

$$\{a_j\} = [a_0 \quad a_1 \quad a_2 \quad a_3]^T \tag{3.40}$$

The shear strain is assumed to be independent of the element axial co-ordinate x^i, in accordance with reference [74], i.e., constant along the finite element

$$\gamma^i_{xy} = \text{const.} = \gamma_0 \tag{3.41}$$

The bending moment M^i_z and the shearing force Q^i_y are related by

$$\frac{\mathrm{d}M^i_z}{dx^i} - Q^i_y = 0, \tag{3.42}$$

and the bending moment-curvature relationship is

$$M^i_z = -E\ I^i_{zz}\ \frac{\partial \theta^i_z}{\partial x^i} \tag{3.43}$$

The shear force is related to the transverse shear strain by the relation

$$Q^i_y = \kappa_y\ G\ A^i\ \gamma^i_{xy} \tag{3.44}$$

where κ_y is the shear correction factor that accounts for the nonuniform distribution of the shear stress over the cross-section A^i. The slope due to bending can be written as

$$\theta_z^i = \frac{\partial v^i}{\partial x^i} - \gamma_{xy}^i = a_1 + 2a_2 x^i + 3a_3 x^{i^2} - \gamma_0 \tag{3.45}$$

Taking the derivative of θ_z^i with respect to x^i and substituting into equation (3.43) yields

$$M_z^i = -2EI_{zz}^i \left(a_2 + 3a_3 x^i\right) \tag{3.46}$$

Taking the derivative of M_z^i with respect to x^i and substituting into equation (3.42) along with (3.41) and (3.44) yields

$$-6EI_{zz}^i a_3 - \kappa_y \, G \, A^i \gamma_0 = 0 \tag{3.47}$$

from which

$$\gamma_0 = -6\Lambda_z^i \, a_3 \tag{3.48}$$

where

$$\Lambda_z^i = \frac{EI_{zz}^i}{\kappa_y \, G \, A^i} \tag{3.49}$$

Substitute equation (3.48) into the expression of θ_z^i, to give

$$\theta_z^i = a_1 + 2a_2 x^i + 3\left(x^{i^2} + 2\Lambda_z^i\right) a_3 \tag{3.50}$$

To express the coefficients a_j in terms of the bending deformations and slopes, the following boundary conditions must be satisfied:

$$\begin{aligned} v^i(0) &= v_1^i \quad \text{and} \quad v^i(l^i) = v_2^i \\ \theta_z^i(0) &= \theta_{z1}^i \quad \text{and} \quad \theta_z^i(l^i) = \theta_{z2}^i \end{aligned} \tag{3.51}$$

and applying these to equations (3.37) and (3.50), gives

$$\begin{aligned} v^i(0) &= a_0 &&= v_1^i \\ \theta_z^i(0) &= a_1 + 6\Lambda_z^i a_3 &&= \theta_{z1}^i \end{aligned}$$

$$
\begin{aligned}
v^i(l^i) &= a_0 + a_1 l^i + a_2 l^{i^2} + a_3 l^{i^3} = v_2^i \\
\theta_z^i(l^i) &= a_1 + 2a_2 l^i + \left(3l^{i^2} + 6\Lambda_z^i\right) a_3 = \theta_{z2}^i
\end{aligned} \tag{3.52}
$$

In matrix form, this can be written as

$$
\left\{ \begin{array}{c} v_1^i \\ \theta_{z1}^i \\ v_2^i \\ \theta_{z2}^i \end{array} \right\} = \left[\begin{array}{cccc} 1 & 0 & 0 & 0 \\ 0 & 1 & 0 & 6\Lambda_z^i \\ 1 & l^i & l^{i^2} & l^{i^3} \\ 0 & 1 & 2l^i & \left(3l^{i^2} + 6\Lambda_z^i\right) \end{array} \right] \left\{ \begin{array}{c} a_0 \\ a_1 \\ a_2 \\ a_3 \end{array} \right\}, \tag{3.53}
$$

or in more compact form

$$
\left\{\delta^i\right\} = [\mathsf{A}] \left\{a_j\right\} \tag{3.54}
$$

from which

$$
\left\{a_j\right\} = [\mathsf{A}]^{-1} \left\{\delta^i\right\} \tag{3.55}
$$

Solving for a_j gives

$$
a_0 = v_1^i \tag{3.56}
$$

$$
a_1 = \overline{\Phi}_z^i \left(-\frac{1}{l^i}\Phi_z^i v_1^i + \left(1 + \frac{\Phi_z^i}{2}\right)\theta_{z1}^i + \frac{1}{l^i}\Phi_z^i v_2^i - \frac{\Phi_z^i}{2}\theta_{z2}^i \right) \tag{3.57}
$$

$$
a_2 = \overline{\Phi}_z^i \left(-\frac{3v_1^i}{l^{i^2}} - \frac{1}{l^i}\left(2 + \frac{\Phi_z^i}{2}\right)\theta_{z1}^i + \frac{3v_2^i}{l^{i^2}} - \frac{1}{l^i}\left(1 - \frac{\Phi_z^i}{2}\right)\theta_{z2}^i \right) \tag{3.58}
$$

$$
a_3 = \overline{\Phi}_z^i \left(\frac{2v_1^i}{l^{i^3}} + \frac{\theta_{z1}^i}{l^{i^2}} - \frac{2v_2^i}{l^{i^3}} + \frac{\theta_{z2}^i}{l^{i^2}} \right) \tag{3.59}
$$

where

$$
\overline{\Phi}_z^i = \frac{1}{(1 + \Phi_z^i)} \tag{3.60}
$$

and

$$
\Phi_z^i = \frac{12\Lambda_z^i}{l^{i^2}} = \frac{12EI_{zz}^i}{\kappa_y\, G\, A^i l^{i^2}} = \left(\frac{12}{\kappa_y}\right)\left(\frac{E}{G}\right)\left(\frac{r_{g_z}^i}{l^i}\right)^2 \tag{3.61}
$$

is the shear deformation parameter that represents the ratio between bending and shear stiffnesses. Since the material of the beam is assumed to be homogeneous and isotropic, the moduli

E and G are constant within the element.

Substitute the values of a_j into the expression of $v^i(\xi^i = x^i/l^i)$ and simplify, one obtains

$$\begin{aligned} v^i(\xi^i) &= \overline{\Phi}^i_z \left(1 - 3\xi^{i^2} + 2\xi^{i^3} + \Phi^i_z \left(1 - \xi^i\right)\right) v^i_1 + l^i \overline{\Phi}^i_z \left(\xi^i - 2\xi^{i^2} + \xi^{i^3} + \frac{\Phi^i_z}{2}\left(\xi^i - \xi^{i^2}\right)\right) \theta^i_{z1} \\ &+ \overline{\Phi}^i_z \left(3\xi^{i^2} - 2\xi^{i^3} + \Phi^i_z \xi^i\right) v^i_2 + l^i \overline{\Phi}^i_z \left(-\xi^{i^2} + \xi^{i^3} + \frac{\Phi^i_z}{2}\left(-\xi^i + \xi^{i^2}\right)\right) \theta^i_{z2} \end{aligned} \tag{3.62}$$

Hence $v^i(\xi^i)$ can be written in compact form as

$$v^i(\xi^i) = \mathcal{S}^i_{v1} v^i_1 + \mathcal{S}^i_{v2} \theta^i_{z1} + \mathcal{S}^i_{v3} v^i_2 + \mathcal{S}^i_{v4} \theta^i_{z2} \tag{3.63}$$

where

$$\begin{aligned} \mathcal{S}^i_{v1} &= \overline{\Phi}^i_z \left(1 - 3\xi^{i^2} + 2\xi^{i^3} + \Phi^i_z \left(1 - \xi^i\right)\right) \\ \mathcal{S}^i_{v2} &= l^i \overline{\Phi}^i_z \left(\xi^i - 2\xi^{i^2} + \xi^{i^3} + \frac{\Phi^i_z}{2}\left(\xi^i - \xi^{i^2}\right)\right) \\ \mathcal{S}^i_{v3} &= \overline{\Phi}^i_z \left(3\xi^{i^2} - 2\xi^{i^3} + \Phi^i_z \xi^i\right) \\ \mathcal{S}^i_{v4} &= l^i \overline{\Phi}^i_z \left(-\xi^{i^2} + \xi^{i^3} + \frac{\Phi^i_z}{2}\left(-\xi^i + \xi^{i^2}\right)\right) \end{aligned} \tag{3.64}$$

Similarly, substitute a_j into the expression for $\theta^i_z(\xi^i)$ and simplify to get

$$\begin{aligned} \theta^i_z(\xi^i) &= \frac{6\overline{\Phi}^i_z}{l^i}\left(-\xi^i + \xi^{i^2}\right) v^i_1 + \overline{\Phi}^i_z \left(1 - 4\xi^i + 3\xi^{i^2} + \Phi^i_z \left(1 - \xi^i\right)\right) \theta^i_{z1} \\ &- \frac{6\overline{\Phi}^i_z}{l^i}\left(-\xi^i + \xi^{i^2}\right) v^i_2 + \overline{\Phi}^i_z \left(-2\xi^i + 3\xi^{i^2} + \Phi^i_z \xi^i\right) \theta^i_{z2} \end{aligned} \tag{3.65}$$

Hence $\theta^i_z(\xi^i)$ can be written in the form

$$\theta^i_z(\xi^i) = \mathcal{S}^i_{\theta z1} v^i_1 + \mathcal{S}^i_{\theta z2} \theta^i_{z1} + \mathcal{S}^i_{\theta z3} v^i_2 + \mathcal{S}^i_{\theta z4} \theta^i_{z2} \tag{3.66}$$

where

$$\begin{aligned} \mathcal{S}^i_{\theta z1} &= \frac{6\overline{\Phi}^i_z}{l^i}\left(-\xi^i + \xi^{i^2}\right) \\ \mathcal{S}^i_{\theta z2} &= \overline{\Phi}^i_z \left(1 - 4\xi^i + 3\xi^{i^2} + \Phi^i_z \left(1 - \xi^i\right)\right) \\ \mathcal{S}^i_{\theta z3} &= -\frac{6\overline{\Phi}^i_z}{l^i}\left(-\xi^i + \xi^{i^2}\right) \\ \mathcal{S}^i_{\theta z4} &= \overline{\Phi}^i_z \left(-2\xi^i + 3\xi^{i^2} + \Phi^i_z \xi^i\right) \end{aligned} \tag{3.67}$$

Shape functions for bending in the (xz)-plane are obtained in a similar manner; the bending slope θ_y^i is given by equation (2.112) while the shear deformation parameter is

$$\Phi_y^i = \frac{12EI_{yy}^i}{\kappa_z\, G\, A^i l^{i2}} = \frac{12}{\kappa_z}\left(\frac{E}{G}\right)\left(\frac{r_{g_y}^i}{l^i}\right)^2 \tag{3.68}$$

and

$$\overline{\Phi}_y^i = \frac{1}{\left(1+\Phi_y^i\right)} \tag{3.69}$$

The corresponding expressions of $w^i(\xi^i)$ and $\theta_y^i(\xi^i)$ can be written as

$$w^i(\xi^i) = \mathcal{S}_{w1}^i w_1^i + \mathcal{S}_{w2}^i \theta_{y1}^i + \mathcal{S}_{w3}^i w_2^i + \mathcal{S}_{w4}^i \theta_{y2}^i \tag{3.70}$$

$$\theta_y^i(\xi^i) = \mathcal{S}_{\theta y1}^i w_1^i + \mathcal{S}_{\theta y2}^i \theta_{y1}^i + \mathcal{S}_{\theta y3}^i w_2^i + \mathcal{S}_{\theta y4}^i \theta_{y2}^i \tag{3.71}$$

Shape functions for bending in the (xz)-plane can be written as

$$\begin{aligned}
\mathcal{S}_{w1} &= \overline{\Phi}_y^i\left(1-3\xi^{i2}+2\xi^{i3}+\Phi_y^i\left(1-\xi^i\right)\right)\\
\mathcal{S}_{w2}^i &= -l^i\overline{\Phi}_y^i\left(\xi^i-2\xi^{i2}+\xi^{i3}+\frac{\Phi_y^i}{2}\left(\xi^i-\xi^{i2}\right)\right)\\
\mathcal{S}_{w3}^i &= \overline{\Phi}_y^i\left(3\xi^{i2}-2\xi^{i3}+\Phi_y^i\xi^i\right)\\
\mathcal{S}_{w4}^i &= -l^i\overline{\Phi}_y^i\left(-\xi^{i2}+\xi^{i3}+\frac{\Phi_y^i}{2}\left(-\xi^i+\xi^{i2}\right)\right)
\end{aligned} \tag{3.72}$$

and the corresponding bending slope shape functions are

$$\begin{aligned}
\mathcal{S}_{\theta y1}^i &= \frac{6\overline{\Phi}_y^i}{l^i}\left(-\xi^i+\xi^{i2}\right)\\
\mathcal{S}_{\theta y2}^i &= -\overline{\Phi}_y^i\left(1-4\xi^i+3\xi^{i2}+\Phi_y^i\left(1-\xi^i\right)\right)\\
\mathcal{S}_{\theta y3}^i &= -\frac{6\overline{\Phi}_y^i}{l^i}\left(-\xi^i+\xi^{i2}\right)\\
\mathcal{S}_{\theta y4}^i &= -\overline{\Phi}_y^i\left(-2\xi^i+3\xi^{i2}+\Phi_y^i\xi^i\right)
\end{aligned} \tag{3.73}$$

By virtue of equations (3.36) (3.64), (3.67), (3.72) and (3.73), the kinematic relations given by equation (3.35) are now expressed as

$$
\begin{aligned}
U^i &= \left(1-\xi^i\right)u_1^i - 6\overline{\Phi}_z^i\left(-\xi^i+\xi^{i^2}\right)\eta^i v_1^i - 6\overline{\Phi}_y^i\left(-\xi^i+\xi^{i^2}\right)\zeta^i w_1^i \\
&+ l^i\overline{\Phi}_y^i\left(1-4\xi^i+3\xi^{i^2}+\Phi_y^i\left(1-\xi^i\right)\right)\zeta^i\theta_{y1}^i - l^i\overline{\Phi}_z^i\left(1-4\xi^i+3\xi^{i^2}+\Phi_z^i\left(1-\xi^i\right)\right)\eta^i\theta_{z1}^i \\
&+ \xi^i u_2^i - 6\overline{\Phi}_z^i\left(\xi^i-\xi^{i^2}\right)\eta^i v_2^i - 6\overline{\Phi}_y^i\left(\xi^i-\xi^{i^2}\right)\zeta^i w_2^i \\
&+ l^i\overline{\Phi}_y^i\left(-2\xi^i+3\xi^{i^2}+\Phi_y^i\xi^i\right)\zeta^i\theta_{y2}^i - l^i\overline{\Phi}_z^i\left(-2\xi^i+3\xi^{i^2}+\Phi_z^i\xi^i\right)\eta^i\theta_{z2}^i \\
V^i &= \overline{\Phi}_z^i\left(1-3\xi^{i^2}+2\xi^{i^3}+\Phi_z^i\left(1-\xi^i\right)\right)v_1^i - l^i\zeta^i\left(1-\xi^i\right)\theta_{x1}^i \\
&+ l^i\overline{\Phi}_z^i\left(\xi^i-2\xi^{i^2}+\xi^{i^3}+\frac{\Phi_z^i}{2}\left(\xi^i-\xi^{i^2}\right)\right)\theta_{z1}^i + \overline{\Phi}_z^i\left(3\xi^{i^2}-2\xi^{i^3}+\Phi_z^i\xi^i\right)v_2^i \qquad (3.74) \\
&- l^i\zeta^i\xi^i\theta_{x2}^i + l^i\overline{\Phi}_z^i\left(-\xi^{i^2}+\xi^{i^3}+\frac{\Phi_z^i}{2}\left(-\xi^i+\xi^{i^2}\right)\right)\theta_{z2}^i \\
W^i &= \overline{\Phi}_y^i\left(1-3\xi^{i^2}+2\xi^{i^3}+\Phi_y^i\left(1-\xi^i\right)\right)w_1^i + l^i\eta^i\left(1-\xi^i\right)\theta_{x1}^i \\
&- l^i\overline{\Phi}_y^i\left(\xi^i-2\xi^{i^2}+\xi^{i^3}+\frac{\Phi_y^i}{2}\left(\xi^i-\xi^{i^2}\right)\right)\theta_{y1}^i + \overline{\Phi}_y^i\left(3\xi^{i^2}-2\xi^{i^3}+\Phi_y^i\xi^i\right)w_2^i \\
&+ l^i\eta^i\xi^i\theta_{x2}^i - l^i\overline{\Phi}_y^i\left(-\xi^{i^2}+\xi^{i^3}+\frac{\Phi_y^i}{2}\left(-\xi^i+\xi^{i^2}\right)\right)\theta_{y2}^i
\end{aligned}
$$

where $\eta^i = \dfrac{y^i}{l^i}$ and $\zeta^i = \dfrac{z^i}{l^i}$ are dimensionless co-ordinates in the y- and z-directions, respectively. In matrix form this can be written as

$$
\left\{d^i\right\}_{3\times 1} = \begin{bmatrix} U^i & V^i & W^i \end{bmatrix}^T = \left[\mathcal{S}^i\right]_{3\times 12}\left\{\overline{e}^i\right\}_{12\times 1} \qquad (3.75)
$$

These results are summarized in the matrix of the shape functions, $\left[\mathcal{S}^i\right]$, shown in Appendix B. If the shear deformation parameters Φ_y^i and Φ_z^i are neglected, then $\left[\mathcal{S}^i\right]$ reduces to the three dimensional Euler- Bernoulli beam shape function derived in reference [92]. However a sign change is required in the fourth and tenth entries of the third column of the shape function matrix, which correspond to the twist terms.

3.6 Stiffness Matrices

3.6.1 Elastic Stiffness Matrix

The composite elemental elastic stiffness matrix of the i^{th} non-spinning tapered Timoshenko beam element of length l^i is given by equation (2.158) as

$$
\left[\overline{k}_{ee}^i\right] = \left[\overline{k}_a^i\right] + \left[\overline{k}_{\theta x}^i\right] + \left[\overline{k}_{b,v}^i\right] + \left[\overline{k}_{b,w}^i\right] + \left[\overline{k}_{b,vw}^i\right] + \left[\overline{k}_{s,v}^i\right] + \left[\overline{k}_{s,w}^i\right]
$$

where each of the previous matrices is given by

$$\left[\overline{k}_a^i\right] = \int_0^{l^i} \left[B_a^i\right]^T EA^i \left[B_a^i\right] \mathrm{d}x^i \tag{3.76}$$

$$\left[\overline{k}_{\theta x}^i\right] = \int_0^{l^i} \left[B_{\theta x}^i\right]^T GJ^i \left[B_{\theta x}^i\right] \mathrm{d}x^i \tag{3.77}$$

$$\left[\overline{k}_{b,v}^i\right] = \int_0^{l^i} \left[B_{\theta z}^i\right]^T EI_{zz}^i \left[B_{\theta z}^i\right] \mathrm{d}x^i \tag{3.78}$$

$$\left[\overline{k}_{b,w}^i\right] = \int_0^{l^i} \left[B_{\theta y}^i\right]^T EI_{yy}^i \left[B_{\theta y}^i\right] \mathrm{d}x^i \tag{3.79}$$

$$\left[\overline{k}_{b,vw}^i\right] = \int_0^{l^i} \left[B_{\theta yz}^i\right]^T EI_{yz}^i \left[B_{\theta yz}^i\right] \mathrm{d}x^i \tag{3.80}$$

$$\left[\overline{k}_{s,v}^i\right] = \int_0^{l^i} \left(\left[B_v^i\right] - \left[\mathcal{S}_{\theta z}^i\right]\right)^T \kappa_y GA^i \left(\left[B_v^i\right] - \left[\mathcal{S}_{\theta z}^i\right]\right) \mathrm{d}x^i \tag{3.81}$$

$$\left[\overline{k}_{s,w}^i\right] = \int_0^{l^i} \left(\left[B_w^i\right] + \left[\mathcal{S}_{\theta y}^i\right]\right)^T \kappa_z GA^i \left(\left[B_w^i\right] + \left[\mathcal{S}_{\theta y}^i\right]\right) \mathrm{d}x^i \tag{3.82}$$

By carrying out the integration of equations (3.76)-(3.82), the explicit expressions of the above elastic stiffness matrices are given in Tables C1 to C7 of Appendix C.

3.6.2 Stiffness Matrices due to Rotation

The elemental stiffness matrix due to the contribution of the strain energy increase induced by the hub rotation of the i^{th} Timoshenko beam element is given by equation (2.168) as

$$\left[\overline{k}_c^i\right] = \left[\overline{k}_{c,v}^i\right] + \left[\overline{k}_{c,w}^i\right]$$

where $\left[\overline{k}_{c,v}^i\right]$ and $\left[\overline{k}_{c,w}^i\right]$ are the elemental centrifugal stiffness matrices in the (xy)- and (xz)-plane respectively, and are given by

$$\left[\overline{k}_{c,v}^i\right] = \int_0^{l^i} \left[B_{c,v}^i\right]^T F_P^i \left[B_{c,v}^i\right] \mathrm{d}x^i \tag{3.83}$$

$$\left[\overline{k}_{c,w}^i\right] = \int_0^{l^i} \left[B_{c,w}^i\right]^T F_P^i \left[B_{c,w}^i\right] \mathrm{d}x^i \tag{3.84}$$

where F_P^i is the centrifugal force acting on the i^{th} element as a consequence of the hub rotation. Here the assumption has been made that the displacements are small such that the higher order terms of the change in the axial direction of the i^{th} element can be neglected. The expression for the tensile force F_P^i acting on a section of the beam and associated with a differential element at point P^i of the i^{th} element is given by

$$\mathrm{d}F_P^i = \rho A^i \Omega^2 (\mathcal{R}_\circ + r_P^i \cos\phi)\mathrm{d}r_P^i \tag{3.85}$$

where $\mathcal{R}_\circ$ is the hub radius, r_P^i is the position vector of point P^i and ϕ is the pre-cone. For small deformations, one can write

$$r_P^i = \left(L^i + x^i\right) = (i-1)l^i + x^i \tag{3.86}$$

Therefore, the expression of F_P^i can be developed by integrating equation (3.85) over the span between point P^i and the free end of the beam, as shown in Figure 3-1, that is

$$F_P^i = \rho\Omega^2 \left(\int_{x^i}^{l^i} \left(\mathcal{R}_\circ + \left((i-1)l^i + x^i\right)\cos\phi\right) A^i \mathrm{d}x^i + \int_{il^i}^{nl^i} \left(\mathcal{R}_\circ + x^i \cos\phi\right) A^i \mathrm{d}x^i \right) \tag{3.87}$$

Carrying out the integration of equation (3.87), the resulting tensile force F_P^i can be written in the form

$$F_P^i = \frac{\rho\Omega^2 A_o}{L_{oy} L_{oz}} \left[\beta_4 - \beta_3 x - \beta_2 x^{i^2} - \beta_1 x^{i^3} - \beta_0 x^{i^4}\right] \tag{3.88}$$

where β_j are constants given by

$$\beta_o = \frac{1}{4}\cos\phi \tag{3.89}$$

$$\beta_1 = \frac{1}{3}\left[\mathcal{R}_\circ + \left(L^i - 2\mu_2\right)\cos\phi\right] \tag{3.90}$$

$$\beta_2 = \frac{1}{2}\left[\mu_1 \cos\phi - 2\mu_2\left(\mathcal{R}_\circ + L^i \cos\phi\right)\right] \tag{3.91}$$

$$\beta_3 = \mu_1\left(\mathcal{R}_\circ + L^i \cos\phi\right) \tag{3.92}$$

$$\begin{aligned}\beta_4 = {} & \frac{1}{12}\left(3n^4 - 3i^4 + 4i - 1\right) l^{i^4}\cos\phi - \frac{1}{3}\left[\left(2n^3 - 2i^3 + 3i - 1\right)\mu_2 \cos\phi - \left(n^3 - i^3 + 1\right)\mathcal{R}_\circ\right] l^{i^3} \\ & + \frac{1}{2}\left[\left(n^2 - i^2 + 2i - 1\right)\mu_1 \cos\phi - 2\left(n^2 - i^2 + 1\right)\mu_2 \mathcal{R}_\circ\right] l^{i^2} + \left(n - i + 1\right)\mu_1 \mathcal{R}_\circ l^i \end{aligned} \tag{3.93}$$

If $\mathcal{R}_o$ and ϕ are neglected, the expression of F_P^i is simplified to the one obtained in [27], while keeping $\mathcal{R}_o$ only, the expression of F_P^i is identical to that obtained in [29]. Carrying out the integration of equations (3.83) and (3.84), the explicit expression of the elemental stiffness matrices $\left[\overline{k}_{c,v}^i\right]$ and $\left[\overline{k}_{c,w}^i\right]$ are respectively given by Tables C8 and C9 of Appendix C.

3.7 Inertia Properties

The composite elemental mass matrix of the i^{th} spinning Timoshenko beam element of length l^i is given by equation (2.66) as

$$\left[\overline{m}_{ee}^i\right] = \left[\overline{m}_a^i\right] + \left[\overline{m}_{\theta x}^i\right] + \left[\overline{m}_{t,v}^i\right] + \left[\overline{m}_{t,w}^i\right] + \left[\overline{m}_{\theta z,v}^i\right] + \left[\overline{m}_{\theta y,w}^i\right] + \left[\overline{m}_{\theta,vw}^i\right]$$

where $\left[\overline{m}_{ee}^i\right]$ is referred to the consistent mass matrix because it is obtained from the same shape functions used to formulate the stiffness matrix. The expressions of the constituents of the mass matrix $\left[\overline{m}_{ee}^i\right]$ are given by

$$\left[\overline{m}_a^i\right] = \int_0^{l^i} \left[\mathcal{S}_a^i\right]^T \rho A^i \left[\mathcal{S}_a^i\right] \mathrm{d}x^i \tag{3.94}$$

$$\left[\overline{m}_{\theta_x}^i\right] = \int_0^{l^i} \left[\mathcal{S}_{\theta x}^i\right]^T \rho J^i \left[\mathcal{S}_{\theta x}^i\right] \mathrm{d}x^i \tag{3.95}$$

$$\left[\overline{m}_{t,v}^i\right] = \int_0^{l^i} \left[\mathcal{S}_v^i\right]^T \rho A^i \left[\mathcal{S}_v^i\right] \mathrm{d}x^i \tag{3.96}$$

$$\left[\overline{m}_{t,w}^i\right] = \int_0^{l^i} \left[\mathcal{S}_w^i\right]^T \rho A^i \left[\mathcal{S}_w^i\right] \mathrm{d}x^i \tag{3.97}$$

$$\left[\overline{m}_{\theta_z,v}^i\right] = \int_0^{l^i} \left[\mathcal{S}_v^i\right]^T \rho I_{zz}^i \left[\mathcal{S}_v^i\right] \mathrm{d}x^i \tag{3.98}$$

$$\left[\overline{m}_{\theta_y,w}^i\right] = \int_0^{l^i} \left[\mathcal{S}_w^i\right]^T \rho I_{yy}^i \left[\mathcal{S}_w^i\right] \mathrm{d}x^i \tag{3.99}$$

$$\left[\overline{m}_{\theta,vw}^i\right] = \int_0^{l^i} \left[\mathcal{S}_v^i\right]^T \rho I_{yz}^i \left[\mathcal{S}_w^i\right] \mathrm{d}x^i \tag{3.100}$$

Carrying out the integration of equations (3.94) to (3.100), the explicit expressions of the constituents of the mass matrix $\left[\overline{m}_{ee}^i\right]$ are given in Tables C10 to C16 of Appendix C.

3.8 Coriolis Matrix

The Coriolis matrix due to the spinning of the i^{th} Timoshenko beam element is given by equation (2.64) as

$$\left[\widetilde{C^i}\right] = \int_0^{l^i} \rho A^i \left[\mathcal{S}^i\right]^T \left[\Re^i\right]^T \left[\widetilde{\mathcal{A}_I}\right]^T \left[\Re^i\right] \left[\mathcal{S}^i\right] \mathrm{d}x^i$$

Carrying out the integration of the previous equation, the explicit expression of the Coriolis matrix $\left[\widetilde{C^i}\right]$ can be given by

$$\left[\widetilde{C^i}\right] = \left[\widetilde{C_1^i}\right] + \left[\widetilde{C_2^i}\right] + \left[\widetilde{C_3^i}\right] \tag{3.101}$$

where the explicit expressions of $\left[\widetilde{C_1^i}\right]$, $\left[\widetilde{C_2^i}\right]$ and $\left[\widetilde{C_3^i}\right]$ are given in Table C17 of Appendix C.

3.9 Quadratic Velocity Terms

The centrifugal inertia forces that result from differentiating the Lagrangian with respect to the generalized co-ordinates and time are referred to as quadratic velocity terms. The expressions of the inertia terms $\left[m^i_{\mathcal{R}_o e}\right]$ and $\left[m^i_{r_{P_o} e}\right]$ are respectively given by equations (2.55) and (2.57) as

$$\begin{aligned}
\left[m^i_{\mathcal{R}_o e}\right] &= \int_0^{l^i} \rho A^i \left\{\mathcal{R}_o\right\}^T \left[\widetilde{\mathcal{A}_I}\right]^T \left[\mathcal{A}_\varphi\right] \left[\Re^i\right] \left[\mathcal{S}^i\right] \left[\overline{\Re^i}\right] \mathrm{d}x^i \\
\left[m^i_{r_{P_o} e}\right] &= \int_0^{l^i} \rho A^i \left[\overline{\Re^i}\right]^T \left[\mathcal{S}^i\right]^T \left[\Re^i\right]^T \left[\mathcal{I}_o\right] \left[\mathcal{A}_o\right] \left\{r^i_{P_o}\right\} \mathrm{d}x^i
\end{aligned}$$

Notice that $\left[m^i_{r_{P_o} e}\right]$ is time invariant while $\left[m^i_{\mathcal{R}_o e}\right]$ is implicit function of time since it is function of φ. Its entries will be iteratively updated as the integration algorithm proceeds forward in time during the solution of the system equations of motion. Carrying out the integration of equations (2.55) and (2.57), the explicit expressions of $\left[m^i_{\mathcal{R}_o e}\right]$ and $\left[m^i_{r_{P_o} e}\right]$ of the i^{th} spinning Timoshenko beam element are given in Tables C18 and C19 of Appendix C.

Chapter 4

Modal Reduction

The contribution of the Coriolis matrix to the system equations of motion of the present model makes the associated eigenvalue problem deviate from the standard one and difficult to solve. However, the state space representation provides an alternative form to the system equations of motion and the associated eigenvalue problem. Consequently, an appropriate scheme is presented and discussed to simplify significantly the eigenvalue problem in hand.

In this chapter the strategy for solving the assembled equations of motion of the rotating three dimensional tapered Timoshenko beam is outlined. The equations of motion of the system when using nodal co-ordinates result in a large dimensionality problem in terms of which a solution becomes impracticable. Hence, reduction of the order of the equations of motion is desirable while retaining the exact dynamic characteristics of the actual equations of motion, to study the time response of the system. Two modal reduction schemes namely the Planar Reduction Order Model (PROM) and the Complex Reduction Order Model (CROM) are introduced and discussed. Implementation of these modal reductions schemes will be given in the next chapter.

4.1 The Eigenvalue Problem

The equations of the free vibration for the rotating three dimensional tapered Timoshenko beam can be written in the assembled general standard compact form as

$$[M_{ee}]\{\ddot{e}\} + 2\Omega\left[\widetilde{C}\right]\{\dot{e}\} + [K^*]\{e\} = \{0\} \tag{4.1}$$

where the matrix $[M_{ee}]$ is real symmetric positive definite mass matrix, $[K^*]$ is real symmetric positive definite or positive semi-definite modified stiffness matrix, whereas $\left[\widetilde{C}\right]$ is real skew symmetric. These constituent matrices are highly banded in nature and are time invariant. The

modified stiffness matrix is given by

$$[K^*] = [K_{ee}] + \Omega^2 \left([\mathbb{K}_c] - [M_{t,w}] \sin\psi \cos\phi \sin(\phi + \psi)\right) \tag{4.2}$$

Equation (4.1) represents a homogeneous time-invariant system, and admits a solution of the form

$$\{e\} = \{\mathbf{u}\} \ \exp(\lambda t) \tag{4.3}$$

where λ is a constant scalar and $\{\mathbf{u}\}$ is a constant vector of amplitudes, both in general complex. Substitute equation (4.3) into equation (4.1) and performing the usual steps of differentiation and algebraic manipulation, one can write

$$\lambda^2 [M_{ee}] \{\mathbf{u}\} + 2\Omega\lambda \left[\widetilde{C}\right] \{\mathbf{u}\} + [K^*] \{\mathbf{u}\} = \{\mathbf{0}\} \tag{4.4}$$

Since both $[M_{ee}]$ and $[K^*]$ are positive definite while $\left[\widetilde{C}\right]$ is skew symmetric it follows that all the eigenvalues are pure imaginary. Hence if one substitutes $\lambda = j\omega$ in equation (4.4), one obtains the eigenvalue problem

$$\left(-\omega^2 [M_{ee}] + j2\Omega\omega \left[\widetilde{C}\right] + [K^*]\right) \{\mathbf{u}\} = \{\mathbf{0}\} \tag{4.5}$$

where ω must satisfy the characteristic equation

$$\det\left[-\omega^2 [M_{ee}] + j2\Omega\omega \left[\widetilde{C}\right] + [K^*]\right] = 0 \tag{4.6}$$

But the determinant of a matrix is equal to the determinant of its transposed matrix. Hence recalling that $[M_{ee}]$ and $[K^*]$ are symmetric and $\left[\widetilde{C}\right]$ is skew symmetric, the characteristic equation can also be written in the form

$$\det\left[-\omega^2 [M_{ee}] + j2\Omega\omega \left[\widetilde{C}\right] + [K^*]\right]^T = \det\left[-\omega^2 [M_{ee}] - j2\Omega\omega \left[\widetilde{C}\right] + [K^*]\right] = 0 \tag{4.7}$$

from which one can conclude that if $j\omega$ is a root of the characteristic equation, then $-j\omega$ is also a root. It follows that the eigenvalues of a gyroscopic conservative system occur in pairs of pure imaginary complex conjugates

$$\lambda_r = j\omega_r, \qquad \overline{\lambda}_r = -j\omega_r, \qquad (r = 1, 2, ..., n) \tag{4.8}$$

where ω_r are recognized as the natural frequencies. The eigenvectors belonging to the eigenvalues $\pm j\omega_r$ are complex conjugates, although they are not necessarily pure imaginary.

4.2 State Space Form Representation

The eigenvalue problem given by equation (4.5) is affected by the presence of the Coriolis and centrifugal forces and contains both ω and ω^2. Though it is not a standard problem to solve and is not convenient for calculating the eigenvalues because it does not have a ready solution. This difficulty can be overcome by recasting the problem in state space form. In this case equation (4.1) can be expressed as a set of $2n$ first order differential equations. An appropriate form which is widely encountered in structural dynamic analysis is to write the system equations given by equation (4.1) in terms of a skew-symmetric matrix $[\mathbf{A}]$ and a symmetric matrix $[\mathbf{B}]$. In order to transform a system of n second order differential equations into a system of $2n$ first order differential equations, define the state vector

$$\{\mathbf{x}\} = \begin{Bmatrix} \{\dot{e}\} \\ \{e\} \end{Bmatrix} \tag{4.9}$$

and the identity $[M_{ee}]\{\dot{e}\} = [M_{ee}]\{\dot{e}\}$ in conjunction with equation (4.1), one may rewrite equation (4.1) as

$$\begin{bmatrix} [0] & -[M_{ee}] \\ [M_{ee}] & 2\Omega\left[\widetilde{C}\right] \end{bmatrix} \begin{Bmatrix} \{\ddot{e}\} \\ \{\dot{e}\} \end{Bmatrix} + \begin{bmatrix} [M_{ee}] & [0] \\ [0] & [K^*] \end{bmatrix} \begin{Bmatrix} \{\dot{e}\} \\ \{e\} \end{Bmatrix} = \begin{Bmatrix} 0 \\ 0 \end{Bmatrix} \tag{4.10}$$

which can be written as

$$[\mathbf{A}]\{\dot{\mathbf{x}}\} + [\mathbf{B}]\{\mathbf{x}\} = \{\mathbf{0}\} \tag{4.11}$$

where

$$[\mathbf{A}] = \begin{bmatrix} [0] & -[M_{ee}] \\ [M_{ee}] & 2\Omega\left[\widetilde{C}\right] \end{bmatrix} \tag{4.12}$$

and

$$[\mathbf{B}] = \begin{bmatrix} [M_{ee}] & [0] \\ [0] & [K^*] \end{bmatrix} \tag{4.13}$$

where $[\mathbf{B}]$ is a symmetric positive definite matrix (only if $[K^*]$ is symmetric positive definite too) and $[\mathbf{A}]$ is skew symmetric.

The solution of equation (4.11) has the exponential form

$$\{\mathbf{x}\} = \{\mathbf{v}\} \ \exp(\lambda t) \tag{4.14}$$

Inserting equation (4.14) into equation (4.11) and dividing through by $\exp(\lambda t)$, one obtains the generalized eigenvalue problem

$$(\lambda[\mathbf{A}] + [\mathbf{B}])\{\mathbf{v}\} = \{\mathbf{0}\} \tag{4.15}$$

which admits $2n$ eigenvectors $\{\mathbf{v}_r\}$ associated with the eigenvalues λ_r obtained by solving the characteristic equation

$$\det(\lambda[\mathbf{A}] \ + [\mathbf{B}]) = 0 \tag{4.16}$$

In order to determine the properties of the eigensolutions of equation (4.15), consider the most general case of a complex eigenmode $\{\mathbf{v}_r\} = y_r + jz_r$ and define the Rayleigh quotient associated with (4.15)

$$\lambda = -\frac{\{\overline{\mathbf{v}}\}^T[\mathbf{B}]\{\mathbf{v}\}}{\{\overline{\mathbf{v}}\}^T[\mathbf{A}]\{\mathbf{v}\}} \tag{4.17}$$

where $\{\overline{\mathbf{v}}\}$is the conjugate of $\{\mathbf{v}\}$. Owing to the skew symmetry of $[\mathbf{A}]$ and the symmetry of $[\mathbf{B}]$, computing (4.17) for mode r successively yields

$$\begin{aligned}\lambda_r &= -\frac{\{\overline{\mathbf{v}}_r\}^T[\mathbf{B}]\{\mathbf{v}_r\}}{\{\overline{\mathbf{v}}_r\}^T[\mathbf{A}]\{\mathbf{v}_r\}} = -\frac{y_r^T[\mathbf{B}]y_r + jy_r^T[\mathbf{B}]z_r - jz_r^T[\mathbf{B}]y_r + z_r^T[\mathbf{B}]z_r}{y_r^T[\mathbf{A}]y_r + jy_r^T[\mathbf{A}]z_r - jz_r^T[\mathbf{A}]y_r + z_r^T[\mathbf{A}]z_r} \\ &= -2j\frac{y_r^T[\mathbf{B}]z_r}{y_r^T[\mathbf{A}]y_r + z_r^T[\mathbf{A}]z_r}\end{aligned} \tag{4.18}$$

showing that the $2n$ eigenvalues λ_r are purely imaginary. Computing also the Rayleigh quotient for the conjugate to the eigenmode $\{\mathbf{v}_r\}$

$$\overline{\lambda}_r = -\frac{\{\mathbf{v}_r\}^T[\mathbf{B}]\{\overline{\mathbf{v}}_r\}}{\{\mathbf{v}_r\}^T[\mathbf{A}]\{\overline{\mathbf{v}}_r\}} = \frac{\{\overline{\mathbf{v}}_r\}^T[\mathbf{B}]\{\mathbf{v}_r\}}{\{\overline{\mathbf{v}}_r\}^T[\mathbf{A}]\{\mathbf{v}_r\}} = -\lambda_r \tag{4.19}$$

shows that if λ_r is an eigenvalue associated with mode $\{\mathbf{v}_r\}$, $-\lambda_r$ is also an eigenvalue with eigenmode $\{\overline{\mathbf{v}}_r\}$. Therefore the $2n$ eigensolutions of (4.15) appear in the form of n pairs of conjugate solutions. Subsequently, the eigenvalues λ will be written as $j\omega$ with ω real.

4.3 MATLAB Implementation

To implement the eigenvalue problem of (4.15), it is required to prepare a suitable program to form the [**A**] and [**B**] matrices from the $[M_{ee}]$, $\left[\widetilde{C}\right]$ and $[K^*]$ matrices. There are many available methods for solving the eigenvalue problem in hand. One such method is the QR algorithm that has been implemented in a package called EISPACK. The details of this method can be found in any advanced algebraic eigenvalue problem textbook. The eigenvalue problem associated with equation (4.15) is solved using MATLAB that uses EISPACK routines.

4.4 Modal Reduction Schemes

Utilizing nodal co-ordinates in the discretization process leads to a large number of degrees of freedom of the model, and consequently, results in a large number of dynamic equations for which a solution becomes impracticable. Moreover, the use of nodal co-ordinates results in a dynamic model of widely spread eigen-spectrum that includes many insignificant modes and consequently, a numerically stiff system[1] is often created which causes the numerical integration scheme to search inefficiently for a solution or may even fail to find one.

Using modal co-ordinates alleviates the problem of large dimensionality incurred by using nodal co-ordinates, and avoids the inclusion of higher insignificant modes when they do not share an appreciable amount of the system's kinetic energy [62]. In general, a subset of eigenvectors which spans the frequency spectrum of the forcing function are retained as significant modes.

The truncation operation aims at eliminating the insignificant modes which are, in general, higher modes that do not contain an appreciable amount of the system's kinetic energy. In general, a subset of eigenvectors which spans the frequency spectrum of the forcing function are retained as significant modes. Moreover the retained modes must include the first few lower ones in terms of which the characteristics of the system must be preserved.

Two modal reduction schemes are established. The first scheme utilizes planar modes obtained by solving the self-adjoint eigenvalue, while the second scheme invokes the complex modes

[1]Stiff systems have eigenvalues of very different magnitudes.

of the non-self-adjoint eigenvalue. In each case, a reduced order modal form of the equations of motion is obtained.

4.5 Planar Modal Transformation

In order to obtain the real eigenvalues and the associated planar modes, one must ignore the Coriolis matrix $[\widetilde{C}]$ in equation (4.1). To this end, the associated homogenous adjoint equation can be written as

$$[M_{ee}]\{\ddot{e}\} + [K^*]\{e\} = \{0\} \tag{4.20}$$

Upon solving the self-adjoint eigenvalue problem associated with equation (4.20), one obtains a set of real eigenvalues and eigenvectors. Let $[\mathbb{P}]$ denotes the modal matrix that comprises a selected subset of the resulting real eigenvectors (planar modes). Now, a transformation from nodal co-ordinate space to modal co-ordinate space can be defined as

$$\{e\} = [\mathbb{P}]\{\nu\} \tag{4.21}$$

where $\{\nu\}$ is the vector of modal co-ordinates. If only a truncated set of significant modes are retained, the corresponding truncated form of equation (2.217) can be written as

$$[\mathbb{P}]^T[M_{ee}][\mathbb{P}]\{\ddot{\nu}\} + 2\Omega[\mathbb{P}]^T[\widetilde{C}][\mathbb{P}]\{\dot{\nu}\} + [\mathbb{P}]^T[K^*][\mathbb{P}]\{\nu\} = [\mathbb{P}]^T\{Q\} \tag{4.22}$$

or simply

$$[M_{eer}]\{\ddot{\nu}\} + 2\Omega[\widetilde{C}_r]\{\dot{\nu}\} + [K_r^*]\{\nu\} = \{Q_r\} \tag{4.23}$$

where $[M_{eer}]$, $[\widetilde{C}_r]$, $[K_r^*]$ and $\{Q_r\}$ are the reduced modal mass, Coriolis, stiffness matrices, and reduced modal force vector, respectively given by

$$\begin{aligned} [M_{eer}] &= [\mathbb{P}]^T[M_{ee}][\mathbb{P}] \\ [\widetilde{C}_r] &= [\mathbb{P}]^T[\widetilde{C}][\mathbb{P}] \\ [K_r^*] &= [\mathbb{P}]^T[K^*][\mathbb{P}] \\ \{Q_r\} &= [\mathbb{P}]^T\{Q\} \end{aligned} \tag{4.24}$$

Equation (4.23) represents the Planar Reduced Order Model (PROM) using planar mode reduction.

4.6 Complex Modal Transformation

In this case, the equation of motion, equation (2.217) is first represented in the state-space form as

$$[\mathbf{A}]\{\dot{y}\} + [\mathbf{B}]\{y\} = \{\mathcal{F}\} \tag{4.25}$$

where $[\mathbf{A}]$, $[\mathbf{B}]$ and $\{y\}$ are respectively given by

$$[\mathbf{A}] = \begin{bmatrix} [0] & -[M_{ee}] \\ [M_{ee}] & 2\Omega\left[\widetilde{C}\right] \end{bmatrix} \tag{4.26}$$

$$[\mathbf{B}] = \begin{bmatrix} [M_{ee}] & [0] \\ [0] & [K^*] \end{bmatrix} \tag{4.27}$$

and

$$\{y\} = \begin{Bmatrix} \{\dot{e}\} \\ \{\dot{e}\} \end{Bmatrix} \tag{4.28}$$

where the matrix $[\mathbf{A}]$ is skew-symmetric and $[\mathbf{B}]$ is symmetric. Notice that if the dimensions of $[M_{ee}]$, $[K^*]$ and $\left[\widetilde{C}\right]$ are $(6n \times 6n)$ where n is the number of nodes, the dimensions of $[\mathbf{A}]$ and $[\mathbf{B}]$ are $(12n \times 12n)$. The force vector on the right hand side of equation (4.25) is given by

$$\{\mathcal{F}\} = \begin{bmatrix} \{0\} & \{Q\} \end{bmatrix}^T \tag{4.29}$$

The two homogeneous adjoint equations can be written as

$$[\mathbf{A}]\{\dot{y}\} + [\mathbf{B}]\{y\} = \{0\} \tag{4.30}$$

and

$$[\mathbf{A}]^T\{\dot{y}\}' + [\mathbf{B}]^T\{y\}' = \{0\} \tag{4.31}$$

Assuming a solution in the form

$$\{y\} = \{\overline{y}\}\exp(\lambda t) \tag{4.32}$$

where $\{\overline{y}\}$ is the vector of displacement amplitudes and $\lambda = j\omega$ is the frequency of harmonic vibrations and $j = \sqrt{-1}$. Substituting equation (4.32) into (4.30) and (4.31), one can write

$$(\lambda_i[\mathbf{A}] + [\mathbf{B}])\{\mathbb{R}_i\} = 0 \tag{4.33}$$

and

$$\left(\lambda_i[\mathbf{A}]^T + [\mathbf{B}]^T\right)\{\mathbb{L}_i\} = \{0\} \tag{4.34}$$

where $\lambda_i = \pm\, j\omega$ denotes the i^{th} eigenvalue associated with right hand and left hand eigenvector $\{\mathbb{R}_i\}$ and $\{\mathbb{L}_i\}$, respectively. For symmetric $[\mathbf{A}]$ and $[\mathbf{B}]$, the eigenvectors $\{\mathbb{R}_i\}$ and $\{\mathbb{L}_i\}$ are equal, otherwise $\{\mathbb{R}_i\}$ and $\{\mathbb{L}_i\}$ are distinct.

Let $[\mathbb{R}]$ and $[\mathbb{L}]$ denote the complex modal matrices of the differential operators of equations (4.33) and (4.34), respectively. Introducing the transformation [73]

$$\{y\} = [\mathbb{R}]\{u\} \tag{4.35}$$

where $\{u\}$ is the vector of modal co-ordinates. If only a subset of significant modes are to be retained, the truncated modal form of the equations of motion can be written as

$$[\mathbb{L}]^T[\mathbf{A}][\mathbb{R}]\{\dot{u}\} + [\mathbb{L}]^T[\mathbf{B}][\mathbb{R}]\{u\} = [\mathbb{L}]^T\{\mathcal{F}\} \tag{4.36}$$

or, simply as

$$[\mathbf{A}_r]\{\dot{u}\} + [\mathbf{B}_r]\{u\} = \{\mathcal{F}_r\} \tag{4.37}$$

in which

$$[\mathbf{A}_r] = [\mathbb{L}]^T[\mathbf{A}][\mathbb{R}] \tag{4.38}$$

$$[\mathbf{B}_r] = [\mathbb{L}]^T[\mathbf{B}][\mathbb{R}] \tag{4.39}$$

$$\{\mathcal{F}_r\} = [\mathbb{L}]^T\{\mathcal{F}\} \tag{4.40}$$

where $[\mathbb{R}]$ and $[\mathbb{L}]$ contain only those complex eigenvectors that represent a subset of selected modes. Equation (4.36) represents the Complex Reduced Order Model (CROM) using complex mode reduction.

Equations (4.23) and (4.36) represent truncated models using planar and complex modal transformations, respectively. In general, a subset of eigenvectors which spans the frequency spectrum of the forcing function are retained as significant modes. Deciding on which modes to retain is not clear in most situations of dynamic response analysis. As a minimum requirement the retained modes must span the low-frequency subsystem in addition to any higher modes spanned by the frequency spectrum of the forcing function.

Chapter 5

Results and Discussions

A computer program has been developed for the implementation of the present finite element model. Solutions of the eigenvalue problem and modal reduction schemes discussed in chapters 4 and 5 are provided. Numerical investigation is performed through a comparative study of the effect of all factors that are contributing into the dynamic characteristics of the present model.

The developed model is valid for any doubly symmetric cross-section and can be used for both hollow or solid cross-sections. It is also valid for many combinations of boundary conditions including clamped clamped, clamped-free, clamped hinged, simply supported, hinged free and free free end beam.

The introduction of taper makes the principal flexural rigidities of the beam unequal except at the root for square and circular cross-sections. When such a tapered beam has a setting angle, coupling occurs between the bending motions in the two mutually perpendicular (xy)- and (xz)- planes containing the y- and z- axes of the cross-section. Such a beam with no setting angle has two independent flexural frequencies about its principal axes which are dependent on the width to depth ratio of the cross-section. Throughout this analysis, the width of the beam is considered larger than its depth. Consequently, the beam is considered to vibrate along its most flexible (xy)-plane and the frequencies of vibration are estimated by considering the ratio of the radius of gyration to the beam length (r_{gy}/L). The separate effects of width taper (or depth taper) as well as the separate effects of pre-cone or the setting angle are considered. The combined effects of the previous complicated factors on the modal characteristics of the rotating tapered Timoshenko beam are also dealt with.

The rotation of the cross-section of the beam with a setting angle ψ does couple the in-plane and out-of-plane motion and deformations. In this case, one cannot distinguish these two modes from each other. When in-plane and out-of-plane displacement variables are coupled, the modes

will not have a simple interpretation. That is, one may be mostly in-plane with a bit of out-of-plane. Depending on the size of deformation in different planes one would be only able to say if the in-plane or the out-of-plane vibration, at this frequency is dominant. In this case, there is no pure in-plane or out-of-plane vibration mode. However, torsion is also coupled with the bending modes through Coriolis effects.

The approach followed in this study is to push the parameter range of values to their (physically possible) limits, so that one can understand to what extent the vibration characteristics are affected. Solutions are given for various cases, in which each parameter is considered alone, as well as combined effects of other factors. In addition, these effects are examined and a variety of simulation results are presented both in tabular and graphical forms. Because results for rotating three dimensional tapered Timoshenko beams including the effects of hub radius, pre-cone and setting angle as well as Coriolis effects are not widely spread in the literature, several special cases which represent degenerate cases of this model were examined to verify and validate the present scheme. Comparisons with the available results in the literature are made wherever possible.

5.1 The Computer Scheme

The present computational scheme carries out the following tasks:

- Generates and assembles the system matrices of the model.
- Evaluates the modal characteristics.
- Implement the desired modal reduction schemes; either Planar Reduction Order Model (PROM) or Complex Reduction Order Model (CROM) to generate the reduced order matrices.
- Integrates the reduced models forward in time to predict the system's time response.

A flow chart of the developed scheme is presented in Figure 5-1.

5.1.1 Input Data

The input data related to the present computer scheme is generated in a separate subroutine. The beam is discretized into a number of finite elements where the material and geometrical properties of each element must be defined.

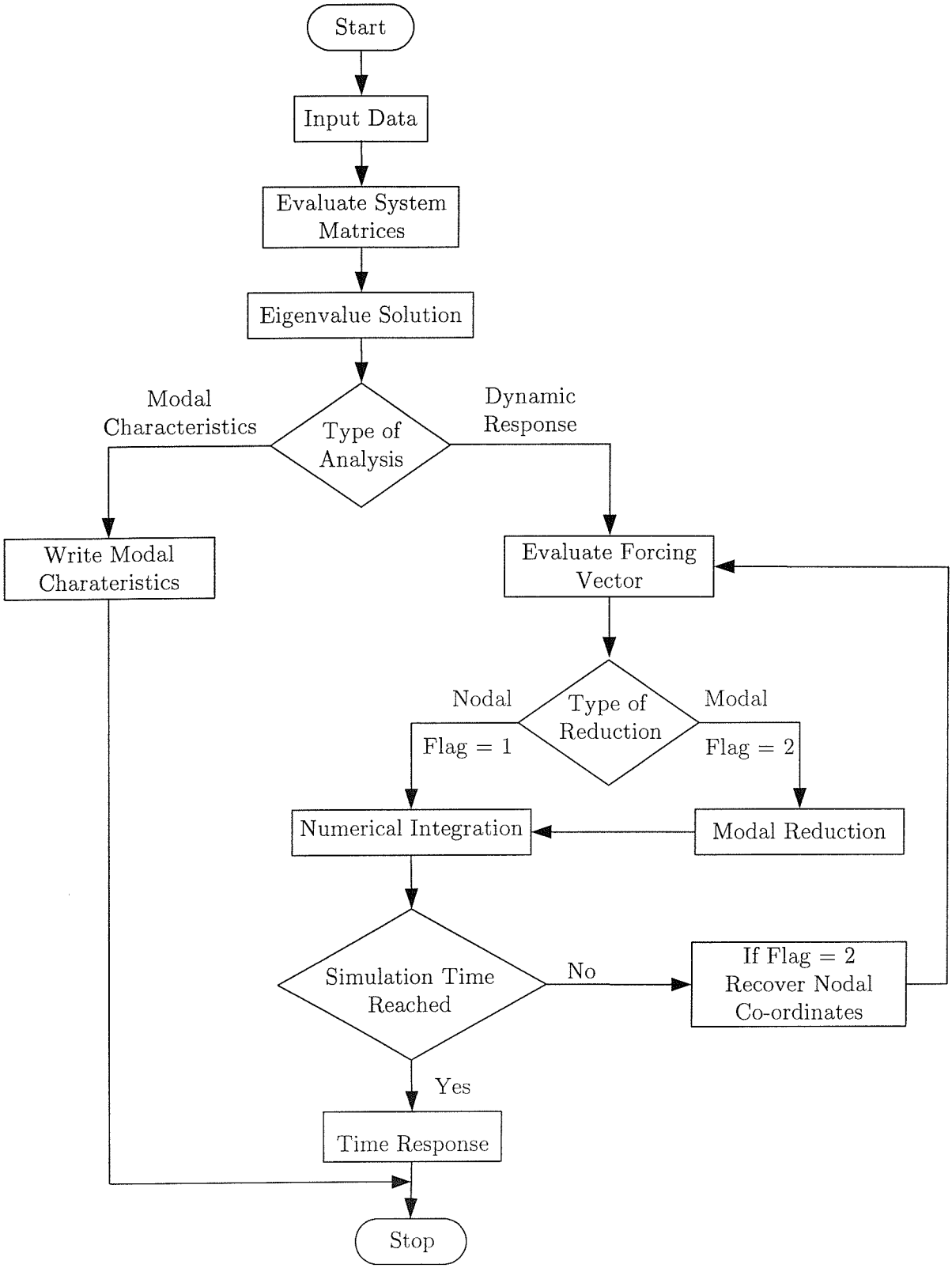

Figure 5-1: The flow chart for the computer scheme.

- **Element Properties**: The two types of element properties that need to be specified for each element are

  - The geometrical properties include element length, breadth and depth, taper ratios in y and z-directions and slenderness ratios and the shear correction factors that depend on the shape of the cross-section. If the taper ratios are zero this corresponds to a uniform beam. When the taper ratios are unity this corresponds to the case of perfect cone for circular cross-section and a pyramid for rectangular cross-section.
  - The material properties include the mass density ρ, Young's modulus of elasticity E, and shear modulus G. The case of Rayleigh beam can be obtained by neglecting shear factors κ_y and κ_z. This implies neglecting the shear stiffness matrices $\left[\overline{k}^i_{s,v}\right]$ and $\left[\overline{k}^i_{s,w}\right]$. The case of Euler-Bernoulli beam can be obtained by neglecting the rotary inertia mass matrices $\left[\overline{m}^i_{r,v}\right]$ and $\left[\overline{m}^i_{r,w}\right]$ in addition to ignoring the shear factors κ_y and κ_z and the shear stiffness matrices $\left[\overline{k}^i_{s,v}\right]$ and $\left[\overline{k}^i_{s,w}\right]$.

- **Type of Analysis**: There are two types of analysis modal analysis and dynamic response analysis.

  - **Modal Analysis**: In this case one must specify wether planar or complex modal characteristics are required as well as the number of eigenvalues and eigenvectors to be retained in the truncation process.
  - **Dynamic Response Analysis**: In this analysis, the user must specify whether the equations of motion are generated in terms of nodal or modal coordinates. If nodal coordinates are chosen, the user must indicate the number of significant modes to be retained and specify whether a planar or complex modal reduction scheme is required for the dynamic response analysis. In either case of the dynamic simulation, however, the simulation time must be specified.

5.1.2 System Matrices

The explicit expressions for the elemental mass, stiffness, Coriolis and quadratic velocity terms matrices are derived in parametric form where all the parameter changes are accounted for. They are presented in Tables C1 to C17 of Appendix C. The elemental mass, stiffness and Coriolis matrices are invariant and can be evaluated once in advance in dynamic analysis while the inertia terms matrices are implicitly time dependent since they are function of the generalized coordinates thus resulting in an inertia variant model.

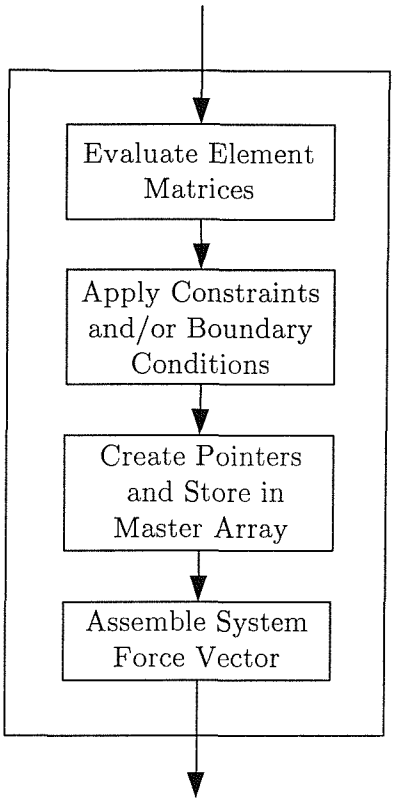

Figure 5-2: The control flow diagram for evaluating the system matrices.

The exact expressions of these matrices have the computational advantage of eliminating the loss of computer time and round-off errors associated with extensive matrix operations required for their numerical evaluation. The boundary conditions are applied and the matrix entries are stored in a master array for assigning pointers for every entry. Elemental matrices for all elements are evaluated and stored in a master array. Pointers created are used to assemble the system matrices. The control flow chart for creating system matrices is shown in Figure 5-2.

5.1.3 Eigenvalue Solution

The presence of the Coriolis matrix in the system equations of motion makes the associated eigenvalue problem deviate from the standard one and conventional modal analysis is not applicable in this case. Therefore, the system matrices contributing into the equations of motion of the rotating beams are arranged in a state space form as defined in Chapter 4 to transform the equations of motion from second order differential equations to first order differential equations. The corresponding eigenvalue problem associated with this formulation is then defined and solved using EISPACK routines.

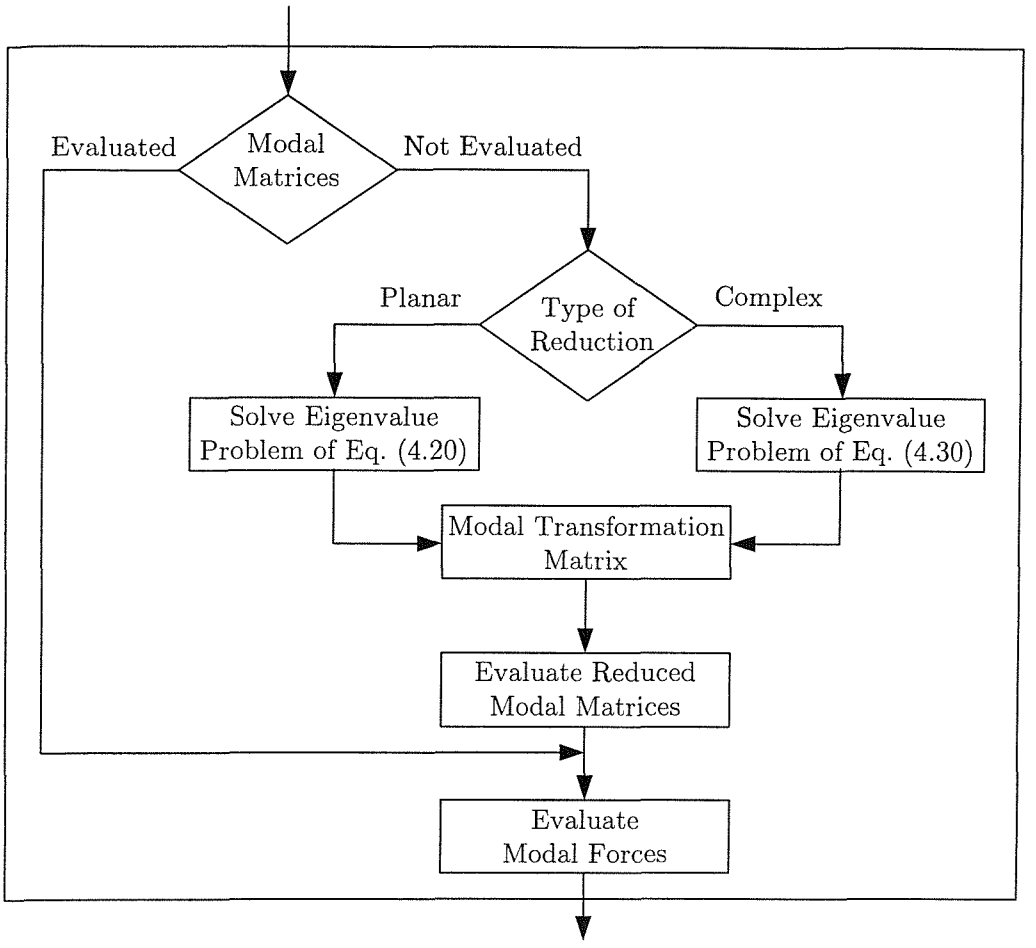

Figure 5-3: The control flow diagram for the implementation of the modal reduction scheme.

5.1.4 Modal Reduction Schemes

Planar and complex reduction schemes are implemented. Modal transformation matrices are built up of subset of selected eigenvectors. The subset of eigenvectors are selected such that the reduced modal matrices span the lower or significant part of the frequency spectrum of the system. The complex reduction scheme is numerically difficult to implement. The entries of the modal transformation matrix are complex which implies that the reduced modal equations have complex coefficients. Considerable programming effort of the resulting complex modal equations is required. Numerical integration of complex modal equations is also time consuming.

Using the planar modal reduction alleviates the difficulties encountered in the complex modal transformations. In planar modal reduction, the planar modes obtained from equation (4.20) are used to reduce the order of equations of motion. The reduced order equation of motion, equation (4.23) has real coefficients. The control flow diagram showing the implementation of the modal reduction scheme is shown in Figure 5-3.

5.1.5 Numerical Integration

The reduced order modal equations are integrated forward in time to predict the time response. The equations of motion are arranged such that the inertia terms are kept on the right hand side along with the external forcing term. In this way, the coefficient matrices of the equations of motion are constant whereas the forcing vector becomes a function of time. Therefore, the forcing vector needs to be updated at every time step. The inertia terms for the whole system is assembled from the elemental inertia matrices. Accordingly the forcing vector for the whole system is updated at every time step. The assembly procedure has to be implemented at every time step which makes the numerical calculation of the forcing term time consuming. At the end of each numerical integration step, the modal co-ordinate vector is computed. The nodal co-ordinates can be recovered using modal transformations. The computed nodal co-ordinate vector is associated with the system matrix. The control flow diagram for the evaluation of the forcing vector is shown in Figure 5-4.

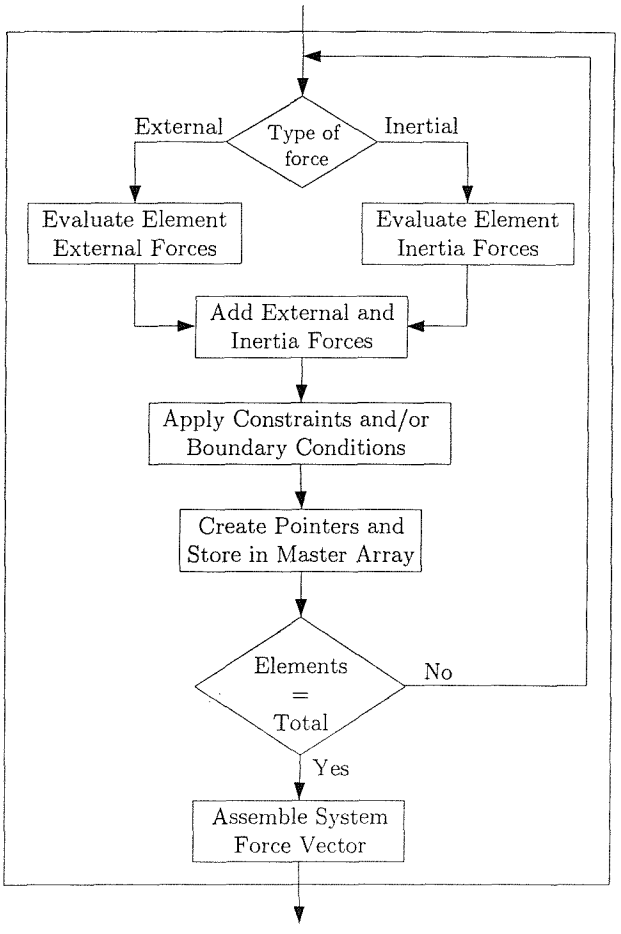

Figure 5-4: The control flow diagram to compute the time dependent forcing vector.

5.2 Modal Characteristics

This section is divided into two subsections. In the first one, the natural frequencies are obtained with no reduction in both graphical and tabular form for a wide range of parameter changes. Wherever possible, the numerical predictions are compared with analytical and other numerical results available in the literature in order to validate the present model.

In the second subsection, the natural frequencies are obtained by using the Planar Reduced Order Model (PROM) and the Complex Reduced Order Model (CROM). These modal reduction schemes will be compared to the natural frequencies of the Full Order Model (FOM).

5.2.1 Validation of the Model

Many examples that represent some special cases of the proposed model are presented. These cover ranges from the simplest case of the non-rotating Euler-Bernoulli beam to the other complicating factors such as taper ratios, pre-cone angle, setting angle, rotary inertia, shear deformation and Coriolis forces. The contribution of these complicating factors is shown and discussed in various examples.

The stiffening effect that is due to the hub rotation, has been introduced as early as 1920 by Lamb and Southwell [3] and refined later by Southwell and Gough [4]. The bending frequency of the i^{th} mode of a rotating beam may be also obtained from the Southwell relation, with knowledge of the non-rotating frequency, the speed of rotation and Southwell coefficient. Therefore, the first four SC's are computed including a wide range of parameter variations. This relationship is very useful not only for its simplicity and rapid estimation for the predictions of the frequencies of rotating beams but also for its accuracy. Because of its importance and practical use in the interpretation of results, the stiffening effect along with Southwell relation will be discussed in a separate subsection.

Unless otherwise stated, the beams considered for this analysis have rectangular cross-sections and are made of steel. In addition, Coriolis forces are included throughout this investigation unless otherwise stated. The material and geometrical properties for the beams used throughout this investigation are summarized in Table 5.1.

To illustrate the relationship between the number of elements in a consistent mass finite element formulation and the accuracy of the predicted frequencies, Tables 5.2 and 5.3 have been provided. It can be seen that the accuracy of the present predictions is increased by increasing the number of elements for both Euler-Bernoulli and Timoshenko beams. Convergence to the exact solution is reached by using 12 elements for Euler-Bernoulli beam and 16 elements for

Table 5.1: Material and geometric properties for Euler-Bernoulli and Timoshenko beam

Property	Value
Density, ρ	7850 kg/m^3
Modulus of elasticity, E	200 GPa
Shear modulus, G	77 GPa
Shear factors, $\kappa_y = \kappa_z = \kappa$	5/6
Ratio (r_{gy}/L)	0.02
Total length of the beam, L	1.00 m for Euler-Bernoulli beam 0.72 m for Timoshenko beam
Number of elements	12 for Euler-Bernoulli beam 16 for Timoshenko beam

Table 5.2: Convergence of the present finite element model for the prediction of planar frequency parameters of rotating uniform cantilever Euler-Bernoulli beam for which $\overline{\Omega} = 6$, $\psi = \phi = 0°$, $R = 0$, Coriolis effects not included

No. of elements	λ_{E1}	λ_{E2}	λ_{E3}	λ_{E4}	λ_{E5}
2	7.3758407	27.044483	79.585624	220.829347	–
4	7.3616947	26.833695	67.129080	127.956538	233.024394
6	7.3606511	26.814435	66.789830	126.888280	208.175403
12	7.3603910	26.809436	66.691143	126.194986	205.497038
Ref. [16]	7.3603730	26.809082	66.683914	–	–

Table 5.3: Convergence of the present finite element model for the prediction of planar frequency parameters of rotating uniform cantilever Timoshenko beam for which $\kappa = 5/6$, $(r_{gy}/L) = 0.02$, $\overline{\Omega} = 6$, $\psi = \phi = 0°$, $R = 0$, Coriolis effects not included

No. of elements	λ_{T1}	λ_{T2}	λ_{T3}	λ_{T4}	λ_{T5}
2	7.361543	26.704330	77.794234	208.980474	–
4	7.342985	26.422381	64.676878	120.054582	220.127038
8	7.337866	26.307245	63.629050	116.351130	183.079204
16	7.335643	26.251373	63.230271	114.651687	177.891752
Ref. [85]	7.3319	26.2488	63.2386	114.5177	–

Timoshenko beam. These results [1] are in excellent agreement when compared to other methods of solution, namely those presented by Wright *et al.* [16] and Nagaraj [85]. It is well known that a consistent mass finite element formulation produces upper bounds to all frequencies as depicted by Tables 5.2 and 5.3. For example, a two element model produces upper bounds to the first and second exact frequencies. The fundamental and second frequencies of the two element model are quite accurate while the third frequency and higher are too high to be of any use.

5.2.2 Natural frequencies

Euler-Bernoulli Beam

Example 1: Non-rotating uniform cantilever beam

Consider the simplest case of a non-rotating prismatic cantilever beam with doubly symmetrical cross-section. The material and geometrical properties outlined in Table 5.4 are provided by Hatch [89]. The present results were obtained by considering 10 equal finite beam elements and are in very good agreement when compared to other numerical and theroretical ones, namely those of reference [89]. The error, between the present estimations f_E, and the theoretical values f_{th} reported in reference [89], for the first sixth modes is quite small, with the maximum error (for the sixth mode) being only 0.5%.

Table 5.4: Planar flapping frequencies f_E expressed in Hertz for a non-rotating cantilever prismatic Euler-Bernoulli beam for which $b_o = 2$ mm, $h_o = 0.2$ mm, $L = 20$ mm, $E = 190$ GPa and $\rho = 7830$ kg/m^3

Mode No.	Present work	Ref. [89]			% Error
		MATLAB	ANSYS	Theoretical	
	f_E	f_E	f_E	f_{th}	$\frac{f_{th} - f_E}{f_{th}} \times 100$
1	397.874912	397.88	397.86	397.874572	−0.0000
2	2493.519911	2493.60	2493.20	2493.437382	−0.0330
3	6983.474461	6984.50	6982.20	6981.696870	−0.0255
4	13694.377072	13703.00	13696.00	13681.339375	−0.0953
5	22673.244501	22727.00	22705.00	22616.234285	−0.2520
6	33967.098741	34194.00	34145.00	33784.737868	−0.5398

[1] For purposes of validation and comparison only, six digits after the decimal point are retained.

Example 2: Effect of taper on non-rotating uniform cantilever beam

The effect of taper is important to the dynamic behavior and modal characteristics of rotating beams for which a specified distribution of strength/weight ratio is required for optimum performance and design criteria in many structures.

Results pertinent to tapered beams are not widely available in the literature, as is the case for uniform beams. However, it has been found that Downs [81], using analytical solutions, could only produce results for non-rotating tapered Euler-Bernoulli and Timoshenko beams. For Euler-Bernoulli beam, he used equal taper ratios while for Timoshenko beam he used a wide range of unequal tapers. Some of Downs's [81] results including the lowest five flapping modes are reproduced in Table 5.5 for the non-rotating case of the doubly tapered beam but including equal tapering in two directions. Again, the present computed frequency estimates are in perfect agreement with those of Downs [81]. These results indicate that as the taper ratios increase all the frequencies decrease except for the fundamental one that exhibits a reverse trend.

Table 5.5: Effect of taper on planar flapping frequency parameters for a non-rotating cantilever Euler-Bernoulli beam

Mode No.	$\nu_y = \nu_z \longrightarrow$	0.2	0.4	0.5	0.6	0.8
1	Present work	3.85512	4.31878	4.62515	5.00904	6.19639
	Ref.[81]	3.84642	4.31738	4.62554	5.00906	6.19634
2	Present work	21.0571	20.0503	19.5479	19.0653	18.3859
	Ref.[81]	21.0569	20.0499	19.5476	19.0649	18.3885
3	Present work	56.6372	51.3411	48.5853	45.7448	39.8403
	Ref.[81]	56.6303	51.3346	48.5789	45.7384	39.8336
4	Present work	109.8135	98.0511	91.8573	85.3870	71.2834
	Ref.[81]	109.7630	98.0050	91.8128	85.3438	71.2418

Table 5.6 shows also the effect of taper on non-rotating Euler-Bernoulli beam but for a complete wedge ($\nu_y = 0.0$, $\nu_z = 1.0$) and a cone ($\nu_y = \nu_z = 1.0$). Comparison of these predictions with those reported in reference [84] reveals a very good agreement. It is clearly shown that the frequencies for a cone are higher than those of a wedge. The ratio of the frequency parameter of the cones to those of the wedge is 1.60 for the first mode and decreases to 1.21 for the fourth mode.

Table 5.6: Planar flapping frequency parameters for non-rotating Euler-Bernoulli cantilever wedge and cone

Mode No.	Wedge ($\nu_y = 0.0,\ \nu_z = 1.0$) (rectangular cross-section)		Cone ($\nu_y = \nu_z = 1.0$) (circular cross-section)	
	Present work	Ref. [84]	Present work	Ref. [84]
1	5.315100	5.315099	8.719263	8.719259
2	15.207484	15.207168	21.146477	21.145662
3	30.026883	30.019809	38.466154	38.463771
4	49.827203	49.763345	60.771255	60.680139

Example 3: Effect of spin and hub radius parameters on uniform cantilever beam

Table 5.7 depicts numerical predictions for the first three lowest frequency parameters of a uniform cantilever beam for various values of spin and hub radius parameters while setting all other parameters to zero. Comparison of these results with the ones obtained by Hodges and Rutkowski [15] indicates an excellent agreement achieved by the FEM solution. From these results it can be concluded that flapping frequency parameters increase as the spin and/or thehub

Table 5.7: Planar flapping frequency parameters for rotating cantilever uniform Euler-Bernoulli beam, $\psi = \phi = 0°$, Coriolis effects not included

$\overline{\Omega}$		λ_{E1}		λ_{E2}		λ_{E3}	
		$R = 0.0$	$R = 1.0$	$R = 0.0$	$R = 1.0$	$R = 0.0$	$R = 1.0$
0.0	Present work	3.516017	3.516017	22.034845	22.034845	61.704878	61.704878
	Ref. [15]	3.516015	3.516015	22.034492	22.034492	61.697214	61.697214
2.0	Present work	4.137321	4.833691	22.615267	23.366382	62.280778	63.075058
	Ref. [15]	4.137319	4.833688	22.614922	23.366042	62.273184	63.067548
4.0	Present work	5.585006	7.475069	24.273684	26.957642	63.974180	66.994039
	Ref. [15]	5.585001	7.475048	24.273349	26.957262	63.966760	66.986772
8.0	Present work	9.256886	13.507646	29.995821	37.954996	70.300100	80.537971
	Ref. [15]	9.256837	13.507389	29.995382	37.953793	70.292962	80.529532
12.0	Present work	13.170361	19.722659	37.604042	51.073973	79.622192	98.541126
	Ref. [15]	13.170150	19.721542	37.603112	51.070134	79.614478	98.526797

radius parameters increase. Since the centrifugal stiffness matrix is a function of the square of the spin and hub radius parameters, it results that the stiffness of the beam increases as these factors increase; thus rendering the beam stiffer. This phenomenon is usually referred to as the stiffening effect of rotation.

Example 4: Effect of spin and hub radius parameters on uniform hinged free beam

In Table 5.8 are shown the first three planar flexural frequency parameters for the previous beam but for hinged free end conditions. These results are in excellent agreement with those of Wright *et al.* [16] who used a power series solution in the form of Frobenius method. As expected, for zero hub radius, this type of boundary conditions allows a rigid body flapping mode whose frequency is equal to the speed of hub rotation as manifested by Table 5.8. For non-rotating beams, there also exists a rigid body mode. For zero hub radius and non-zero spin parameter, the fundamental frequency parameter is exactly equal to the spin parameter. Further, for rotating beams with non-zero hub radius parameter, the fundamental frequency does not represent a rigid body mode. Similar to the previous example, it can be seen here that for the hinged-free end conditions, the flapping frequency parameters also exhibit a stiffening effect.

Table 5.8: Planar flapping frequency parameters for rotating hinged-free Euler-Bernoulli beam, $\psi = \phi = 0°$, Coriolis effects not included

$\overline{\Omega}$		λ_{E1}		λ_{E2}		λ_{E3}	
		$R = 0.0$	$R = 1.0$	$R = 0.0$	$R = 1.0$	$R = 0.0$	$R = 1.0$
0.0	Present work	0.0	0.0	15.4183	15.4183	49.9689	49.9689
	Exact, Ref. [16]	0.0	0.0	15.4182	15.4182	49.9649	–
2.0	Present work	2.0	3.1586	16.2262	17.3180	50.6800	51.7108
	Exact, Ref. [16]	2.0	3.1586	16.2261	17.3179	50.6760	–
4.0	Present work	4.0	6.3056	18.4314	21.9898	52.7502	56.5699
	Exact, Ref. [16]	4.0	6.3056	18.4313	21.9897	52.7463	–
8.0	Present work	8.0	12.5864	25.3436	34.5374	60.2547	72.3698
	Exact, Ref. [16]	8.0	12.5865	25.3436	34.5373	60.2513	–
12.0	Present work	12.0	18.8665	33.7604	48.3573	70.8405	92.0391
	Exact, Ref. [16]	12.0	18.8665	33.7603	48.3572	70.8373	–

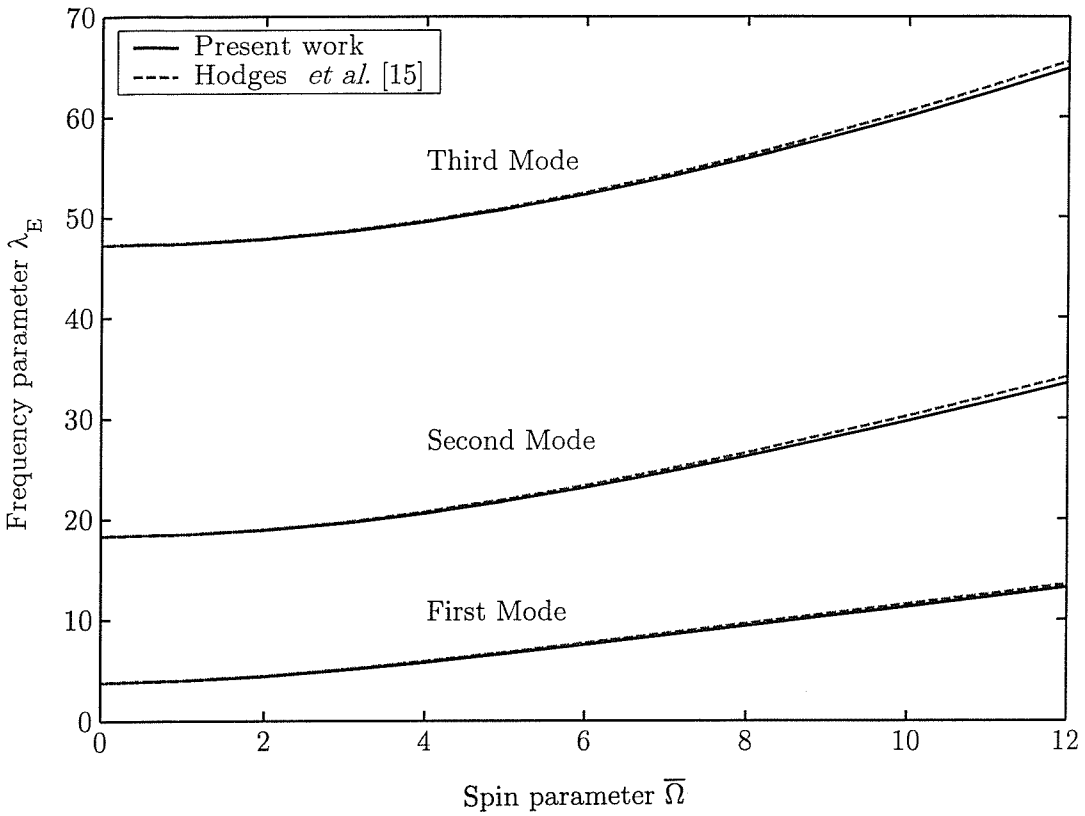

Figure 5-5: Frequency parameter for rotating tapered Euler-Bernoulli beam, $\nu_y = 0.0$ (uniform), $\nu_z = 0.5$, Coriolis effect not included.

Example 5: Effect of taper on rotating Euler-Bernoulli beam

Results showing the effect of tapering on the frequency parameters of rotating Euler-Bernoulli beams using other methods of solutions could not be found in the literature except those reported by Hodges and Rutkowsky [15]. Predictions of simulation showing tapering effect (taper in the depth direction only $\nu_z = 0.5$) on the frequency parameters for rotating Euler-Bernoulli beam are shown in Figure 5-5 along with those of Hodges and Rutkowsky [15]. From this figure it can be concluded that the present results are in a very good agreement with those reported in reference [15].

Example 6: Effect of pre-cone angle on rotating uniform beam

Pre-cone is another design solution that satisfy aerodynamic requirements. It alleviates the large blade flapping bending problem. In order to give insight to the effect of varying the pre-cone on the frequency parameters of an Euler-Bernoulli beam with zero setting angle, the eigenvalue problem was solved for a rotational speed ratio of $\left(\overline{\Omega}/\lambda_{E_o}\right) = 1.0$ where λ_{E_o} denotes the flapping

frequency parameter of a non-rotating uniform Euler-Bernoulli beam and is equal to 3.51602. The results of simulation shown in Table 5.9 are compared to those of Subrahmanyam an Kaza [45] who used the Galerkin method. The percentage difference between the present predictions and those of reference [45] has been calculated and found to be negligible. Therefore, it can be concluded that the two methods of solutions produce very similar results. Pertinent to these numerical facts, it can be concluded that for a given spin parameter and thickness ratio, the flapping mode frequencies decrease with increasing pre-cone. This may be attributed to the fact that as the pre-cone increases, the arm $\left(\mathcal{R}_o + r_P^i \cos\phi\right)$ associated to the centrifugal force decreases. This arm reaches its maximum $\left(\mathcal{R}_o + r_P^i\right)$ for $\phi = 0°$ and its minimum $\mathcal{R}_o$ for $\phi = 90°$. On the other hand, it can be seen that when the pre-cone increases from 10° to 30°, the percent decrease in the frequency values is 3.27% for the first mode, 0.85% for the second mode, and 0.32% for the third mode. The influence of the pre-cone is clearly seen to be of significance on the fundamental mode and is negligible on higher ones. The reason for this is attributed to the fact that the softening term $\Omega^2 \sin\psi \cos\phi \sin(\psi + \phi)$ is constant regardless of the mode considered therefore; it has more influence on modes with small frequency values. This phenomenon is called a softening effect that counteract the stiffening one for rotating beams.

Table 5.9: Effect of pre-cone on the flapping frequency parameters of rotating uniform cantilever Euler-Bernoulli beam, $R = 0$, $\psi = 0°$, $(h_0/b_0) = 0.05$, and $\left(\overline{\Omega}/\lambda_{E_o}\right) = 1.0$, Coriolis effects included

ϕ	Mode No.	Present work	Ref. [45]	% Error
0°	1	$0 \pm 5.1915i$	-	-
	2	$0 \pm 23.7835i$	-	-
	3	$0 \pm 63.4661i$	-	-
10°	1	$0 \pm 5.1704i$	5.1713	-0.01
	2	$0 \pm 23.7573i$	23.7553	0.01
	3	$0 \pm 63.4346i$	63.4246	0.01
20°	1	$0 \pm 5.0015i$	4.9749	0.05
	2	$0 \pm 23.6811i$	23.6709	0.04
	3	$0 \pm 63.3563i$	63.3234	0.05
30°	1	$0 \pm 5.0015i$	4.9749	0.53
	2	$0 \pm 23.5562i$	23.5282	0.12
	3	$0 \pm 63.2282i$	63.1612	0.11

Example 7: Coriolis effects on rotating uniform beam

The effect of rotation on the bending frequencies of the above rotating pre-coned uniform Euler-Bernoulli beam has also been examined for a wide range of speed ratio $(\overline{\Omega}/\lambda_{E_o})$ for the case where the Coriolis effects are accounted for. The results shown in Table 5.10 are in perfect agreement with those of Subrahmanyam an Kaza [45]. From these results, it can be concluded that for a given pre-cone, the frequencies increase as the spin ratio increases as expected. This is also in agreement with the stiffening effect discussed in the previous examples. From the predictions shown it can be concluded that the Coriolis effects depress the frequency values in general. At low speed ratios however, as is the case in this example, the Coriolis effect is very small and therefore can be neglected.

Table 5.10: The first three lowest bending frequency parameters of rotating uniform Euler-Bernoulli beam, $\phi = 15°$, $\psi = 0°$, $R = 0$ $(h_o/b_o) = 0.05$, (Numbers between parentheses indicate that Coriolis effects are not included)

$(\overline{\Omega}/\lambda_{E_o})$	Mode No.	Present work		Ref. [45]		% Error
0.3	1	$0 \pm 3.6937i$	(3.6937)	3.6804	(3.7062)	0.36
	2	$0 \pm 22.1920i$	(22.1920)	22.1860	(22.2934)	0.03
	3	$0 \pm 61.8548i$	(61.8549)	61.8475	(62.1044)	0.02
0.5	1	$0 \pm 3.9893i$	(3.9893)	3.9652	(3.9950)	0.61
	2	$0 \pm 22.4692i$	(22.4692)	22.4572	(22.5585)	0.05
	3	$0 \pm 62.1300i$	(62.1301)	62.1169	(62.3354)	0.03
1.0	1	$0 \pm 5.1439i$	(5.1439)	5.1444	(5.1781)	−0.01
	2	$0 \pm 23.7254i$	(23.7255)	23.7203	(23.7926)	0.02
	3	$0 \pm 62.7949i$	(62.7949)	62.7763	(62.8837)	0.03
2.0	1	$0 \pm 8.2153i$	(8.2153)	8.3777	(8.3385)	−1.97
	2	$0 \pm 28.1929i$	(28.1929)	28.3037	(28.3445)	−0.39
	3	$0 \pm 67.5191i$	(67.5193)	68.0724	(68.0883)	−0.82

Timoshenko Beam

The effects of shear deformation and rotary inertia become of particular importance if the cross-sectional dimensions of the beam are not small when compared to its length and if higher bending modes are required.

Example 1: Effect of shear deformation and rotary inertia on cantilever uniform beam

Because the literature lacks sufficient information to adequately reproduce the same results based on Timoshenko beam theory, the following material properties for steel are used to reproduce the results obtained by Downs [81]. Poisson's ratio $\nu = 0.3$, and shear correction factor $\kappa = 0.85$ for rectangular cross-section. These results were obtained by using 16 finite Timoshenko beam elements and cover a range for which (r_{gy}/L) varies from 0.01 to 0.1. In Table 5.11, the four lowest flapping frequencies for a non-rotating uniform cantilever Timoshenko beam are compared with those obtained by Downs [81]. Natural frequencies in reference [81] were computed from analytical solutions by means of Bessel functions. Again the agreement between the present predictions and those of reference [81] is seen to be excellent. Compared to the previous results of the non-rotating Euler-Bernoulli beam $(\overline{\Omega} = 0)$ depicted in Table 5.7, these frequencies show that the shear deformation and rotary inertia tend to lower the frequencies of oscillation. It is seen also that their effects is more pronounced for beams with higher values of (r_{gy}/L) and has more influence at higher modes as would be expected. Moreover, it can be concluded that as the ratio (r_{gy}/L) increases a decrease in natural frequencies is seen for all modes.

Table 5.11: Planar frequency parameters of non-rotating uniform cantilever Timoshenko beam for $R = 0$, $\psi = \phi = 0°$

	(r_{gy}/L)	0.01	0.02	0.05	0.08	0.1
λ_{T1}	Present work	3.51279	3.50285	3.43429	3.31907	3.22381
	Ref.[81]	3.51270	3.50284	3.43643	3.32405	3.23093
λ_{T2}	Present work	21.89920	21.48205	19.08092	16.19539	14.42662
	Ref.[81]	21.8910	21.4805	19.1391	16.2890	14.5309
λ_{T3}	Present work	60.82010	58.27917	46.59630	36.52280	31.49168
	Ref.[81]	60.7548	58.1980	46.7510	36.70780	31.6707
λ_{T4}	Present work	117.84800	109.70562	79.19250	58.19272	48.06992
	Ref.[81]	117.564	109.180	79.2392	58.2788	48.2281

The percentage difference between Euler-Bernoulli and Timoshenko beam frequencies is shown in Figure 5-6 as a function of the ratio (r_{gy}/L). This comparison includes the first four frequency parameters and covers a wide range for which $0.01 \leq (r_{gy}/L) \leq 0.1$. From these

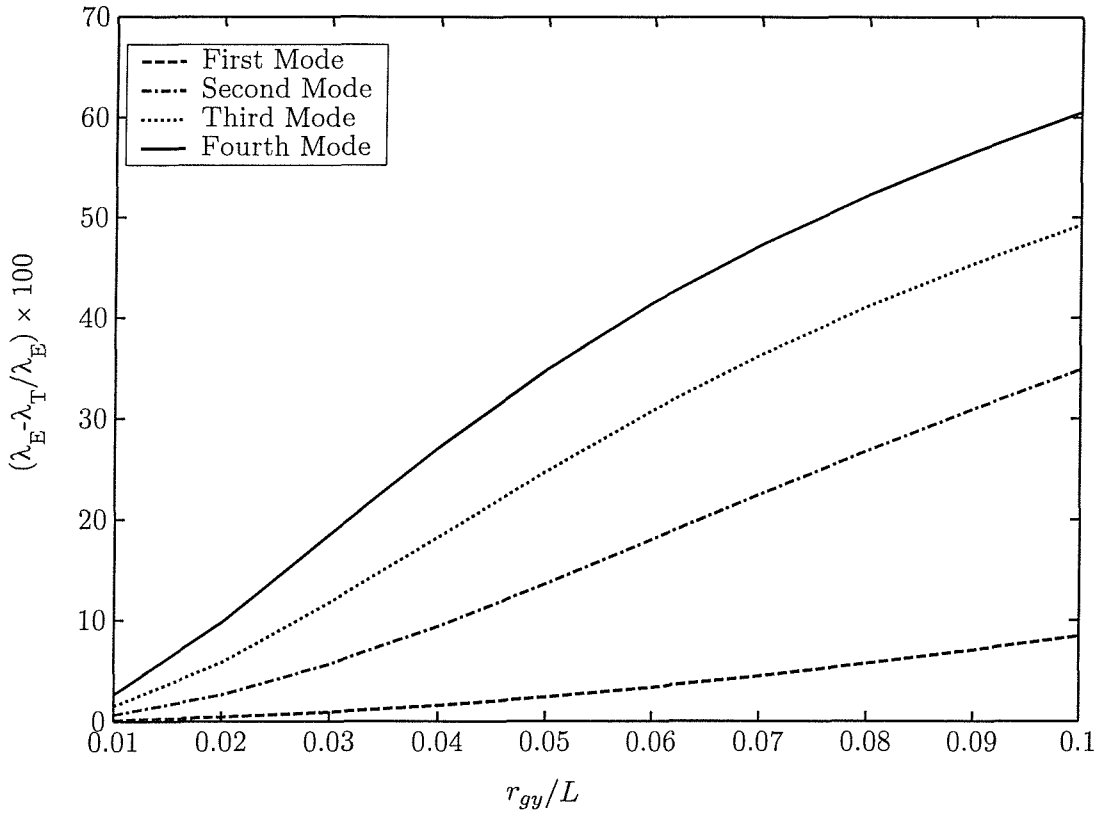

Figure 5-6: Percentage difference in frequency values between EBT and TBT as a function of (r_{gy}/L) for non-rotating beams.

predictions, it can be seen that as the ratio (r_{gy}/L) increases, the beam becomes thicker, resulting in a percentage decrease of the frequency values. For instance, the percentage difference for the case of $(r_{gy}/L) = 0.01$ is insignificant when compared to the case of $(r_{gy}/L) = 0.1$. Further, the shear deformation and rotary inertia effects can clearly be seen to be more pronounced at higher modes as mentioned in the above discussion. For example for a very thick beam with $(r_{gy}/L) = 0.1$, the percent decrease for the first mode is 8.3% while for the second, third and fourth mode it is 34.5%, 48.9% and 60%, respectively which is quite significant.

Example 2: Effect of slenderness ratio and rotation on cantilever uniform beam

In this example, the effect of varying the slenderness ratio along with the spin rotation on the fundamental frequency parameter λ_T of a uniform Timoshenko beam is examined. For purpose of comparison the geometrical and material properties heading Table 5.12 are taken from reference [23]. The hub radius, pre-cone and setting angle are set to zero. In Table 5.12 are shown the variations of the fundamental frequency parameter with respect to the slenderness

ratio (L/r_{gy}) for the non-rotating and rotating beam, respectively. The frequency parameter λ_E in the expression of Δ is taken to be 3.516016 for $\overline{\Omega} = 0$ and 6.449548 for $\overline{\Omega} = 5$. Again, the agreement between the present predictions and those of Lee and Kuo [23] is excellent for both rotating and non-rotating case. The frequency parameters for $\overline{\Omega} = 5$ are higher than those of the non-rotating beam due to the stiffening effect that is clearly seen to increase the frequency values for all slenderness ratios. On the other hand, it is worthwhile mentioning that as the slenderness ratio increases, the percentage difference Δ between Euler-Bernoulli beam and Timoshenko beam decreases, and it becomes zero when the slenderness ratio becomes very large[2] showing that TBT converges to EBT. In other words, as (L/r_{gy}) increases, the frequency parameters for Timoshenko beams are shown to increase until they reach the Euler-Bernoulli frequencies at very high slenderness ratio as shown in Table 5.12.

Table 5.12: Planar fundamental flapping frequency parameter λ_T for Timoshenko cantilever beam, $\rho = 7850$ kg/m^3, $E = 200$ GPa, $E/\kappa G = 3.059$,$\psi = \phi = 0°$, $R = 0$, $\lambda_E = 3.5160$ and $\Delta = \frac{\lambda_E - \lambda_T}{\lambda_E} \times 100\%$

$\left(\frac{L}{r_{gy}}\right)$	$\overline{\Omega} = 0$			$\overline{\Omega} = 5$		
	Present work λ_T	Ref. [23] λ_T	Δ	Present work λ_T	Ref. [23] λ_T	Δ
20	3.4331	3.4364	2.36	6.3275	6.3241	1.89
40	3.4947	3.4954	0.60	6.4171	6.4179	0.50
80	3.5108	3.5108	0.14	6.4416	6.4418	0.12
100	3.5128	3.5126	0.09	6.4446	6.4446	0.07
200	3.5153	3.5152	0.02	6.4484	6.4485	0.02
300	3.5157	3.5155	0.01	6.4491	6.4493	0.01
∞	3.5160	3.5160	0.00	6.4495	6.4497	0.00

Example 3: Effect of taper on non-rotating cantilever beam

Results showing the effect of taper on the frequency parameters of rotating Timoshenko beams using other methods of solutions could not be found in the literature except the few ones presented in a graphical form by Mulmule *et al.* [25] who used the FEM. However, it has been

[2]tends to ∞

found that Downs [82] using dynamic discretization technique could only produce results for non-rotating tapered Timoshenko beam where he used a wide range of unequal tapers. To study the effect of taper in Timoshenko beams some of Downs's predictions are reproduced in Table 5.13 for the three lowest flexural frequency parameters of the non-rotating Timoshenko beam including 8 combinations of unequal tapering in breadth and depth direction. As can be seen from these predictions, there is a very good agreement between the results obtained by the present model and the solution provided by Downs [82]. Similar to the case of Euler-Bernoulli beam, the numerical predictions show that as the taper ratio ν_y increases the thickness toward the tip becomes smaller which results in a decrease in mass and stiffness of the beam. Consequently, the frequency parameters for all modes increase as shown in Table 5.13. For the taper in the other direction, it is seen that the first mode preserves the same behavior while the second and the third modes exhibit a reverse trend.

Table 5.13: Planar flapping frequency parameters for non-rotating tapered Timoshenko cantilever beam, $(r_{gy}/L) = 0.08$, $\kappa = 0.85$, $R = 0$, and $\psi = \phi = 0°$

ν_y		λ_{E1}		λ_{E2}		λ_{E3}	
		$\nu_z = 0.3$	$\nu_z = 0.6$	$\nu_z = 0.3$	$\nu_z = 0.6$	$\nu_z = 0.3$	$\nu_z = 0.6$
0.0	Present work	3.4826	3.7601	15.5753	14.6154	34.6146	31.6762
	Ref. [82]	3.4869	3.7623	15.6411	14.6449	34.6625	31.6243
0.3	Present work	3.8487	4.1318	16.1132	15.1038	35.0760	32.1259
	Ref. [82]	3.8535	4.1339	16.1766	15.1297	35.1026	32.0582
0.6	Present work	4.4557	4.7477	16.9675	15.8892	35.8647	32.8618
	Ref. [82]	4.4611	4.7498	17.0229	15.9107	35.8346	32.7692
0.9	Present work	5.7774	6.0891	19.09381	17.9053	38.2554	34.9817
	Ref. [82]	5.7836	6.0927	19.1076	17.9264	37.9753	34.8498

Example 4: Effect of spin on rotating cantilever uniform beam

The case of a rotating uniform Timoshenko beam with low and high values of (r_{gy}/L) ratio has also been reproduced in order to see the effect of rotation along with this ratio on the frequency parameters. Table 5.14 shows the variation of the first four planar flapping frequency parameters of such beams. It is seen that the frequency parameters increase as the spin parameter increases for all modes and for both low and high ratio (r_{gy}/L). On the other hand, and within the

present numerical facts, it can be concluded that as the ratio (r_{gy}/L) increases the frequency values decrease. This would confirm that the effect of rotary inertia tends to lower the frequency values. The agreement with the frequencies reported by Nagaraj [85] is excellent. This validates the accuracy of the results of the present model.

Table 5.14: Planar frequency parameters of rotating uniform cantilever Timoshenko beam for different values of (r_{gy}/L), $R = 0$, and $\psi = \phi = 0°$, Coriolis effect not included

		$(r_{gy}/L) = 0.01$		$(r_{gy}/L) = 0.1$	
$\overline{\Omega}$	Mode No.	Present work	Ref.[85]	Present work	Ref.[85]
0	1	3.5026	3.5026	3.2273	3.2274
	2	21.4691	21.4698	14.4803	14.4689
	3	58.1765	58.1498	31.5992	31.5025
	4	109.2609	109.0275	48.2100	47.9090
6	1	7.3359	7.3319	6.9311	6.8509
	2	26.2571	26.2488	19.8483	19.6787
	3	63.2656	63.2386	38.7717	38.5785
	4	114.7635	114.5177	55.4906	56.2950
12	1	13.1089	13.1046	12.4657	12.1665
	2	36.9947	36.9790	30.0027	29.3024
	3	76.2875	76.2744	52.0115	51.2741
	4	129.6420	129.3472	80.2560	79.0558

Example 5: Effect of setting angle for rotating uniform Timoshenko beam

To examine the effect of the setting angle on the bending frequencies of rotating uniform Timoshenko beams, the first four flapping frequency parameters have been evaluated for $\psi = 0°$, $45°$ and $90°$ as shown in Table 5.15. The material and geometric properties for this beam are similar to those of reference [22]. The present results are in excellent agreement when compared to other methods of solutions, namely the one presented by Wang [21] who used shifted Legendre polynomials as shape functions in conjunction with the extended Galerkin's method. Based on the numerical results obtained for this case, it can be confirmed that the frequencies decrease as the setting angle increases. However, its effect on the frequencies reduces for higher modes. In fact, the effect of ψ becomes negligible beyond the second mode according the present results

and to those found in references [21] and [22]. For the case of $(r_{gy}/L) = 0.1$, a decrease of 4.64% and 0.1% is seen for the first and third mode respectively, when the setting angle changes from 0° to 45°.

It is worth mentioning that the case of $\psi = 45°$ represents a three dimensional vibration with two types of bending mode; a flapping and a lagging component mode. However, for square cross-section and in the absence of coupling due to Coriolis effects these two modes of bending are equal.

Table 5.15: The first four planar frequency parameters of rotating uniform cantilever Timoshenko beam with $\phi = 0°$, $R = 3$, $\overline{\Omega} = 10$, $\rho = 7860$ kg/m^3, $\kappa = 0.85$, and $\nu = 0.3$, Coriolis effect not included

		$(r_{gy}/L) = 0.05$			$(r_{gy}/L) = 0.1$		
	ψ	0°	45°	90°	0°	45°	90°
λ_{T1}	Present work	23.519	22.441	21.308	23.047	21.975	20.863
	Ref. [21]	23.514	22.436	21.302	23.037	21.974	20.850
	Ref. [22]	23.524	22.446	21.313	23.050	21.987	20.867
λ_{T2}	Present work	56.088	55.678	55.266	45.385	44.569	44.693
	Ref. [21]	56.072	55.662	55.250	45.428	45.194	44.955
	Ref. [22]	56.105	55.696	55.284	45.598	45.359	45.115
λ_{T3}	Present work	97.111	96.891	96.670	66.889	66.822	66.686
	Ref. [21]	97.011	96.792	96.570	66.854	66.763	66.668
	Ref. [22]	97.188	96.968	96.747	67.716	67.619	67.520
λ_{T4}	Present work	144.256	144.115	143.974	72.723	72.643	72.108
	Ref. [21]	143.815	143.673	143.531	72.313	72.146	71.982
	Ref. [22]	144.490	144.349	144.208	73.076	72.914	72.756

Predictions made so far as depicted in Tables 5.2 to 5.15 and Figures 5-5 to 5-6 represent special cases of the present model. They were presented in order to build confidence with the proposed model. As can be seen, the present scheme shows excellent agreement with other numerical results available in the literature for these special cases.

Effects of other factors pertinent to the variation in frequency parameters of the present rotating three dimensional Timoshenko beam model are investigated at a wide range of parameter changes as shown in Tables 5.16 to 5.23 and Figures 5-7 to 5-14.

Many other results pertinent to the frequency parameter variations are presented in three dimensional graphical representation. In these predictions both taper ratios as well as pre-cone and setting angle vary while keeping the other factors constant. In Figures 5-7 to 5-11 and Tables 5.16 to 5.19, the first four bending frequency parameters are estimated at 56 combinations of taper ratios that vary simultaneously. In Figure 5-7 are shown the first four bending modes for which the pre-cone, the setting angle and the hub radius parameter are set to zero while the rotational speed parameter is fixed to $\overline{\Omega} = 10$. It can be seen that the first and third bending mode that correspond the first and second flapping mode exhibit a decrease in frequency values as both taper ratios increase. However, for a fixed ν_y the second bending mode (the first lead-lag mode) exhibits an increase in frequency values when the taper ratio ν_z increases. For $0.4 \leq \nu_z < 0.6$, these frequencies are seen to increase as the taper ratio ν_y increases, while for $0.0 \leq \nu_z < 0.4$ they are seen to increase up to a certain value of ν_y and then decrease. For a fixed ν_z the fourth mode (second flapping mode) is seen to decrease as the taper ratio in the y-direction increases. When ν_y is fixed while varying ν_z these frequencies are seen to increase when $0.0 \leq \nu_z < 0.1$ and it decreases for $\nu_z > 0.1$.

Figure 5-8 shows the variation of the first four bending modes for the same beam above but for $R = 1$. It is clear that the variation of the frequency values shows the same trend as in the previous case but with higher magnitudes as would be expected when varying R from 0 to 1 for all modes. For example, the percent increase when $\nu_y = \nu_z = 0.0$ is 32.51% and it is 26.69% for ($\nu_y = 0.7$, and $\nu_z = 0.6$) for the first flapping mode. For the second flapping mode (third bending mode), the percent increase is 24.33% and 17.92% for the same values of taper ratios considered therein. From these numerical facts (percent increase) and Figures 5-7 and 5-8, it can be concluded that the hub radius parameter has more influence on frequency values of lower modes.

In Figure 5-9 the setting angle is taken to be 90° while keeping all other parameters as in the previous case. As can be seen from this figure, the frequency parameter values are lower than those of Figure 5-8. This is because the setting angle depresses the frequency values and therefore it has a softening effect that counteracts the stiffening one induced by the hub rotation $\overline{\Omega}$ and hub radius parameter R. The combined effect of taper ratios as well as the setting angle is seen to decrease the values of the frequency parameters for the first and third bending mode as both taper ratios increase. However, For the second and fourth modes, these values are seen to increase and decrease in irregular pattern as the taper ratios increase in both directions. For instance, for a fixed ν_y the frequencies corresponding to the second mode increase as the taper ratio ν_z increases from 0.0 to 0.4 and they decrease for $\nu_z > 0.4$. The same behavior can be

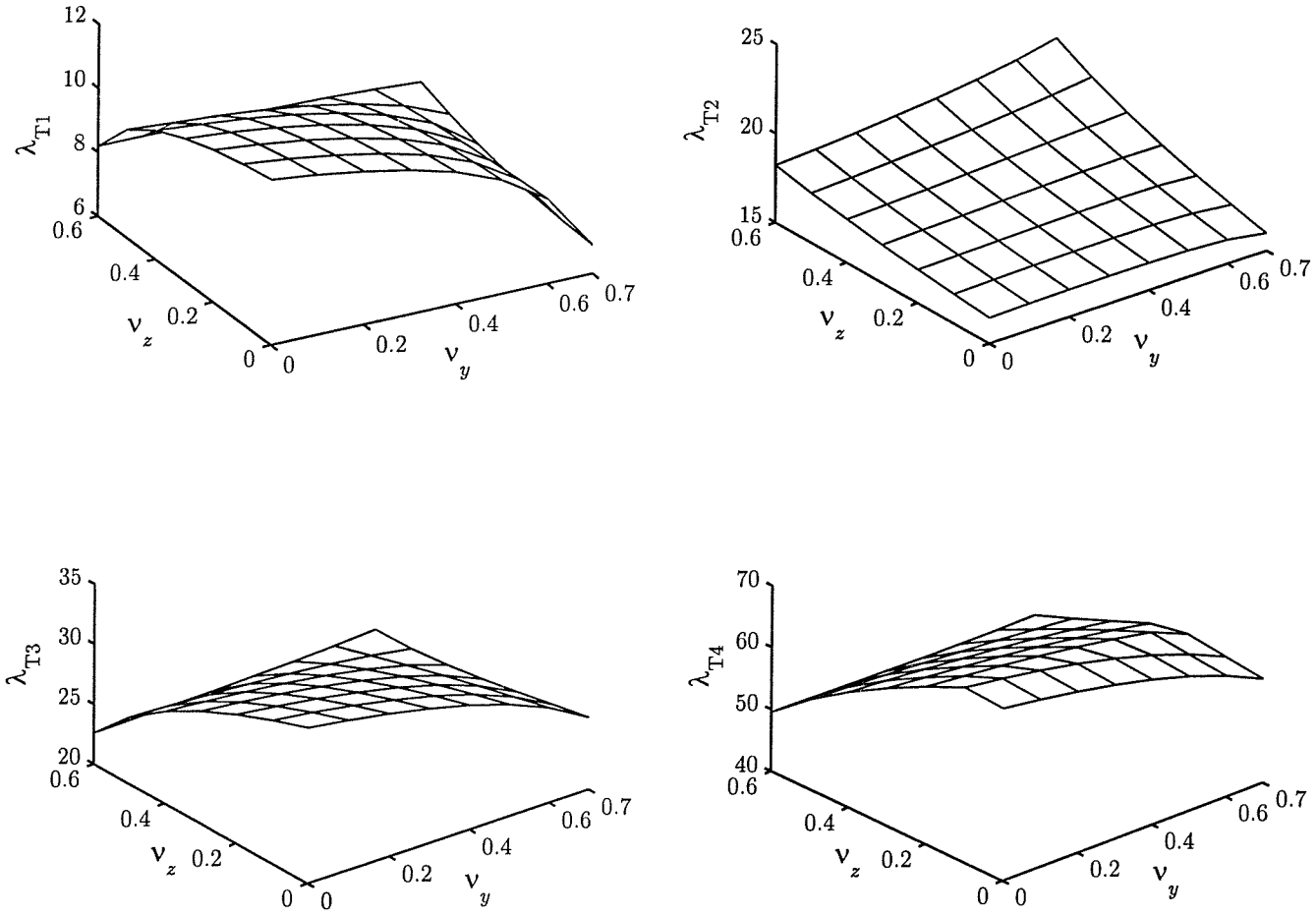

Figure 5-7: Variation of the first four bending modes as a function of taper ratios ν_y and ν_z, $\overline{\Omega} = 10$, $R = 0.0$, $\psi = \phi = 0°$.

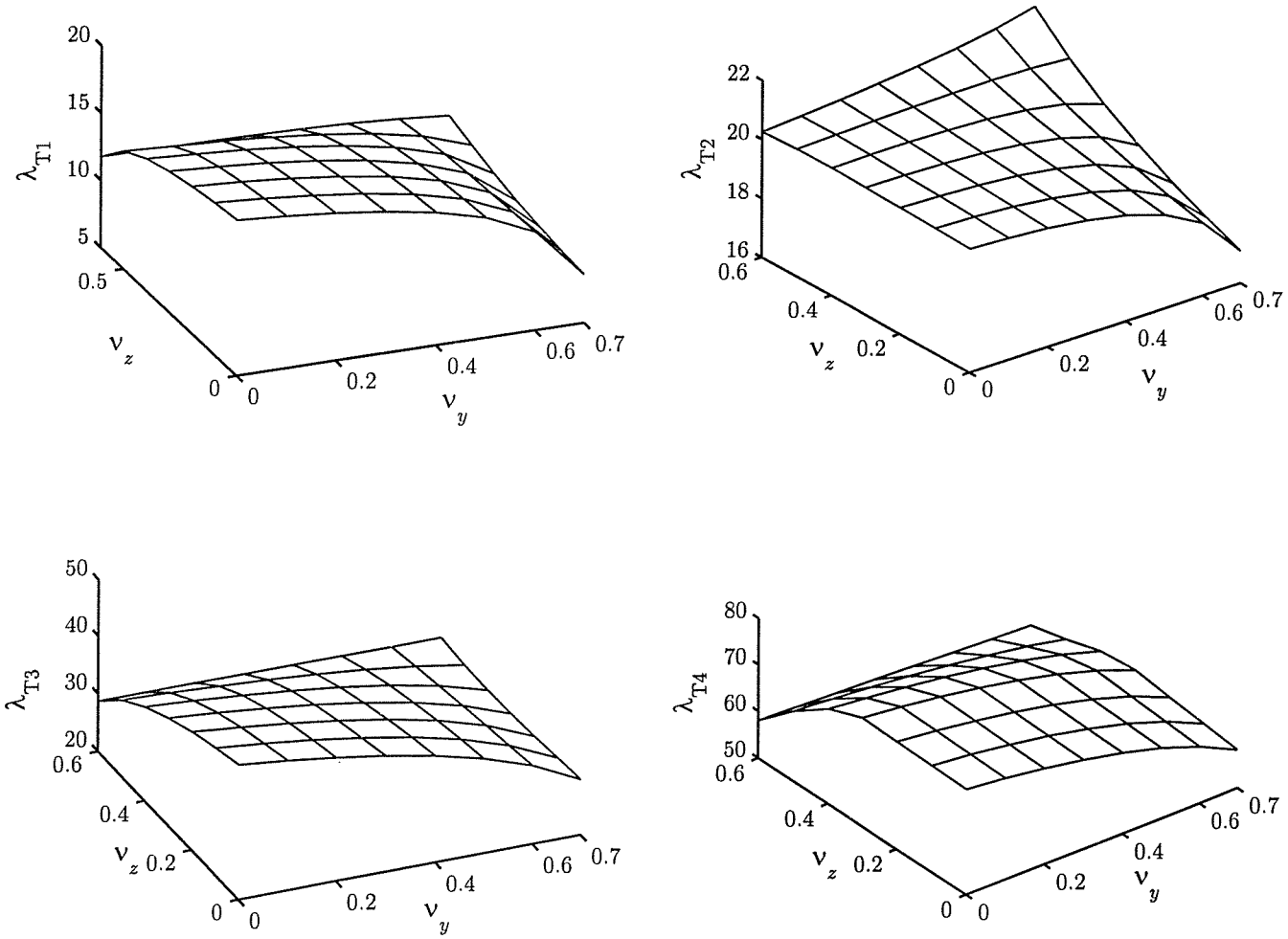

Figure 5-8: Variation of the first four bending modes as a function of taper ratios ν_y and ν_z, $\overline{\Omega} = 10$, $R = 1.0$, $\psi = \phi = 0°$.

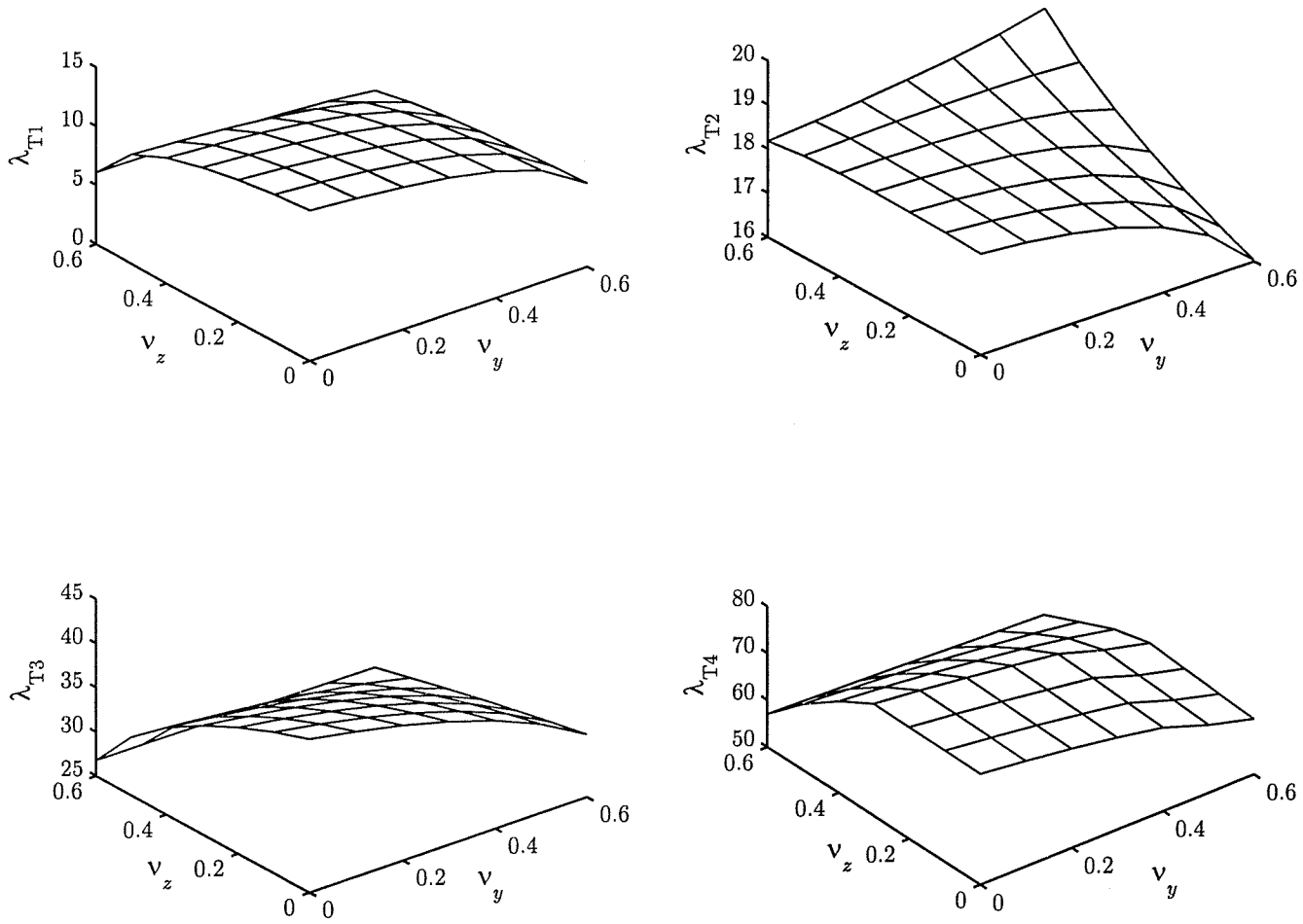

Figure 5-9: Variation of the first four bending modes as a function of taper ratios ν_y and ν_z, $\overline{\Omega} = 10$, $R = 1.0$, $\phi = 0°$ and $\psi = 90°$.

seen for the frequency parameters corresponding to the fourth mode.

It is of interest to estimate the percent decrease in actual frequency values with those of the previous figure. For example, the percent decrease when $\nu_y = \nu_z = 0.0$ is 22.76% and it is 54.35% for ($\nu_y = 0.7$, and $\nu_z = 0.6$) for the first flapping mode. Comparison of these percentage decreases reveals that for uniform beam $\nu_y = \nu_z = 0.0$, the first and frequency parameter of Figure 5-8 is reduced by more than 1/5 of its value when the setting angle $\psi = 90°$. For tapered beam ($\nu_y = 0.7$, and $\nu_z = 0.6$) the frequency value of the fundamental mode experienced a decrease which is more than 1/2 of its value as ψ varies from 0° to 90°. To see the influence of varying the setting angle on higher modes, the percentage decrease of the third bending mode is calculated for both uniform and tapered beam. In this case, the percent decrease is 3.06% for uniform beam and 6.82% for the tapered beam ($\nu_y = 0.7$, and $\nu_z = 0.6$). It is clear that these numbers are quite small when compared to those of the fundamental one. The conclusion that can be drawn here is that the effect of setting angle is of significance at lower modes but its influence becomes negligible at higher ones.

Combined effects of both pre-cone and setting angle are also investigated as shown in Figures 5-10 and 5-11. In Figure 5-10 the relationships among the first four frequency parameters and taper ratios are shown. The hub radius parameter and the spin parameter are similar to the previous cases. The setting angle ψ and the pre-cone ϕ are taken to be 45° and 15°, respectively. Predictions of the fundamental and third bending modes show that the frequency values decrease as both taper ratios increase. For a fixed $\nu_z \leq 0.4$, the second bending mode is seen to decrease for all values of ν_y. However, for $\nu_z = 0.5$ these frequencies are seen to increase until they reach a maximum value at $\nu_y = 0.5$ and then they decrease for $\nu_y > 0.5$. For $\nu_z = 0.6$, these frequency values are seen to decrease for all values of ν_y. For all values of ν_y considered, the fourth bending mode is seen to increase for $0.0 \leq \nu_z \leq 0.4$. It reaches its maximum for $\nu_z = 0.3$ and then it starts decreasing for $\nu_z > 0.3$. On the other hand, it is seen also that for a fixed ν_z all the frequency values decrease as the taper ν_y increases.

Compared to the previous cases, it can be conclude that the combined effect of including both pre-cone and setting angle tends to lower the frequency values in general because this effect is considered as a softening one. The non-zero pre-cone value has two majors contributions in the estimation of the frequency parameters. It tends to decrease the arm $\left(\mathcal{R}_o + r_P^i \cos\phi\right)$ associated to the centrifugal force and contributes to the softening term $\Omega^2 \sin\psi \cos\phi \sin\left(\psi + \phi\right)$. However, these effects are very small at higher modes and have more influence on modes with small frequency values. For $\psi = 45°$ and $\phi = 15°$, the softening term is equal to $0.59\Omega^2$.

Similar simulation tests have been conducted for the case where $\psi = 60°$ and $\phi = 30°$ while keeping all other parameters as in the previous example. The results are shown in Figure 5-11.

For all modes, these frequencies are seen to vary according to the variation of taper ratios. In general, these predictions are seen to be lower than those of Figure 5-10. This is due to the fact that for $\psi = 60°$ and $\phi = 30°$, the softening term $\Omega^2 \sin\psi \cos\phi \sin(\psi + \phi)$ is equal to $0.75\Omega^2$ which is greater than $0.59\Omega^2$. Therefore, as the softening term becomes large the frequencies of the rotating vibrational motion decrease.

It can be seen from Table 5.16 that for a given taper ratio ν_z, the fundamental frequency parameter decreases as the taper ratio ν_y increases. For $0.0 \leq \nu_y < 0.7$ it decreases as ν_z increases. However, for $\nu_y = 0.7$, it increases as ν_z increases. In Table 5.17 it is seen that for a given ν_y, the second frequency parameter is shown to increase as ν_z increases. For $0.0 \leq \nu_z \leq 0.4$ it is seen to decrease as ν_z increases while for $0.4 < \nu_z \leq 0.6$ it increases as ν_y increases. The third bending mode shown in Table 5.18 is seen to decrease for most values of taper ratios ν_y and ν_z considered. However this behavior is reversed when $\nu_y = 0.7$ and $\nu_z = 0.6$. Table 5.19 shows the variations of the fourth frequency parameters. For a fixed ν_y, these frequencies are seen to increase for all taper ratios $\nu_z \geq 0.3$. However, λ_{T4} decreases for $0.3 < \nu_z \leq 0.6$. For a fixed ν_z these frequencies decrease for all values of ν_y.

Table 5.16: Effect of taper on the fundamental bending frequency of rotating Timoshenko beam for which $R = 1.0$, $\overline{\Omega} = 10$, $\psi = 0°$ and $\phi = 30°$

	λ_{T1}							
$\nu_y \rightarrow$ $\nu_z \downarrow$	0.0	0.1	0.2	0.3	0.4	0.5	0.6	0.7
0.0	16.0879	15.8358	15.5122	15.0820	14.4817	13.5797	12.0403	8.5463
0.1	15.8287	15.5824	15.2668	14.8484	14.2665	13.3970	11.9274	8.6755
0.2	15.4936	15.2555	14.9514	14.5494	13.9936	13.1697	11.7988	8.8832
0.3	15.0433	14.8179	14.5308	14.1536	13.6360	12.8790	11.6494	9.1855
0.4	14.4029	14.1982	13.9395	13.6026	13.1466	12.4933	11.4716	9.5920
0.5	13.3986	13.2366	13.0342	12.7747	12.4307	11.9542	11.2499	10.0949
0.6	11.4771	11.4454	11.4027	11.3439	11.2608	11.1393	10.9539	10.6539

The percentage difference among the frequency values pertinent to the change in taper ratios may also be investigated. When the taper ratio ν_y varies from 0.0 to 0.1 for a fixed $\nu_z = 0.0$, the

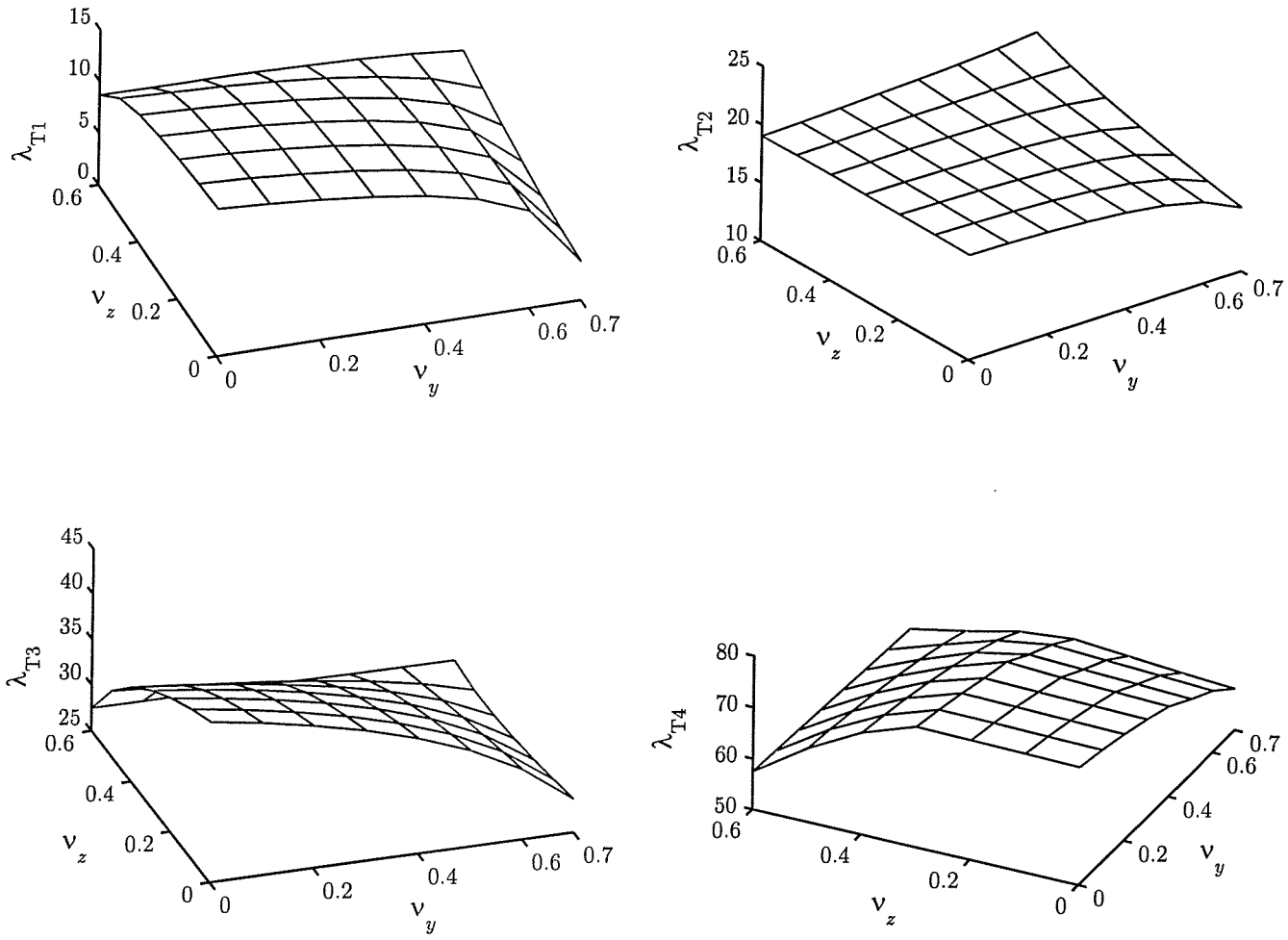

Figure 5-10: Variation of the first four bending modes as a function of taper ratios ν_y and ν_z, $\overline{\Omega} = 10$, $R = 1.0$, $\phi = 15°$ and $\psi = 45°$.

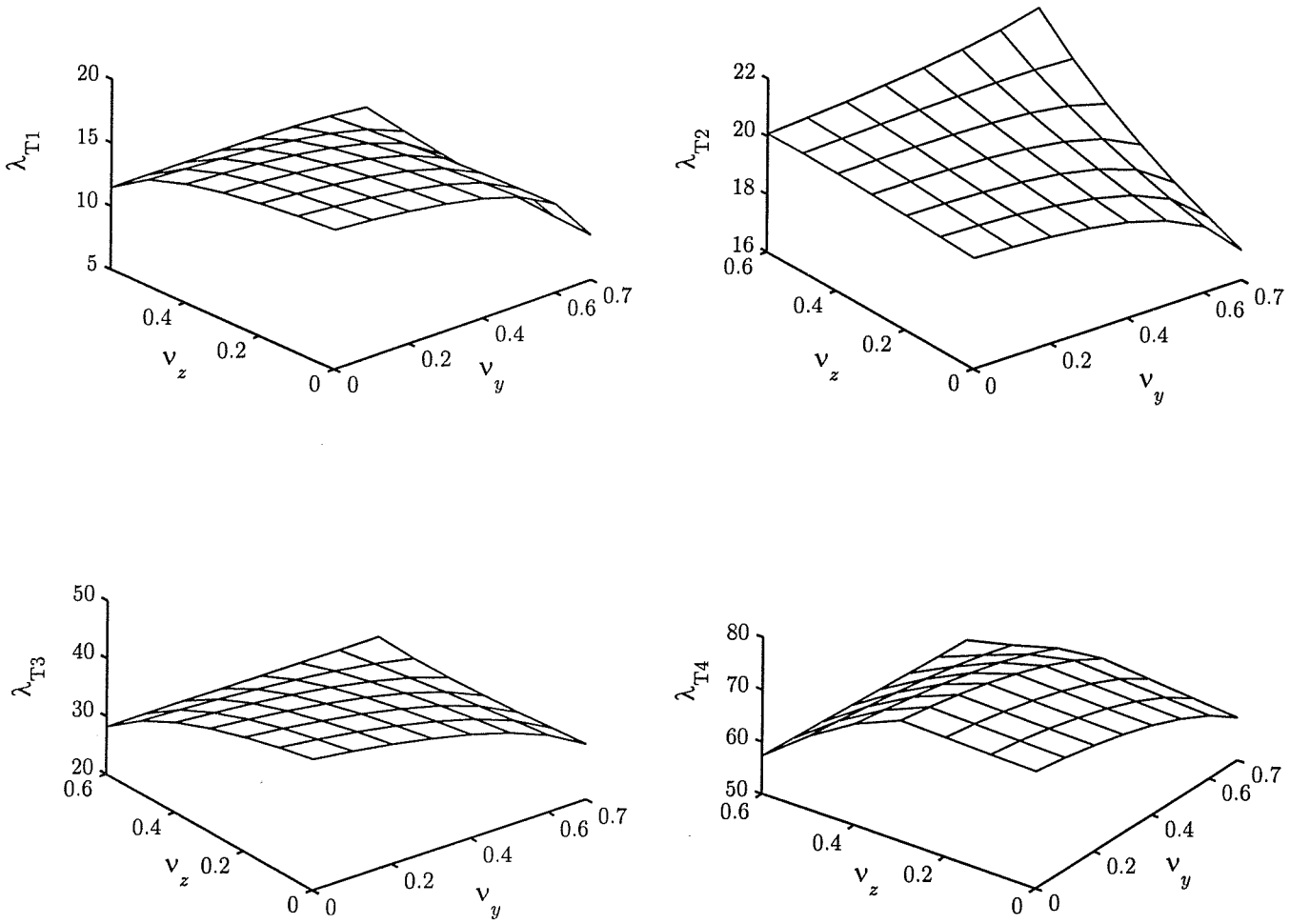

Figure 5-11: Variation of the first four bending modes as a function of taper ratios ν_y and ν_z, $\overline{\Omega} = 10$, $R = 1.0$, $\phi = 30°$ and $\psi = 60°$.

percent decrease in the fundamental frequency is estimated to be 1.56% and it increases to 6.2% and 12.78% when the taper ratio ν_y varies from 0.4 to 0.5 and from 0.5 to 0.6, respectively. On the other hand, for $\nu_y = 0.0$, the percentage difference in the frequency values is more sensitive to the change in the taper ratio ν_z. For instance, the decrease is 1.61% when ν_z varies from 0.0 to 0.1 and is 7% and 14.31% when the taper ratio ν_z varies from 0.4 to 0.5 and from 0.5 to 0.6, respectively.

Table 5.17: Effect of taper on the second bending frequency of rotating Timoshenko beam $R = 1.0$, $\overline{\Omega} = 10$, $\psi = 0°$ and $\phi = 30°$

	λ_{T2}							
$\nu_y \rightarrow$ $\nu_z \downarrow$	0.0	0.1	0.2	0.3	0.4	0.5	0.6	0.7
0.0	19.8555	19.8030	19.7128	19.5662	19.3311	18.9477	18.2897	17.0350
0.1	19.9190	19.8791	19.8058	19.6825	19.4809	19.1488	18.5775	17.4978
0.2	19.9802	19.9560	19.9036	19.8089	19.6483	19.3783	18.9104	18.0314
0.3	20.0362	20.0319	20.0058	19.9471	19.8376	19.6442	19.3009	18.6545
0.4	20.0819	20.1034	20.1113	20.0989	20.0546	19.9575	19.7672	19.3934
0.5	20.1085	20.1644	20.2177	20.2667	20.3078	20.3349	20.3362	20.2859
0.6	20.0988	20.2028	20.3193	20.4528	20.6101	20.8027	21.0500	21.3891

Table 5.18: Effect of taper on the third bending frequency of rotating Timoshenko beam $R = 1.0$, $\overline{\Omega} = 10$, $\psi = 0°$ and $\phi = 30°$

	λ_{T3}							
$\nu_y \rightarrow$ $\nu_z \downarrow$	0.0	0.1	0.2	0.3	0.4	0.5	0.6	0.7
0.0	42.7311	41.8554	40.8174	39.5642	38.0139	36.0309	33.3757	29.5996
0.1	41.3924	40.5635	39.5821	38.3976	36.9321	35.0575	32.5474	28.9739
0.2	39.8323	39.0669	38.1610	37.0685	35.7176	33.9918	31.6850	28.4049
0.3	37.9669	37.2875	36.4844	35.5175	34.3252	32.8073	30.7884	27.9333
0.4	35.6509	35.0932	34.4362	33.6484	32.6826	31.4632	29.8598	27.6250
0.5	32.6108	32.2383	31.8032	31.2871	30.6636	29.8923	28.9064	27.5852
0.6	28.2565	28.2003	28.1411	28.0804	28.0216	27.9715	27.9442	27.9688

Table 5.19: Effect of taper on the fourth bending frequency of rotating Timoshenko beam $R = 1.0$, $\overline{\Omega} = 10$, $\psi = 0°$ and $\phi = 30°$

	λ_{T4}							
$\nu_y \rightarrow$ $\nu_z \downarrow$	0.0	0.1	0.2	0.3	0.4	0.5	0.6	0.7
0.0	72.4518	71.5791	70.4400	69.0056	67.2189	64.9792	62.1042	58.2246
0.1	72.6804	71.7790	70.6350	69.2167	67.4693	65.2997	62.5428	58.8700
0.2	72.9035	71.9830	70.8411	69.4459	67.7466	65.6598	63.0411	59.6089
0.3	73.1269	72.1959	71.0633	69.6996	68.0594	66.0718	63.6172	60.4694
0.4	69.4323	68.5786	67.6089	66.4944	65.1932	63.6478	61.7654	59.3965
0.5	64.0927	63.4503	62.7271	61.9043	60.9589	59.8573	58.5521	56.9744
0.6	57.3667	57.0468	56.7036	56.3376	55.9525	55.5591	55.1853	54.9051

In another attempt, the first four frequency parameters corresponding to the bending modes have been investigated at 70 combinations of pre-cone and setting angle as shown in Figures 5-12 and 5-14.

Figure 5-12 shows the variation of the first four bending modes for a uniform beam ($\nu_y = \nu_z = 0$). Except for the case where $\psi = 90°$, it is seen that the first three bending modes exhibit a decrease when both the pre-cone and setting angle increase. When $\psi = 90°$, the first and second bending mode only decrease for increasing pre-cone. For any value of ψ, the fourth bending mode decreases when the pre-cone increases. On the other hand, for a fixed value of the pre-cone it is seen to increase for $0° \leq \psi \leq 30°$ and it decreases for $30° < \psi \leq 90°$.

The hub radius parameter and spin parameter in Figures 5-13 and 5-14 remain similar to the previous case. The taper ratios are taken to be ($\nu_y = 0.1$, $\nu_z = 0.2$) for Figure 5-13 and ($\nu_y = 0.5$, $\nu_z = 0.35$) for Figure 5-14. The trend in the variation of the frequencies of these figures, is similar to the one of Figure 5-12. The effect of tapering is seen to reduce the frequency values for all modes when compared to the previous case of uniform beam. This is because taper would reduce both the out-board cross-section area and the mass of the beam. Therefore, both the stiffness and mass matrix becomes small and this would lead to smaller eigenvalues. Moreover, comparison of these predictions reveals that larger taper ratios give lower frequency values.

Many other frequency predictions versus the spin parameter are shown in terms of taper ratios, pre-cone, setting angle as parameters. Figure 5-15 shows the lowest three flexural frequency

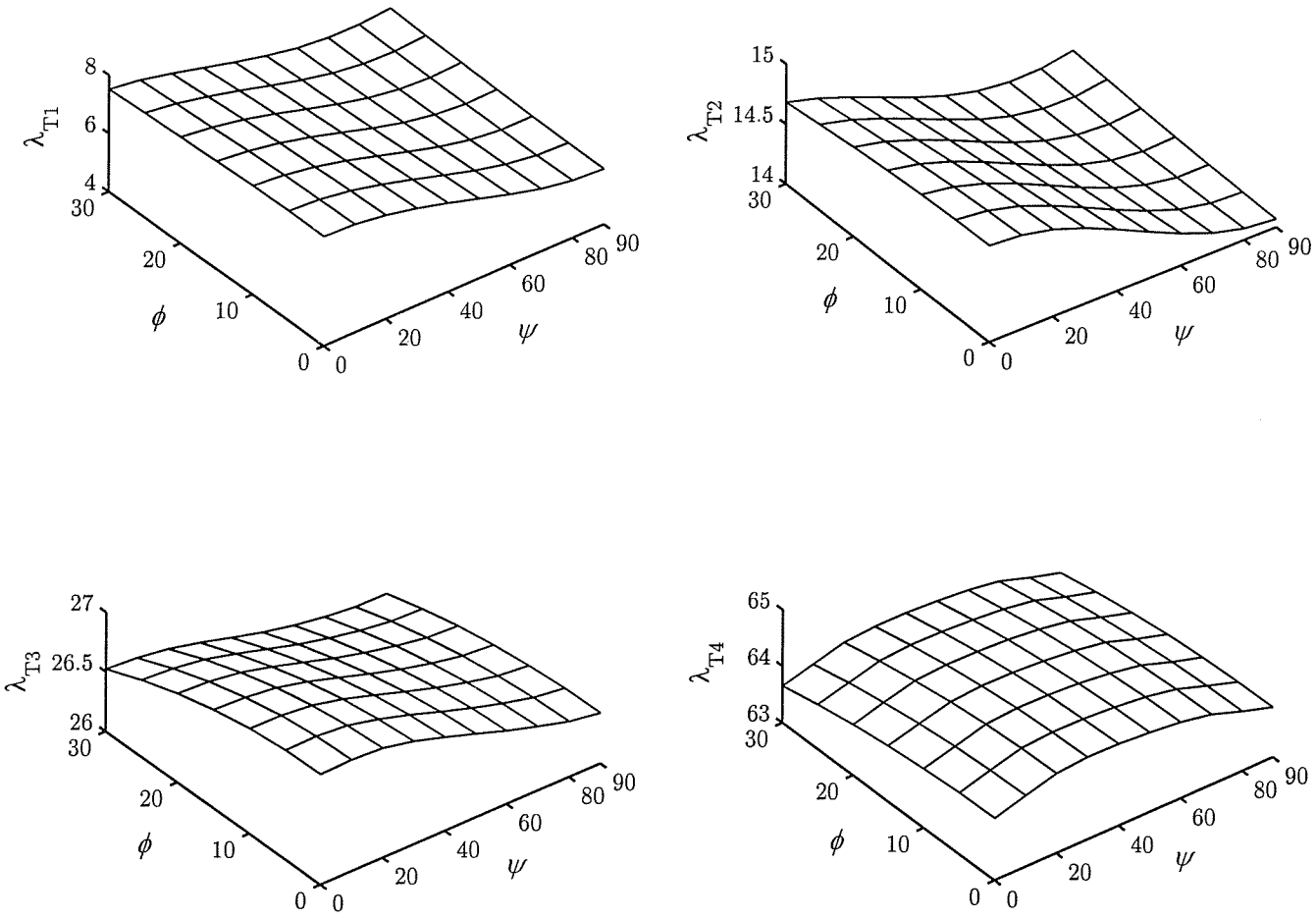

Figure 5-12: Effects of pre-cone and setting angle on the variation of the first four bending modes for uniform Timoshenko beam, $\overline{\Omega} = 5$ and $R = 0.5$.

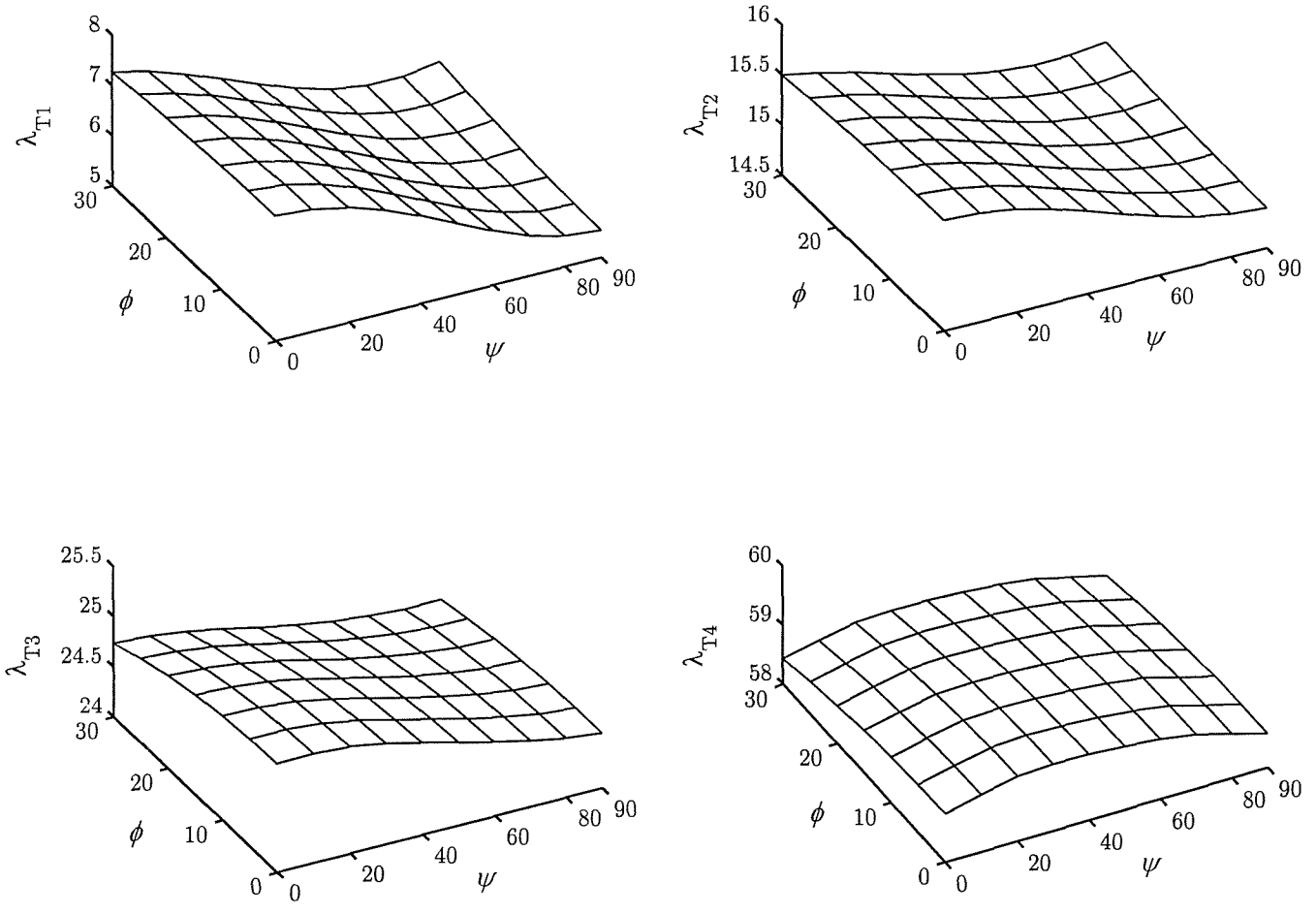

Figure 5-13: Effects of pre-cone and setting angle on the variation of the first four bending modes for tapered Timoshenko beam, $\nu_y = 0.1$, $\nu_z = 0.2$, $\overline{\Omega} = 5$ and $R = 0.5$.

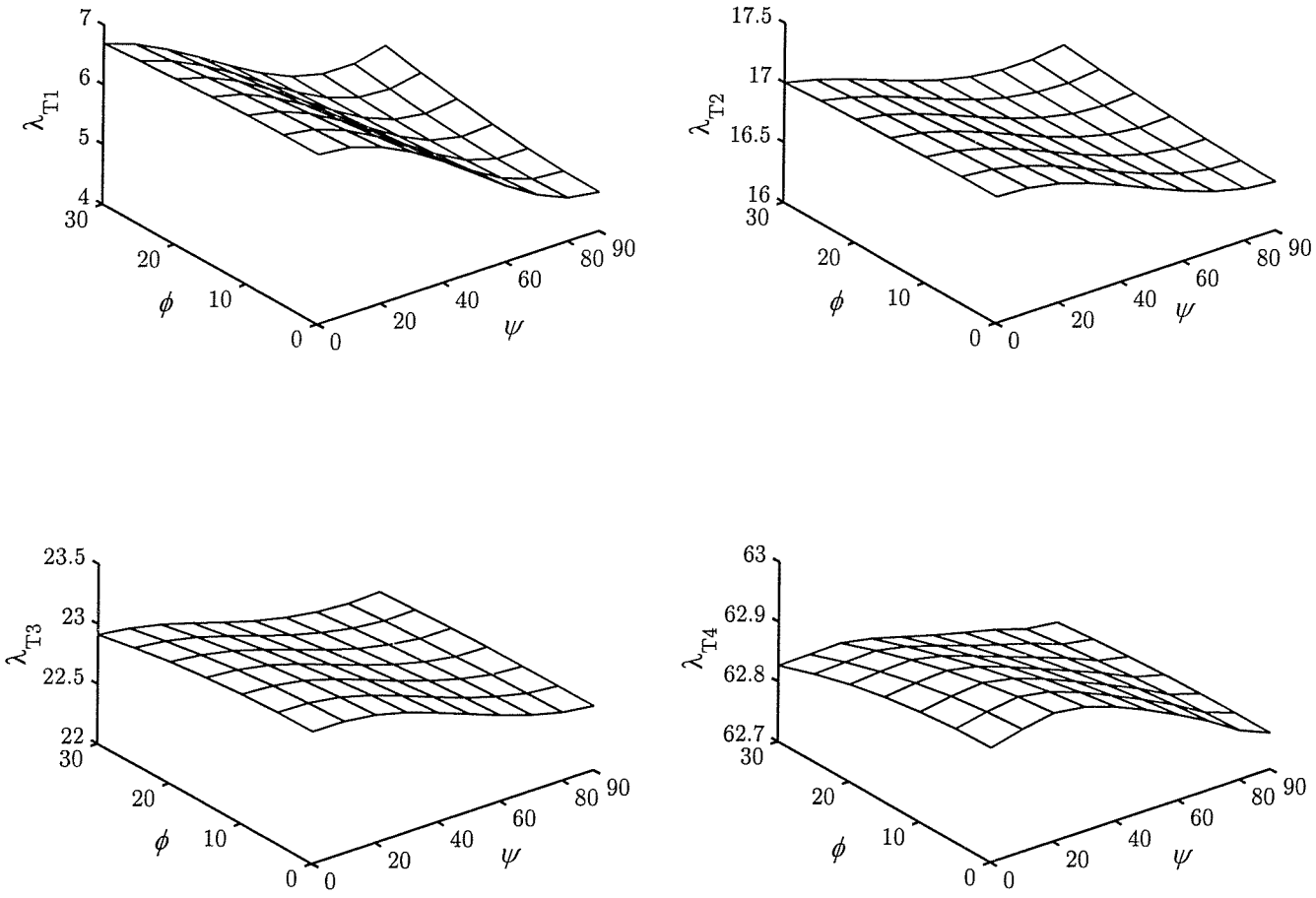

Figure 5-14: Effects of pre-cone and setting angle on the variation of the first four bending modes for tapered Timoshenko beam, $\nu_y = 0.5$, $\nu_z = 0.35$, $\overline{\Omega} = 5$ and $R = 0.5$.

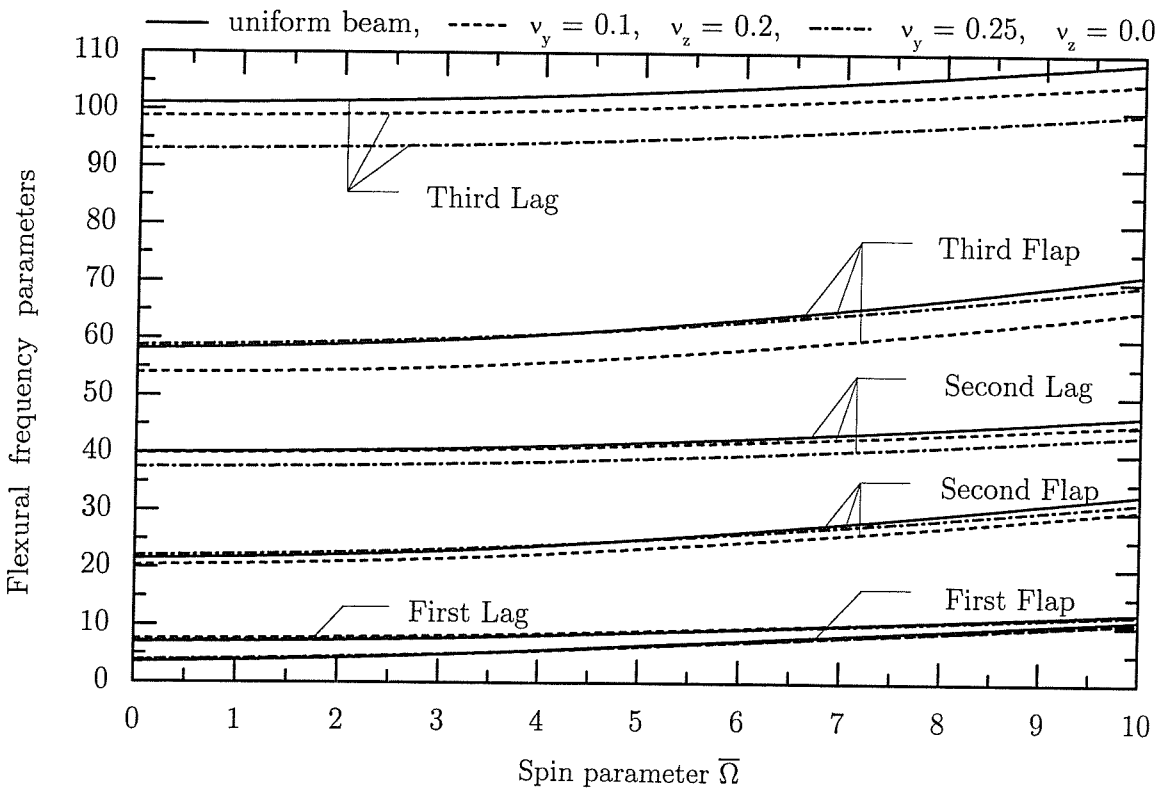

Figure 5-15: Frequency parameters of rotating uniform and tapered Tiomshenko beam with $(r_{gy}/L) = 0.02$, $\psi = \phi = 0°$ and $R = 0$.

parameters for both uniform and tapered Timoshenko beams at which the pre-cone, setting angle and hub radius parameter are set to zero. As can be seen from this figure, all modes are affected by the spin and experience a stiffening behavior for both uniform and tapered beams. Consequently, it is seen that for a given mode the difference between the lag and flap frequencies decreases as the spin parameter increases. In addition to that, a cross-over between the different modes at different tapers of the beam can also be seen.

In Figure 5-16 are shown the lowest three flexural frequency parameters for rotating tapered Euler-Bernoulli and Timoshenko beams for which $\nu_y = 0.1$, $\nu_z = 0.2$, with a setting angle $\psi = 45°$ and zero hub radius and pre-cone. These frequencies show that all modes share the stiffening characteristic induced by the hub rotation. On the other hand, frequencies with shear deformation and rotary inertia effects are shown to be lower than those for Euler-Bernoulli beam. The effect of shear is insignificant in the fundamental flapping and lead-lag modes and becomes only important in the higher modes. This fact has been addressed previously for the case of two dimensional beam and is seen to be true in this case. Moreover, it is of interest to notice that the shear effect is more pronounced in lag modes rather than flapping

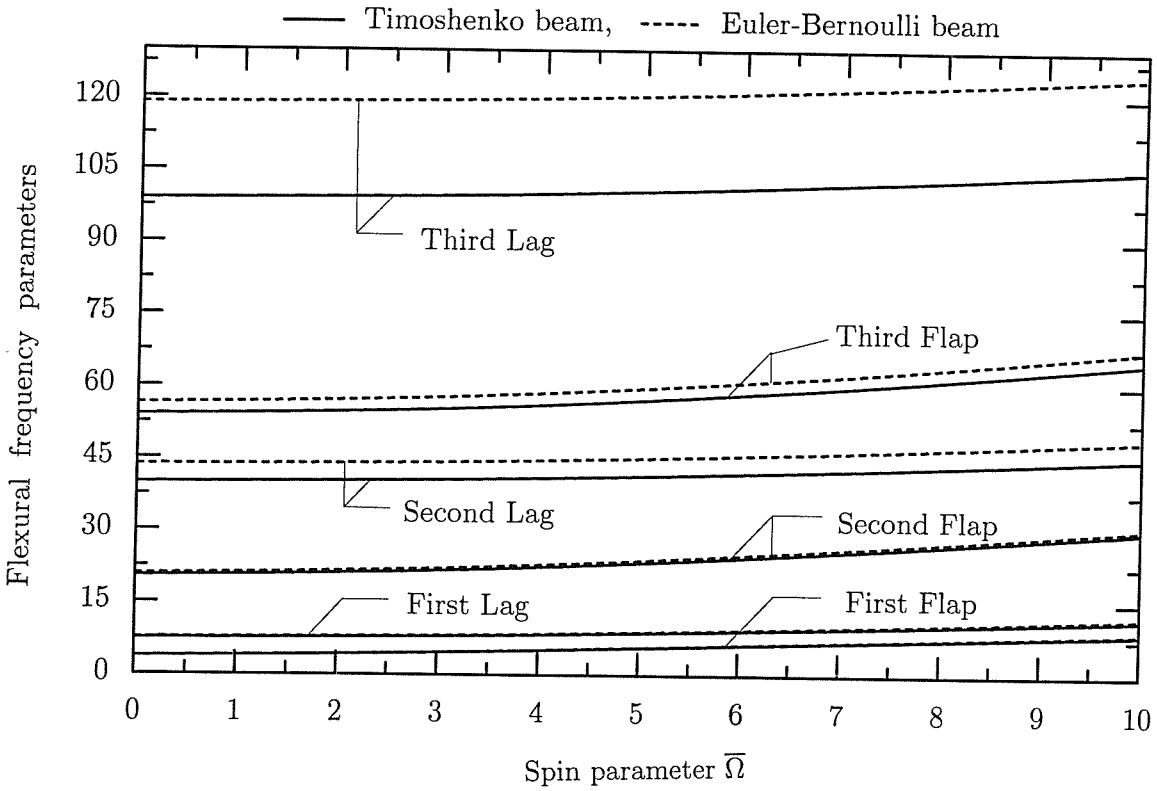

Figure 5-16: Frequency parameters of rotating tapered Euler-Bernoulli and Timoshenko beams with $\nu_y = 0.1$, $\nu_z = 0.2$, $\psi = 45°$, $\phi = 0°$ and $R = 0$.

modes. The reason for this could be attributed to the fact that for a setting angle $\psi = 45°$, the shear effect is unimportant in flapping bending modes and is important in the lead-lag ones.

In order to see the effect of orientation of the cross-section on the lowest three flexural frequencies of the previous beam, values of 15° and 90° were respectively assigned to the pre-cone and setting angle. Figure 5-17 shows that at these specific hub radius, taper ratios, pre-cone and setting angle, the lead-lag frequencies are higher than those of the flapping motion. Similar stiffening behavior to that shown in the previous figure is seen with the exception that the difference between the first flap and lag frequencies increases as the spin parameter increases. This trend can be clearly seen since the lead-lag modes experience a stiffening effect while the flap modes shows a very small stiffening behavior as the spin increases. The reason for that may be attributed to the fact that the softening effect starts dominating the stiffening effect for the flapping modes when the setting angle is 90°.

Figure 5-18 shows the flexural behavior of a rotating beam at different beam cross-section orientations. From these predictions, it is seen that as the setting angle increases the frequencies corresponding to the flapping modes decrease.

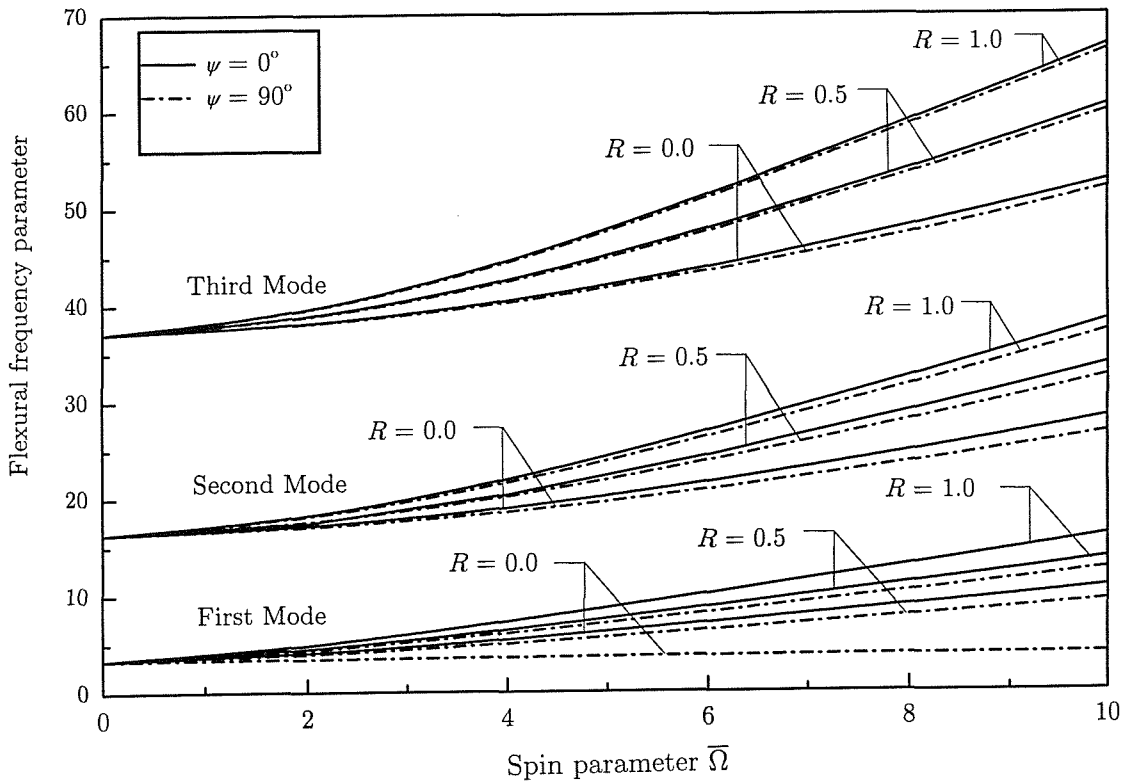

Figure 5-17: Variation of the first three frequency parameters of rotating uniform Timoshenko beam with $\phi = 15°$.

Except for the case where $\psi = 90°$ and $\phi = 0°$, predictions shown in this figure experience a stiffening effect that is manifested by an increase in the frequency values as the spin parameter increases. However, for $\psi = 90°$ and $\phi = 0°$, the slope of the curve representing the fundamental flapping mode is seen to be negative. This indicates a decrease in frequency values as the spin parameter increases. Thus one sees the evidence of a softening effect which is opposing and dominating the stiffening effect in this case.

Accurate prediction of the dynamic characteristics of rotating structures is necessary in the early stages of the design process in order to avoid any possible conditions susceptible to resonance within the range of operating speed, and to prevent any failure that may occur as a result of sustained vibration at or near the resonant frequency range.

An investigation has been made to check whether there is excitation at appropriate frequencies that may lead to a coincidence of the rotational speed of the hub with the fundamental mode of the beam in the range $0 \leq \overline{\Omega} \leq 10$.

In Figure 5-19, the fundamental flapping mode variations have been plotted for a tapered beam at different values of pre-cone and setting angle along with the line $\lambda = \overline{\Omega}$. Three resonant frequencies are seen to occur at a setting angle of 90° and different pre-cones. The first one occurs at $\lambda = 6.133$ where $\phi = 0°$, the second one occurs at $\lambda = 6.368$ where $\phi = 15°$ and the

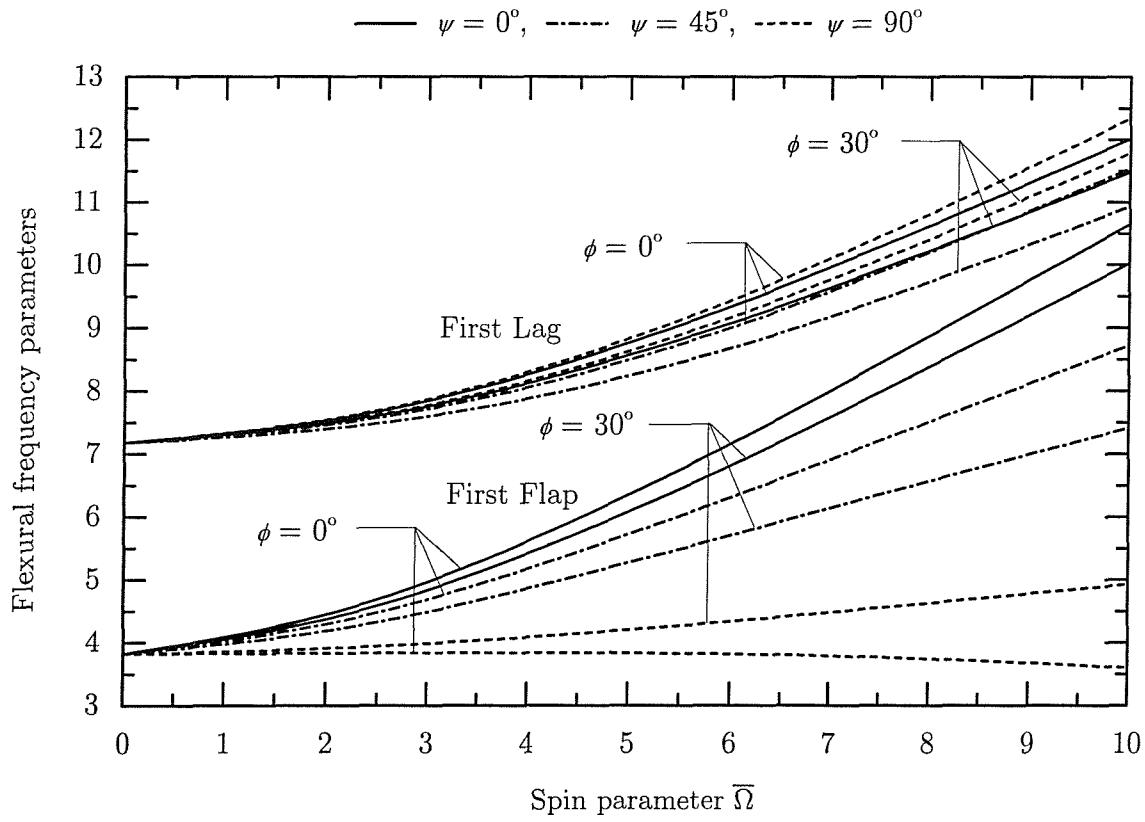

Figure 5-18: Fundamental flexural frequency parameter of rotating tapered Timoshenko beam with $\nu_y = 0.25$, $\nu_z = 0.0$, and $R = 0$.

third one occurs at $\lambda = 7.129$ where $\phi = 30°$. At these particular values, the beam exhibits excessive vibrations with very high amplitudes that may cause failure to the beam.

Because of its importance in vibration, the fundamental frequency parameter of flexural vibration is always examined in early stage design in order to avoid resonance conditions that may lead to substantial vibrations that cause failure of the beam. In view of that, it is again examined here at a wide range of spin and hub radius parameters for two extreme setting angles $\psi = 0°$ and $\psi = 90°$ where the pre-cone is fixed to 15° as shown in Figure 5-20. For higher spin parameters, frequency dependence on R depends strongly on the setting angle ψ; thus for $\psi = 0°$, the fundamental frequency is still near linear with hub radius parameter R, but for $\psi = 90°$, not only is the relationship no longer linear, but also shows much greater sensitivity to changes in hub radius; this is due to the relative contributions of both stiffening and softening effects, the former depending on R, the latter on ψ. On the other hand, it is of interest to notice again the dominance of the softening effect over the stiffening effect for the case of $R = 0$ and $\overline{\Omega} = 10$. Moreover, one can also observe that for a fixed $\overline{\Omega}$, the difference between the flapping and lead-lag frequency decreases as the hub radius increases.

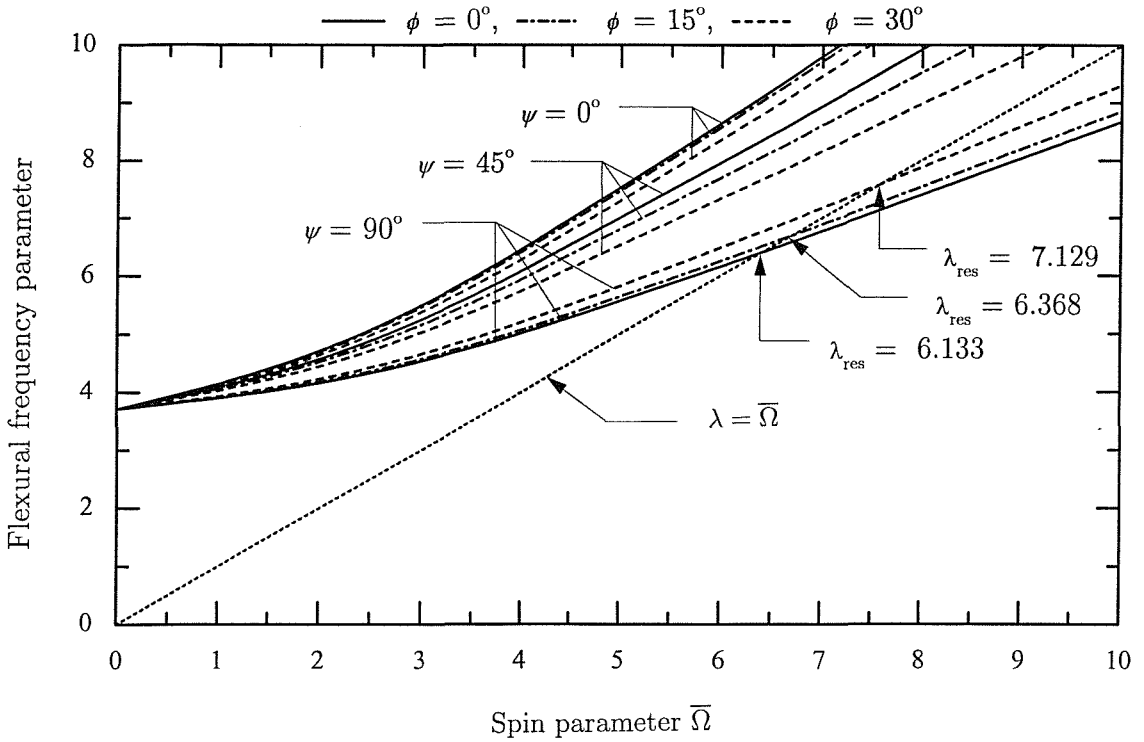

Figure 5-19: Resonance in the fundamental flapping frequency parameter of rotating tapered Timoshenko beam with $\nu_y = 0.1$, $\nu_z = 0.2$, and $R = 0.5$.

5.2.3 Southwell Coefficients

In order to better understand the effects of all factors considered in this model, such as taper ratios, shear deformation, rotary inertia, hub radius, setting angle, pre-cone, rotational spin parameter on the modal characteristics of a rotating doubly tapered Timoshenko beam, many other cases have been presented with a variety of combinations in the form of Southwell coefficients. Solutions are given for several cases, in which each effect is considered alone, as well as combined effects. In addition, these effects are examined and a variety of simulation results are presented graphically as shown in Figures 5-21 to 5-33. The explicit form of the Southwell relation for the lowest four vibration modes of rotating beams with several combinations of taper ratios, pre-cones, setting angles and various slenderness ratios is presented. Consequently, the first four frequency parameters can be easily computed from knowledge of the non-rotating frequency parameters and the Southwell relation.

The stiffening effect due to rotation was introduced by Lamb and Southwell [3] and refined by Southwell and Gough [4] through the equation

$$\lambda_{Ri}^2 = \lambda_{Ni}^2 + S_i \overline{\Omega}^2 \tag{5.1}$$

where the subscript i refers to the i^{th} mode, λ_{Ri} refers the i^{th} rotating frequency parameter, λ_{Ni}

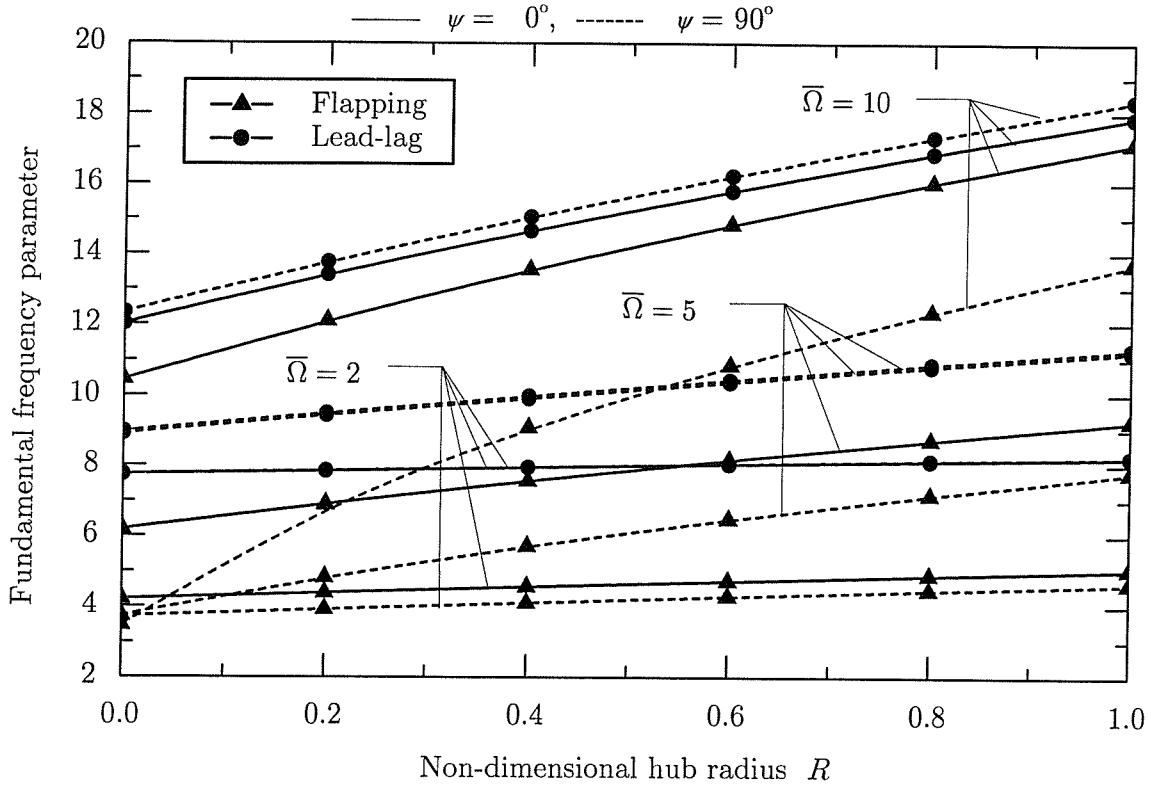

Figure 5-20: Variation of the fundamental flexural frequency parameter of rotating tapered Timoshenko beam with $\nu_y = 0.1$, $\nu_z = 0.2$, and $\phi = 15°$.

is the corresponding frequency parameter of the non-rotating beam, $\overline{\Omega}_i$ is the spin parameter and S_i the Southwell coefficient. Upon plotting λ_{Ri}^2 versus $\overline{\Omega}^2$, it can be seen that this equation represents a linear relationship between λ_{Ri}^2 and $\overline{\Omega}^2$, for which S_i represents the slope and λ_{Ni}^2 represents the intercept. In this analysis, our concern is to focus on the refinement of the expression of S_i and its dependence on the different parameters included in the formulation of the beam model.

It is of interest to investigate whether the flexural frequencies of rotating cantilever tapered Timoshenko beams would fit into some form of Southwell linear approximation. It is worthwhile trying to fit results of simulation into Southwell form and obtain Southwell coefficients for several parameter changes. Results presented in this form are more economical and useful from a practical point of view than a table of frequency parameters at various values of parameter changes.

In this analysis an attempt has been made for the first time to obtain Southwell coefficients for three dimensional rotating uniform and tapered Timoshenko beams. Because results pertinent to SC's for rotating three dimensional tapered Timoshenko beams including the effects of hub radius, pre-cone and setting angle as well as Coriolis effects could not be found in the literature, several special cases which represent degenerate cases of this model were examined

to build confidence and validate the present scheme. Comparisons with available results in the literature are made wherever possible. Except otherwise stated, Coriolis effects are accounted for throughout this study.

Figure 5-21 shows Southwell coefficient S_{E1}, which corresponds to the fundamental flapping mode[3]. In this figure, S_{E1} is shown as a function of the hub radius parameter $R = \mathcal{R}_o/L$, and the setting angle ψ. The relationship between S_{E1} and R is a linear one. It is worthwhile noting

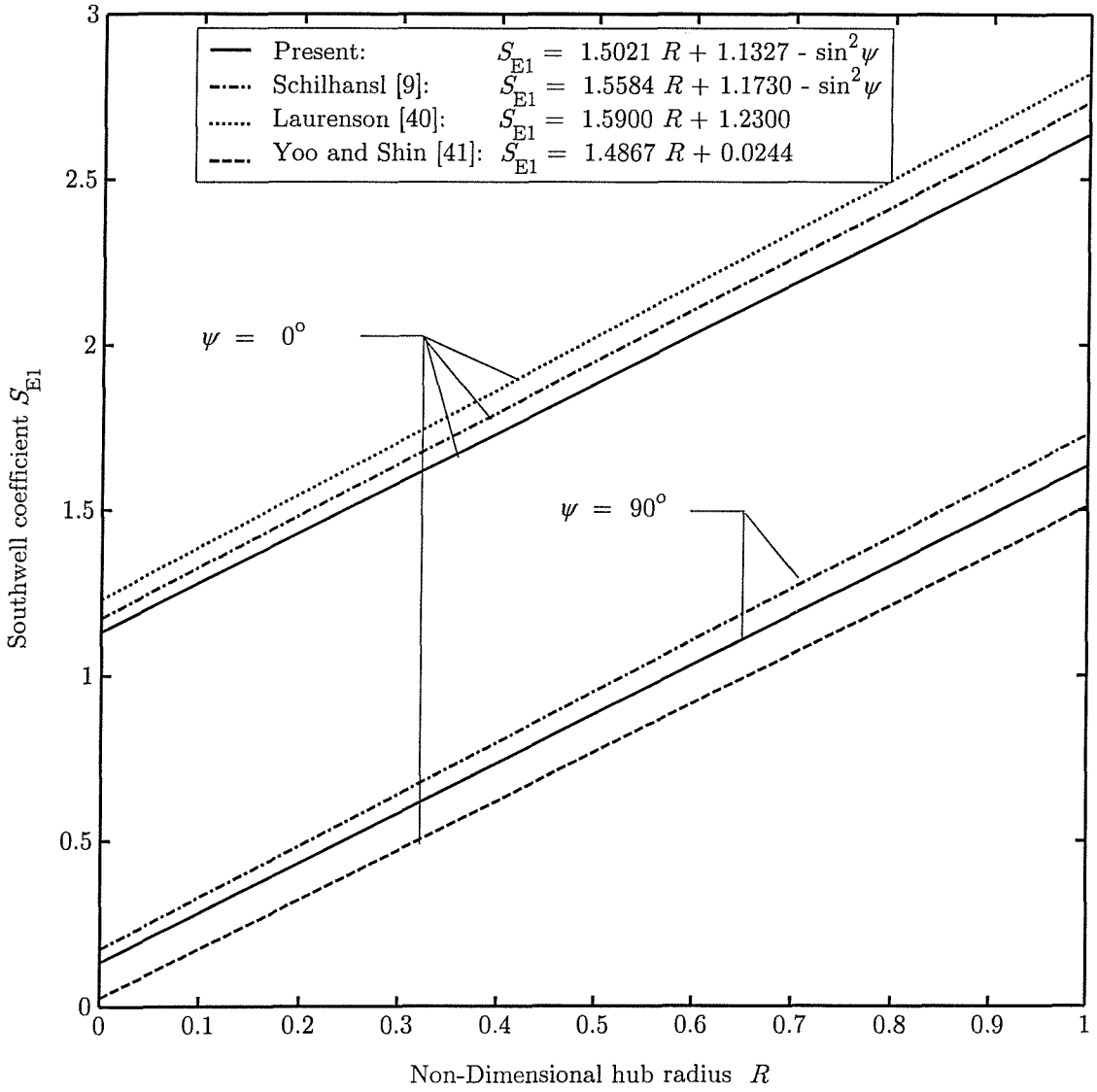

Figure 5-21: Southwell coefficient S_{E1} for uniform Euler-Bernoulli beam with $\phi = 0°$.

[3] S_{Ei}, S_{Ti} : i^{th} mode Southwell coefficient for Euler-Bernoulli and Timoshenko beam, respectively.

that S_{E1} corresponding to the flapping motion ($\psi = 0°$) is parallel to the one of lead-lag motion ($\psi = 90°$) and the difference between them is independent of R and is equal to unity.

The explicit expression for S_{E1} is also presented and compared with the ones proposed by Schilhansl [9], Laurenson [41] and Yoo and Shin [86]. The expression for S_{E1} is in excellent agreement with those presented by Schilhansl [9] and Laurenson [41]. It is clear that the predictions presented by Yoo and Shin [86] are in error. The intercept of the Southwell relation is almost zero. This is not true. The intercept of the lead lag motion cannot be smaller than the one for the flapping motion as can be verified by the present predictions and those of Schilhansl [9] and Laurenson [41]. This could be attributed to the a wrong interpolation of the Southwell coefficients.

To show the effect of shear deformation and rotary inertia on Southwell coefficients, Figure 5-22 is produced. In this figure, SC's for the first four modes for both Euler-Bernoulli and Timoshenko beams are shown. Only the flapping motion of the rotating uniform Euler-Bernoulli and Timoshenko beams are considered in this example. The expressions for SC's are shown to be in a linear relationship with R for all four modes. The lines representing SC's for both Euler Bernoulli and Timoshenko beams increase as the hub radius increases. In addition, they are not parallel. This is due to the differences in the geometrical properties of Euler-Bernoulli and Timoshenko beams. It is clearly shown that the slope and intercept for these expressions increase as the mode number increases, as would be expected. Those corresponding to S_{E1} are greater than those of S_{T1}. This explains the inclusion of rotary inertia and shear deformation in Timoshenko beam would reduce the frequency values as reflected by the variation of SC's. On the other hand, it is also shown that for the first mode, S_{E1} and S_{T1} cannot be distinguished, while as the mode number increases, the difference between EBT and TBT is quite noticeable as manifested by the variation of S_{E4} and S_{T4} of the fourth mode. This shows that the shear effect is not important at lower modes while it becomes more pronounced as the mode number increases. Further, the difference between EBT and TBT increases as the hub radius parameter increases.

Figure 5-23 depicts the first four SC of the flapping motion for rotating tapered Timoshenko beams at a wide range of taper ratios while keeping both the pre-cone and setting angle to be zero. Again, from this figure, it is seen that the relationship between SC and the hub radius parameter is linear. The slope and intercept of the different lines depend strongly on taper ratios ν_y and ν_z where it is shown that, as the taper ratios increase the slope and the intercept of the corresponding lines decrease. Consequently, this leads to the conclusion that as the taper

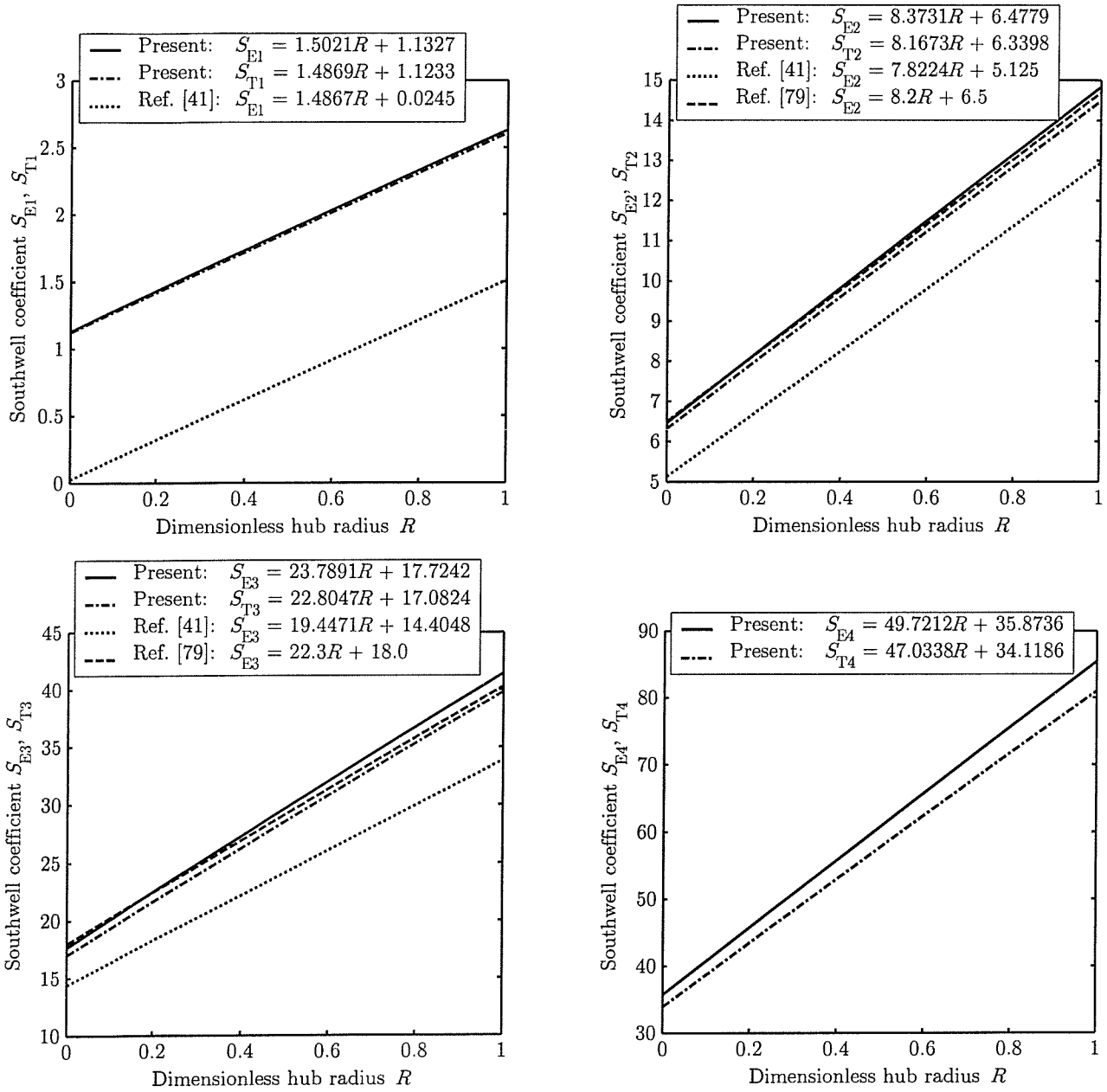

Figure 5-22: Variation of the first four SC's for uniform Euler-Bernoulli and Timoshenko beam with $(r_{gy}/L) = 0.08$ and $\phi = \psi = 0°$.

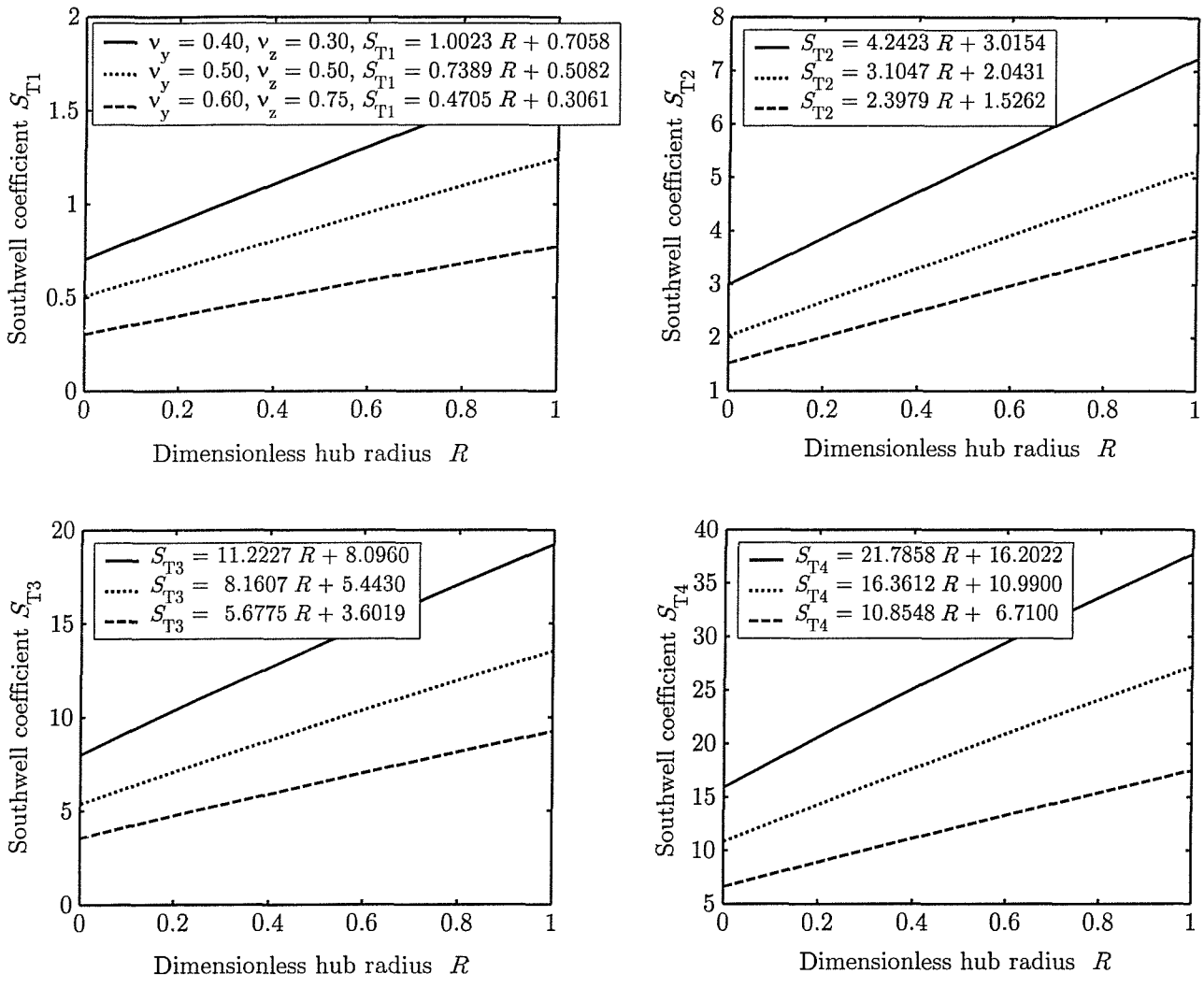

Figure 5-23: Variation of the first four SC's for tapered Timoshenko beam with $(r_{gy}/L = 0.08)$ and $\psi = \phi = 0°$.

ratios increase simultaneously the frequencies decrease, owing to a softening effect. The reason behind this could be attributed to several combining factors. The tapers lead to a decrease of the cross-section area which renders the beam stiffer toward the tip. The shear deformation and rotary inertia tend to lower the frequencies of vibration. The rotation due to the centrifugal force field tends to increase the frequencies. The combining effect of these factors could result in a net softening effect. Of particular interest is the difference among the several lines, which is noticed to increase, as the hub radius increases. Explicit expressions for SC are derived and presented for each case showing the parameter variations for the first four modes. A successful attempt has been made to combine each set of the four modes of Figure 5-23 into one single general equation as a function of the parameter variations. The resulting explicit expressions for SC corresponding to the first four modes are given by

$$S_{T1} = (2.006 - 2.434\nu_y - 0.100\nu_z)\,R + (1.451 - 1.796\nu_y - 0.090\nu_z) \tag{5.2}$$

$$S_{T2} = (13.101 - 28.608\nu_y + 8.616\nu_z)\,R + (11.459 - 27.939\nu_y + 9.108\nu_z) \tag{5.3}$$

$$S_{T3} = (29.263 - 53.772\nu_y + 11.576\nu_z)\,R + (26.827 - 59.006\nu_y + 16.238\nu_z) \tag{5.4}$$

$$S_{T4} = (42.676 - 50.974\nu_y - 1.636\nu_z)\,R + (46.370 - 89.410\nu_y + 18.644\nu_z) \tag{5.5}$$

Each of the above equations represents an equation of a plane in the $(\nu_y\nu_z)$-plane with R as a parameter or an equation of a straight line of the form

$$S_{Ti} = m_i R + p_i \tag{5.6}$$

where $m_i = m_i\,(\nu_y, \nu_z)$ and $p_i = p_i\,(\nu_y, \nu_z)$ represent respectively the slope and intercept of the above linear relationship.

On the other hand, since the difference between the flapping and lagging modes expressed in terms of SC is exactly unity, the expression of S_{T1} to S_{T4} corresponding to the lagging motion of the rotating tapered Timoshenko beam can be easily obtained by subtracting 1 from the above equations. Lead-lag expressions of S_{T1} to S_{T4} of rotating tapered Timoshenko beam can be obtained from those of flapping mode by considering the results obtained from equations (5.2) to (5.5) as explained above.

In Figure 5-24, the taper ratio in the y-direction is kept constant ($\nu_y = 0.25$) while varying ν_z. The first four SC's shown in this figure correspond to the flapping and lead-lag motion for a rotating Timoshenko beam where $(r_{gy}/L) = 0.02$.

Similar conclusions to the previous case can be drawn from this figure namely, SC's and R

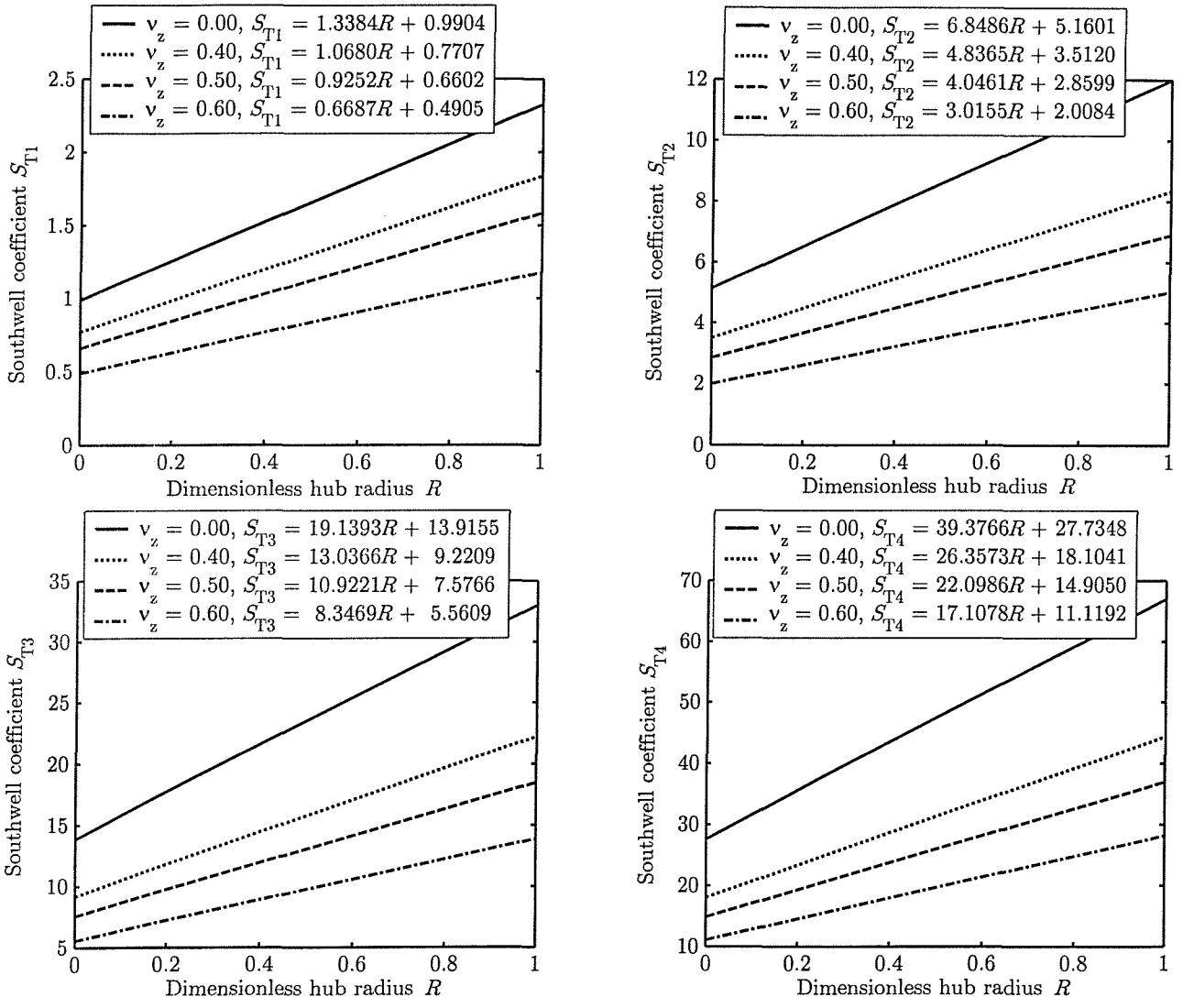

Figure 5-24: Variation of the first four SC's for tapered Timoshenko beam with $(r_{gy}/L = 0.02)$, $\nu_y = 0.25$ and $\psi = \phi = 0°$.

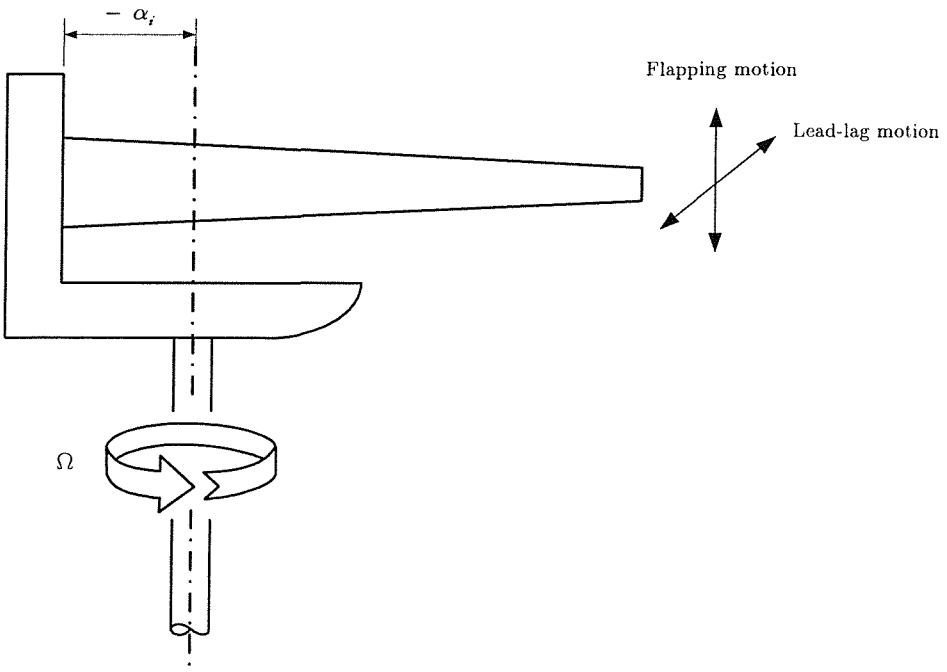

Figure 5-25: Frequency parameters near independent of the spin parameter.

represent, once again a linear relationship but with higher values of slope and intercept than those of the previous figure. This explains that as (r_{gy}/L) increases SC's decrease which is in perfect agreement with TBT. For the four modes considered, SC's are seen to increase as the hub radius increases. In addition, the difference among SC's is seen to increase as the hub radius increases. It is interesting to notice, from this figure and the previous one, that for a fixed mode, all lines representing SC's nearly intersect at some point, say (α_i, β_i). In this case one may translate the Southwell lines to the new axes $\overline{R}$, $\overline{S}_{Ti}$ via the translation $R = \overline{R} - \beta_i$ and $S_{Ti} = \overline{S}_{Ti} - \alpha_i$ where all lines will be perfectly linear i.e., according to following equation

$$S^*_{Ti} = m\overline{R}$$

where $S^*_{Ti} = \overline{S}_{Ti} - \alpha_i - p_i + m\beta_i$ is the modified Southwell coefficient for the i^{th} mode and $\overline{R}$ is the modified hub radius parameter.

From the previous figures, it can be seen that the smaller values of m are associated with the larger taper ratios; this is as one would expect, since the stiffening effect of rotation is greater when one has a larger beam mass at a large radius. Moreover this expression suggests that the natural frequency of vibration of the beam will be largely independent of the hub speed Ω, if the beam is mounted such that $R = -\alpha_i$ as sketched in Figure 5-25.

Figure 5-26, shows the first four SC's for which the taper ratio in the z-direction is kept constant ($\nu_z = 0.30$) while varying ν_y. Again, it can be seen from this figure that SC's corresponding to the first four modes increase as the hub radius increases. Comparison of these predictions with those of the previous figure, reveals that increasing the taper ratio in the y-direction renders the values of SC's of the overtone modes lower than those of Figure 5-24. In contrast, the slopes of the S_{T1} lines experience a reverse trend. In addition, it is seen that S_{T4} for the fourth bending mode (the second lagging mode) experiences great sensitivity to R and does not vary linearly with it for $R > 0.75$ as shown in Figure 5-26.

In another example, the first four SC's of the previous beam have been computed and illustrated as shown in Figure 5-27 for the case where the taper ratios ν_y and ν_z vary simultaneously. The combined effect of these taper ratios is clearly seen to influence the dynamic characteristics as compared to the previous figures. While the first, third and fourth SC exhibit a decrease as the taper ratios increase, the second one experiences an opposite trend for highest taper ratios. Further, it is of interest to notice that the S_{T2} lines corresponding to taper ratios ($\nu_y = 0.15,\ \nu_z = 0.25$) and ($\nu_y = 0.60,\ \nu_z = 0.70$) intersect at $R = 0.5438$ which corresponds to $S_{T2} = 1.402$. Although S_{T2} is the same for these two lines, it cannot be concluded that the frequency parameters are similar because the Southwell relationship defined by equation (5.1) depends also on the non-rotating frequency parameter value λ_{Ni}, which can be different from one beam to another because of the taper ratios.

For the case where the taper ratios are relatively large such as ($\nu_y = 0.60,\ \nu_z = 0.70$), S_{T2} has a larger intercept and therefore has a larger value for $R < 0.5438$. For smaller taper ratios, ($\nu_y = 0.15,\ \nu_z = 0.25$), SC is the largest one for the first, third and fourth mode. However, for the second mode it is larger when $R > 0.5438$. For the fourth mode, it is shown that S_{T4} for ($\nu_y = 0.15,\ \nu_z = 0.25$) only, does not vary linearly with R as shown in Figure 5-27.

The effect of pre-cone on bending frequencies of the above rotating Timoshenko beam has also been examined in terms of SC's. Predictions have been provided for a wide range of pre-cone angles and hub radius parameters R. The taper ratios in the y- and z-directions were taken to be $\nu_y = 0.20$, and $\nu_z = 0.3$, respectively. Similar to the previous cases, the predictions depicted in Figure 5-28 show that SC's increase as the hub radius increases and they decrease as the pre-cone increases for all modes. For the first three modes, all the lines representing the relationship between SC's and R are parallel, regardless of the pre-cone angle. For the fourth mode when $\phi = 0°$ and $\phi = 30°$, the relationship between S_{T4} and R is no longer linear for $R \geq 0.75$. In addition, the S_{T4} lines become closer to each other indicating that pre-cone is not

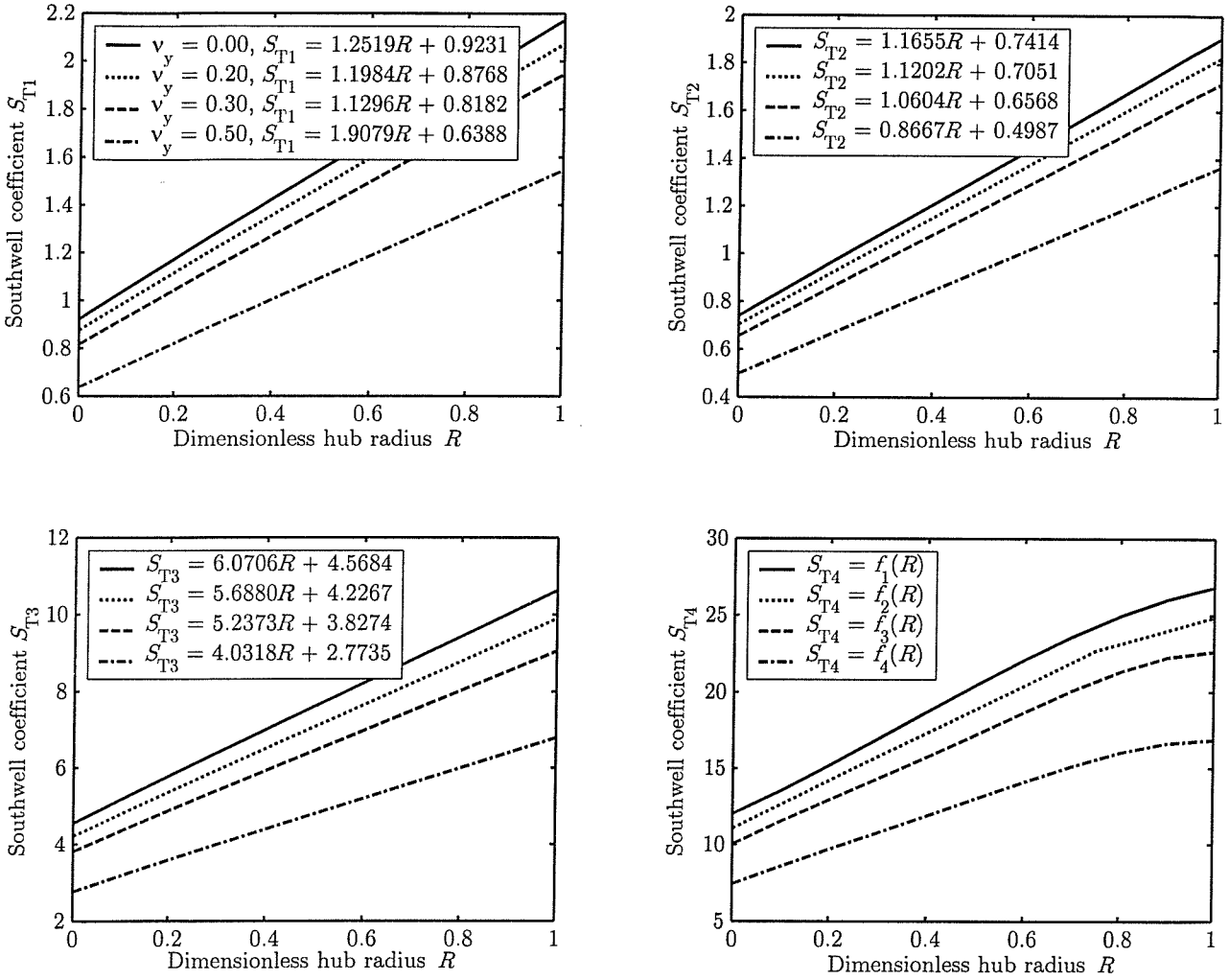

Figure 5-26: Variation of the first four SC's for tapered Timoshenko beam with $(r_{gy}/L = 0.02)$, $\nu_z = 0.3$ and $\psi = \phi = 0°$, where $f_1(R) = -23.3995R^4 + 37.6005R^3 - 18.9947R^2 + 19.5238R + 12.0033$, $f_2(R) = -17.4837R^4 + 26.2768R^3 - 12.4017R^2 + 17.4069R + 11.0833$, $f_3(R) = -17.1467R^4 + 25.8021R^3 - 12.1723R^2 + 16.1212R + 10.0399$, $f_4(R) = -10.4384R^4 + 13.9285R^3 - 6.1332R^2 + 12.0899R + 7.4239$.

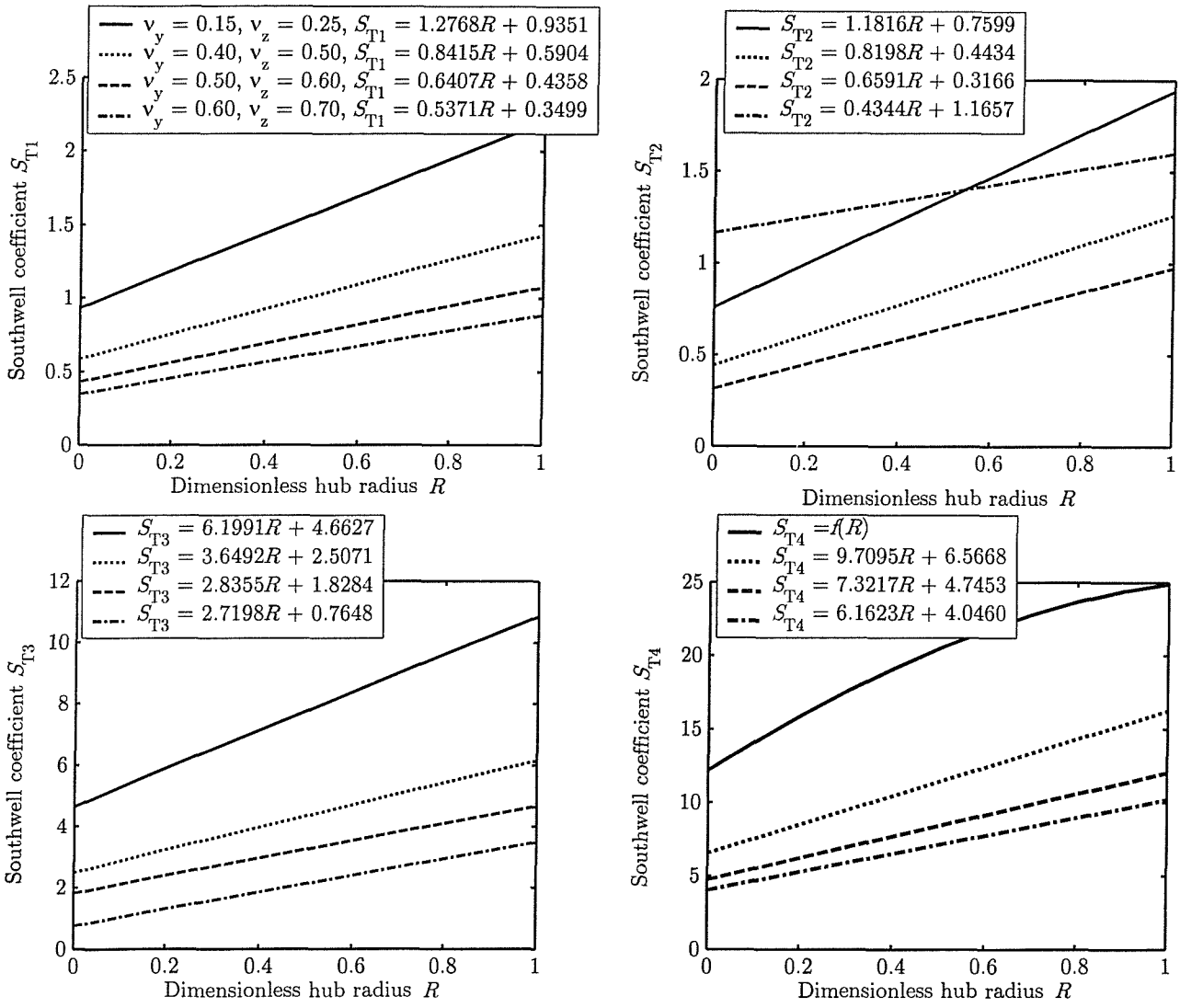

Figure 5-27: Variation of the first four SC's for tapered Timoshenko beam with $(r_{gy}/L = 0.02)$ and $\psi = \phi = 0°$, where $f(R) = -1.8496R^3 - 5.0041R^2 + 19.5377R + 12.2135$.

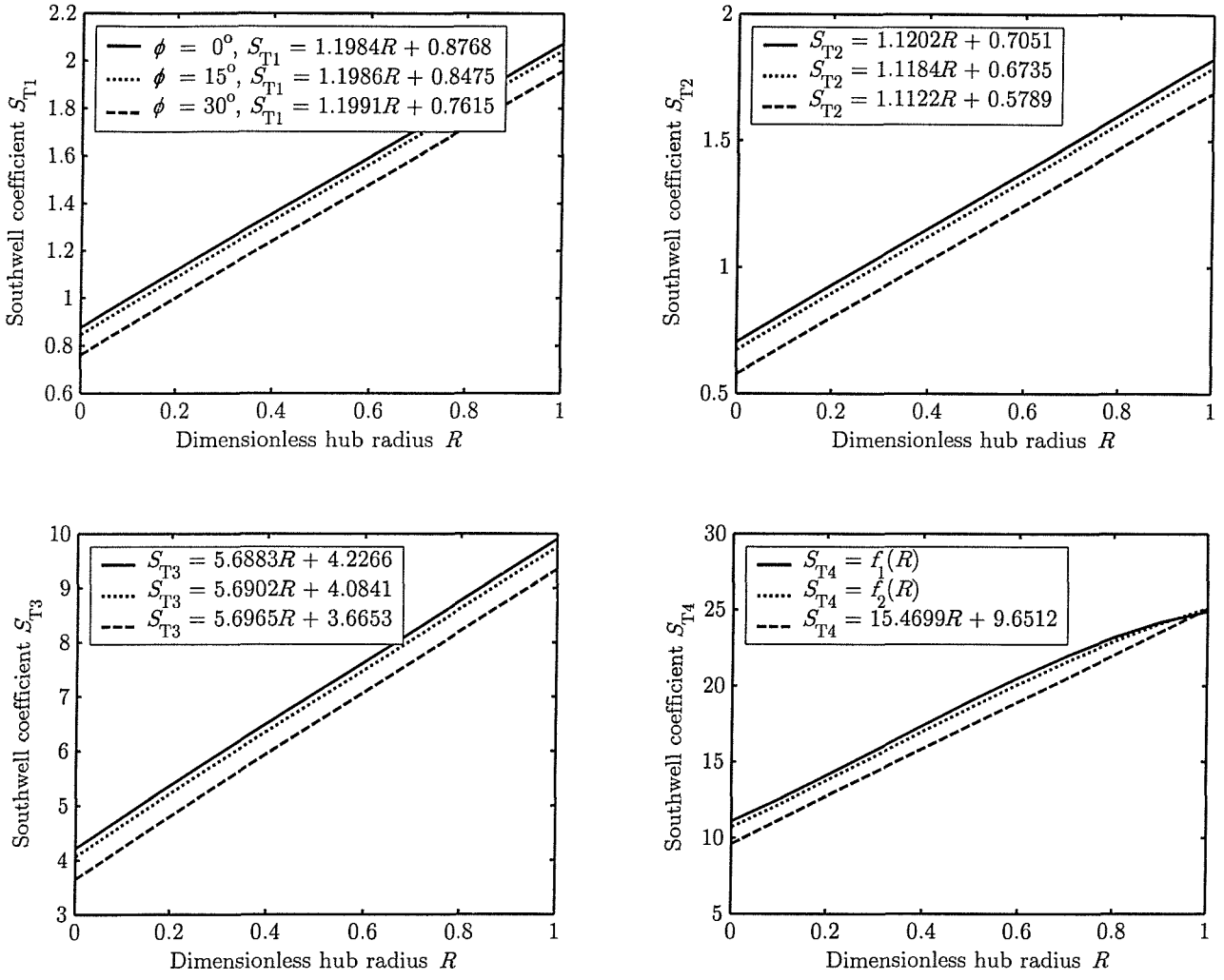

Figure 5-28: Variation of the first four SC's for tapered Timoshenko beam with $(r_{gy}/L = 0.02)$, $\nu_y = 0.2$, $\nu_z = 0.3$ and $\psi = 0^{\circ}$, where $f_1(R) = -8.6800R^3 + 8.9712R^2 + 13.5063R + 11.1075$, $f_2(R) = -5.5861R^3 + 5.6597R^2 + 14.3135R + 10.7259$.

significant as the mode number increases.

To check the accuracy of the Southwell formula, the first four frequency parameters of the above example were computed using the present simulation program and equation (5.1). The results depicted in Table 5.20 show a very good agreement with those obtained using SC'. Thus Southwell method can be regarded as an accurate and rapid estimate of the frequencies of rotating tapered Timoshenko beam without recourse to further computations or interpolation charts.

Table 5.20: Comparison of the frequency parametrs computed with two different methods for rotating tapered Timoshenko beam, $(r_{gy}/L) = 0.02$ and $\overline{\Omega} = 10$

	$\phi = 30°$			
Mode No.	$\lambda_{Ni}^2\left(\overline{\Omega}=0\right)$	Eq. (5.1)	Simulation Program	% Error
1	15.210	151.315	151.392	0.051
2	253.834	367.334	367.217	−0.032
3	396.288	1047.643	1048.553	0.087
4	2644.787	4380.937	4386.700	0.131

In Figure 5-29, the pre-cone angle ($\phi = 0°$) and taper ratios ($v_y = 0.5,\ v_z = 0.25$) were held constant while varying the setting angle ψ for a wide range of change. It is of interest to observe that for a specified mode, the lines defining SC's are all parallel. Also, the predictions show that as the setting angle increases, the SC lines decrease leading to a decrease in frequency values. The effect of varying the setting angle in the first two lower modes is more pronounced than the effect of varying the pre-cone. Further, the effect of the setting angle is significant in the first two lowest modes and is negligible on the higher ones. The reason for this is attributed to the fact that the softening term $\Omega^2 \sin\psi \cos\phi \sin(\psi + \phi)$ appearing in the equation of motion (2.217) is constant regardless of the mode considered, therefore it has more influence on modes with small frequency parameter values. Moreover, for the first two lowest modes, SC's vanish at $R = 0.086$ and $\psi = 90°$. For this case, equation (5.1) becomes $\lambda_{Ri}^2 = \lambda_{Ni}^2$, describing a rigid body mode.

It is worthwhile checking the accuracy of the Southwell formula for these first two modes where S_{T1} and S_{T2} are negative. The first two frequency parameters were computed using the present simulation program and checked with equation (5.1). To illustrate this, values of

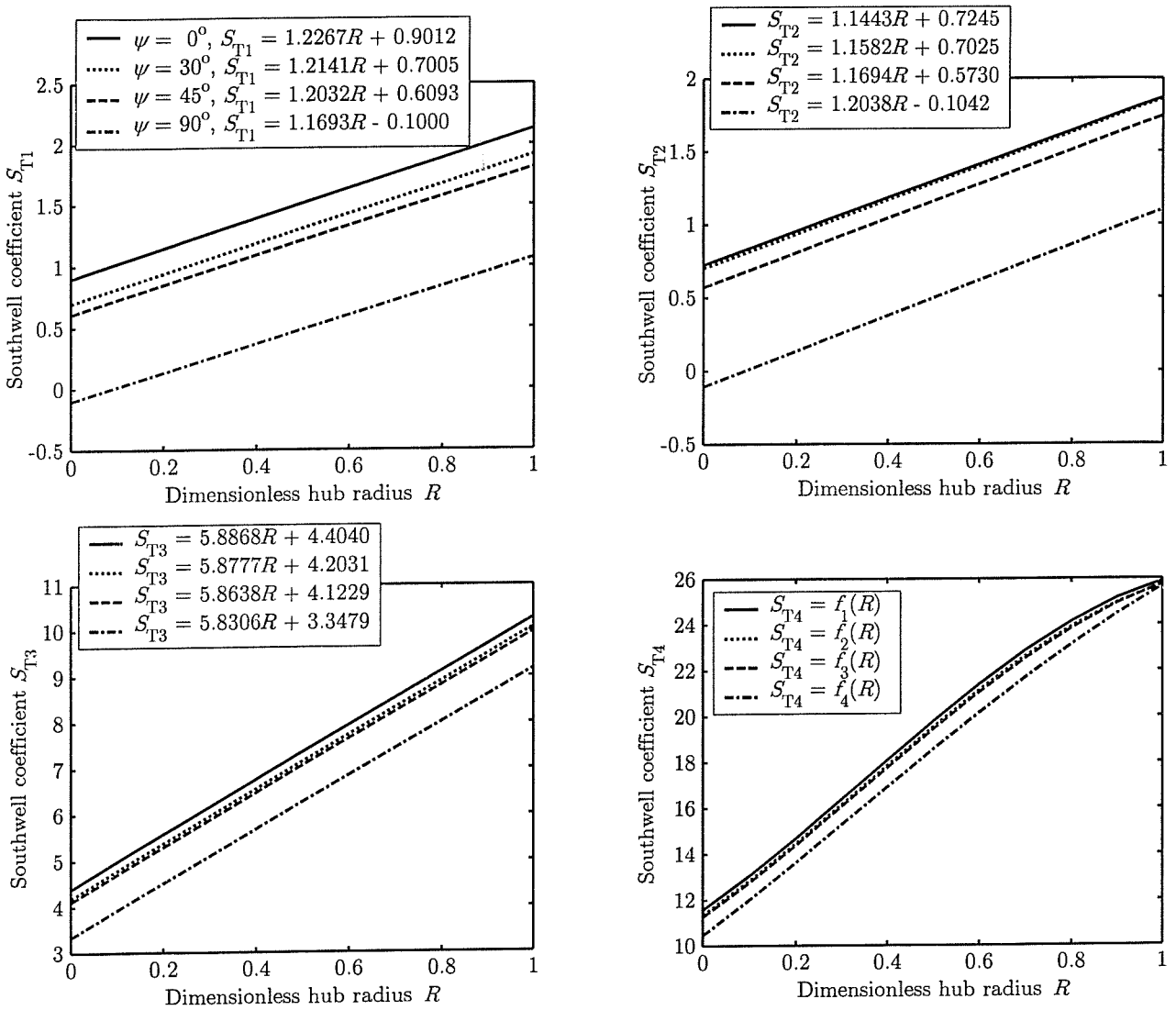

Figure 5-29: Variation of the first four SC's for tapered Timoshenko beam with $(r_{gy}/L = 0.02)$, $\nu_y = 0.5$, $\nu_z = 0.25$, $\phi = 0°$ where $f_1(R) = -8.9056R^3 + 9.2061R^2 + 14.0131R + 11.5820$, $f_2(R) = -8.4576R^3 + 8.7034R^2 + 14.1254R + 11.3683$, $f_3(R) = -7.8443R^3 + 8.0544R^2 + 14.2647R + 11.2737$, $f_4(R) = -3.7883R^3 + 3.7166R^2 + 15.2764R + 10.4630$.

$\psi = 90°$, $R = 0$, and $\overline{\Omega} = 10$ are taken for that purpose. Upon computing the above values, it was found that $\lambda_{N1}^2 = 14.6849$ and $\lambda_{N2}^2 = 225.3306$. Substituting these values into the Southwell formula gives $\lambda_{R1}^2 = 4.6899$ and $\lambda_{R1}^2 = 215.3306$ while the program gives values of $\lambda_{R1}^2 = 4.5645$ and $\lambda_{R1}^2 = 214.8616$. As can be seen, these two estimates are in very close agreement. Therefore, Southwell formula provides a quick and well suited tool for frequency prediction. The conclusion that can be drawn from this investigation is that for these particular configurations of parameter changes, the softening effect dominates the stiffening one thus rendering the frequency values of the rotating beam lower than those of the non-rotating one.

To see the combined effect of the pre-cone and setting angle on the dynamic characteristic of a rotating tapered Timoshenko beam, another example was considered and predictions are shown in Figure 5-30. In this attempt, the taper ratios in both y- and z-directions were fixed $\nu_y = 0.2$ and $\nu_z = 0.3$ while varying the pre-cone and setting angle simultaneously. From this figure it is seen that for a fixed mode the SC's lines are almost parallel, the difference between these lines is largest for the lowest mode and becomes smaller as the mode number increases. In addition, it is seen that as the pre-cone and setting angle increase simultaneously, SC's decrease and hence the frequency parameters decrease for all modes. The effect of varying these angles is highly manifested at lower modes and is insignificant at higher ones. Furthermore, for $\phi = 30°$ and $\psi = 90°$, the Southwell coefficients S_{T1} and S_{T2} pass through the origin. Comparing the results of this figure to those of Figure 5-28, it may be concluded that the combined effect of the pre-cone and setting angle is clearly shown to depress the frequency parameters to lower values than those of Figure 5-28. This is due to the fact that both the pre-cone and setting angle effects are added as a softening one that depresses the frequency values of the beam. The fourth mode is shown to exhibit a nonlinear relationship between S_{T4} and R for values that are slightly greater than 0.75.

Of particular interest is to study the case where the beam is tapered in one direction and uniform in the other one. This case is encountered in many structural components and find practical applications in flexible mechanisms, robot manipulators and spinning space structures.

Figures 5-31 and 5-32 represent the Southwell coefficients for tapered beams at a wide range of setting angles. Comparison of figures 5-31 and 5-32 reveals that the slopes and intercepts of the S_{Ti} lines corresponding to the first three modes are nearly identical; this suggests that for the parameters considered ($\nu_y = 0.0$, $\nu_z = 0.15$) and ($\nu_y = 0.15$, $\nu_z = 0.0$), the plane in which the beam is tapered is largely irrelevant when considering the effect of rotation. On the other hand, it may be seen that while the beam is uniform in the z-direction the S_{T_i} lines preserve

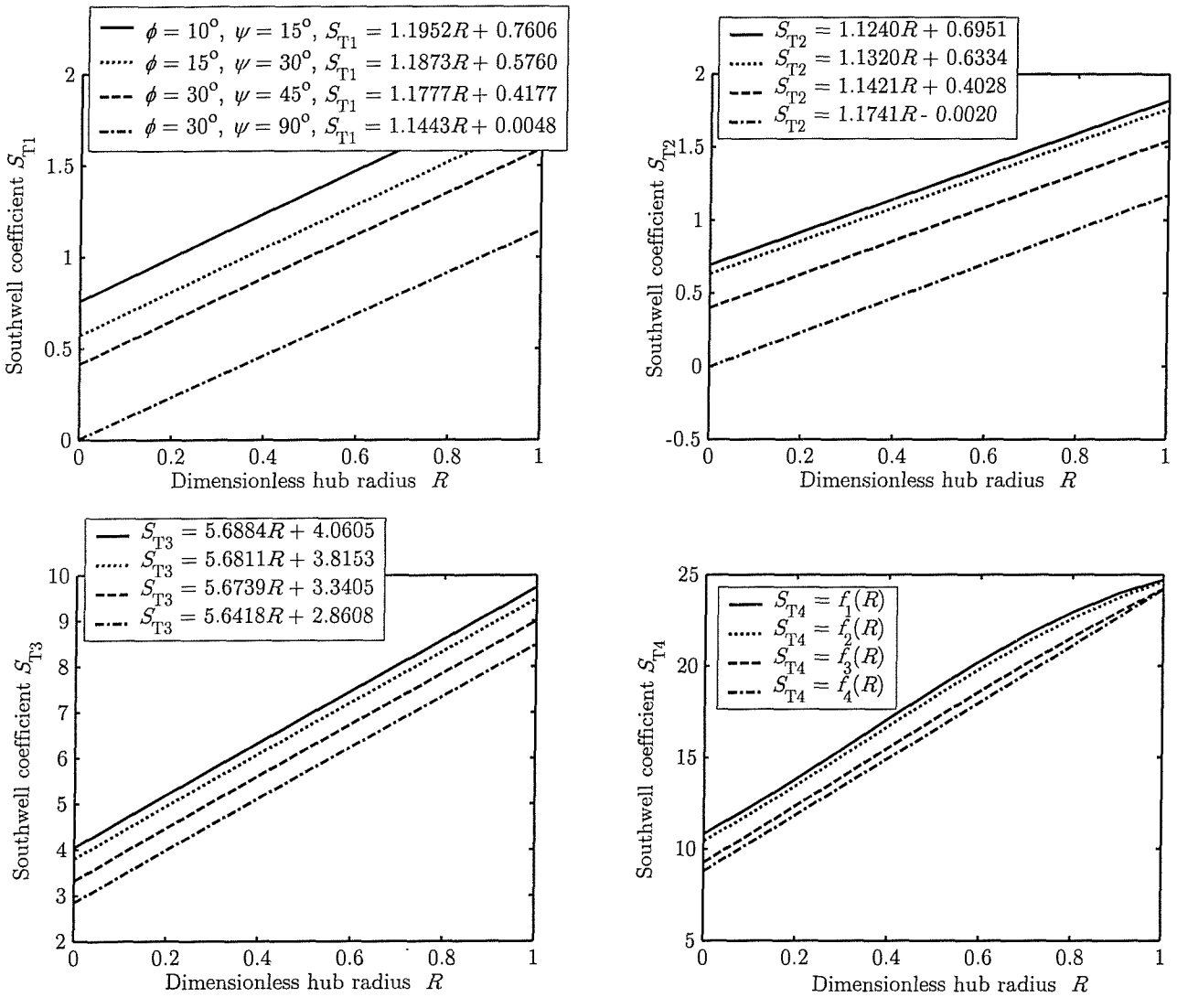

Figure 5-30: Variation of the first four SC's for tapered Timoshenko beam with $(r_{gy}/L = 0.02)$, and $\nu_y = 0.2$, $\nu_z = 0.3$ where $f_1(R) = -8.2565R^3 + 8.5065R^2 + 13.6257R + 10.8345$, $f_2(R) = -6.5429R^3 + 6.6744R^2 + 14.0611R + 10.4480$, $f_3(R) = -2.5717R^3 + 2.4257R^2 + 15.1000R + 9.2709$, $f_4(R) = 15.4068R + 8.7978$.

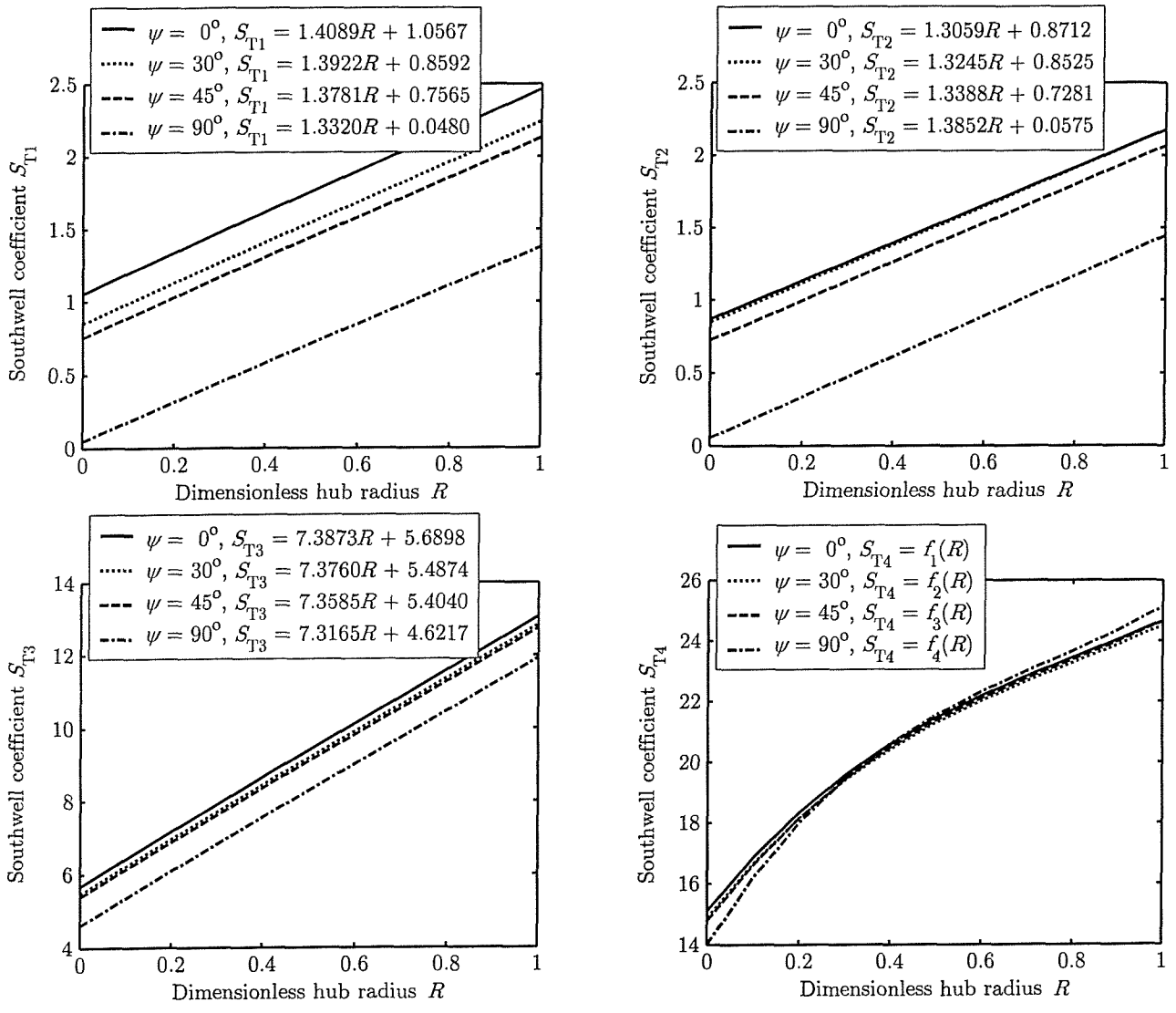

Figure 5-31: Variation of the first four SC's for tapered Timoshenko beam with $(r_{gy}/L = 0.02)$, $\phi = 0°$ and $\nu_y = 0.0$ (uniform), $\nu_z = 0.15$ where $f_1(R) = -19.0464R^4 + 44.5099R^3 - 39.224R^2 + 23.2905R + 15.0958$, $f_2(R) = -18.4139R^4 + 43.5643R^3 - 39.0043R^2 + 23.4580R + 14.8755$, $f_3(R) = -20.8053R^4 + 48.7781R^3 - 42.7621R^2 + 24.6262R + 14.7758$, $f_4(R) = -36.4725R^4 + 83.4427R^3 - 68.2949R^2 + 32.4248R + 13.9677$.

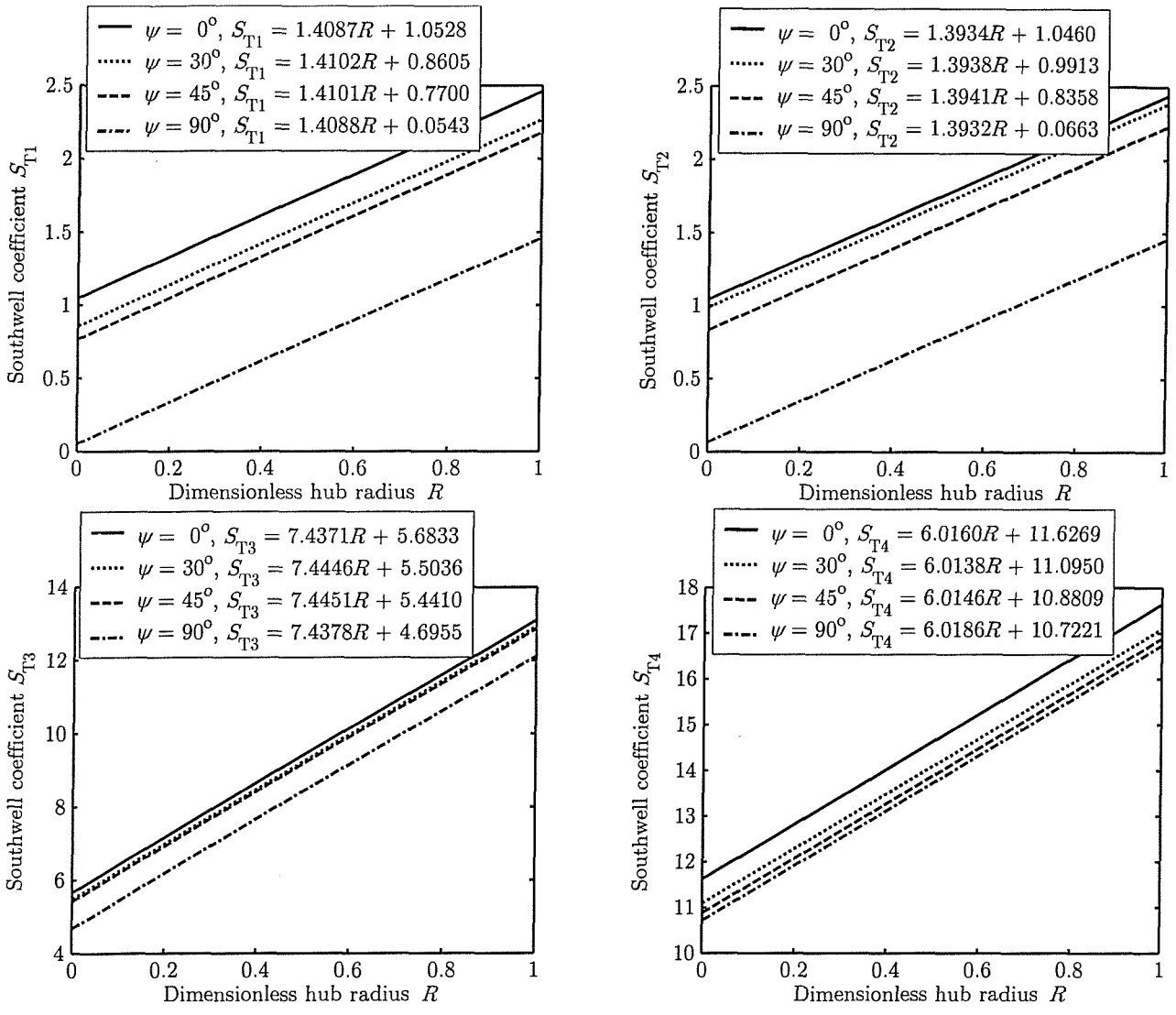

Figure 5-32: Variation of the first four SC's for tapered Timoshenko beam with $(r_{gy}/L = 0.02)$, $\phi = 0°$ and $\nu_y = 0.15$, $\nu_z = 0.0$ (uniform).

their linearity properties, and increase as the hub radius parameter increases. In contrast, when the beam is uniform in the y-direction, the S_{T4} lines are no longer linear. The difference between the resulting different curves pertinent to the fourth mode for different setting angles cannot be distinguished. The S_{T4} curves corresponding the fourth mode have positive slopes. Those with $\psi = 0°$ and $\psi = 45°$ intersect at $R = 0.39$ and $S_{T4} = 20.5$. Similar to the previous figures 5-28 and 5-29, it may be seen that the effect of the setting angle is significant at lower modes but negligible at higher modes.

Figure 5-33 shows the variation of SC's that correspond to the first four modes. In this figure, the taper ratios, as well as the pre-cone and setting angle vary simultaneously. Except for the fourth mode when ($\nu_y = 0.10$, $\nu_z = 0.25$, $\phi = 0°$ and $\psi = 30°$), the relationship between S_{Ti} and R is linear. The predictions show that the slopes and intercepts of the S_{Ti} lines decrease as the taper ratios and the pre-cone and setting angle increase. It can also be seen that as the hub radius parameter increases the difference among the S_{Ti} lines increases. It is interesting to notice that for the case when ($\nu_y = 0.50$, $\nu_z = 0.75$, $\phi = 30°$ and $\psi = 90°$), S_{T1} and S_{T2} are negative for all values of R. This can be attributed to the fact that for these particular values of parameter changes, the softening effect dominates the stiffening one thus depressing the frequency values.

Based on the previous discussion, a general formula for Southwell coefficients can be found. An attempt was made to get the S_{Ti} lines pertinent to Figure 5-33 as a general parametric equation. The resulting explicit expressions for SC corresponding to the first four modes are given by

$$\begin{aligned}
S_{T1} &= (-17.2553\nu_y + 11.4067\nu_z + 0.6147 \sin\psi \cos\phi \sin(\psi+\phi))\, R \\
&\quad - (14.1074\nu_y - 6.7666\nu_z - 1.9011 \sin\psi \cos\phi \sin(\psi+\phi)) \qquad (5.7) \\
S_{T2} &= (-15.9670\nu_y + 10.7650\nu_z + 0.4973 \sin\psi \cos\phi \sin(\psi+\phi))\, R \\
&\quad - (13.9700\nu_y - 6.9417\nu_z - 1.6743 \sin\psi \cos\phi \sin(\psi+\phi)) \qquad (5.8) \\
S_{T3} &= (-86.1600\nu_y + 62.6060\nu_z - 2.5831 \sin\psi \cos\phi \sin(\psi+\phi))\, R \\
&\quad - (66.1220\nu_y - 48.8340\nu_z + 3.8240 \sin\psi \cos\phi \sin(\psi+\phi)) \qquad (5.9) \\
S_{T4} &= (36.2640\nu_y - 37.3860\nu_z + 13.2110 \sin\psi \cos\phi \sin(\psi+\phi))\, R^3 \\
&\quad + (63.9410\nu_y - 65.9210\nu_z + 23.2940 \sin\psi \cos\phi \sin(\psi+\phi))\, R^2 \\
&\quad - (287.3100\nu_y - 199.1700\nu_z + 4.7430 \sin\psi \cos\phi \sin(\psi+\phi))\, R \\
&\quad - (186.2600\nu_y - 121.2800\nu_z - 3.1570 \sin\psi \cos\phi \sin(\psi+\phi)) \qquad (5.10)
\end{aligned}$$

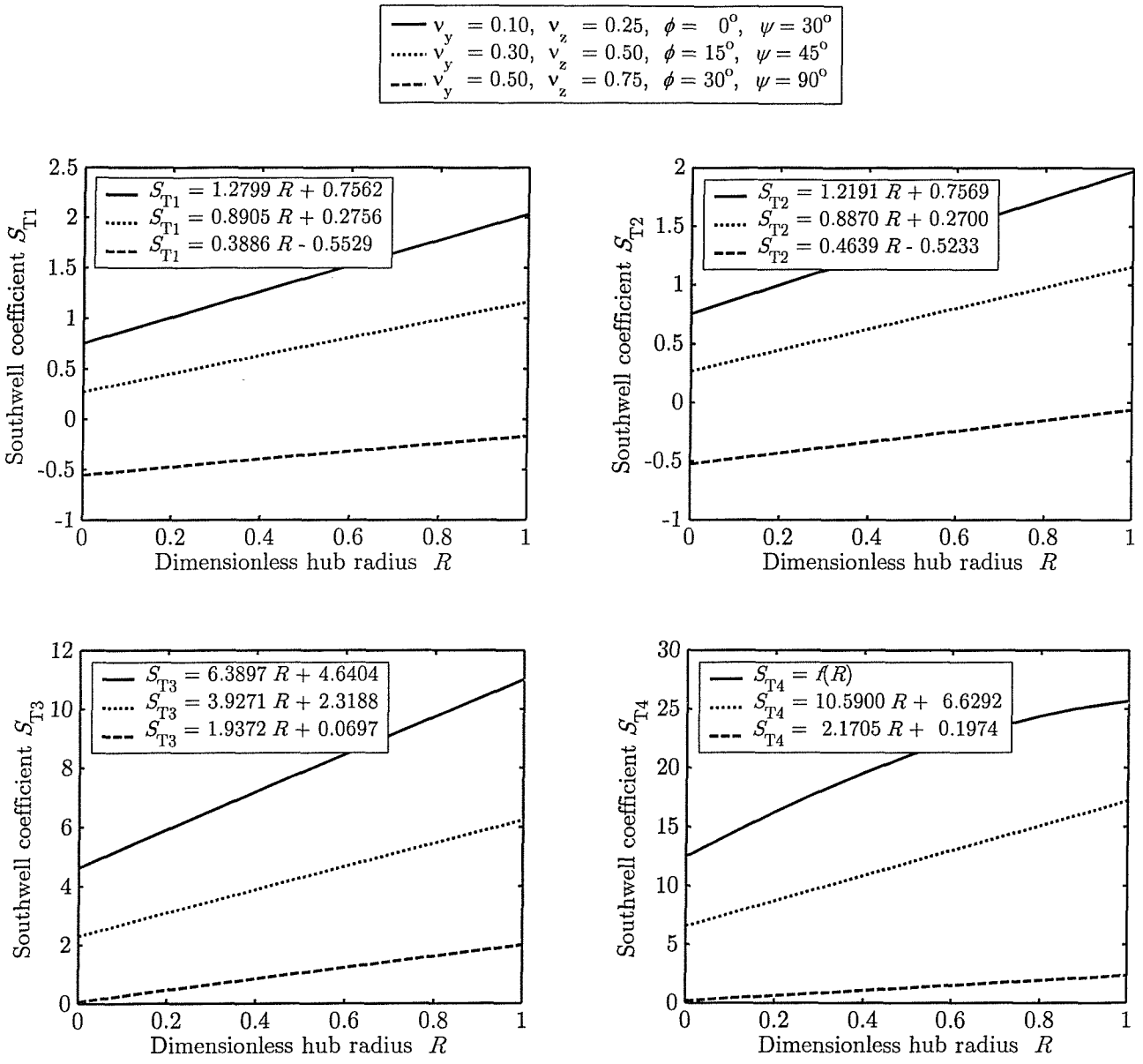

Figure 5-33: Variation of the first four SC's for tapered Timoshenko beam with $(r_{gy}/L = 0.02)$, where $f(R) = -2.4176R^3 - 4.2627R^2 + 19.8774R + 12.4832$

A single closed form solution is thus obtained for each mode within the parameter variations. The slopes and intercepts of the respective lines are seen to be a function of both taper ratios as well as the pre-cone and setting angle. It is interesting to notice that the expression for S_{T4} in its general form, does not represent a linear relationship with R. Nevertheless, it verifies the straight lines of S_{T4} for which ($\nu_y = 0.30$, $\nu_z = 0.50$ and $\phi = 15°, \psi = 45°$) and ($\nu_y = 0.50$, $\nu_z = 0.75$ and $\phi = 30°, \psi = 90°$).

Based on the above equations, it may be concluded that Southwell coefficients depend on the non-dimensional hub radius, taper ratios, the pre-cone and setting angle.

5.2.4 Reduction Schemes

The natural frequencies calculated so far were obtained using the actual full order matrices obtained from the present finite element formulation.

In this section, the natural frequencies are obtained by implementing the modal reduction schemes to illustrate the usefulness and efficiency of these techniques. Comparison will be made with the actual natural frequencies obtained from the full-order finite element formulation.

The total number of degrees of freedom for a 16 beam elements[4] is 102. When the boundary conditions are applied to a cantilever beam, the size of the system matrices given by equation (4.1) becomes of order (96×96). The planar or real eigenvalues are computed by using equation (4.20) in which the system matrices are of the same order as that of equation (4.1), resulting in 96 real eigenvalues. The complex eigenvalues are computed by means of equation (4.33) where the system matrices are of order (192×192), thus resulting in 96 conjugate pairs of pure imaginary ones which represent the natural frequencies of the beam.

Table 5.21 shows the lowest twenty frequencies of a cantilever uniform Timoshenko beam rotating at 5000 rpm. The lowest six eigenvalues are retained in the reduced system for comparison with the eigenvalues obtained using full order model.

The eigenvalues representing the planar modal reduction scheme that are presented in the second column of Table 5.22 are computed using the homogeneous part of equation (4.23). In this case the eigenvectors corresponding to the lowest six eigenvalues that are presented in the first to the sixth rows of the second column of Table 5.21 are used to form the planar modal transformation matrix of equation (4.21).

The eigenvalues representing complex modal reduction that are presented in the third column of Table 5.22 are computed using the homogeneous part of equation (4.37). Here the complex

[4]This results in having 17 nodes and each node has 6 d.o.f , so that the total d.o.f. is $17 \times 6 = 102$.

eigenvectors corresponding to the lowest six complex conjugate eigenvalues that are presented in the first to the sixth rows of the third column of Table 5.21 are used to form the complex modal transformation matrices of equation (4.38) and (4.39).

Table 5.21: The lowest twenty natural frequencies in (rad/s) of the finite element model $\Omega = 5000$ rpm, $\nu_y = 0.15$, $\nu_z = 0.3$, $R = 0.5$, $\phi = 15°$ and $\psi = 30°$

Mode No.	Planar Modes Neglecting Coriolis effect Equation (4.20)	Complex Modes Including Coriolis effect Equation (4.30)	% Difference
1	781.7068	$\pm 781.0383i$	0.085
2	2177.4729	$\pm 2171.7127i$	0.264
3	3107.2958	$\pm 3106.7616i$	0.017
4	7602.1838	$\pm 7601.7101i$	0.006
5	7919.1354	$\pm 7917.0373i$	0.026
6	9313.9896	$\pm 9308.7281i$	0.056
7	12197.9946	$\pm 12247.0237i$	−0.402
8	14016.5875	$\pm 14016.3130i$	0.002
9	20271.6294	$\pm 20255.6233i$	0.079
10	20646.1238	$\pm 20658.2633i$	−0.059
11	22151.5606	$\pm 22151.2268i$	0.001
12	31822.6458	$\pm 31822.2613i$	0.001
13	32328.3908	$\pm 32323.1537i$	0.016
14	33590.8559	$\pm 33607.8850i$	−0.051
15	34130.1945	$\pm 34132.5357i$	−0.007
16	42898.9686	$\pm 42898.6774i$	0.001
17	45104.8242	$\pm 45101.6968i$	0.007
18	48042.2541	$\pm 48043.1700i$	−0.019
19	55308.3906	$\pm 55307.8007i$	0.011
20	55630.5509	$\pm 55626.8899i$	0.066

From these predictions it can be seen that the planar modes (neglecting Coriolis effects) are higher than the complex modes (including Coriolis effects). Coriolis effects are seen to depress

the frequencies of vibration. The difference between the planar modes and complex modes is very small. Moreover, it can be concluded that Coriolis effects can be neglected at low speeds.

The planar reduction maintains almost the same level of accuracy obtained with the complex reduction, which in turn converges to the solution given by the full order model.

Table 5.22: Eigenvalues of the reduced modal matrices

Mode No.	Planar Reduction PROM = 6	Complex Reduction CROM = 6
1	$\pm 781.706522i$	$\pm 781.038273i$
2	$\pm 2177.363691i$	$\pm 2171.712750i$
3	$\pm 3107.293103i$	$\pm 3106.761606i$
4	$\pm 7602.169490i$	$\pm 7601.710152i$
5	$\pm 7917.412885i$	$\pm 7917.037327i$
6	$\pm 9316.513035i$	$\pm 9308.728118i$

In Tables 5.23 to 5.27 are presented the natural frequencies of the rotating Timoshenko beam at a wide range of parameter changes were results are presented to serve as a source of design data for applications within the given range of the tabulated parameters. In these tables, only the lowest seven frequencies were retained in order to identify the type of each mode present in this range. The torsional and axial frequencies are seen to change their position in the spectrum according to the parameter changes.

Table 5.23 shows the variation of the first seven natural frequencies for a uniform beam ($\nu_y = \nu_z = 0.0$). These frequencies increase with the rotational speed. It is interesting to notice that for this special configuration when $R = 0.5$, $\phi = 15°$ and $\psi = 45°$, torsional and axial modes are not affected by the change of spin when Coriolis effects are neglected, see Table 5.23. The Coriolis effects are seen to depress the natural frequencies for the bending and torsional modes.

The ratio of the first axial frequency to the fundamental bending mode was seen to decrease with the increase of speed. For instance, it has been found that $\omega_a/\omega_{T1} = 20$, 14 and 6.82 for $\Omega = 2000$, 5000 and 10000 rpm, respectively. Since for the given geometrical configuration of the beam, the first axial frequency remains unchanged, the ratio ω_a/ω_{T1} is decreasing because of the increase in the bending modes due to the stiffening effect of the hub rotation. In contrast,

Table 5.23: The first seven natural frequencies in (rad/s) of rotating uniform Timoshenko beam $R = 0.5$, $\phi = 15°$ and $\psi = 45°$

Ω (rpm)	Mode No.	Modal Type	Planar Modes FOM = 96	Complex Modes FOM = 192	CROM = 8	PROM = 8
2000	1	B	547.7268	$\pm 547.5426i$	$\pm 547.5426i$	$\pm 547.5443i$
	2	B	1875.5433	$\pm 1874.8602i$	$\pm 1874.8602i$	$\pm 1874.8650i$
	3	B	3090.7552	$\pm 3090.5655i$	$\pm 3090.5655i$	$\pm 3090.6655i$
	4	T	6704.4023	$\pm 6703.9221i$	$\pm 6703.9221i$	$\pm 6704.0228i$
	5	B	8294.2716	$\pm 8294.1096i$	$\pm 8294.1093i$	$\pm 8294.2509i$
	6	B	9088.5041	$\pm 9088.0700i$	$\pm 9088.0699i$	$\pm 9088.3655i$
	7	A	11016.4571	$\pm 11025.1748i$	$\pm 11025.1750i$	$\pm 11025.1782i$
5000	1	B	775.6657	$\pm 774.01967i$	$\pm 774.0324i$	$\pm 774.0197i$
	2	B	1950.8937	$\pm 1946.4678i$	$\pm 1946.4983i$	$\pm 1946.4678i$
	3	B	3436.0196	$\pm 3434.7604i$	$\pm 3435.4615i$	$\pm 3434.7605i$
	4	T	6704.4023	$\pm 6701.5404i$	$\pm 6702.1683i$	$\pm 6701.5404i$
	5	B	8675.0225	$\pm 08673.9501i$	$\pm 8674.8851i$	$\pm 8673.9502i$
	6	B	9196.3688	$\pm 9193.3865i$	$\pm 9195.2531i$	$\pm 9193.3865i$
	7	A	11016.4571	$\pm 11071.1142i$	$\pm 11071.1378i$	$\pm 11071.1141i$
10000	1	B	1277.8082	$\pm 1266.7303i$	$\pm 1266.7303i$	$\pm 1266.7942i$
	2	B	2196.5871	$\pm 2177.0204i$	$\pm 2177.0204i$	$\pm 2177.1418i$
	3	B	4447.3844	$\pm 4441.3354i$	$\pm 4441.3353i$	$\pm 4445.0375i$
	4	T	6704.4023	± 6694.5644i	± 6694.5644i	± 6697.0532i
	5	B	9570.6060	$\pm 9554.8947i$	$\pm 9554.8947i$	$\pm 9562.7179i$
	6	B	9897.4550	$\pm 9892.4507i$	$\pm 9892.4503i$	$\pm 9896.7042i$
	7	A	11016.4571	$\pm 11237.6546i$	$\pm 11237.6545i$	$\pm 11237.8350i$

B: Bending, T: Torsion, A: Axial

the axial modes are seen to increase with the spin when Coriolis effects are included. This is due to the coupling induced by the second term of equation (2.218) that includes the Coriolis forces $2\Omega\left[\widetilde{C}\right]\{\dot{e}\}$. Further, torsional modes are not affected by the spin as seen in Table 5.23. Coriolis effects are not important for low speeds, but they become of significance when the speed becomes important. For example at 2000 rpm the percentage difference between the frequencies when the Coriolis effects are accounted for and when they are neglected, is calculated to be 0.03% for the first mode and 0.04% for the second mode. For $\Omega = 10000$ rpm, this difference is seen to increase to 0.87% and 0.89% for the first and second mode, respectively. Therefore, Coriolis effects can be safely neglected at low speed for this type of rotating structures.

Table 5.24 shows the variations of the first seven frequencies with pre-cone. In this example taper ratios have been taken to be $(\nu_y = 0.25,\ \nu_z = 0.375)$. For zero setting angle, the flexural frequencies decrease as the pre-cone increases. Thus the pre-cone has a softening effect in this case. From these predictions, it can be seen that the axial and torsional frequencies are not affected by the change in pre-cone while the bending modes decrease as the pre-cone increases. This is because their constituent matrices do not depend on the setting angle and pre-cone.

Comparison of these results with those of the previous case shows that the taper ratios reduce the axial frequency and increases the torsional mode. Taper ratios are seen to increase the second mode, while they decrease the remaining bending modes of the spectrum. Notice that the torsional mode is now shifted to the fifth position, thus occupying mode number 5.

In Table 5.25 frequencies's variation are shown as a function of the setting angle ψ. Torsional modes decrease with increase in ψ, whereas the axial frequencies remains unchanged. On the other hand, the bending frequencies are seen to decrease with increasing ψ. Thus, the setting angle has a softening effect that depresses the frequency values.

In Tables 5.26 and 5.27 the taper ratios are varying while other parameters are kept constant. When the taper ratios vary, all the frequencies change according to the change in the cross-section area and the second moments of inertias resulting from the taper. When the taper ratio ν_z increases, the torsional and the second flap mode decrease while the lowest two lag modes along with the first and the third flap modes increase. When the taper ratio ν_y increases, the axial and torsional frequencies increase along with the lowest three flap modes and the first lag mode while the second lag decreases. This could be attributed to the decrease in cross-section area due to taper which renders the beam stiffer toward the tip.

Table 5.24: The first seven natural frequencies in (rad/s) of rotating tapered Timoshenko beam, $R = 0.0$, $\nu_y = 0.25$, $\nu_z = 0.375$, $\psi = 45°$ and $\Omega = 5000$ rpm

ϕ	Mode No.	Modal Type	Planar Modes FOM = 96	Complex Modes FOM = 192	CROM = 8	PROM = 8
0°	1	B	634.1266	$\pm 633.1436i$	$\pm 633.1436i$	$\pm 633.1570i$
	2	B	2224.0618	$\pm 2220.3795i$	$\pm 2220.3795i$	$\pm 2220.4181i$
	3	B	2893.3925	$\pm 2892.4303i$	$\pm 2892.4303i$	$\pm 2892.9676i$
	4	B	7183.4714	$\pm 7182.6207i$	$\pm 7182.6207i$	$\pm 7183.3740i$
	5	T	8637.1903	$\pm 8628.9737i$	$\pm 8628.9738i$	$\pm 8629.6171i$
	6	B	9224.6504	$\pm 9228.7057i$	$\pm 9228.7057i$	$\pm 9230.5307i$
	7	A	12753.0888	$\pm 12797.6191i$	$\pm 12797.6191i$	$\pm 12797.6504i$
15°	1	B	607.9264	$\pm 606.9843i$	$\pm 606.9843i$	$\pm 606.9971i$
	2	B	2216.9145	$\pm 2213.2447i$	$\pm 2213.2447i$	$\pm 2213.2832i$
	3	B	2883.1593	$\pm 2882.2002i$	$\pm 2882.2002i$	$\pm 2882.7355i$
	4	B	7175.4961	$\pm 7174.6459i$	$\pm 7174.6464i$	$\pm 7175.3988i$
	5	T	8637.1903	$\pm 8628.9325i$	$\pm 8628.9325i$	$\pm 8629.5759i$
	6	B	9221.7204	$\pm 9225.8199i$	$\pm 9225.8199i$	$\pm 9227.6441i$
	7	A	12753.0888	$\pm 12797.5984i$	$\pm 12797.5983i$	$\pm 12797.6296i$
30°	1	B	589.5859	$\pm 588.6727i$	$\pm 588.6727i$	$\pm 588.6852i$
	2	B	2212.1620	$\pm 2208.5006i$	$\pm 2208.5006i$	$\pm 2208.5390i$
	3	B	2865.7145	$\pm 2864.7599i$	$\pm 2864.7598i$	$\pm 2865.2917i$
	4	B	7157.1169	$\pm 7156.2703i$	$\pm 7156.2692i$	$\pm 7157.0195i$
	5	T	8637.1903	$\pm 8628.8637i$	$\pm 8628.8634i$	$\pm 8629.5070i$
	6	B	9216.8095	$\pm 9220.9827i$	$\pm 9220.9826i$	$\pm 9222.0549i$
	7	A	12753.0888	$\pm 12797.5610i$	$\pm 12797.5614i$	$\pm 12797.5929i$

B: Bending, T: Torsion, A: Axial

Table 5.25: The first seven natural frequencies in (rad/s) of rotating tapered Timoshenko beam $R = 0.0$, $\nu_y = 0.5$, $\nu_z = 0.35$, $\phi = 0°$ and $\Omega = 5000$ rpm

ψ	Mode No.	Modal Type	Planar Modes FOM = 96	Complex Modes FOM = 192	CROM = 8	PROM = 8
15°	1	B	706.1584	$\pm 706.0292i$	$\pm 706.0313i$	$\pm 706.0292i$
	2	B	2317.3042	$\pm 2311.3439i$	$\pm 2311.4326i$	$\pm 2311.3439i$
	3	B	2969.7397	$\pm 2969.6115i$	$\pm 2969.6856i$	$\pm 2969.6116i$
	4	B	7304.5836	$\pm 7304.4629i$	$\pm 7304.5699i$	$\pm 7304.4633i$
	5	T	8744.1562	$\pm 8737.1692i$	$\pm 8740.2838i$	$\pm 8737.1692i$
	6	A	10322.5066	$\pm 10322.6872i$	$\pm 10322.7636i$	$\pm 10322.6871i$
	7	B	13493.7995	$\pm 13493.4297i$	$\pm 13493.5289i$	$\pm 13493.4292i$
30°	1	B	662.8435	$\pm 662.3928i$	$\pm 662.3928i$	$\pm 662.4000i$
	2	B	2305.3923	$\pm 2300.5929i$	$\pm 2300.5929i$	$\pm 2300.6638i$
	3	B	2962.1085	$\pm 2961.6381i$	$\pm 2961.6382i$	$\pm 2961.9089i$
	4	B	7315.9398	$\pm 7315.5131i$	$\pm 7315.5145i$	$\pm 7315.8943i$
	5	T	8743.74289	$\pm 8737.5683i$	$\pm 8737.5684i$	$\pm 8740.1443i$
	6	A	10322.5066	$\pm 10323.1785i$	$\pm 10323.1785i$	$\pm 10323.4434i$
	7	B	13543.3790	$\pm 13541.4177i$	$\pm 13541.4242i$	$\pm 13541.7706i$
60°	1	B	580.2648	$\pm 579.0854i$	$\pm 579.0854i$	$\pm 579.1044i$
	2	B	2283.3480	$\pm 2281.6448i$	$\pm 2281.645i$	$\pm 2281.6685i$
	3	B	2944.8329	$\pm 2943.4320i$	$\pm 2943.4319i$	$\pm 2944.2344i$
	4	B	7309.0278	$\pm 7307.7730i$	$\pm 7307.7731i$	$\pm 7308.8961i$
	5	T	8738.1752	$\pm 8734.2245i$	$\pm 8734.2244i$	$\pm 8735.3385i$
	6	A	10322.5066	$\pm 10324.5165i$	$\pm 10324.5165i$	$\pm 10325.2953i$
	7	B	13539.6901	$\pm 13533.9663i$	$\pm 13533.9675i$	$\pm 13534.9625i$

B: Bending, T: Torsion, A: Axial

Table 5.26: The first seven natural frequencies in (rad/s) of rotating tapered Timoshenko beam, $R = 0$, $\nu_y = 0.35$, $\Omega = 5000$ rpm, $\phi = 0°$ and $\psi = 0°$

ν_z	Mode No.	Modal Type	Planar Modes FOM = 96	Complex Modes FOM = 192	CROM = 8	PROM = 8
0.1	1	B	750.6896	$\pm 750.6888i$	$\pm 750.6887i$	$\pm 750.6887i$
	2	B	2088.2869	$\pm 2081.1362i$	$\pm 2081.1362i$	$\pm 2081.2138i$
	3	B	3228.7876	$\pm 3228.7745i$	$\pm 3228.7745i$	$\pm 3228.7745i$
	4	B	8146.8907	$\pm 8146.8153i$	$\pm 8146.8149i$	$\pm 8146.8194i$
	5	T	8626.8199	$\pm 8626.9050i$	$\pm 8626.9050i$	$\pm 8626.9164i$
	6	B	8774.7549	$\pm 8765.7989i$	$\pm 8765.7989i$	$\pm 8769.2889i$
	7	A	12234.7839	$\pm 12283.8861i$	$\pm 12283.8862i$	$\pm 12283.9219i$
0.25	1	B	746.3667	$\pm 746.3662i$	$\pm 746.3662i$	$\pm 746.3662i$
	2	B	2186.2857	$\pm 2179.2928i$	$\pm 2179.2928i$	$\pm 2179.3738i$
	3	B	3070.9405	$\pm 3070.9342i$	$\pm 3070.9342i$	$\pm 3070.9342i$
	4	B	7627.7055	$\pm 7627.6896i$	$\pm 7627.68965i$	$\pm 7627.6927i$
	5	B	8918.0559	$\pm 8909.5037i$	$\pm 8909.5037i$	$\pm 8913.0276i$
	6	T	8951.2007	$\pm 8951.2178i$	$\pm 8951.2178i$	$\pm 8951.2252i$
	7	B	12662.1332	$\pm 12709.3143i$	$\pm 12709.3143i$	$\pm 12709.3528i$
0.5	1	B	730.0808	$\pm 730.0807i$	$\pm 730.0807i$	$\pm 730.0807i$
	2	B	2414.2957	$\pm 2407.6054i$	$\pm 2407.6054i$	$\pm 2407.6947i$
	3	B	2768.2740	$\pm 2768.2587i$	$\pm 2768.2727i$	$\pm 2768.2733i$
	4	B	6663.8009	$\pm 6663.8370i$	$\pm 6663.7985i$	$\pm 6663.8008i$
	5	B	9239.1762	$\pm 9231.3035i$	$\pm 9231.3035i$	$\pm 9234.8872i$
	6	T	9624.8046	$\pm 9624.8033i$	$\pm 9624.8033i$	$\pm 9624.8065i$
	7	B	12248.5079	$\pm 12248.4683i$	$\pm 12248.5095i$	$\pm 12248.5128i$

B: Bending, T: Torsion, A: Axial

Table 5.27: The first seven natural frequencies in (rad/s) of rotating tapered Timoshenko beam, $R = 0$, $\nu_z = 0.0$, $\Omega = 5000$ rpm, $\phi = 0°$ and $\psi = 0°$

ν_y	Mode No.	Modal Type	Planar Modes FOM = 96	Complex Modes FOM = 192	CROM = 8	PROM = 8
0.1	1	B	751.0988	$\pm 751.0972i$	$\pm 751.0979i$	$\pm 751.0979i$
	2	B	1963.1385	$\pm 1955.1572i$	$\pm 1955.1573i$	$\pm 1955.2216i$
	3	B	3295.8558	$\pm 3295.8444i$	$\pm 3295.8360i$	$\pm 3295.8361i$
	4	T	7120.5680	$\pm 7120.5787i$	$\pm 7120.5787i$	$\pm 7120.5869i$
	5		8443.9017	$\pm 8443.9147i$	$\pm 8443.9169i$	$\pm 8443.9208i$
	6	B	9031.4954	$\pm 9019.3427i$	$\pm 9019.3427i$	$\pm 9023.0071i$
	7	A	11252.5521	$\pm 11308.6650i$	$\pm 11308.6650i$	$\pm 11308.7061i$
0.25	1	B	752.2307	$\pm 752.2302i$	$\pm 752.2297i$	$\pm 752.2297i$
	2	B	2002.2695	$\pm 1994.7102i$	$\pm 1994.7102i$	$\pm 1994.7806i$
	3	B	3313.2122	$\pm 3313.1924i$	$\pm 3313.1923i$	$\pm 3313.1923i$
	4	T	7853.7392	$\pm 7853.7039i$	$\pm 7853.7039i$	$\pm 7853.7154i$
	5	B	8459.4082	$\pm 8459.4657i$	$\pm 8459.4660i$	$\pm 8459.4708i$
	6	B	8843.6044	$\pm 8833.3559i$	$\pm 8833.3559i$	$\pm 8836.9237i$
	7	A	11664.7812	$\pm 11717.3267i$	$\pm 11717.3269i$	$\pm 11717.3626i$
0.5	1	B	751.4573	$\pm 751.4560i$	$\pm 0751.4560i$	$\pm 751.4560i$
	2	B	2091.0733	$\pm 2084.3469i$	$\pm 2084.3469i$	$\pm 2084.4329i$
	3	B	3354.1807	$\pm 3354.1591i$	$\pm 3354.1599i$	$\pm 3354.1599i$
	4	B	8418.8169	$\pm 8410.8856i$	$\pm 8410.8856i$	$\pm 8414.1423i$
	5	B	8509.2436	$\pm 8509.1549i$	$\pm 8509.1570i$	$\pm 8509.1646i$
	6	T	9474.8768	$\pm 9474.9709i$	$\pm 9474.9709i$	$\pm 9474.9929i$
	7	B	12580.8430	$\pm 12627.7209i$	$\pm 12627.7247i$	$\pm 12627.7601i$

B: Bending, T: Torsion, A: Axial

5.3 Dynamic Analysis

Unless otherwise stated, the material and geometrical properties for the different beams used throughout this section are similar to those summarized in Table 5.1. Several other parameters such as taper ratios, hub speed, hub radius, setting angle and pre-cone will be specified for each case under study.

The Timoshenko beam is discretized into 16 equally spaced elements. Each element has two nodes with 6 degrees of freedom for each node. The total number of degrees of freedom of is then 102. When the boundary conditions are applied to a cantilever beam, the size of the system matrices becomes of order (96×96). When the equations of motion are transformed into state space form, their order is doubled. By invoking either planar or complex reduction, only the first x lowest modes are selected and retained. Therefore the reduced state space modal equations are of order $(2x \times 2x)$. Planar Reduction Order Model (PROM) or Complex Reduction Order Model (CROM) are used by specifying the number of mode solution to be retained. The displacement profiles for each case are compared to the Full Order Model (FOM).

External loads of different types and magnitudes are applied in the vertical direction at several positions of the beam. The corresponding profile responses due to these excitations are plotted accordingly. For non-rotating beams, the profile response versus time is plotted, while for rotating beams, it is plotted versus beam rotation scaled at $\tau = t \times \Omega = t \times (2\pi N/60)$ expressed in radians. In the previous expression, t is the time, the speed N is expressed in rpm and Ω in rad/s. The frequency spectrum of the forced time signal response is obtained using Fast Fourier Transform (FFT). Unless otherwise stated, throughout this study, the sampling time is chosen to be 1 ms while the sampling frequency is 1000 Hz.

5.3.1 Non-Rotating Beam

In this section, the system equations is solved using the PROM and compared to the FOM of the Timoshenko beam.

Step Excitation

Figure 5-34 shows the flexural flapping deformations for the tip and the midpoint of the non-rotating uniform Timoshenko beam with zero setting angle and pre-cone. The input excitation is a step load of a magnitude of 100 N and is applied at the tip of the beam in the vertical direction. The peak deflections remain similar to the first one as there is no damping in the system. The two mode solution shows a small difference with the FOM.

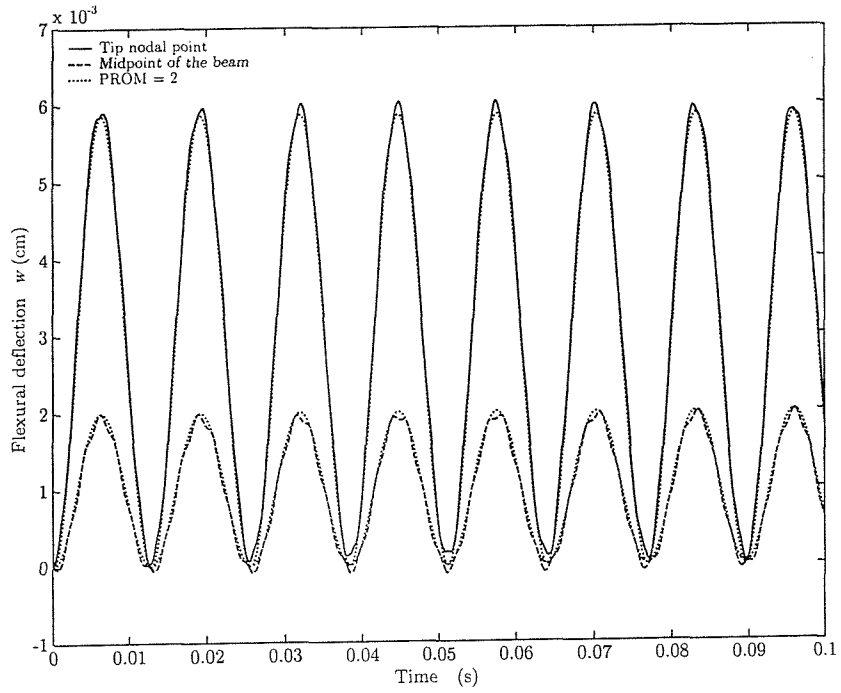

Figure 5-34: Two-mode solution for a step input load of 100 N applied at the tip of the non-rotating uniform Timoshenko beam, $\psi = \phi = 0°$ and $\mathcal{R}_o = 0$.

Increasing the selected modes to four mode solution PROM = 4 did not show any difference between the four-mode solution and the FOM, as shown in Figure 5-35. This shows that the four mode solution is sufficient to predict the system behavior and no further increase in the retained modes is required. Therefore, based on the predictions shown in Figure 5-35, it can be concluded that the planar modal reduction agrees very well with that of the FOM and results in a solution of equivalent accuracy.

Analytical Solution

An attempt has been made to obtain analytical expressions of the two mode solution in the above example by means of the convolution integral. For non-rotating beam, the reduced order model differential equation is given by

$$[M_{eer}]\{\ddot{\nu}\} + [K_r^*]\{\nu\} = \{Q_r\}$$

where the reduced mass and stiffness matrices as well the forcing vector were found to be:

$$[M_{eer}] = \begin{bmatrix} 1 & 0 \\ 0 & 1 \end{bmatrix}, \quad [K_r^*] = 10^6 \begin{bmatrix} 0.2411 & 0 \\ 0 & 3.4592 \end{bmatrix} \quad \text{and } \{Q_r\} = \begin{Bmatrix} 2.3875 \\ 7.2456 \end{Bmatrix}.$$

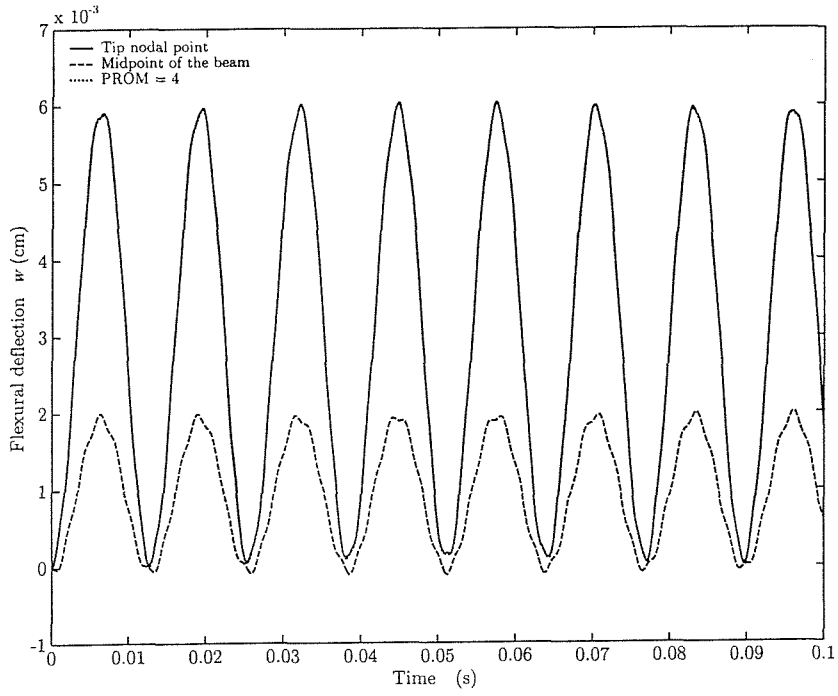

Figure 5-35: Four-mode solution for a step input load of 100 N applied at the tip of the non-rotating uniform Timoshenko beam, $\psi = \phi = 0°$ and $\mathcal{R}_o = 0$.

It is clear that the above matrices are diagonal and $[M_{eer}] = [I]$ while the stiffness matrix $[K_r^*] = diag\left[\omega^2\right]$. This results in obtaining uncoupled undamped equations of motion for which a simple solution can be obtained. The fundamental frequency of the above non-rotating uniform Timoshenko beam is $\omega_1 = 491.0717$ rad/s while the modal matrix is the identity matrix.

For zero initial conditions the solution of each equation, is the undamped convolution integral[5]

$$\{\nu\} = \frac{1}{\omega} \int_0^t Q_i(\tau) \sin \omega \left(t - \tau\right) d\tau$$

where τ is a dummy variable and $Q_i(\tau)$ is the forcing term. Therefore, the previous expression becomes

$$\{\nu\} = \frac{Q_i(t)}{\omega^2} \left[1 - \cos\left(\omega t\right)\right]$$

Recalling that $\{e\} = [\mathbb{P}]\{\nu\}$, the tip nodal point as well as the mid-point deformations of the

[5]also known as Duhamel's integral.

beam are respectively given by

$$\begin{aligned} \{w\}_{tip} &= 3.0046 \times 10^{-3} [1 - \cos(491.0717t)] \quad \text{cm} \\ \{w\}_{mid} &= 9.9004 \times 10^{-4} [1 - \cos(491.0717t)] \quad \text{cm} \end{aligned}$$

The plot of the above responses is identical to the one shown in Figure 5-34.

Damped Response

In the previous example the reduced mass and stiffness matrices using two mode planar reduction to predict the step input response were given by the above matrices $[M_{eer}]$ and $[K_r^*]$.

It is convenient to describe the damping of a structural system by a damping matrix $[D_{eer}]$ that is proportional to the mass matrix and the stiffness matrix according to Rayleigh [1]

$$[D_{eer}] = \alpha [M_{eer}] + \beta [K_{eer}] \tag{5.11}$$

where α and β are given constants. This type of damping is called proportional damping. Proportional damping has found significant applications in FEA where damping needs to be incorporated in order to carry out meaningful response analysis and prediction.

The corresponding two mode damped flexural flapping responses for the tip and the midpoint of the non-rotating uniform Timoshenko beam are shown in Figures 5-36 and 5-37 for the cases where $\alpha = 0.005$ and $\beta = 0.001$ and $\alpha = \beta = 0.05$, respectively. Figure 5-36 shows an oscillatory decaying behavior of an underdamped system with a maximum percent overshoot of 4.26×10^{-3} cm for the tip nodal point and 1.45×10^{-3} cm for the mid point of the beam. It is clearly shown that the vibration amplitude decays in time and the motion dies out.

5.3.2 Rotating Beam

This section discusses the stiffening effect induced by the hub rotation and its impact on the response profile of the beam as well as the interaction with effects from other parameters included in the model . It is divided into two subsections. The first one treats centrifugal inertia forces that are built in the model. They arise from the formulation of the problem. The second one deals with externally applied forces in addition to the centrifugal inertia forces. The response of some of the deformations versus beam rotation are shown at a wide parameter change.

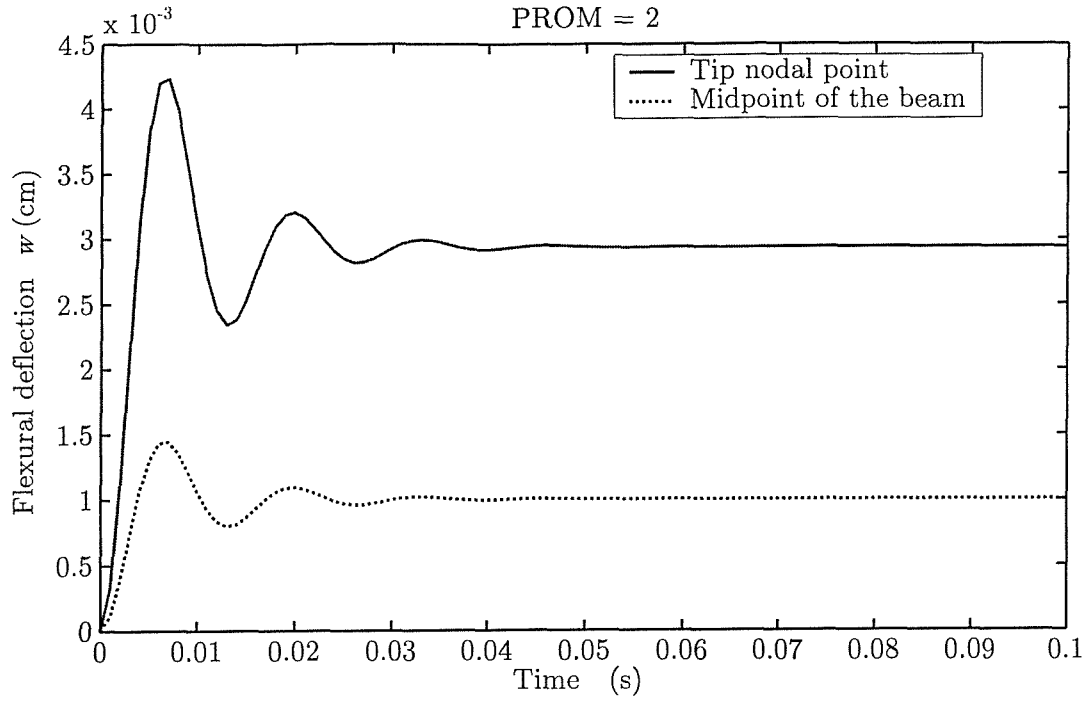

Figure 5-36: Two-mode damped response for a step input load of 100 N applied at the tip of the non-rotating uniform Timoshenko beam, $\alpha = \beta = 0.001$, $\psi = \phi = 0°$ and $\mathcal{R}_o = 0$.

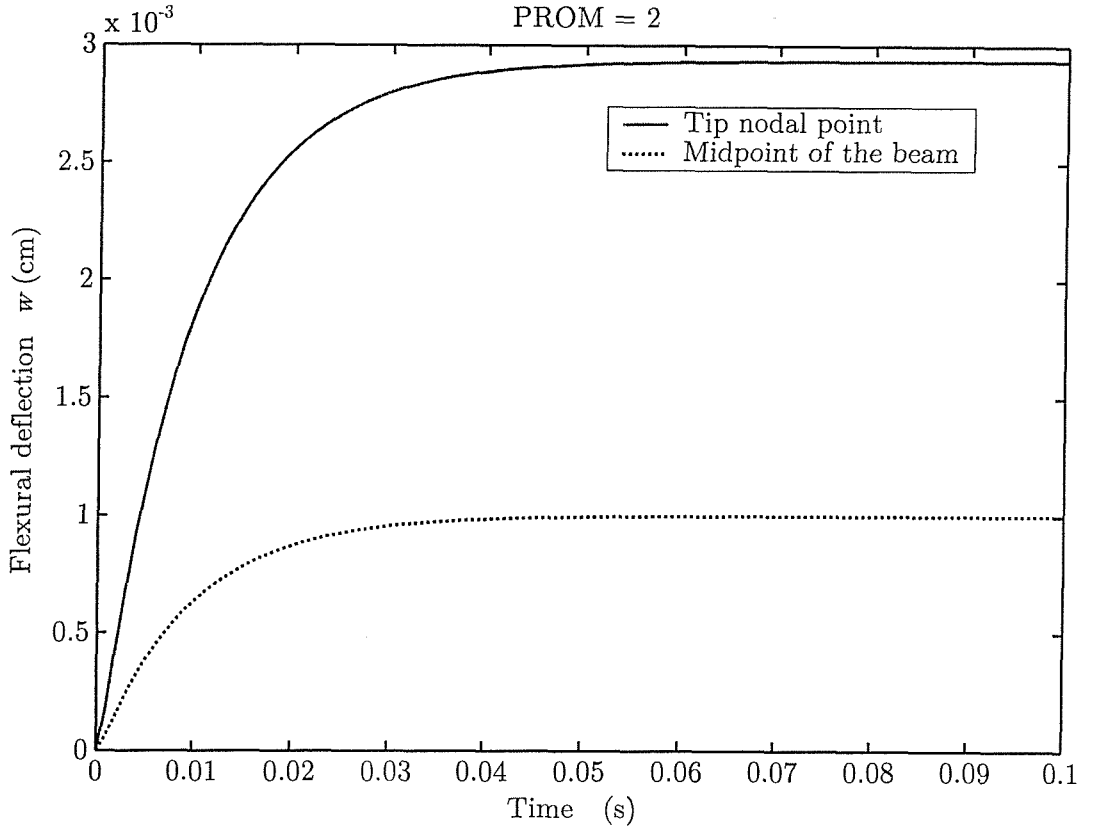

Figure 5-37: Two-mode damped response for a step input load of 100 N applied at the tip of the non-rotating uniform Timoshenko beam, $\alpha = 0.05$, $\beta = 0.01$, $\psi = \phi = 0°$ and $\mathcal{R}_o = 0$.

Centrifugal Inertia Forces

When the beam is rotating at constant speed, centrifugal elemental inertia forces $\{f_e^{i*}\} = \left(\left[m^i_{\mathcal{R}_o e}\right]^T + \left[m^i_{r_{P_o e}}\right]\right)\Omega^2$ given by equation (2.201) arise from differentiating the Lagrangian with respect to the generalized co-ordinates and time. The expressions of $\left[m^i_{\mathcal{R}_o e}\right]$ and $\left[m^i_{r_{P_o e}}\right]$ are respectively given by equations (2.55) and (2.57). Notice that $\left[m^i_{r_{P_o e}}\right]$ is invariant while $\left[m^i_{\mathcal{R}_o e}\right]$ is implicit function of time since it is function of $\varphi = \Omega t$. These forces being dependent on the position vector $r^i_{P_o}$ of the undeformed state of point P^i_o and the hub radius $\mathcal{R}_o$ exhibit a change of significance to the deformation of the structure since they are also function of Ω^2. Therefore, they should not be overlooked in this type of structures when dynamic response analysis is concerned. On the other hand, It is worthwhile to notice that the entries of the inertia forces corresponding to nodal co-ordinates w^i, θ^i_x, θ^i_y are zeros.

Figure 5-38 shows the tip flapping and lead-lag deformations of a rotating tapered Timoshenko beam for which $\nu_y = 0.35$ and $\nu_z = 0.50$. The 3.6 cm hub radius is rotating at a speed of 2000 rpm while the pre-cone and setting angle were set to 15°and 60°, respectively.

In the first trial, two-mode planar and complex reductions have been selected to predict the response of the beam. The approximate PROM and CROM solutions agree well with the full order solution as shown in Figure 5-38. However, the corresponding curves do not match perfectly at the maximum, minimum and sharp end points. The retained modes now include four-modes. A magnification (not shown here) of the resulting profiles revealed some minor mismatching with the FOM. Therefore, the truncation process is extended further to eight-mode planar and complex reductions. The eight mode-solution planar and complex reduction are seen to be in perfect agreement with the full order model since no noticeable difference could be found.

The tip profile of the lagging and flapping vibrations based on eight-mode complex solution are shown in Figure 5-39 along with those of torsional and axial deformations. Comparing the two flexural deformations, the lead-lag profile shows a very sensitive behavior to the centrifugal inertia forces. This is manifested by comparatively larger peaks. This is not surprising since the lead-lag deformations are caused mainly by the centrifugal inertia forces that are directed toward the lagging direction. In addition, the lead-lag motion is not seen to have a periodic response in the interval shown. In contrast, the flapping motion is showing a profile that is similar to a beating phenomenon with a period of 0.24 s and a maximum peak of approximately 0.25 cm. Notice that the flapping-deflections are caused by the coupling in bending due to the presence of the setting angle and the Coriolis forces induced into the system as a result of the

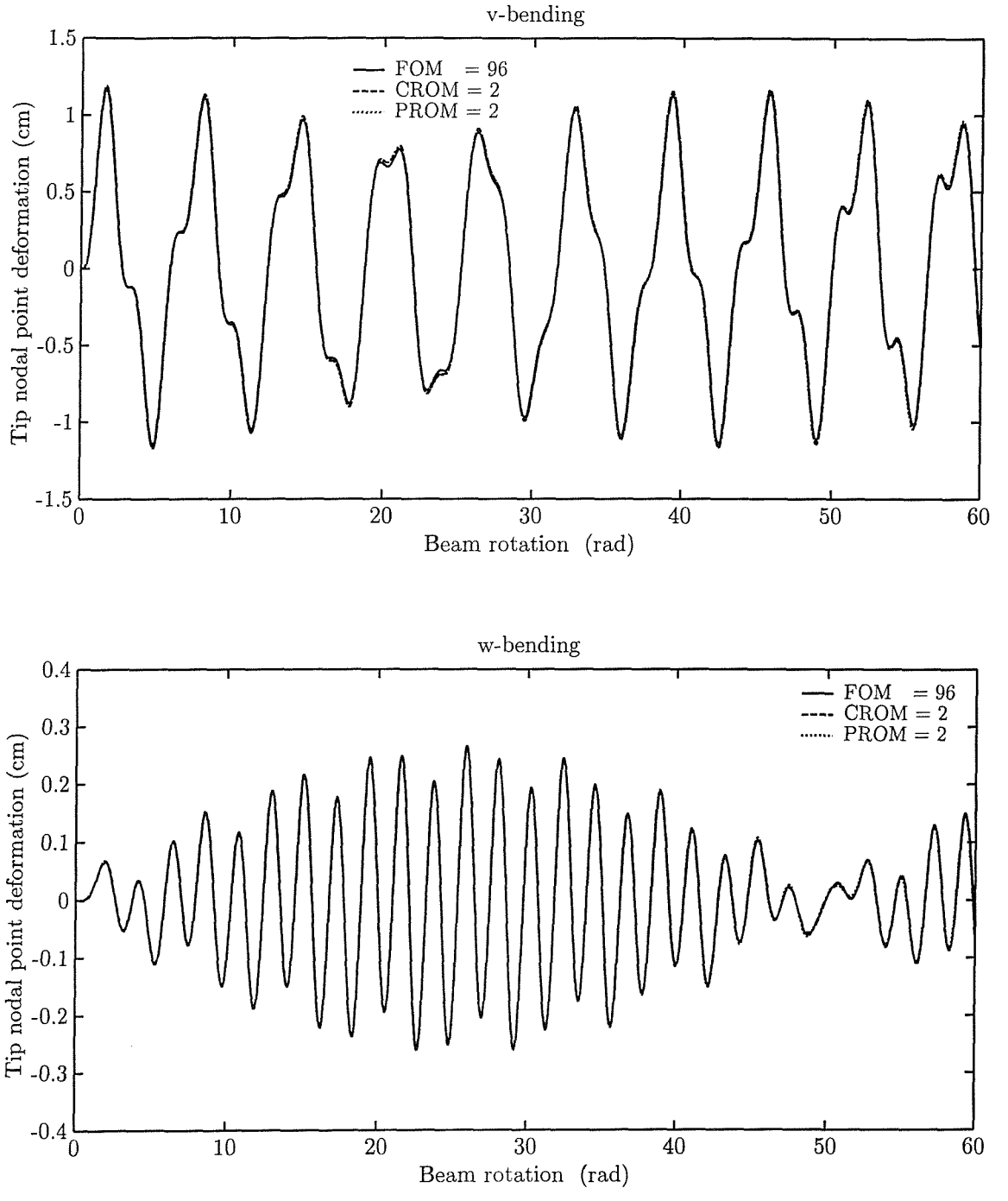

Figure 5-38: Two-mode solution for flexural responses due to centrifugal inertia forces of the rotating tapered Timoshenko beam, $\Omega = 2000$ rpm, $\nu_y = 0.35$, $\nu_z = 0.50$, $\psi = 60°$, $\phi = 15°$ and $\mathcal{R}_o = 3.6$ cm.

hub rotation.

The axial deformations are seen to have a similar shape to that of the flapping motion but with smaller amplitudes. The torsional profile shows a fluctuating behavior and have smaller magnitudes than those of the axial motion. The first four natural frequencies were found to be 596.45726, 622.8545, 2650.2540 and 2879.7938 rad/s.

Of particular importance in the domain of dynamic analysis of rotating beams is to investigate whether the frequencies resulting from the forced signal representing the lead-lag response can be represented in the frequency domain. An attempt has been made to predict the frequency spectrum of the present signal using FFT. Figure 5-39 shows the signal representing the response of the lead-lag motion for the previous beam along with the spectral density of that signal using FFT. The lowest six dominant frequencies and their corresponding magnitudes are shown along with the frequency spectrum of Figure 5-39. The first forced frequency is 27.92321 Hz which is equivalent to 175.4467 rad/s or 0.3 times the first natural frequency.

In order to better understand the effect of the setting angle on the dynamics characteristics of the previous beam, another example is given. In this attempt, the setting angle is set to zero, while the other factors have been kept unchanged. This eliminated the coupling due to bending. As a result, the response representing the amplitude of the flapping deformation is reduced to zero while the lead-lag deformations remain fluctuating with different shapes and smaller amplitudes as shown in Figure 5-40. The natural frequencies of the beam have increased. The first four natural frequencies were found to be 625.6186, 650.4243, 2656.9401 and 2885.5883 rad/s. This explains that the inclusion of a setting angle reduces the natural frequencies of the beam and therefore increases the amplitudes of the vibrational lead-lag motion. It is interesting to notice that beam rotation corresponding to 30 rad that is to say $t = 0.143$ s represent an axis of symmetry to the lead lag profile.

The torsional deformations have a similar pattern to that of the lead-lag deformations but with a smaller amplitudes. The axial deformations are seen to decrease in magnitudes and have a smaller period of time. Noting that the axial and torsional deformations are caused by the coupling caused by the Coriolis forces.

The effect of neglecting the pre-cone on the dynamic characteristics of the previous beam is examined. This is manifested by the profiles shown in Figure 5-41. As a result, the first four natural frequencies experience a slight increase when compared to the previous case. They were found to be 626.3586, 651.1342, 2657.6835 and 6544.4497 rad/s. This is due the fact that the arm associated with the radial component of the centrifugal force depends on the quantity

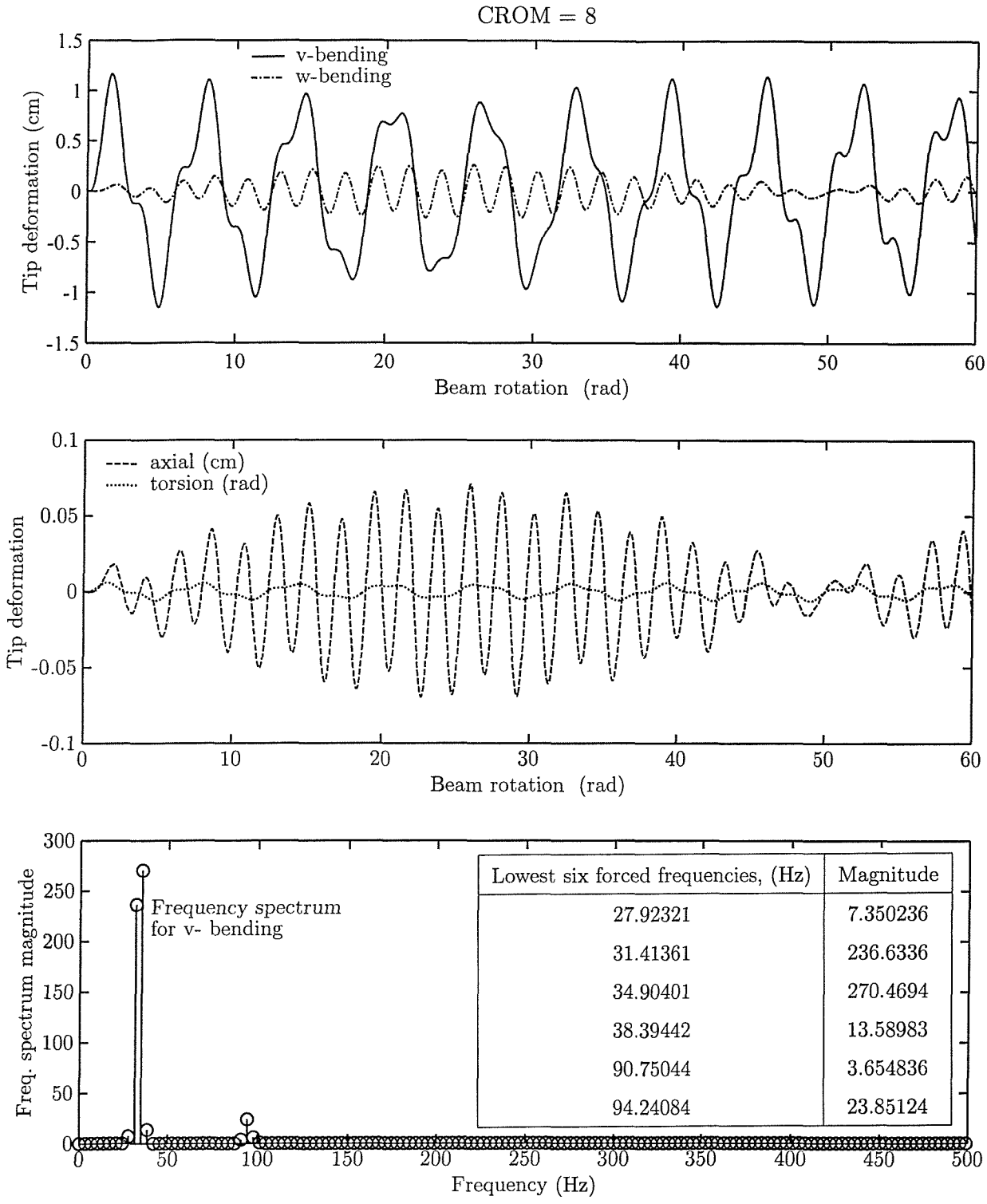

Lowest six forced frequencies, (Hz)	Magnitude
27.92321	7.350236
31.41361	236.6336
34.90401	270.4694
38.39442	13.58983
90.75044	3.654836
94.24084	23.85124

Figure 5-39: Response due to centrifugal inertia forces of the rotating tapered Timoshenko beam and its corresponding frequency spectrum using FFT. (Ω = 2000 rpm, ν_y = 0.35, ν_z = 0.50, $\psi = 60°$, $\phi = 15°$ and $\mathcal{R}_o$ = 3.6 cm).

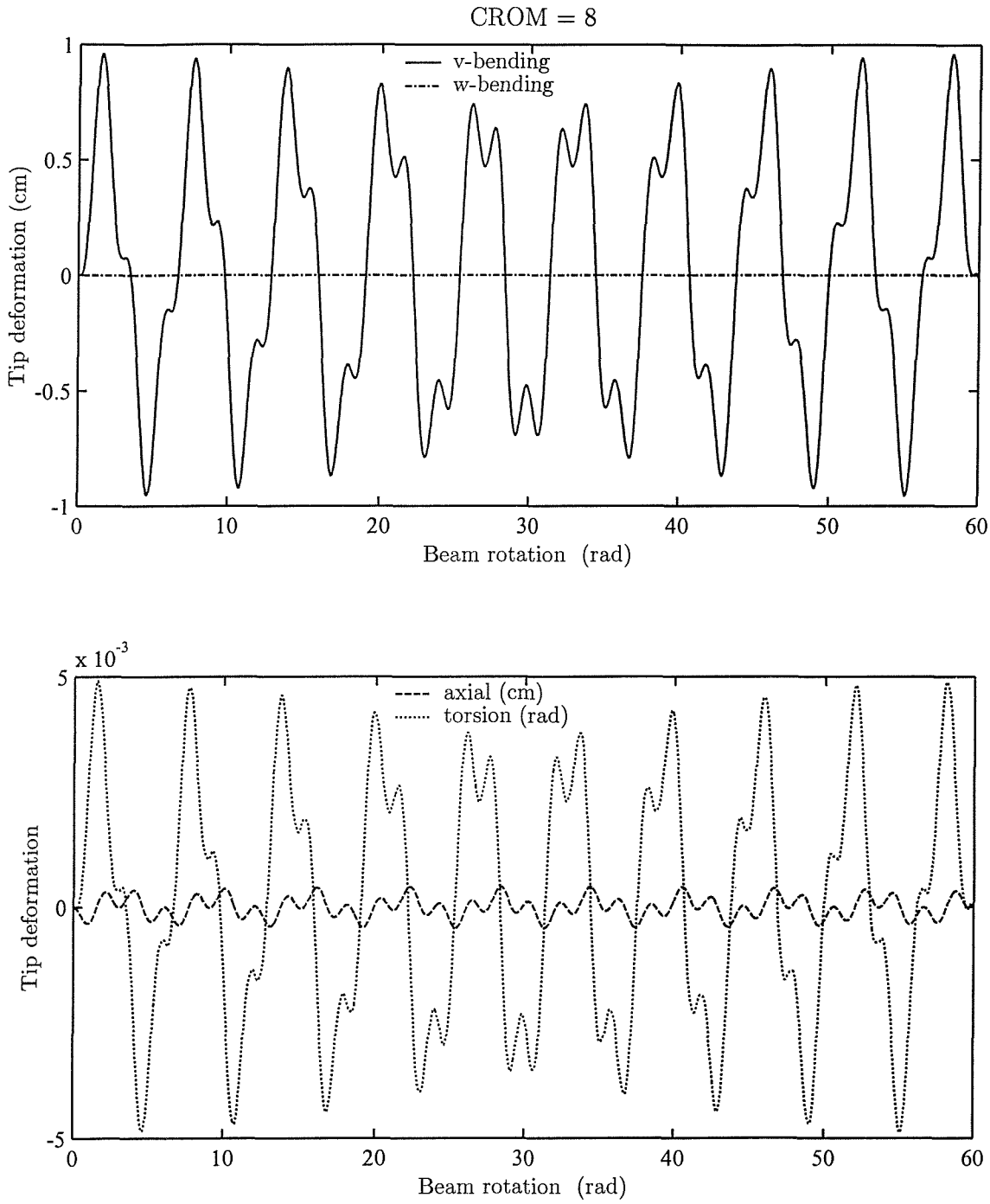

Figure 5-40: Effect of neglecting the setting angle on the response due to centrifugal inertia forces of the rotating tapered Timoshenko beam ($\Omega = 2000$ rpm, $\nu_y = 0.35$, $\nu_z = 0.50$, $\psi = 0°$, $\phi = 15°$ and $\mathcal{R}_o = 3.6$ cm).

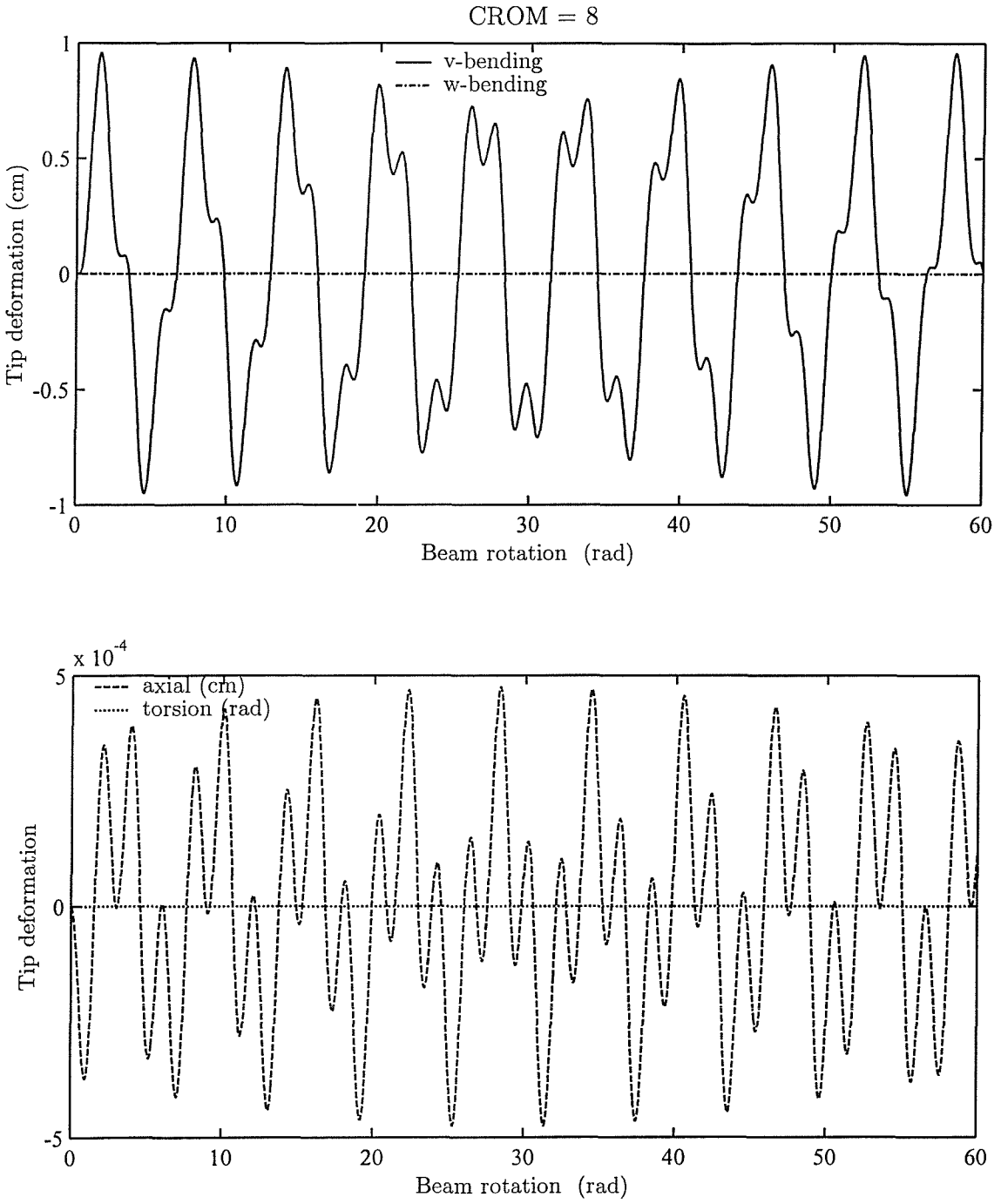

Figure 5-41: Effect of neglecting the pre-cone on the response due to centrifugal inertia forces of the rotating tapered Timoshenko beam, (Ω = 2000 rpm, $\nu_y = 0.35$, $\nu_z = 0.50$, $\psi = \phi = 0°$, and $\mathcal{R}_o = 3.6$ cm).

$(\mathcal{R}_o + r_P^i \cos\phi)$, which is maximum for $\phi = 0°$. This renders the beam stiffer, which in turn would increase the frequency values. The flexural deformations were seen to be unaffected while the torsional deformations were seen to be zero. The axial deformations are seen to be fluctuating with a very small amplitudes when compared to the previous case. Again these deformations are caused by the coupling in bending-axial deformations due to Coriolis forces. It can be concluded that the neglect of the pre-cone would result in eliminating the coupling bending-torsion that results from Coriolis forces.

To see to what extent the Coriolis forces can contribute to the dynamic characteristics of the previous beam, the Coriolis effects have been eliminated by taking the Coriolis matrix to be the null matrix. The resulting response is shown in Figure 5-42. From this figure it is clearly seen that the axial deformations becomes zero as a result of neglecting the Coriolis forces. All the other deformations remain as stated before.

To see the effect of increasing the hub speed on the dynamic characteristics of the previous tapered beam ($\nu_y = 0.35$, $\nu_z = 0.50$), a value of $\Omega = 3000$ rpm was selected. The other geometrical and material properties remain similar to those depicted in the caption of Figure 5-38. This would increase the frequencies of vibration due to the stiffening effect induced by the hub rotation if there were no setting angle. The magnitude of the centrifugal inertia forces would also increase. Consequently, this would produce a larger deformations of the beam.

Notice that although the rotating speed has increased the first two natural frequencies have decreased by 1.31% and 1.18% respectively while other higher frequencies were all exhibiting a stiffening effect. This can be explained by the fact that at high speed, the softening term $\Omega^2 \sin\psi \cos\phi \sin(\psi + \phi)$ dominates the stiffening effect and becomes more influential at high speed and lower modes rather than at higher ones since the term $\Omega^2 \sin\psi \cos\phi \sin(\psi + \phi)$ does not vary with the mode number.

The response pertinent to the deformations of the beam is shown in Figure 5-43. These profiles are characterized by higher amplitudes and different shapes. The amplitudes of the lead-lag deformations are larger than those of the flapping ones. The axial deformations have larger peaks than those of the torsional ones. In addition, the amplitudes of axial and torsional deformations are very small when compared to the flexural ones. The torsional and axial modes are higher then the flexural ones and this explains why they produce smaller deformations than the bending ones. For instance, the first axial and torsional frequencies for this example are respectively, 12154.8692 rad/s and 7209.3847 rad/s. These frequencies are respectively 20.65 and 12.25 times greater than the fundamental flexural mode.

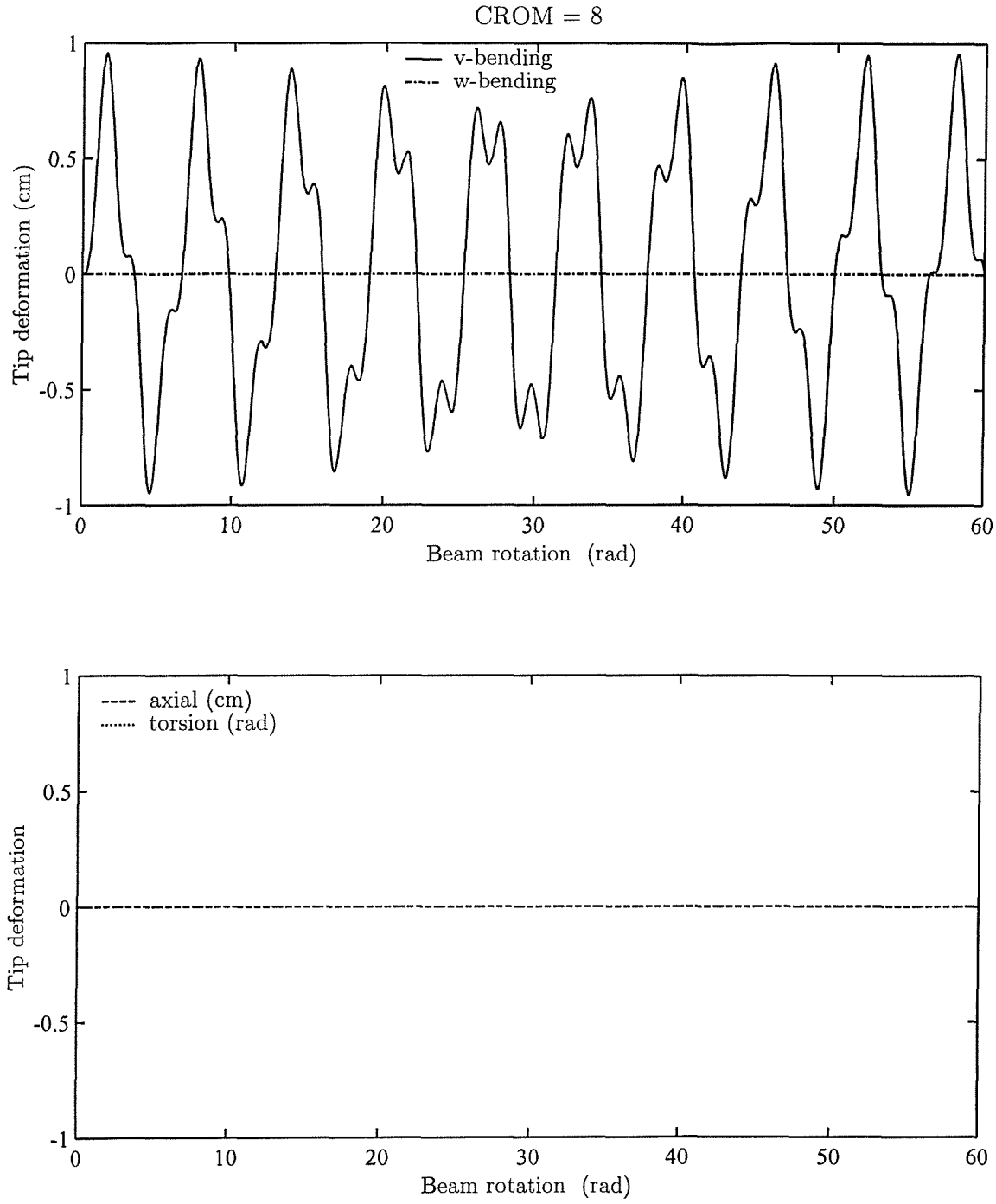

Figure 5-42: Effect of neglecting Coriolis forces on the response due to centrifugual inertia forces of the rotating tapered Timoshenko beam, ($\Omega = 2000$ rpm, $\nu_y = 0.35$, $\nu_z = 0.50$, $\psi = 0°$, $\phi = 15°$ and $\mathcal{R}_o = 3.6$ cm).

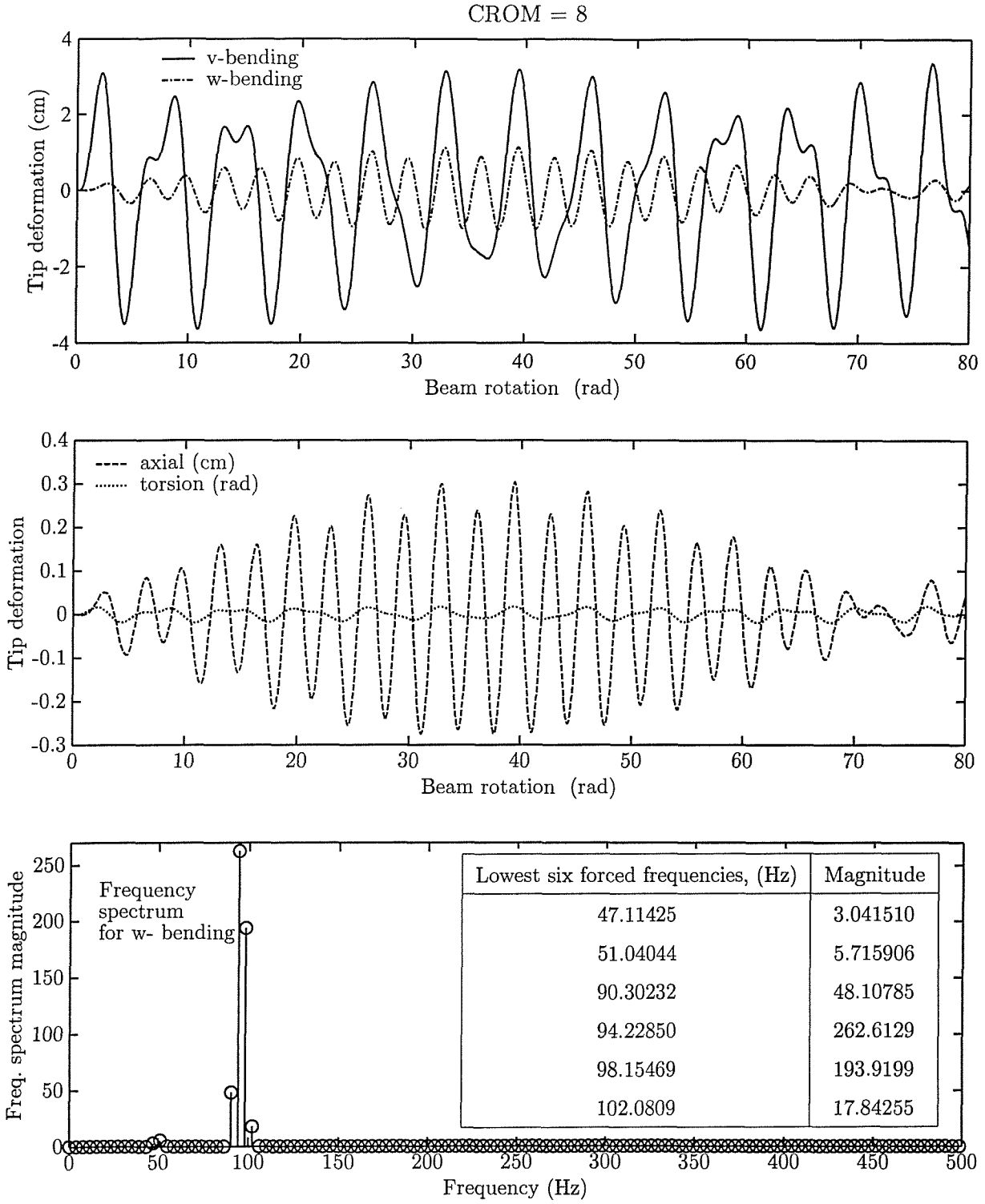

Lowest six forced frequencies, (Hz)	Magnitude
47.11425	3.041510
51.04044	5.715906
90.30232	48.10785
94.22850	262.6129
98.15469	193.9199
102.0809	17.84255

Figure 5-43: Effect of increasing the hub speed on the response due to centrifugal inertia forces of the rotating tapered Timoshenko beam and its corresponding frequency spectrum using FFT. ($\Omega = 3000$ rpm, $\nu_y = 0.35$, $\nu_z = 0.50$, $\psi = 60°$, $\phi = 15°$ and $\mathcal{R}_o = 3.6$ cm).

Figure 5-44 shows respectively, the flexural, axial and torsional tip deformations of the rotating Timoshenko beam. In this example, the beam spinning at 2500 rpm, is tapered ($\nu_y = 0.25$) in the y-direction and uniform ($\nu_z = 0.0$) in the z-direction . The setting angle and pre-cone are equal to 45° and 15°, respectively. It is clear from these figures that the eight-mode solution based on complex reduction is equivalent to the solution provided by the full order solution.

The peaks of the present flexural deformations are lower than those of the previous example. This is due to the combination of the different parameters and their effects, namely the decrease in hub speed, the change in taper ratios and pre-cone and setting angle. The decrease in hub speed reduces the centrifugal stiffness matrix, thus reducing the centrifugal forces. Further, the taper ratio decreases both the stiffness and mass of the beam. Consequently, the total stiffness of the beam is reduced.

On the other hand, it is seen that the flapping and lead-lag profiles are in phase. The peaks of the lead-lag deformations are higher than those of the flapping one.

From Figure 5-44 it can be seen that the amplitudes of axial and torsional deformations are very small when compared to the flexural ones. The torsional deformations are of negligible magnitude when compared to the axial ones. The torsional and axial frequencies are higher than the flexural ones and this explains why they produce smaller deformations than the bending ones. For instance, the first axial and torsional frequencies for this example are respectively, 11677.2560 rad/s and 8353.0295 rad/s. These frequencies are respectively 20.68 and 14.79 times greater than the fundamental flexural mode. The axial deformations have a similar pattern to that of the flexural deformations but with smaller peaks.

Notice that the value for which the beam rotation is equal to 30 (i.e., $t = 0.114$ s) constitutes an axis of symmetry for the flexural profiles as well as the axial one.

The frequencies resulting from the forced signal representing the flapping response have been computed and represented in the frequency domain. The frequency spectrum of the signal is represented along with the spectral density of that signal as shown in Figure 5-44. The lowest six frequencies and their corresponding magnitudes are shown along with the frequency spectrum of Figure 5-44.

External Forces

Impulsive and sinusoidal loads are imposed either in the vertical or lateral direction at specified nodal points such as the tip or the midpoint of the rotating tapered cantilever Timoshenko beam. The impulsive load is known to excite higher frequencies. A sinusoidal load is applied

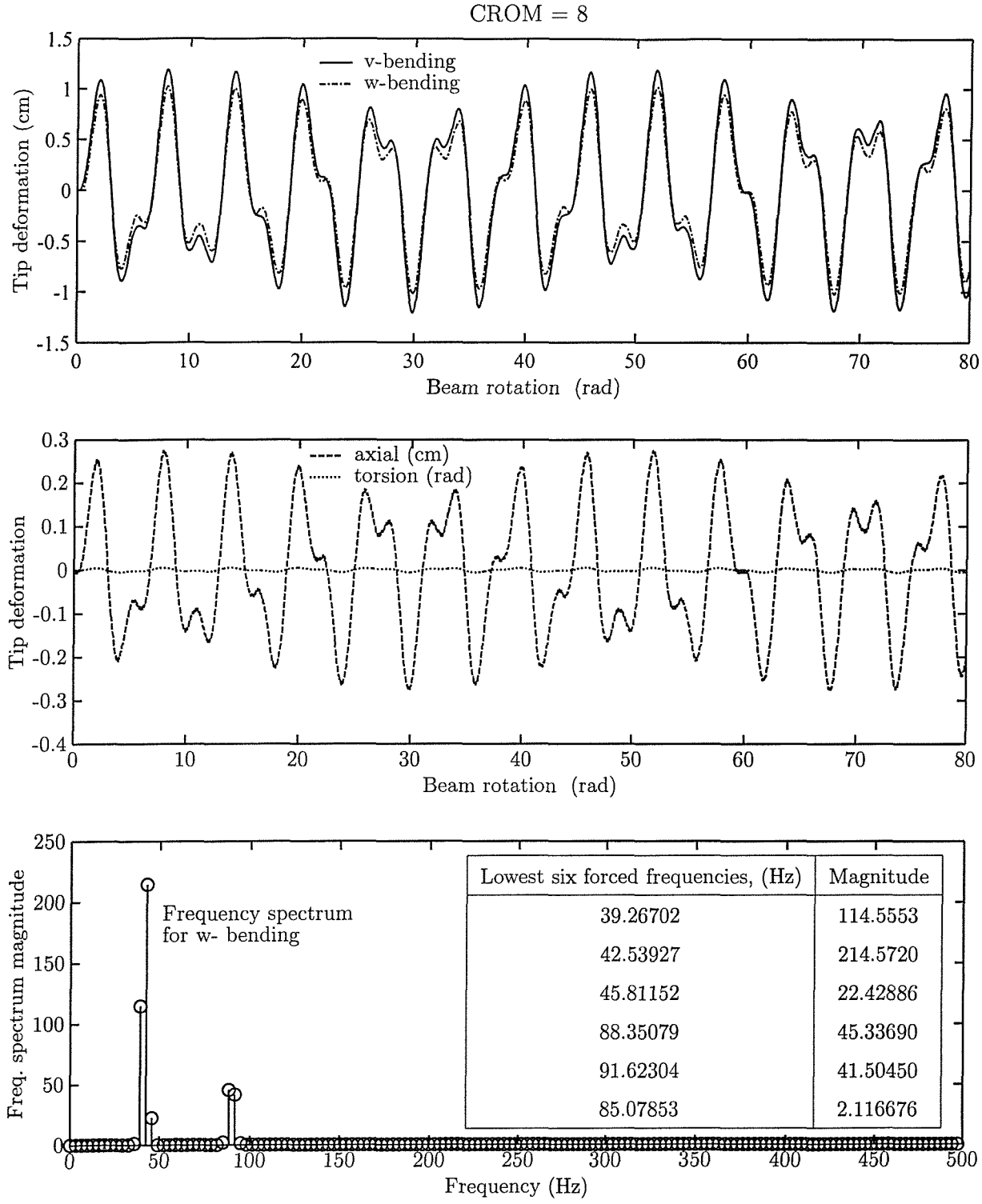

Lowest six forced frequencies, (Hz)	Magnitude
39.26702	114.5553
42.53927	214.5720
45.81152	22.42886
88.35079	45.33690
91.62304	41.50450
85.07853	2.116676

Figure 5-44: Respone due to centrifugal inertia forces for the rotating tapered Timoshenko beam and its corresponding frequency spectrum using FFT. (Ω = 2500 rpm, ν_y = 0.25, ν_z = 0.0, $\psi = 45°$, $\phi = 15°$ and $\mathcal{R}_o = 3.6$ cm).

to the structure with different magnitudes and frequencies. The effects of these external forces is added to the centrifugal inertia forces and the response of the structure is shown for several parameter changes of the beam. Unless otherwise stated the Timoshenko beam is offset with 3.6 *cm hub radius and rotating at 2000 rpm.*

Impulse excitation

In this section an impulsive load of 100 N is applied in the vertical direction at the midpoint of the beam. Impulsive loads are known to excite all the modes including the higher ones. Consequently, this load affects the whole structure and several deflected locations of the beam will be shown accordingly.

In the first trial, four-mode planar and complex reductions have been selected to predict the response of the beam. The impulsive load is applied at the midpoint vertical direction of the uniform beam where the pre-cone and setting angle are both set equal to zero. The approximate PROM and CROM solutions agree well with the full order solution as shown in Figure 5-45. However, the corresponding curves do not match perfectly at the maximum, minimum and sharp end points. The process of selecting the first few modes has been extended to include eight-mode solution. A magnification (not shown here) of the resulting profiles revealed some minor mismatching with the FOM. Therefore, the truncation process is extended further to include twelve-mode planar and complex reductions. The corresponding twelve-mode tip profile response of the beam is shown in Figure 5-46. The twelve mode-solution planar and complex reduction are seen to be in perfect agreement with the full order model since no noticeable difference could be found.

Figure 5-46 shows that the flapping motion (in the direction of force) is very sensitive to the applied force. This is manifested by comparatively larger peaks, very sharp ends and smaller period of time. This difference is due to the fact that the flapping deformations are caused only by the applied impulsive load while the lead-lag deformations are the result of the contribution of both the built in centrifugal inertia forces and the coupling due to the Coriolis forces. In Figure 5-46 are also shown the first six dominant forced frequencies and their respective magnitudes for the flapping motion.

Figure 5-47 depicts the tip response of a tapered beam for which $\nu_y = 0.1$ and $\nu_z = 0.2$ where the pre-cone and setting angle were respectively set to 0° and 45°. It is seen that the flapping and lead-lag deformations have similar fluctuating profiles but with a phase shift between them. However, unlike the previous case, the lead-lag deformations are seen to respond to the excitation with greater sensitivity because of the change in setting angle and taper ratios. This

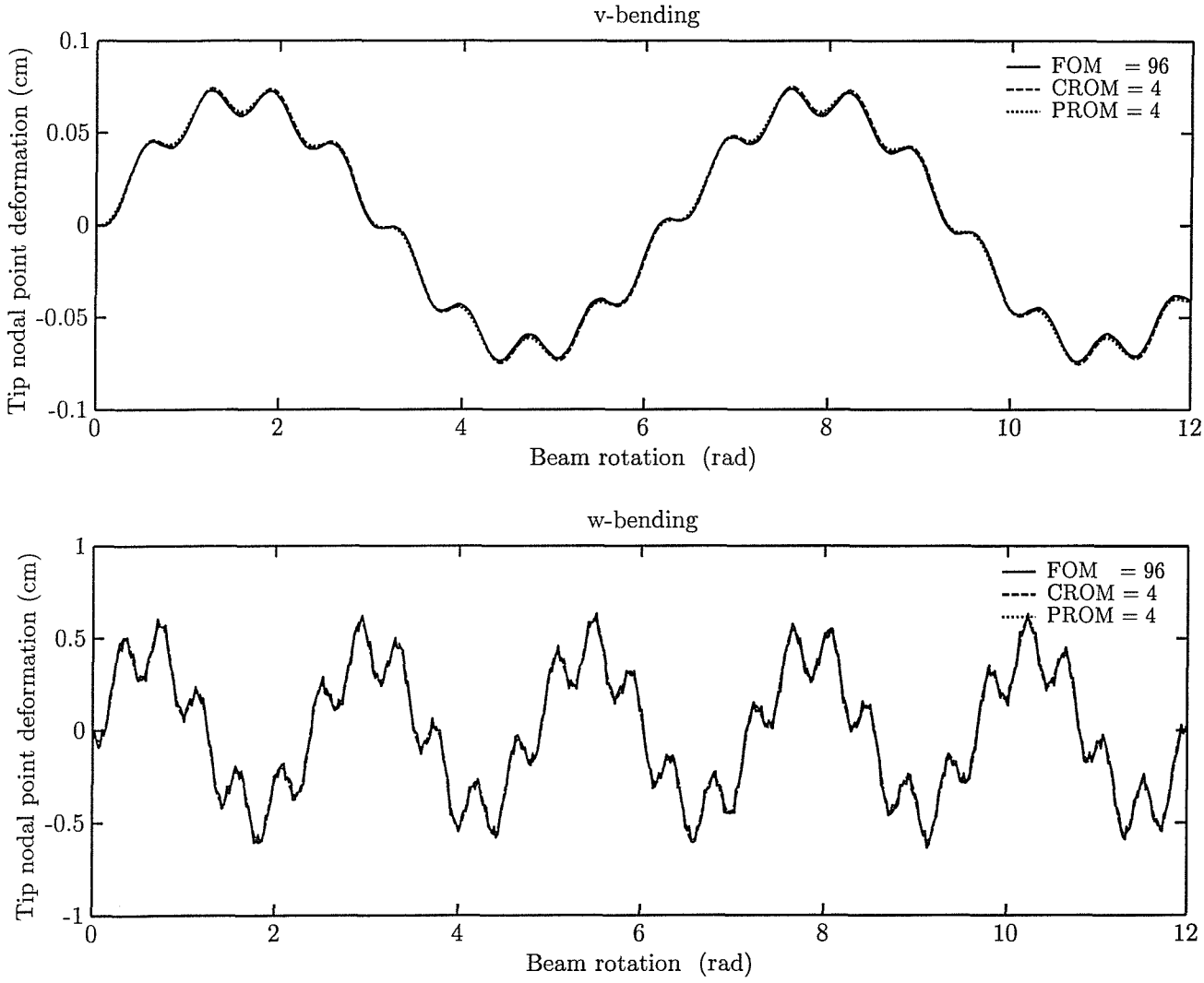

Figure 5-45: Four-mode flexural response to an impulsive load of 100 N applied at the midpoint of the rotating uniform Timoshenko beam, ($\Omega = 2000$ rpm, $\psi = \phi = 0°$ and $\mathcal{R}_o = 3.6$ cm).

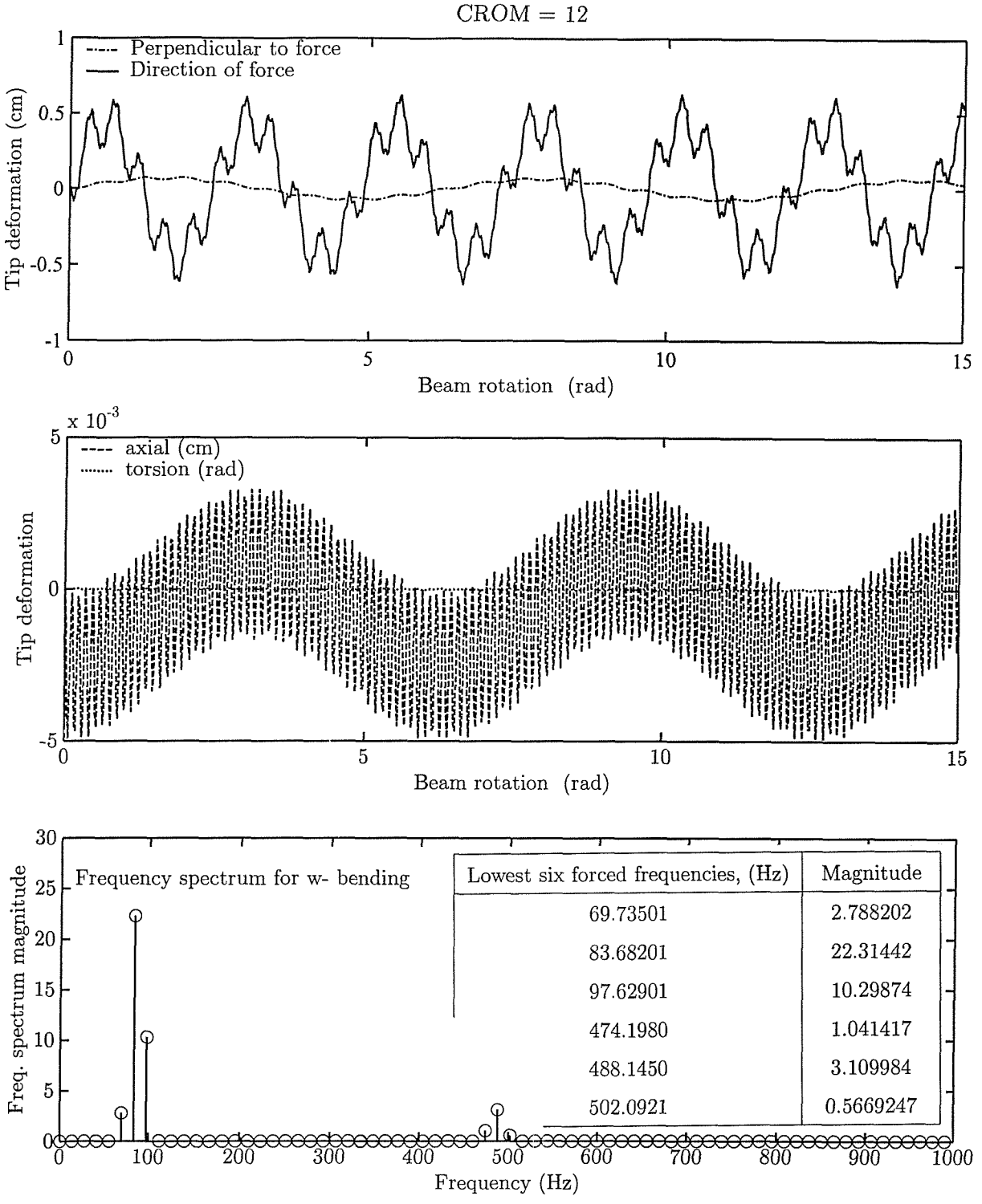

Lowest six forced frequencies, (Hz)	Magnitude
69.73501	2.788202
83.68201	22.31442
97.62901	10.29874
474.1980	1.041417
488.1450	3.109984
502.0921	0.5669247

Figure 5-46: Twelve-mode response to an impulsive load of 100 N applied at the midpoint of the rotating uniform Timoshenko beam and its corresponding frequency spectrum using FFT, ($\Omega = 2000$ rpm, $\psi = \phi = 0°$ and $\mathcal{R}_o = 3.6$ cm).

is characterized by larger flexural deflections which is not surprising since the impulsive load for this case is applied at the tip nodal point. The torsion and axial profiles have smaller peaks and periods of time as shown in Figure 5-47. They are characterized by having higher frequency values. On the other hand, the lowest six dominant forced frequencies are displayed along with the frequency spectrum for the forced flapping response. The range for these frequencies vary from 20.94241 to 94.24084 Hz with a maximum magnitude of 65.72164 Hz.

To better understand the effect of increasing the setting angle on the dynamic characteristics of the rotating tapered Timoshenko beam, the cross-section of the previous beam is oriented by a setting angle of 90° while the pre-cone remained equal to zero. The same impulsive load was applied vertically to the end point of the beam. The corresponding tip deformations are shown in Figure 5-48. It has been shown in the previous sections that the increase in the setting angle would decrease the natural frequencies of the rotating beam. This is known as the softening effect which opposes the stiffening one caused by the rotation of the beam. For instance, comparing the first two frequencies with those of the previous example, the decrease in frequency values is seen to be 3.8% for the first mode and 0.3% for the second mode. On the other hand, the maximum peaks of the tip lagging deflections are approximately three times larger than that of the flapping ones. Further, the period of the lagging deformations is approximately 12.082 rad (or 0.061 s). The flapping deformations are not seen to have any periodic motion. The torsion and axial profiles are seen to have very small amplitudes when compared to those of the bending ones.

In Figure 5-49 are shown the tip profiles of the previous beam where the impulsive load of 100 N in magnitude is applied in the lateral y-direction. The flapping and torsional motions are zero since there is no force applied in that direction. In contrast the lead-lag deformations have no periodic signal. They show more sensitivity to the excitation applied load that is manifested by sharp profile ends and higher magnitudes. This is due to the fact that these profiles are caused by both the contribution of the built in centrifugal inertia forces and the externally applied impulsive load. The frequency spectrum of the lead-lag response is shown along with the different profiles. The first five forced frequencies are seen to be lower than those of the previous example but with higher magnitudes.

Sinusoidal excitation

Sinusoidal external loads of different magnitudes and frequencies are applied at the tip nodal point of the beam. The effect of this load on the deformed structure is shown and the corre-

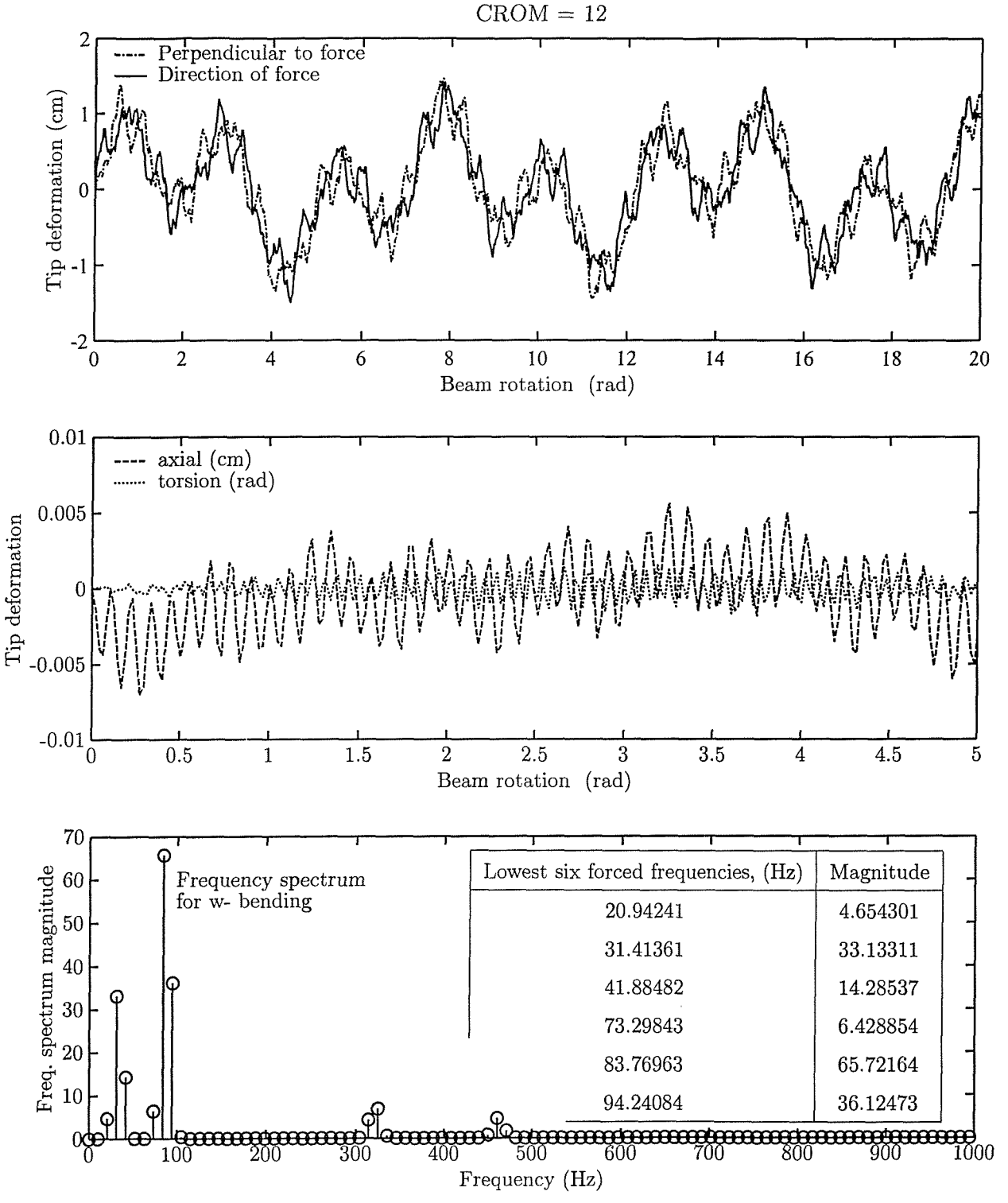

Lowest six forced frequencies, (Hz)	Magnitude
20.94241	4.654301
31.41361	33.13311
41.88482	14.28537
73.29843	6.428854
83.76963	65.72164
94.24084	36.12473

Figure 5-47: Twelve-mode response to an impulsive load of 100 N applied at the tip of the rotating uniform Timoshenko beam and its corresponding frequency spectrum using FFT, ($\Omega =$ 2000 rpm, $\nu_y = 0.1$, $\nu_z = 0.2$, $\psi = 45°$, $\phi = 0°$ and $\mathcal{R}_o = 3.6$ cm).

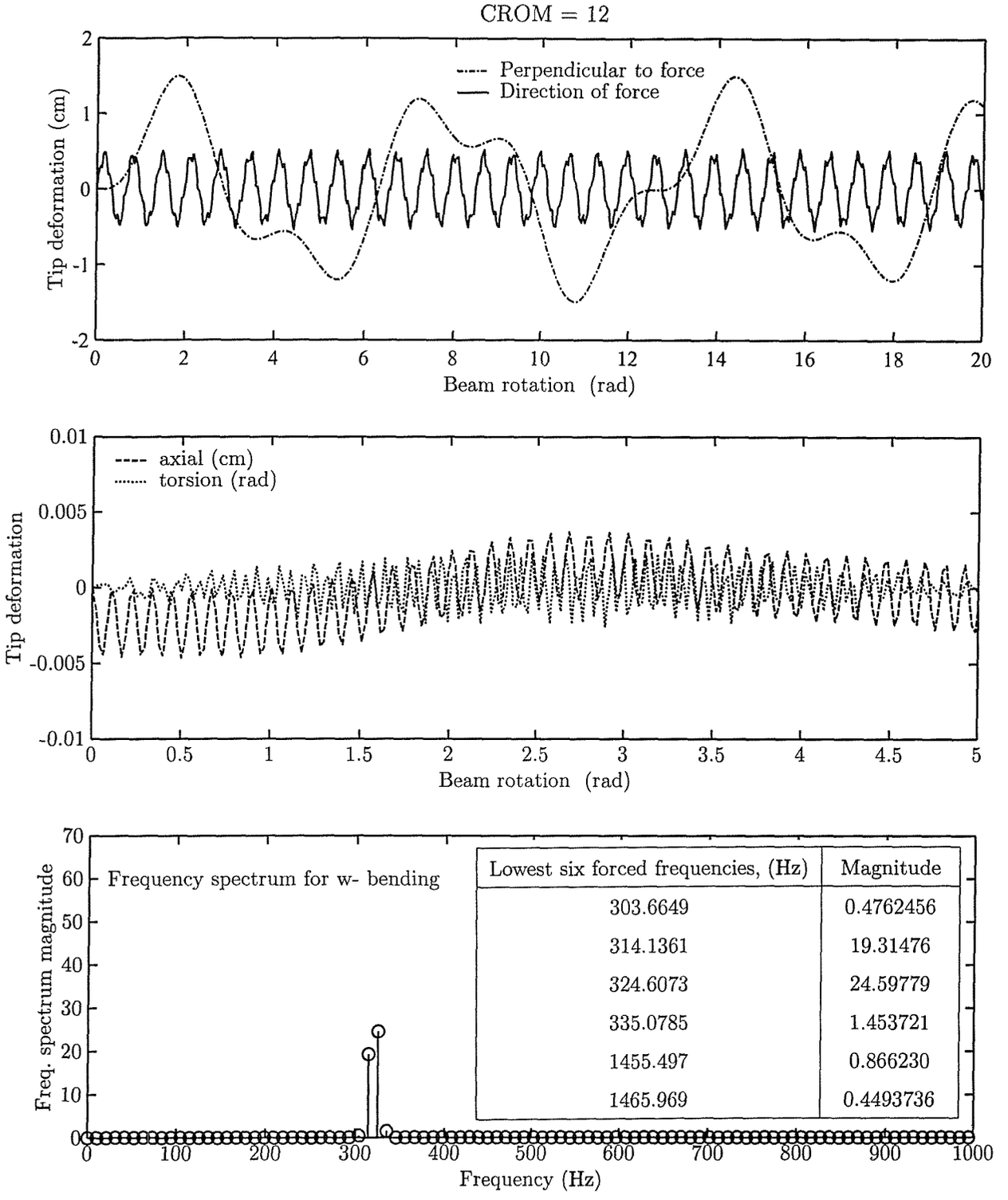

Lowest six forced frequencies, (Hz)	Magnitude
303.6649	0.4762456
314.1361	19.31476
324.6073	24.59779
335.0785	1.453721
1455.497	0.866230
1465.969	0.4493736

Figure 5-48: Twelve-mode response to an impulsive load of 100 N applied at the tip of the rotating uniform Timoshenko beam and its corresponding frequency spectrum using FFT, ($\Omega =$ 2000 rpm, $\nu_y = 0.1$, $\nu_z = 0.2$, $\psi = 90°$, $\phi = 0°$ and $\mathcal{R}_o = 3.6$ cm).

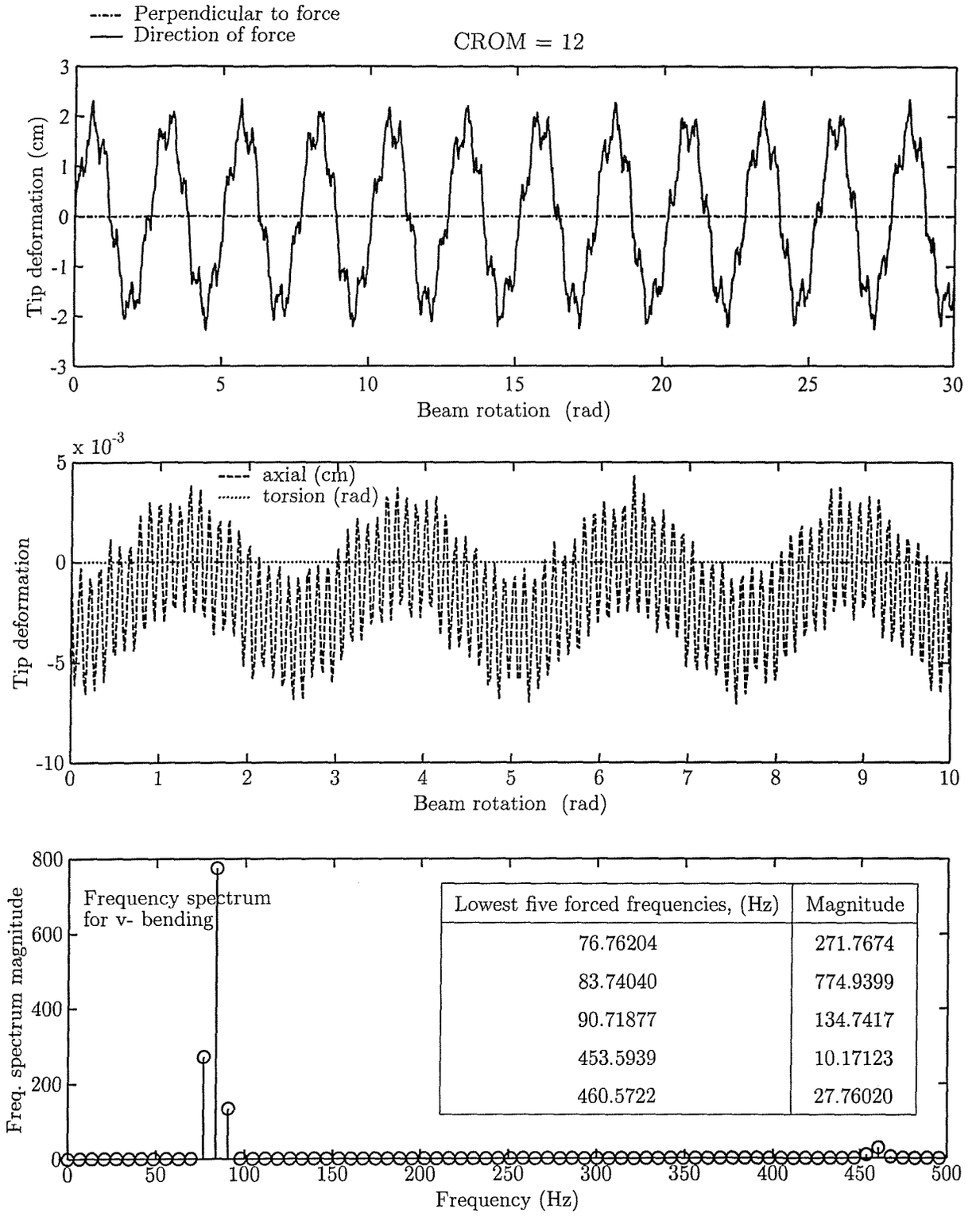

Lowest five forced frequencies, (Hz)	Magnitude
76.76204	271.7674
83.74040	774.9399
90.71877	134.7417
453.5939	10.17123
460.5722	27.76020

Figure 5-49: Twelve-mode response to an impulsive load of 100 N applied in the y-direction at the tip of the rotating uniform Timoshenko beam and its corresponding frequency spectrum using FFT, ($\Omega = 2000$ rpm, $\nu_y = 0.1$, $\nu_z = 0.2$, $\psi = 90°$, $\phi = 0°$ and $\mathcal{R}_\circ = 3.6$ cm).

sponding different response profiles is manifested at several locations of the beam.

Figure 5-50 shows the four-mode solution tip flexural deformations of the beam pertinent to complex and planar reductions. The beam is rotating at 2000 rpm and is tapered in the two planes where $\nu_y = 0.15$ and $\nu_z = 0.25$. The pre-cone and setting angle are set to 30° and 75°, respectively. The hub radius is set to zero. The applied load has the form $F(t) = 7500 \sin(610t)$ N imposed at the tip nodal point of the beam in the vertical direction. The forcing frequency $\Omega = 610$ rad/s is near the fundamental frequency of the beam $\omega = 534.4726$ rad/s. Therefore, the flexural responses of the beam are seen to exhibit a beating phenomenon as expected. This is shown in Figure 5-50. The four-mode planar solution for these profiles is shown to produce some small differences when compared to the four-mode complex solution and the full order model solution. An increase in the number of the retained modes would certainly improve the solution given by the planar reduction and converge to the full order model solution. Although the lead-lag deformations are seen to be higher than the flapping ones, they are seen to have a similar beam rotation period 22 rad or 0.084 s. Besides the coupling due to Coriolis forces and the coupling due to bending caused by the inclination of the beam with a setting angle ψ, the deformations of the beam are caused by the externally applied force and the contribution of the centrifugal inertia forces.

In another example, the same load is applied in the y-direction for the previous beam with 90° setting angle and zero pre-cone. The eight mode approximate solution matches perfectly the FOM solution. The deflections in the direction of the applied force are seen to be higher than those of the previous case as shown Figure 5-51. For $\psi = 90°$, the flapping deformation (perpendicular to the applied force) are seen to be zero since there is no force applied to the beam in that direction. The coupling in bending is eliminated at $\psi = 90°$ as shown before. The torsional deformations are also seen to be zero while the axial deformations exhibit a fluctuating profile with smaller amplitudes and higher frequencies. The frequency spectrum for the lead-lag deformation is shown also in Figure 5-51. The first frequency corresponds to 76.76202 Hz or 482.31 rad/s, which is smaller than the first natural frequency of the beam $\omega = 523.9362$ rad/s.

In the following example, the retained modes were kept to four for both planar and complex reductions while the previous beam has been excited by a sinusoidal input of 15 kN and a forcing frequency of 8000 rad/s. This frequency lies between the sixth and seventh mode of the frequency spectrum of the system. The corresponding responses are depicted in Figure 5-52. Comparison between the two approximate solutions shows some discrepancies. But, when compared to the FOM the four mode planar solution shows a noticeable difference. This difference means that a

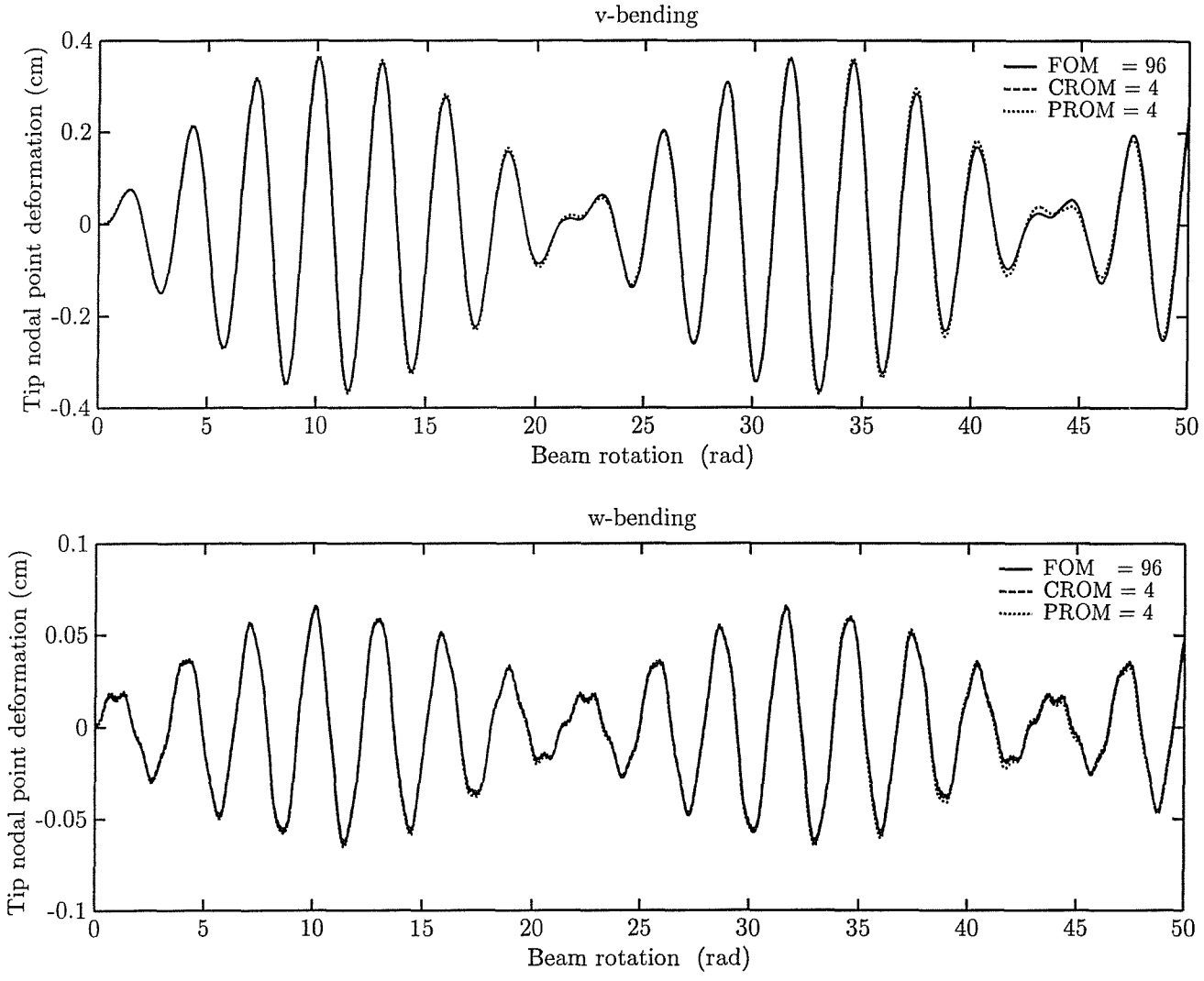

Figure 5-50: Four-mode flexural response to a sinusoidal load of $F(t) = 7500\sin(610t)$ N applied in the z-direction at the tip of the rotating tapered Timoshenko beam and its corresponding frequency spectrum using FFT, ($\Omega = 2500$ rpm, $\nu_y = 0.15$, $\nu_z = 0.25$, $\psi = 75°$, $\phi = 30°$ and $\mathcal{R}_o = 0.0$ cm).

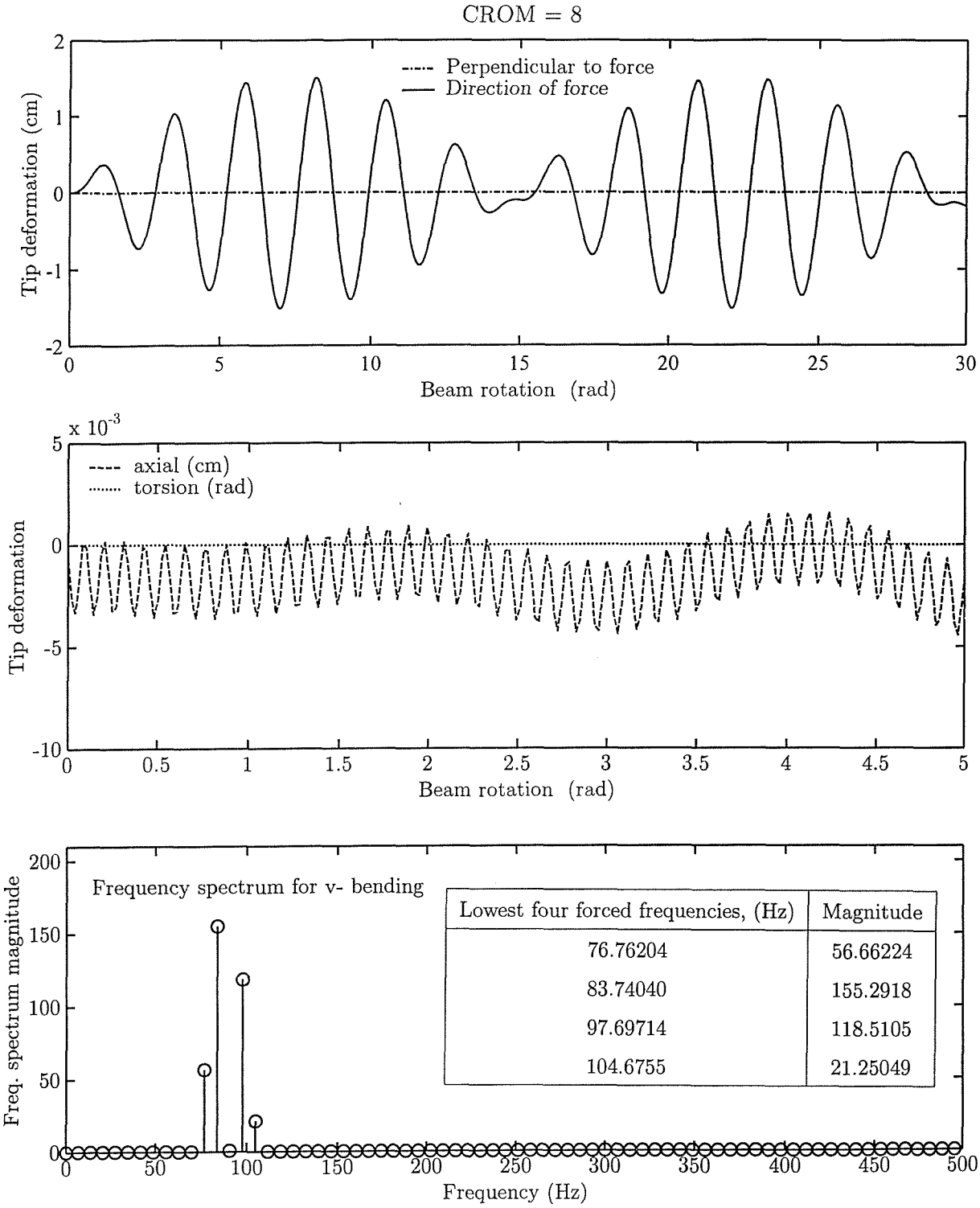

Lowest four forced frequencies, (Hz)	Magnitude
76.76204	56.66224
83.74040	155.2918
97.69714	118.5105
104.6755	21.25049

Figure 5-51: Eight-mode response to a sinusoidal load of $F(t) = 7500\sin(610t)$ N applied in the y-direction at the tip of the rotating tapered Timoshenko beam and its corresponding frequency spectrum using FFT, ($\Omega = 2000$ rpm, $\nu_y = 0.1$, $\nu_z = 0.2$, $\psi = 90°$, $\phi = 0°$ and $\mathcal{R}_o = 0.0$ cm).

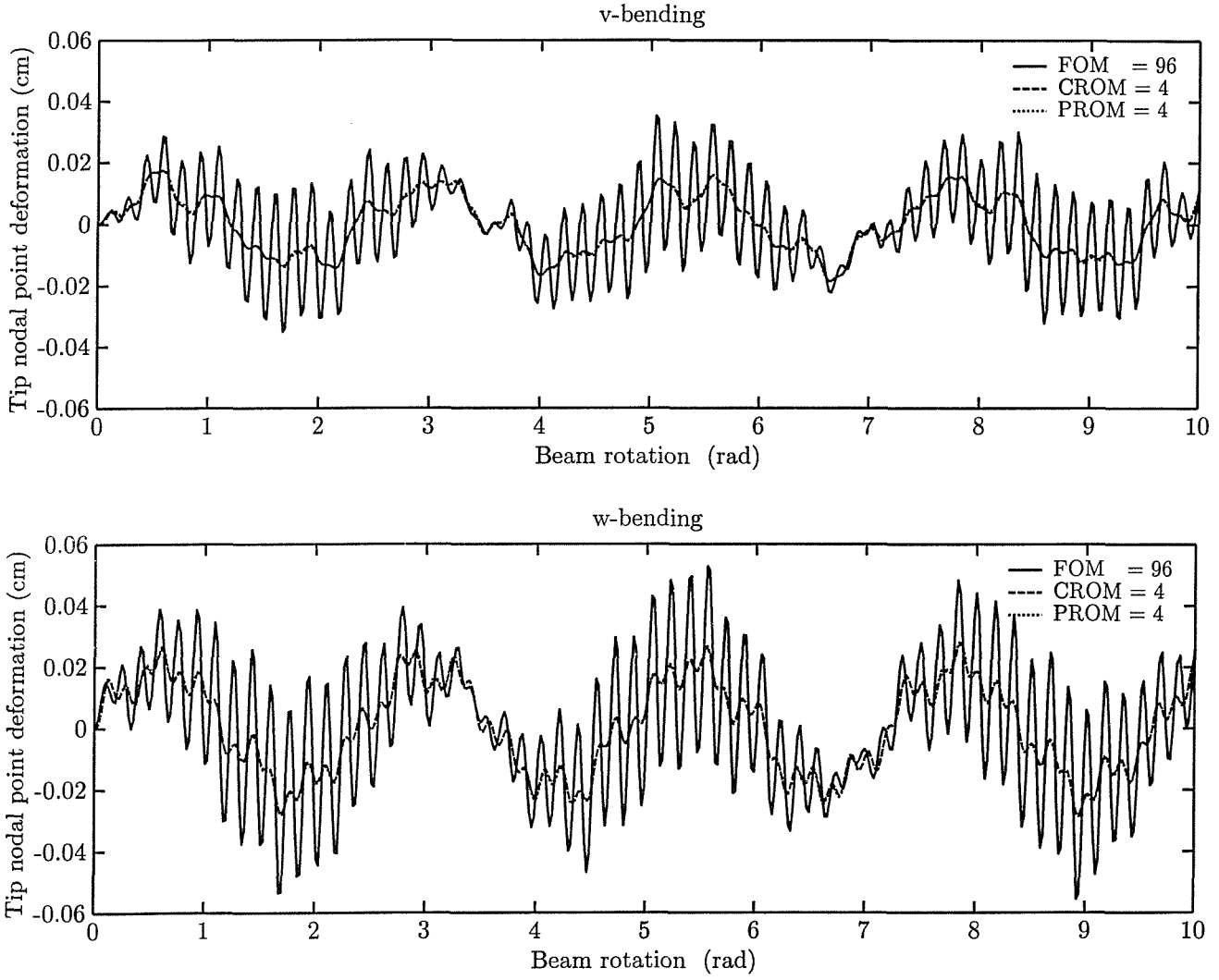

Figure 5-52: Four-mode flexural response to a sinusoidal load of $F(t) = 15000\sin(8000t)$ N applied in the z-direction at the tip of the rotating tapered Timoshenko beam and its corresponding frequency spectrum using FFT, ($\Omega = 2000$ rpm, $\nu_y = 0.1$, $\nu_z = 0.2$, $\psi = 30°$, $\phi = 15°$ and $\mathcal{R}_o = 0.0$ cm).

satisfactory solution is not reached yet. A suggestion of increasing the number of retained modes would be strongly recommended in order to reach a solution of the same order of comparison because the retained modes spectrum does not contain the forcing frequency. This renders the reduced order model "blind" to the exciting frequency. The retained modes have been extended to eight-mode approximate solution and the corresponding response match perfectly with the FOM and a converged solution to the FOM has been obtained as shown in Figure 5-53.

In Figure 5-54 are shown the flexural, torsional and the axial deformations of the beam as well as the corresponding frequency spectrum for the w-deformations. The frequency spectrum ranges from 62.7615 to 481.1715 Hz.

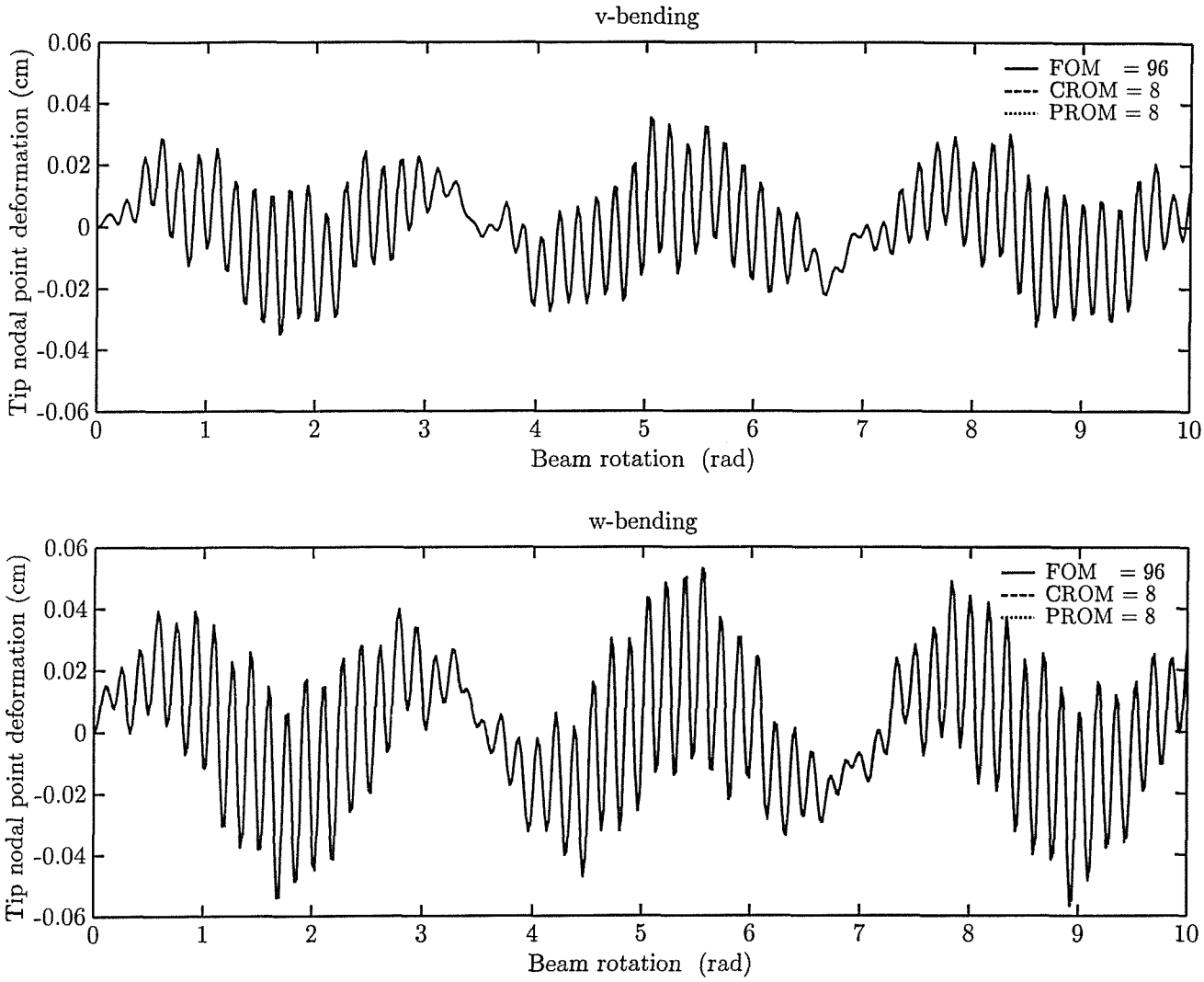

Figure 5-53: Eight-mode flexural response to a sinusoidal load of $F(t) = 15000\sin(8000t)$ N applied in the z-direction at the tip of the rotating tapered Timoshenko beam and its corresponding frequency spectrum using FFT, ($\Omega = 2000$ rpm, $\nu_y = 0.1$, $\nu_z = 0.2$, $\psi = 30°$, $\phi = 15°$ and $\mathcal{R}_o = 0.0$ cm).

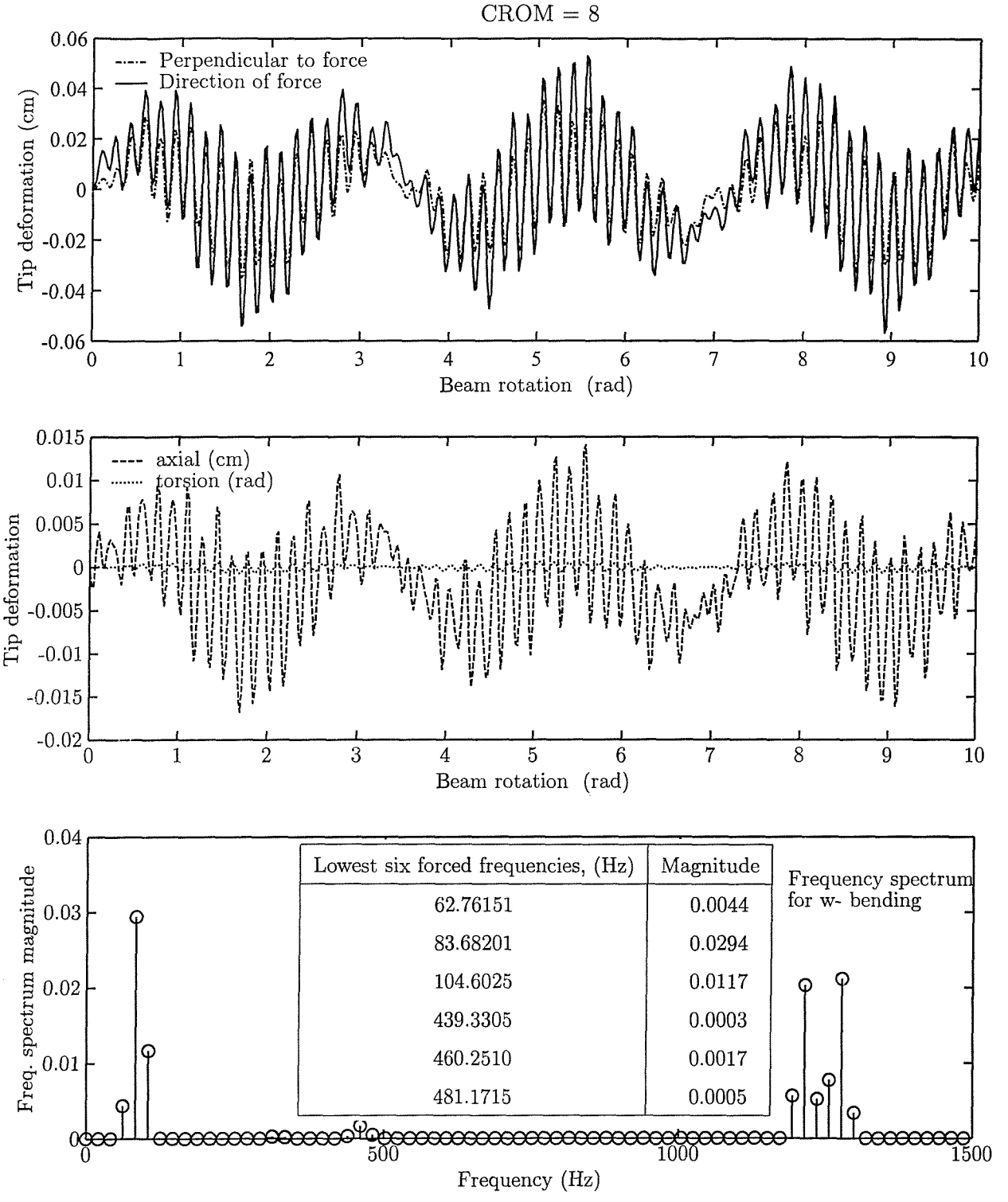

Figure 5-54: Response to a sinusoidal load of $F(t) = 15000\sin(8000t)$ N applied in the z-direction at the tip of the rotating tapered Timoshenko beam and its corresponding frequency spectrum using FFT, ($\Omega = 2000$ rpm, $\nu_y = 0.1$, $\nu_z = 0.2$, $\psi = 30°$, $\phi = 15°$ and $\mathcal{R}_o = 0.0$ cm).

Chapter 6

Conclusions and Recommendations

6.1 Conclusions

A finite element consistent mass formulation is employed to discretize the beam element. Each element has two nodes and each node has six degrees of freedom-three translations and three rotations. The effect of shear deformation rotary inertia, angular settings, hub radius, unequal breadth and depth taper ratios as well as spinning rotation and Coriolis effects are considered. This formulation permits unequal element lengths, and may be applied to tapered and uniform beams with solid or hollow rectangular and circular cross-sections. This model can be easily reduced to Euler-Bernoulli beam by ignoring the rotary inertia and shear effects. The uniform beam can be obtained by setting the taper ratios to zero.

The shape functions for the three dimensional Timoshenko beam element are derived. Exact expressions of the element stiffness, Coriolis and inertia matrices are derived in parametric form where all the parameter changes are accounted for. The exact expressions of these matrices have the computational advantage of eliminating the loss of computer time and round-off errors associated with extensive matrix operations required for their numerical evaluation.

The equations of motion for the forced vibrations of three dimensional rotating tapered Timoshenko beam are derived using a suitable formulation of the Lagrangian form in conjunction with the finite element technique. These equations take into account the coupling in bending deformations and include the effect of Coriolis forces, shear deformation and rotary inertia, hub radius, taper ratios and angular settings of the beam. A mixed set of generalized co-ordinates that accounts for inertia coupling between reference motion and local elastic deformations is employed. The coupling terms that represent the inertia coupling between the reference motion and small elastic deformations are expressed in terms of a set of time invariant quantities (scalars

and matrices) that depend on the assumed displacement field, rotary inertia, shear deformation, angular settings, hub radius and taper ratios.

The use of the present formulation is demonstrated first by casting the system equations in state space form in order to accommodate the Coriolis effect. The eigenvalue problem is defined and solved for both full order model (FOM) and reduced order models (ROM).

Two reduced order models using modal reduction have been successfully applied to the analysis and prediction of the vibrational response of a spinning tapered Timoshenko beam. The reduction process results in retaining a set of significant modes which account for almost the total amount of the kinetic energy content in the system. In general, the lowest modes spanning the lower end of the frequency spectrum, in addition to other modes which span the frequency spectrum of the forcing function are retained as significant modes. Several types of excitation such as step, impulsive and sinusoidal loadings have been applied to the beam. Few retained modes are shown to preserve the exact behavior of the rotating beam for different parameter variations.

The frequency spectrum of the forced time signal response is computed and plotted along with the response profiles for a wide range of parameter variation using the FFT algorithm.

The developed finite element model is implemented into a computational scheme for calculating natural frequencies and dynamic time response analysis. Some conclusions pertinent to the results of simulations are summarized and stated below.

The reference rotation tends to stiffen the beam, thus increasing strain energy stored during elastic deformation. On the other hand such stiffening effect tends to increase the modal frequencies, consequently increasing the amount of kinetic energy associated with the elastic modes of the system. This is known as a stiffening effect due to the rotation.

Southwell relationship is extended to include the effects of taper ratios, hub radius, pre-cone and setting angle as well as Coriolis forces. The explicit expressions for the Southwell relation for the lowest four vibrational flexural modes of rotating beams with several combinations of taper ratios, pre-cones, setting angles and various slenderness ratios were presented. The bending frequency of the i^{th} mode of a rotating beam may be obtained from the Southwell relation, with knowledge of the non-rotating frequency, the speed of rotation and SC. The Southwell relationship is seen to be very useful not only for its simplicity and rapid estimation for the predictions of the frequencies of rotating beams but also for its accuracy. Southwell coefficients are seen to be in linear relationship with the hub radius. The separate effect of taper ratios is seen to have more influence on the slope and intercept of the SC. However, while the intercepts

of these lines are seen to vary with the pre-cone and setting angle, the slopes are seen to be not affected.

A closed form solution was obtained for each mode within the parameter variations. The slopes and intercepts of the respective lines are seen to be a function of both taper ratios as well as the pre-cone and setting angle. It was observed that the expression for S_{T4} in its general form, does not represent a linear relationship with R. Based on these numerical observations, it may be concluded that Southwell Coefficients depend upon the non-dimensional hub radius R, taper ratios ν_y and ν_z, the pre-cone ϕ and setting angle ψ and upon the rotational spin parameter $\overline{\Omega}$.

The effect of setting angle is examined on the dynamic characteristics of rotating uniform Timoshenko beams. The first four frequency parameters have been evaluated at a wide range of setting angles. Based on the numerical results obtained from this investigation, it can be confirmed that the frequencies decrease as the setting angle increases. However, its effect on the frequencies reduces for higher modes. In fact, the effect of ψ becomes negligible beyond the second mode according to the present results. The reason for this is attributed to the fact that the softening term $\Omega^2 \sin^2 \psi$ is constant regardless of the mode considered therefore; it has more influence on modes with small frequency parameters. There are certain cases of parameter changes where the softening effects dominates the stiffening effects which result in a decrease of frequencies as the spin increases.

With knowledge of the spin and the out-of-plane or in-plane frequency parameters along with Lo and Renbarger [6] relationship in hand, the in-plane or out-of-plane frequency parameter may be easily investigated without recourse to further extensive calculations.

It was shown that if the relationship given by Lo and Renbarger [6] is substituted into the Southwell relation, the resulting out-of-plane and in-plane Southwell coefficients differ by unity, regardless of the mode considered. This formula along with the Southwell relation provides a well suited tool for frequency estimates at a preliminary stage design.

The rotation of the cross-section of the beam with a setting angle ψ does couple the in-plane and out-of-plane motion and deformations. In this case, one cannot distinguish these two modes from each other. When in-plane and out-of-plane displacement variables are coupled, the modes will not have a simple interpretation. That is, one may be mostly in-plane with a bit of out-of-plane. Depending on the size of deformation in different planes one would be only able to say if the in-plane or the out-of-plane vibration, at this frequency is dominant. In this case, there is no pure in-plane or out-of-plane vibration mode. However, torsion is also coupled with the

bending modes through Coriolis effects.

Pre-cone is a design solution that satisfies aerodynamic requirements. Numerical predictions were presented showing the effect of pre-cone on the dynamic characteristics of the present rotating tapered Timoshenko beam. Pertinent to these numerical observations, it can be concluded that for a given spin parameter and thickness ratio, the flapping mode frequencies decrease with increasing pre-cone. This may be due to the fact that as the pre-cone increases, the arm $\left(\mathcal{R}_o + r_P^i \cos\phi\right)$ associated to the centrifugal force decreases. From the equations of motion and the present results, the pre-cone was shown to have a softening effect that is similar to the effect of setting angle. The influence of the pre-cone is clearly seen to be of significance on the fundamental mode and is negligible on higher ones. The reason for this is that the softening term $\Omega^2 \sin\psi \cos\phi \sin(\psi + \phi)$ is constant regardless of the mode considered, therefore it has more influence on modes with small frequency values. This phenomenon is often called a softening effect that counteract the stiffening behavior encountered in rotating beams. However, the effect of the pre-cone on the dynamic characteristics of the rotating beam is seen to be less influential than the effect of the setting angle.

One way of controlling the mass and stiffness matrices of such structures is by introducing a taper either in width or depth direction or both. The effect of taper is important to the dynamic behavior and modal characteristics of rotating beams for which a specified distribution of strength/weight ratio is required for optimum performance and design criteria in many structures.

The introduction of taper makes the principal flexural rigidities of the beam unequal except at the root for square and circular cross-sections. When such a tapered beam is set with a setting angle ψ, coupling occurs between the bending motions in the two mutually perpendicular (xy)- and (xz)- planes containing the y- and z- axes of the cross-section. Such a beam with no setting angle has two independent flexural frequencies about its principal axes which are dependent on the width to depth ratio of the cross-section.

Based on the results obtained from this investigation, it may be concluded that the dynamic characteristics of the rotating beam depend upon the taper ratios of the beam in addition to other parameters built into the model. Depending on the taper ratios, the mass and stiffness of the beam may increase or decrease and consequently, the dynamic characteristics are seen to be affected accordingly.

Some numerical predictions show that as the taper ratio ν_y increases the thickness toward the tip becomes smaller which results in a decrease in mass and stiffness of the beam. Consequently,

the frequency parameters for all modes increase. For the taper in the other direction, it is seen that the first mode preserves the same behavior while the second and third mode exhibits a reverse trend.

The Coriolis forces result from the precession of reference axes. From the predictions shown, in general, the Coriolis effects depress the frequency values. At low speed ratios the Coriolis effect is very small and therefore can be neglected. Coriolis forces introduce coupling in bending-torsion, bending-axial, bending-bending and axial-torsion modes when the setting angle is different from 0° and 90°. However for zero setting angle the Coriolis forces have no coupling effects that influence the dynamic characteristics of the rotating tapered beam and therefore can be safely ignored.

Numerical solutions show that the slenderness ratio has a significant effect for short beams and for higher modes. The predictions show that the shear is more pronounced in higher modes and is of no significance at the lower ones.

The inertia forces result as a natural phenomena due to rotation and are of significant importance as far as dynamic analysis is concerned. It is observed that these forces produce the largest deflections.

Based on the results of simulation, and with data presented in this investigation, planar and complex modal reductions maintain the same order of comparison for this type of structures. The former is considerably easier to apply, the latter is more realistic. However, for complex structures the complex modal reduction would be expected to produce more accurate results.

6.2 Recommendations

Further investigations are required for the extensions of the present work. The following recommendations are made for future research:

- Extending the present model to include the effect of pre-twist.
- Extending the present model to include the torsional coupling.
- Studying the effect of the warping of the cross-section during torsion.
- Extending the present model to include an airfoil cross-section where the center of flexure does not coincide with the center of mass of the beam.
- The present model can be extended to include structural and viscous damping.

- The spin rotation is assumed to be constant. This assumption yields a constant Coriolis matrix. During the start-up and shut down the spin rotation is not constant. If a variable spin is considered, it yields a time dependent Coriolis matrix. The present study can be extended to study the time dependent Coriolis matrix on the dynamic analysis of the rotating tapered Timoshenko beam.

- Extending the present formulation to account for aerodynamic forces.

References

[1] Lord Rayleigh, 1877, *Theory of Sound*, Mcmillan and Co., London.

[2] S. P. Timoshenko, 1921, On the Correction for Shear of the Differential Equation for Transverse Vibration of Prismatic Bars, *Philosophical Magazine*, **41**, 744-746.

[3] H. Lamb and R. V. Southwell, 1921, The Vibrations of a Spinning Disc, *Proceedings of The Royal Society*, **99**, 272-280.

[4] R. V. Southwell and B. S. Gough, 1921, On The Free Transverse Vibrations of Airscrew Blades, *British A. R. C. Reports and Memoranda No.* 766 (*Ae.* 26), 358-368.

[5] R. L. Sutherland, 1949, Bending Vibration of a Rotating Blade Vibrating in the Plane of Rotation, *Transactions of the ASME, Journal of Applied Mechanics*, **16**, 389-394.

[6] H. Lo and J. L. Renbarger, 1951, Bending Vibrations of a Rotating Beam, *First US National Congress of Applied Mechanics, Chicago, Ill., June* 1951, 75-79.

[7] H. Lo, 1952, A Non-Linear Problem in the Bending Vibration of a Rotating Beam, *Transactions of the ASME, Journal of Applied Mechanics*, **19**, 461-464.

[8] W. Carnegie, 1959, Vibrations of Rotating Cantilever Blading: Theoretical Approaches to the Frequency Problem Based on Energy Methods, *Journal of Mechanical Engineering Sciences*, **1**, 235-240.

[9] M. Schilhansl, 1958, Bending Frequency of a Rotating Cantilever Beam, *Transactions of the ASME, Journal of Applied Mechanics*, **25**, 28-30.

[10] D. Pnueli, 1972, Natural Bending Frequency Comparable to Rotational Frequency in Rotating Cantilever Beam, *Transactions of the ASME, Journal of Applied Mechanics,* **39,** 602-604.

[11] J. S. Rao and W. Carnegie, 1969, Non-Linear Vibrations of Rotating Cantilever Beams, *The Aeronautical Journal of The Royal Aeronautical Society*, **74**, 161-165.

[12] L. H. Jones, 1975, The Transverse Vibration of a Rotating Beam with Tip Mass: The Method of Integral Equations, *Quarterly of Applied Mathematics*, **33**, 193-203.

[13] S. V. Hoa, 1979, Vibration of a Rotating Beam with Tip Mass, *Journal of Sound and Vibration*, **67**, 369-381.

[14] S. V. Hoa, D. H. Hodges and M. J. Rutkowski, 1979, Comments on "Vibration of a Rotating Beam with Tip Mass", *Journal of Sound and Vibration*, **72**, 547-549.

[15] D. H. Hodges and M. J. Rutkowski, 1981, Free Vibration Analysis of Rotating Beams by a Variable-Order Finite-Element Method, *American Institute of Aeronautics and Astronautics Journal*, **19**, 1459-1466.

[16] A. D. Wright, C. E Smith, R. W. Thresher and J. L. C. Wang, 1982, Vibration Modes of Centrifugally Stiffened Beams, *Transactions of the ASME, Journal of Applied Mechanics*, **49**, 197-202.

[17] R. B. Bhat, 1986, Transverse Vibrations of a Rotating Uniform Cantilever Beam with Tip Mass as Predicted by Using Beam Characteristic Orthogonal Polynomials in the Rayleigh-Ritz Method, *Journal of Sound and Vibration*, **105**, 199-210.

[18] C. S. Kim and S. M. Dickinson, 1987, Comment on "Transverse Vibrations of a Rotating Uniform Cantilever Beam with Tip Mass as Predicted by Using Beam Characteristic Orthogonal Polynomials in the Rayleigh-Ritz Method", *Journal of Sound and Vibration*, **112**, 377-378.

[19] Y. A. Khulief, 1989, Vibration Frequencies of a Rotating Tapered Beam with End Mass, *Journal of Sound and Vibration*, **134**, 87-97.

[20] H. Du, M. K. Lim and K. M. Liew, 1994, A Power Series Solution for Vibrations of a Rotating Timoshenko Beam, *Journal of Sound and Vibration*, **175**, 505-523.

[21] J. T. S. Wang, O. Mahrenholtz and J. Böhm, 1976, Extended Galerkin's Method for Rotating Beam Vibrations Using Legendre Polynomials, *Solid Mechanics Archives*, **1**, 341-365.

[22] T. Yokoyama, 1988, Free Vibration Characteristics of Rotating Timoshenko Beams, *International Journal of Mechanical Sciences*, **30**, 743-755.

[23] S. Y. Lee and, Y. H. Kuo, 1993, Bending Frequency of a Rotating Timoshenko Beam with General Elastically Restrained Root, *Journal of Sound and Vibration,* **162**, 243-250.

[24] S. Putter and H. Manor, 1978, Natural Frequencies of Radial Rotating Beams, *Journal of Sound and Vibration*, **56**, 175-185.

[25] S. Mulmule, G. Singh and G. Venkateswara Rao, 1993, Flexural Vibration of Rotating Tapered Timoshenko Beams, *Journal of Sound and Vibration*, **160**, 372-377.

[26] S. Naguleswaran, 1994, Comments on: Flexural Vibration of Rotating Tapered Timoshenko Beams, *Journal of Sound and Vibration*, **172**, 559-560.

[27] A. Bazoune and Y. A. Khulief, 1992, A Finite Beam Element for Vibration Analysis of Rotating Tapered Timoshenko Beams, *Journal of Sound and Vibration*, **156**, 141-164.

[28] Y. A. Khulief and A. Bazoune, 1992, Frequencies of Rotating Tapered Timoshenko Beams with Different Boundary Conditions, *Computers and Structures,* **42**, 781-795.

[29] A. Bazoune, Y. A. Khulief and N. G. Stephen, 1999, Further Results on Modal Characteristics of Rotating Tapered Timoshenko Beams, *Journal of Sound and Vibration*, **219**, 155-172.

[30] J. R. Banerjee, 2000, Free Vibration of Centrifugally Stiffened Uniform and Tapered Beams Using The Dynamic Stiffness Method, *Journal of Sound and Vibration*, **233**, 857-875.

[31] J. S. Rao, 1973, Natural Frequencies of Turbine Blading - A Survey, *Shock and Vibration Digest*, **5**, 3-16.

[32] A. Leissa, 1981, Vibrational Aspects of Rotating Turbomachinery Blades, *Applied Mechanics Review*, **34**, 629-635.

[33] A. Rosen, 1991, Structural and Dynamic Behavior of Pre-twisted Rods and Beams, *Applied Mechanics Review*, **44**, 483-515.

[34] D. L. Kunz, 1994, Survey and Comparison of Engineering Beam Theories for Helicopter Rotor Blades, *Journal of Aircraft*, **31**, 473-479.

[35] J. C. Houbolt and G. W. Brooks, 1958, Differential Equations of Motion for Combined Flapwise Bending, Chordwise Bending, and Torsion of pre-twisted Nonuniform Rotor Blades, *NACA Report* 1346.

[36] V. R. Murthy, 1976, Dynamic Characteristics of Rotor Blades, *Journal of Sound and Vibration*, **49**, 483-500.

[37] M. Swaminathan and J. S. Rao, 1977, Vibration of Rotating Pre-twisted and Tapered Blades, *Mechanism and Machine Theory*, **12**, 331-337.

[38] G. Isakson and J. G. Eisley, 1960, Natural Frequencies in Bending of Pre-twisted Rotating Blades, *NASA TN D*-371.

[39] D. H. Hodges and E. H. Dowell, 1974, Nonlinear Equations of Motion for the Elastic Bending and Torsion of pre-twisted Nonuniform Rotor Blades, *NASA TN D*-7818.

[40] J. S. Rao and S. Banerjee, 1977, Coupled Bending-Torsional Vibration of Rotating Cantilever Blades: Method of Polynomial Frequency Equation, *Mecahnism and Machine Theory*, **12**, 271-280.

[41] R. M. Laurenson, 1976, Modal Analysis of Rotating Flexible Structures, *American Institute of Aeronautics and Astronautics Journal,* **14**, 1444-1450.

[42] H. H. Yoo and S. H. Shin, 1998, Vibration Analysis of Rotating Cantilever Beams, *Journal of Sound and Vibration,* **212**, 807-828.

[43] K. B. Subrahmanyam and K. R. V. Kaza, 1985, Vibration Analysis of Rotating Turbomachinery Blades by an Improved Finite Difference Method, *International Journal for Numerical Methods in Engineering,* **21**, 1871-1886.

[44] K. B. Subrahmanyam and K. R. V. Kaza, 1986, Vibration and Buckling of Rotating, Pretwisted, pre-coned Beams Including Coriolis Effects, *Transactions of the ASME, Journal of Vibration Acoustics Stress and Reliability in Design,* **108**, 140-149.

[45] K. B. Subrahmanyam and K. R. V. Kaza, 1987, Non-linear Flap-Lag-Extensional Vibrations of Rotating, Pre-twisted, Pre-coned Beams Including Coriolis Effects, *International Journal of Mechanical Sciences,* **29**, 29-43.

[46] K. B. Subrahmanyam and K. R. V. Kaza, G. V. Brown and C. Lawrence, 1987, Nonlinear Vibration and Stability of Rotating, Pre-twisted, Pre-coned Blades Including Coriolis Effects, *Journal of Aircraft,* **24**, 342-352.

[47] R. O. Stafford and V. Giurgiutiu, 1975, Semi-Analytic Method for Rotating Timoshenko Beams, *International Journal of Mechanical Sciences,* **17**, 719-727.

[48] K. A. Ansari, 1975, Nonlinear Vibrations of a Rotating Pre-twisted Blade, *Computers and Structures,* **5**, 101-118.

[49] R. M. Krupka and A. M. Baumanis, 1969, Bending-Bending Mode of a Rotating Tapered Pre-twisted Turbomachine Blade Including Rotary Inertia and Shear Deformation, *Transactions of the ASME, Journal of Engineering for Industry*, **91**, 1017-1024.

[50] K. B. Subrahmanyam, S. V. Kulkarni and J. S. Rao, 1982, Application of the Reissner Method to Derive the Coupled Bending-Torsion Equations of Dynamic Motion of Rotating Pre-twisted Cantilever Blading with Allowance for Shear Deflection, Rotary Inertia, Warping and Thermal Effects, *Journal of Sound and Vibration,* **84**, 223-240.

[51] H. Du, D. Hitchings and G. A. O. Davies, 1992, A Finite Element Structural Dynamics Model of a Beam with an Arbitrary Moving Base, Part I: Formulations, *Finite Elements in Analysis and Design,* **12**, 118-131.

[52] H. Du, D. Hitchings and G. A. O. Davies, 1992, A Finite Element Structural Dynamics Model of a Beam with an Arbitrary Moving Base, Part II: Numerical Examples and Solutions, *Finite Elements in Analysis and Design,* **12**, 133-150.

[53] H. H. Yoo, R. R. Ryan and R. A. Scott, 1995, Dynamics of Flexible Beams Undergoing Overall Motions, *Journal of Sound and Vibration*, **181**, 261-278.

[54] N. L. Pedersen and M. L. Pedersen, 1998, A Direct Derivation of Motion for 3-D Flexible Mechanical Systems, *International Journal for Numerical Methods in Engineering*, **41**, 697-719.

[55] A. Yigit, R. A. Scott and A. G. Ulsoy, 1988, Flexural Motion of a Radially Rotating Beam Attached to a Rigid Body, *Journal of Sound and Vibration*, **121**, 201-210.

[56] T. R. Kane R. R. Ryan and A. K. Banerjee, 1987, Dynamics of a Cantilever Beam Attached to a Moving Base, *Journal of Guidance, Control and Dynamics*, **10**, 139-151.

[57] Z. E. Boutaghou and A. G. Erdman 1991, A Unified Approach for the Dynamics of Beams Undergoing Arbitrary Spatial Motion, *Journal of Vibration and Acoustics*, **113**, 494-502.

[58] Steven H. Y. Lai, 1994, Nonlinear Finite Element Modeling of a High Speed Rotating Timoshenko Beam Structure, *International Journal of Mechanical Sciences,* **36**, 849-861.

[59] B. Fallahi, S. H.-Y. Lai and R. Gupta, 1994, Full Beam Formulation of a Rotating Beam-Mass System, *Journal of Vibration and Acoustics*, **116**, 93-99.

[60] A. M. Bakr and A. A. Shabana, 1987, Timoshenko Beams and Flexible Multibody System Dynamics, *Journal of Sound and Vibration*, **116**(1), 89-107.

[61] D. C. D. Oguamanam and G. R. Heppler, 1998, Geometric Stiffening of Timoshenko Beams, *Transactions of the ASME, Journal of Applied Mechanics*, **65**, 923-929.

[62] Y. A. Khulief, 1992, On The Finite Element Dynamic Analysis of Flexible Mechanisms, *Computer Methods in Applied Mechanics and Engineering*, **97**, 23-32.

[63] R. J. Guyan, 1965, Reduction of Stiffness and Mass Matrices, *American Institute of Aeronautics and Astronautics Journal*, **3**, 380.

[64] B. Irons, 1965, Structural Eigenvalue Problems: Elimination of Unwanted Variables, *American Institute of Aeronautics and Astronautics Journal*, **3**, 961.

[65] R. L. Kidder, 1975, Reduction of Structural Frequency Equations, *American Institute of Aeronautics and Astronautics Journal*, **11**, 892.

[66] W. C. Hurty, 1965, Dynamic Analysis of Structural Systems Using Components Modes, *American Institute of Aeronautics and Astronautics Journal*, **3**, 678-684.

[67] R. R. Craig, Jr. and C. C. Bampton, 1968, Coupling of Substructures for Dynamic Analyses, *American Institute of Aeronautics and Astronautics Journal*, **6**, 1313-1319.

[68] W. A. Benfield and R. F. Hruda,1971, Vibration Analysis of Structures by Component Mode Substitution, *American Institute of Aeronautics and Astronautics Journal*, **8**, 1255-1261.

[69] L. U. Ojalvo and M. Newman,1970, Vibration Modes of Large Structures by an Automatic Matrix-Reduction Method, *American Institute of Aeronautics and Astronautics Journal*, **8**, 1234-1239.

[70] P. W. Likins, 1972, Finite Element Appendage Equations for Hybrid Coordinate Dynamic Analysis, *International Journal of Solids and Structures*, **8**, 709-731.

[71] A. A. Shabana and R. A. Wehage, 1983, A Coordinate Reduction Technique for Dynamic Analysis of Spatial Substructures with Large Angular Rotations, *Journal of Structural Mechanics*, **11**, 401-431.

[72] K. Kane and B. J. Torby, 1991, The Extended Modal Reduction Method Applied to Rotor Dynamic Problems, *Journal of Vibration and Acoustics*, **113**, 79-84.

[73] Y. A. Khulief and M. A. Mohiuddin, 1997, On The Dynamic Analysis of Rotors Using Modal Reduction, *Finite Elements in Analysis and Design*, **26**, 41-55.

[74] R. Narayanaswami and H. M. Adelman, 1974, Inclusion of Transverse Shear Deformation in Finite Element Displacement Formulations, *American Institute of Aeronautics and Astronautics Journal*, 12(11), 1613-1614.

[75] A. Bazoune, Y. A. Khulief and N. G. Stephen, 2003, Shape Functions of Three Dimensional Timoshenko Beam Element, *Journal of Sound and Vibration*, **259**, 473-480.

[76] A. Bazoune, Y. A. Khulief, N. G. Stephen and M. A. Mohiuddin, 2001, Dynamic Response of Spinning Tapered Timoshenko Beams Using Modal Reduction, *Finite Elements in Analysis and Design*, **37**, 199-219.

[77] A. A. Shabana and R. Wehage, 1981, Variable Degree-of-Freedom Component Mode Analysis of Inertia Variant Flexible Mechanical Systems, *Technical Report No.* 81-12, *Center of Computer Aided Design, The University of Iowa.*

[78] G. R. Cowper, 1966, The shear coefficient in Timoshenko's beam theory, *Transactions of the ASME, Journal of Applied Mechanics*, **33**, 335-340.

[79] N. G. Stephen and M. Levinson, 1979, A Second Order Beam Theory, *Journal of Sound and Vibration,* **67**, 293-305.

[80] M. A. Dokainish and S. Rawtani, 1971, Vibration Analysis of Rotating Cantilever Plates, *International Journal for Numerical Methods in Engineering*, **3**, 233-248.

[81] B. Downs, 1978, Reference Frequencies for The Validation of Numerical Solutions of Transverse Vibrations of Non-uniform Beams, *Journal of Sound and Vibration*, **61**, 71-78.

[82] B. Downs, 1977, Transverse Vibrations of Cantilever Beams Having Unequal Breadth and Depth Tapers, *Transactions of the ASME, Journal of Applied Mechanics*, **46**, 737-742.

[83] S. Naguleswaran, 1994, Lateral Vibration of a Centrifugally tensioned Euler-Bernoulli Beam, *Journal of Sound and Vibration*, **176**, 613-624.

[84] S. Naguleswaran, 1994, A Direct Solution for The Transverse Vibration of Euler-Bernoulli Wedge and Cone Beams, *Journal of Sound and Vibration*, **172**, 289-304.

[85] V. T. Nagaraj, 1996, Approximate Formula for the Frequencies of a Rotating Timoshenko Beam, *Journal of Aircraft*, **33**, 637-639.

[86] H. H. Yoo and S. H. Shin, 1998, Vibration Analysis of Rotating Cantilever Beams, *Journal of Sound and Vibration*, **212**, 807-828.

[87] W. R. Chen and L. M. Keer, 1993, Transverse Vibrations of a Rotating Twisted Timoshenko Beam Under Axial Loading, *Journal of Vibrations and Acoustics*, **155**, 285-294.

[88] H. Ashley, 1967, Observations on the Dynamic Behavior of Large Flexible Bodies in Orbit, *American Institute of Aeronautics and Astronautics Journal*, 5(3), 460-469.

[89] M. R. Hatch, 2001, *Vibration Simulation Using* MATLAB *and* ANSYS, Chapman & Hall/CRC.

[90] S. S. Rao, 1995, *Mechanical Vibrations*, Third Edition, Addison Wesley.

[91] S. Timoshenko and D. H Young, 1955, *Vibration Problems in Engineering*, Third Edition, Van Nostrand Reinhold.

[92] J. S. Przemeniecki, 1968, *Theory of Matrix Structural Analysis*, Mc Graw-Hill.

[93] A. A. Shabana, 1989, *Dynamics of Multibody Systems*, John Wiley.

[94] R. D. Cook, D. S. Malkus and M. E. Plesha, 1989, *Concepts and Applications of Finite Element Analysis*, Third Edition, John Wiley.

[95] P. E. Nikravesh, 1988, *Computer Aided Analysis of Mechanical Systems*, Prentice-Hall.

[96] L. Meirovitch, 1997, *Principles and Techniques of Vibrations*, Prentice-Hall.

Appendix A

Transformation Matrices

In order to perform co-ordinate transformation from the element co-ordinate system to the body co-ordinate system, the rotation matrix $\left[\Re^i\right]$ is required. Direction cosines for the $\left(x^i y^i z^i\right)$ axes can be found directly by geometric considerations. Let (x_1, y_1, z_1) and (x_2, y_2, z_2) be the locations of the nodes of the i^{th} beam element. The transformation matrix from the element axes to the body fixe co-ordinate system is given by [88]

$$\left[\Re^i\right] = \begin{bmatrix} c_x^i & \dfrac{-c_x^i c_y^i}{\sqrt{\left(c_x^i\right)^2 + \left(c_z^i\right)^2}} & \dfrac{-c_z^i}{\sqrt{\left(c_x^i\right)^2 + \left(c_z^i\right)^2}} \\ c_y^i & \sqrt{\left(c_x^i\right)^2 + \left(c_z^i\right)^2} & 0 \\ c_z^i & \dfrac{-c_x^i c_z^i}{\sqrt{\left(c_x^i\right)^2 + \left(c_z^i\right)^2}} & \dfrac{c_x^i}{\sqrt{\left(c_x^i\right)^2 + \left(c_z^i\right)^2}} \end{bmatrix} \tag{A.1}$$

where

$$c_x^i = \frac{x_2^i - x_1^i}{l^i}, \qquad c_y^i = \frac{y_2^i - y_1^i}{l^i}, \qquad c_z^i = \frac{z_2^i - z_1^i}{l^i}$$

and l^i is the length of the i^{th} element, given by

$$l^i = \sqrt{\left(x_2^i - x_1^i\right)^2 + \left(y_2^i - y_1^i\right)^2 + \left(z_2^i - z_1^i\right)^2}$$

It can be easily verified that the matrix $\left[\Re^i\right]$ is orthogonal, a property that is utilized throughout the development of this work.

The preceding transformation $\left[\Re^i\right]$ is valid for all positions of the element, except when the

element x_2^i axis coincides with the body axis x_2 axis. In this case, the transformation matrix $\left[\Re^i\right]$ is given by [88]

$$\left[\Re^i\right] = \begin{bmatrix} 0 & -c_y^i & 0 \\ c_y^i & 0 & 0 \\ 0 & 0 & 1 \end{bmatrix} \tag{A.2}$$

If the rotations at the nodes with respect to body axes are infinitesimal, the same matrix $\left[\Re^i\right]$ can be used to transform rotations from the element axes to the body co-ordinate system. That is, the matrix $\left[\overline{\Re}^i\right]$ of equation is given by

$$\left[\overline{\Re}^i\right] = \begin{bmatrix} \left[\Re^i\right] & 0 & 0 & 0 \\ 0 & \left[\Re^i\right] & 0 & 0 \\ 0 & 0 & \left[\Re^i\right] & 0 \\ 0 & 0 & 0 & \left[\Re^i\right] \end{bmatrix}^T$$

Appendix B

Shape Functions Matrix

The three dimensional elemental shape functions matrix is given by

$$
\left[\mathcal{S}^i\right]^T = \begin{bmatrix}
\left(1-\xi^i\right) & 0 & 0 \\
6\overline{\Phi}_z^i\left(\xi^i-\xi^{i^2}\right)\eta^i & \overline{\Phi}_z^i\left(1-3\xi^{i^2}+2\xi^{i^3}+\Phi_z^i\left(1-\xi^i\right)\right) & 0 \\
6\overline{\Phi}_y^i\left(\xi^i-\xi^{i^2}\right)\zeta^i & 0 & \overline{\Phi}_y^i\left(1-3\xi^{i^2}+2\xi^{i^3}+\Phi_y^i\left(1-\xi^i\right)\right) \\
0 & -\left(1-\xi^i\right)l^i\zeta^i & \left(1-\xi^i\right)l^i\eta^i \\
l^i\overline{\Phi}_y^i\left(1-4\xi^i+3\xi^{i^2}+\Phi_y^i\left(1-\xi^i\right)\right)\zeta^i & 0 & -l^i\overline{\Phi}_y^i\left(\xi^i-2\xi^{i^2}+\xi^{i^3}+\dfrac{\Phi_y^i}{2}\left(\xi^i-\xi^{i^2}\right)\right) \\
-l^i\overline{\Phi}_z^i\left(1-4\xi^i+3\xi^{i^2}+\Phi_z^i\left(1-\xi^i\right)\right)\eta^i & l^i\overline{\Phi}_z^i\left(\xi^i-2\xi^{i^2}+\xi^{i^3}+\dfrac{\Phi_z^i}{2}\left(\xi^i-\xi^{i^2}\right)\right) & 0 \\
\xi^i & 0 & 0 \\
6\overline{\Phi}_z^i\left(-\xi^i+\xi^{i^2}\right)\eta^i & \overline{\Phi}_z^i\left(3\xi^{i^2}-2\xi^{i^3}+\Phi_z^i\xi^i\right) & 0 \\
6\overline{\Phi}_y^i\left(-\xi^i+\xi^{i^2}\right)\zeta^i & 0 & \overline{\Phi}_y^i\left(3\xi^{i^2}-2\xi^{i^3}+\Phi_y^i\xi^i\right) \\
0 & -\xi^i l^i\zeta^i & \xi^i l^i\eta^i \\
l^i\overline{\Phi}_y^i\left(-2\xi^i+3\xi^{i^2}+\Phi_y^i\xi^i\right)\zeta^i & 0 & -l^i\overline{\Phi}_y^i\left(-\xi^{i^2}+\xi^{i^3}-\dfrac{\Phi_y^i}{2}\left(\xi^i-\xi^{i^2}\right)\right) \\
-l^i\overline{\Phi}_z^i\left(-2\xi^i+3\xi^{i^2}+\Phi_z^i\xi^i\right)\eta^i & l^i\overline{\Phi}_z^i\left(-\xi^{i^2}+\xi^{i^3}-\dfrac{\Phi_z^i}{2}\left(\xi^i-\xi^{i^2}\right)\right) & 0
\end{bmatrix}
$$

Appendix C

Element Matrices

The exact explicit expressions of the element matrices of the i^{th} spinning tapered Timoshenko beam element are given by

Table C.1: Elemental axial stiffness matrix

$$\left[\overline{k}_a^i\right]_{12\times12} = \frac{EA_o}{L_{oy}L_{oz}l^i}\left[k_{p,q}^a\right], \quad p,q = 1,2,...,12$$

where the nonzero entries of the lower triangular part of $\left[k_{p,q}^a\right]$ are given by

$$k_{1,1}^a = -k_{7,1}^a = k_{7,7}^a = \mu_1 - \mu_2 l^i + \frac{1}{3}l^{i^2}$$

Table C.2: Elemental torsional stiffness matrix

$$\left[\overline{k}_{\theta_x}^i\right]_{12\times12} = \frac{G}{l^i}\left[k_{p,q}^{\theta_x}\right], \quad p,q = 1,2,...,12$$

where the nonzero entries of the lower triangular part of $\left[k_{p,q}^{\theta_x}\right]$ are given by

$$\begin{aligned} k_{4,4}^{\theta_x} = -k_{10,4}^{\theta_x} = k_{10,10}^{\theta_x} &= \Gamma_{yy}\left(\alpha_{z_0} - \frac{1}{2}\alpha_{z_1}l^i + \frac{1}{3}\alpha_{z_2}l^{i^2} - \frac{1}{4}\alpha_{z_3}l^{i^3} + \frac{1}{5}l^{i^4}\right) \\ &+\Gamma_{zz}\left(\alpha_{y_0} - \frac{1}{2}\alpha_{y_1}l^i + \frac{1}{3}\alpha_{y_2}l^{i^2} - \frac{1}{4}\alpha_{y_3}l^{i^3} + \frac{1}{5}l^{i^4}\right) \end{aligned}$$

Table C.3: Elemental bending stiffness matrix in the (xy)-plane

$$\left[\overline{k}_v^i\right]_{12\times 12} = \frac{E\overline{\Phi}_z^{i^2}}{l^{i^3}}\left[k_{p,q}^v\right], \quad p,q = 1,2,...,12$$

where the nonzero entries of the lower triangular part of $\left[k_{p,q}^v\right]$ are given by

$$\begin{aligned}
k_{2,2}^v = -k_{8,2}^v = k_{8,8}^v &= \Gamma_{yy}\left(\frac{132}{35}l^{i^4} - \frac{21}{5}\alpha_{z_3}l^{i^3} + \frac{24}{5}\alpha_{z_2}l^{i^2} - 6\alpha_{z_1}l^i + 12\alpha_{z_0}\right)\sin^2\psi \\
&+ \Gamma_{zz}\left(\frac{132}{35}l^{i^4} - \frac{21}{5}\alpha_{y_3}l^{i^3} + \frac{24}{5}\alpha_{y_2}l^{i^2} - 6\alpha_{y_1}l^i + 12\alpha_{y_0}\right)\cos^2\psi
\end{aligned}$$

$$\begin{aligned}
k_{6,2}^v = -k_{8,6}^v &= \Gamma_{yy}\left(\begin{array}{l} -\frac{2}{35}\left(14\Phi_z^i - 19\right)l^{i^5} + \frac{3}{10}\left(3\Phi_z^i - 4\right)\alpha_{z_3}l^{i^4} \\ -\frac{1}{5}\left(5\Phi_z^i - 7\right)\alpha_{z_2}l^{i^3} + \left(\Phi_z^i - 2\right)\alpha_{z_1}l^{i^2} + 6\alpha_{z_0}l^i \end{array}\right)\sin^2\psi \\
&+ \Gamma_{zz}\left(\begin{array}{l} -\frac{2}{35}\left(14\Phi_z^i - 19\right)l^{i^5} + \frac{3}{10}\left(3\Phi_z^i - 4\right)\alpha_{y_3}l^{i^4} \\ -\frac{1}{5}\left(5\Phi_z^i - 7\right)\alpha_{y_2}l^{i^3} + \left(\Phi_z^i - 2\right)\alpha_{y_1}l^{i^2} + 6\alpha_{y_0}l^i \end{array}\right)\cos^2\psi
\end{aligned}$$

$$\begin{aligned}
k_{12,2}^v = -k_{12,8}^v &= \Gamma_{yy}\left(\begin{array}{l} \frac{2}{35}\left(14\Phi_z^i + 47\right)l^{i^5} - \frac{3}{10}\left(3\Phi_z^i + 10\right)\alpha_{z_3}l^{i^4} \\ +\frac{1}{5}\left(5\Phi_z^i + 17\right)\alpha_{z_2}l^{i^3} - \left(\Phi_z^i + 4\right)\alpha_{z_1}l^{i^2} + 6\alpha_{z_0}l^i \end{array}\right)\sin^2\psi \\
&+ \Gamma_{zz}\left(\begin{array}{l} \frac{2}{35}\left(14\Phi_z^i + 47\right)l^{i^5} - \frac{3}{10}\left(3\Phi_z^i + 10\right)\alpha_{y_3}l^{i^4} \\ +\frac{1}{5}\left(5\Phi_z^i + 17\right)\alpha_{y_2}l^{i^3} - \left(\Phi_z^i + 4\right)\alpha_{y_1}l^{i^2} + 6\alpha_{y_0}l^i \end{array}\right)\cos^2\psi
\end{aligned}$$

$$\begin{aligned}
k_{6,6}^v &= \Gamma_{yy}\left(\begin{array}{l} \frac{1}{35}\left(7\Phi_z^{i^2} - 14\Phi_z^i + 12\right)l^{i^6} - \frac{1}{20}\left(5\Phi_z^{i^2} - 8\Phi_z^i + 8\right)\alpha_{z_3}l^{i^5} \\ +\frac{1}{15}\left(5\Phi_z^{i^2} - 5\Phi_z^i + 8\right)\alpha_{z_2}l^{i^4} - \frac{1}{2}\left(\Phi_z^{i^2} + 2\right)\alpha_{z_1}l^{i^3} \\ +\left(\Phi_z^{i^2} + 2\Phi_z^i + 4\right)\alpha_{z_0}l^{i^2} \end{array}\right)\sin^2\psi \\
&+ \Gamma_{zz}\left(\begin{array}{l} \frac{1}{35}\left(7\Phi_z^{i^2} - 14\Phi_z^i + 12\right)l^{i^6} - \frac{1}{20}\left(5\Phi_z^{i^2} - 8\Phi_z^i + 8\right)\alpha_{y_3}l^{i^5} \\ +\frac{1}{15}\left(5\Phi_z^{i^2} - 5\Phi_z^i + 8\right)\alpha_{y_2}l^{i^4} - \frac{1}{2}\left(\Phi_z^{i^2} + 2\right)\alpha_{y_1}l^{i^3} \\ +\left(\Phi_z^{i^2} + 2\Phi_z^i + 4\right)\alpha_{y_0}l^{i^2} \end{array}\right)\cos^2\psi
\end{aligned}$$

$$\begin{aligned}
k_{12,6}^v &= \Gamma_{yy}\left(\begin{array}{l} -\frac{1}{35}\left(7\Phi_z^{i^2} + 14\Phi_z^i - 26\right)l^{i^6} + \frac{1}{20}\left(5\Phi_z^{i^2} + 10\Phi_z^i - 16\right)\alpha_{z_3}l^{i^5} \\ -\frac{1}{15}\left(5\Phi_z^{i^2} + 10\Phi_z^i - 13\right)\alpha_{z_2}l^{i^4} + \frac{1}{2}\left(\Phi_z^{i^2} + 2\Phi_z^i - 2\right)\alpha_{z_1}l^{i^3} \\ -\left(\Phi_z^2 + 2\Phi_z^i - 2\right)\alpha_{z_0}l^{i^2} \end{array}\right)\sin^2\psi \\
&+ \Gamma_{zz}\left(\begin{array}{l} -\frac{1}{35}\left(7\Phi_z^{i^2} + 14\Phi_z^i - 26\right)l^{i^6} + \frac{1}{20}\left(5\Phi_z^{i^2} + 10\Phi_z^i - 16\right)\alpha_{y_3}l^{i^5} \\ -\frac{1}{15}\left(5\Phi_z^{i^2} + 10\Phi_z^i - 13\right)\alpha_{y_2}l^{i^4} + \frac{1}{2}\left(\Phi_z^{i^2} + 2\Phi_z^i - 2\right)\alpha_{y_1}l^{i^3} \\ -\left(\Phi_z^{i^2} + 2\Phi_z^i - 2\right)\alpha_{y_0}l^{i^2} \end{array}\right)\cos^2\psi
\end{aligned}$$

$$
\begin{aligned}
k^v_{12,12} &= \Gamma_{yy}\left\{\begin{array}{l}
\frac{1}{35}\left(7\Phi_z^{i^2}+42\Phi_z^i+68\right)l^{i^6}-\frac{1}{20}\left(5\Phi_z^{i^2}+28\Phi_z^i+44\right)\alpha_{z_3}l^{i^5}\\
+\frac{1}{15}\left(5\Phi_z^{i^2}+25\Phi_z^i+38\right)\alpha_{z_2}l^{i^4}-\frac{1}{2}\left(\Phi_z^{i^2}+4\Phi_z^i+6\right)\alpha_{z_1}l^{i^3}\\
+\left(\Phi_z^{i^2}+2\Phi_z^i+4\right)\alpha_{z_0}l^{i^2}
\end{array}\right\}\sin^2\psi\\
&+ \Gamma_{zz}\left\{\begin{array}{l}
\frac{1}{35}\left(7\Phi_z^{i^2}+42\Phi_z^i+68\right)l^{i^6}-\frac{1}{20}\left(5\Phi_z^{i^2}+28\Phi_z^i+44\right)\alpha_{y_3}l^{i^5}\\
+\frac{1}{15}\left(5\Phi_z^{i^2}+25\Phi_z^i+38\right)\alpha_{y_2}l^{i^4}-\frac{1}{2}\left(\Phi_z^{i^2}+4\Phi_z^i+6\right)\alpha_{y_1}l^{i^3}\\
+\left(\Phi_z^{i^2}+2\Phi_z^i+4\right)\alpha_{y_0}l^{i^2}
\end{array}\right\}\cos^2\psi
\end{aligned}
$$

where

$$
\Gamma_{yy}=\frac{I_{oyy}}{L_{oy}L_{oz}^3}\qquad\text{and}\qquad\Gamma_{zz}=\frac{I_{ozz}}{L_{oz}L_{oy}^3}
$$

Table C.4: Elemental bending stiffness matrix in the (xz)-plane

$$
\left[\overline{k}_w^i\right]_{12\times12}=\frac{E\overline{\Phi}_y^{i^2}}{l^{i^3}}\left[k^w_{p,q}\right],\quad p,q=1,2,...,12
$$

where the nonzero entries of the lower triangular part of $\left[k^w_{p,q}\right]$ are given by

$$
\begin{aligned}
k^w_{3,3} &= -k^w_{9,3} = k^w_{9,9} = \Gamma_{yy}\left(\frac{132}{35}l^{i^4}-\frac{21}{5}\alpha_{z_3}l^{i^3}+\frac{24}{5}\alpha_{z_2}l^{i^2}-6\alpha_{z_1}l^i+12\alpha_{z_0}\right)\cos^2\psi\\
&+ \Gamma_{zz}\left(\frac{132}{35}l^{i^4}-\frac{21}{5}\alpha_{y_3}l^{i^3}+\frac{24}{5}\alpha_{y_2}l^{i^2}-6\alpha_{y_1}l^i+12\alpha_{y_0}\right)\sin^2\psi
\end{aligned}
$$

$$
\begin{aligned}
k^w_{5,3} &= -k^w_{9,5} = \Gamma_{yy}\left\{\begin{array}{l}
\frac{2}{35}\left(14\Phi_y^i-19\right)l^{i^5}-\frac{3}{10}\left(3\Phi_y^i-4\right)\alpha_{z_3}l^{i^4}\\
+\frac{1}{5}\left(5\Phi_y^i-7\right)\alpha_{z_2}l^{i^3}-\left(\Phi_y^i-2\right)\alpha_{z_1}l^{i^2}-6\alpha_{z_0}l^i
\end{array}\right\}\cos^2\psi\\
&+ \Gamma_{zz}\left\{\begin{array}{l}
\frac{2}{35}\left(14\Phi_y^i-19\right)l^{i^5}-\frac{3}{10}\left(3\Phi_y^i-4\right)\alpha_{y_3}l^{i^4}\\
+\frac{1}{5}\left(5\Phi_y^i-7\right)\alpha_{y_2}l^{i^3}-\left(\Phi_y^i-2\right)\alpha_{y_1}l^{i^2}-6\alpha_{y_0}l^i
\end{array}\right\}\sin^2\psi
\end{aligned}
$$

$$
\begin{aligned}
k^w_{11,3} &= -k^w_{11,9} = \Gamma_{yy}\left\{\begin{array}{l}
-\frac{2}{35}\left(14\Phi_y^i+47\right)l^{i^5}+\frac{3}{10}\left(3\Phi_y^i+10\right)\alpha_{z_3}l^{i^4}\\
-\frac{1}{5}\left(5\Phi_y^i+17\right)\alpha_{z_2}l^{i^3}+\left(\Phi_y^i+4\right)\alpha_{z_1}l^{i^2}-6\alpha_{z_0}l^i
\end{array}\right\}\cos^2\psi\\
&+ \Gamma_{zz}\left\{\begin{array}{l}
-\frac{2}{35}\left(14\Phi_y^i+47\right)l^{i^5}+\frac{3}{10}\left(3\Phi_y^i+10\right)\alpha_{y_3}l^{i^4}\\
-\frac{1}{5}\left(5\Phi_y^i+17\right)\alpha_{y_2}l^{i^3}+\left(\Phi_y^i+4\right)\alpha_{y_1}l^{i^2}-6\alpha_{y_0}l^i
\end{array}\right\}\sin^2\psi
\end{aligned}
$$

$$
\begin{aligned}
k^w_{5,5} &= \Gamma_{yy}\left\{\begin{array}{l}
\frac{1}{35}\left(7\Phi_y^{i^2}-14\Phi_y^i+12\right)l^{i^6}-\frac{1}{20}\left(5\Phi_y^{i^2}-8\Phi_y^i+8\right)\alpha_{z_3}l^{i^5}\\
+\frac{1}{15}\left(5\Phi_y^{i^2}-5\Phi_y^i+8\right)\alpha_{z_2}l^{i^4}-\frac{1}{2}\left(\Phi_y^{i^2}+2\right)\alpha_{z_1}l^{i^3}\\
+\left(\Phi_y^{i^2}+2\Phi_y^i+4\right)\alpha_{z_0}l^{i^2}
\end{array}\right\}\cos^2\psi\\
&+ \Gamma_{zz}\left\{\begin{array}{l}
\frac{1}{35}\left(7\Phi_y^{i^2}-14\Phi_y^i+12\right)l^{i^6}-\frac{1}{20}\left(5\Phi_y^{i^2}-8\Phi_y^i+8\right)\alpha_{y_3}l^{i^5}\\
+\frac{1}{15}\left(5\Phi_y^{i^2}-5\Phi_y^i+8\right)\alpha_{y_2}l^{i^4}-\frac{1}{2}\left(\Phi_y^{i^2}+2\right)\alpha_{y_1}l^{i^3}\\
+\left(\Phi_y^{i^2}+2\Phi_y^i+4\right)\alpha_{y_0}l^{i^2}
\end{array}\right\}\sin^2\psi
\end{aligned}
$$

$$
\begin{aligned}
k^w_{11,5} &= \Gamma_{yy}\left\{\begin{array}{l}
-\frac{1}{35}\left(7\Phi_y^{i^2}+14\Phi_y^i-26\right)l^{i^6}+\frac{1}{20}\left(5\Phi_y^{i^2}+10\Phi_y^i-16\right)\alpha_{z_3}l^{i^5}\\
-\frac{1}{15}\left(5\Phi_y^{i^2}+10\Phi_y^i-13\right)\alpha_{z_2}l^{i^4}+\frac{1}{2}\left(\Phi_y^{i^2}+2\Phi_y^i-2\right)\alpha_{z_1}l^{i^3}\\
-\left(\Phi_y^{i^2}+2\Phi_y^i-2\right)\alpha_{z_0}l^{i^2}
\end{array}\right\}\cos^2\psi\\
&+ \Gamma_{zz}\left\{\begin{array}{l}
-\frac{1}{35}\left(7\Phi_y^{i^2}+14\Phi_y^i-26\right)l^{i^6}+\frac{1}{20}\left(5\Phi_y^{i^2}+10\Phi_y^i-16\right)\alpha_{y_3}l^{i^5}\\
-\frac{1}{15}\left(5\Phi_y^{i^2}+10\Phi_y^i-13\right)\alpha_{y_2}l^{i^4}+\frac{1}{2}\left(\Phi_y^{i^2}+2\Phi_y^i-2\right)\alpha_{y_1}l^{i^3}\\
-\left(\Phi_y^{i^2}+2\Phi_y^i-2\right)\alpha_{y_0}l^{i^2}
\end{array}\right\}\sin^2\psi
\end{aligned}
$$

$$
\begin{aligned}
k^w_{11,11} &= \Gamma_{yy}\left\{\begin{array}{l}
\frac{1}{35}\left(7\Phi_y^{i^2}+42\Phi_y^i+68\right)l^{i^6}-\frac{1}{20}\left(5\Phi_y^{i^2}+28\Phi_y^i+44\right)\alpha_{z_3}l^{i^5}\\
+\frac{1}{15}\left(5\Phi_y^{i^2}+25\Phi_y^i+38\right)\alpha_{z_2}l^{i^4}-\frac{1}{2}\left(\Phi_y^{i^2}+4\Phi_y^i+6\right)\alpha_{z_1}l^{i^3}\\
+\left(\Phi_y^{i^2}+2\Phi_y^i+4\right)\alpha_{z_0}l^{i^2}
\end{array}\right\}\cos^2\psi\\
&+ \Gamma_{zz}\left\{\begin{array}{l}
\frac{1}{35}\left(7\Phi_y^{i^2}+42\Phi_y^i+68\right)l^{i^6}-\frac{1}{20}\left(5\Phi_y^{i^2}+28\Phi_y^i+44\right)\alpha_{y_3}l^{i^5}\\
+\frac{1}{15}\left(5\Phi_y^{i^2}+25\Phi_y^i+38\right)\alpha_{y_2}l^{i^4}-\frac{1}{2}\left(\Phi_y^{i^2}+4\Phi_y^i+6\right)\alpha_{y_1}l^{i^3}\\
+\left(\Phi_y^{i^2}+2\Phi_y^i+4\right)\alpha_{y_0}l^{i^2}
\end{array}\right\}\sin^2\psi
\end{aligned}
$$

Table C.5: Elemental stiffness matrix due to coupling in bending

$$
\boxed{\left[\overline{k}^i_{vw}\right]=\frac{E\overline{\Phi}^i_y\overline{\Phi}^i_z\sin 2\psi}{2l^{i^3}}\left[k^{vw}_{p,q}\right],\quad p,q=1,2,...,12}
$$

where the nonzero entries of the lower triangular part of $\left[k^{vw}_{p,q}\right]$ are given by

$$
\begin{aligned}
k^{vw}_{3,2}=-k^{vw}_{9,2}=-k^{vw}_{8,3}=k^{vw}_{9,8} &= \Gamma_{yy}\left(\frac{132}{35}l^{i^4}-\frac{21}{5}\alpha_{z_3}l^{i^3}+\frac{24}{5}\alpha_{z_2}l^{i^2}-6\alpha_{z_1}l^i+12\alpha_{z_0}\right)\\
&- \Gamma_{zz}\left(\frac{132}{35}l^{i^4}-\frac{21}{5}\alpha_{y_3}l^{i^3}+\frac{24}{5}\alpha_{y_2}l^{i^2}-6\alpha_{y_1}l^i+12\alpha_{y_0}\right)
\end{aligned}
$$

$$
\begin{aligned}
k^{vw}_{5,2} = -k^{vw}_{8,5} &= \Gamma_{yy}\left\{\begin{array}{l}
\frac{2}{35}\left(14\Phi^i_y-19\right)l^{i^5}-\frac{3}{10}\left(3\Phi^i_y-4\right)\alpha_{z_3}l^{i^4}\\
+\frac{1}{5}\left(5\Phi^i_y-7\right)\alpha_{z_2}l^{i^3}-\left(\Phi^i_y-2\right)\alpha_{z_1}l^{i^2}-6\alpha_{z_0}l^i
\end{array}\right\}\\
&- \Gamma_{zz}\left\{\begin{array}{l}
\frac{2}{35}\left(14\Phi^i_y-19\right)l^{i^5}-\frac{3}{10}\left(3\Phi^i_y-4\right)\alpha_{y_3}l^{i^4}\\
+\frac{1}{5}\left(5\Phi^i_y-7\right)\alpha_{y_2}l^{i^3}-\left(\Phi^i_y-2\right)\alpha_{y_1}l^{i^2}-6\alpha_{y_0}l^i
\end{array}\right\}
\end{aligned}
$$

$$
\begin{aligned}
k^{w}_{11,2} = -k^{vw}_{11,8} &= \Gamma_{yy}\left\{\begin{array}{l}
-\frac{2}{35}\left(14\Phi^i_y+47\right)l^{i^5}+\frac{3}{10}\left(3\Phi^i_y+10\right)\alpha_{z_3}l^{i^4}\\
-\frac{1}{5}\left(5\Phi^i_y+17\right)\alpha_{z_2}l^{i^3}+\left(\Phi^i_y+4\right)\alpha_{z_1}l^{i^2}-6\alpha_{z_0}l^i
\end{array}\right\}\\
&- \Gamma_{zz}\left\{\begin{array}{l}
-\frac{2}{35}\left(14\Phi^i_y+47\right)l^{i^5}+\frac{3}{10}\left(3\Phi^i_y+10\right)\alpha_{y_3}l^{i^4}\\
-\frac{1}{5}\left(5\Phi^i_y+17\right)\alpha_{y_2}l^{i^3}+\left(\Phi^i_y+4\right)\alpha_{y_1}l^{i^2}-6\alpha_{y_0}l^i
\end{array}\right\}
\end{aligned}
$$

$$
\begin{aligned}
k^{vw}_{6,3} = -k^{vw}_{9,6} &= \Gamma_{yy}\left\{\begin{array}{l}
-\frac{2}{35}\left(14\Phi^i_z-19\right)l^{i^5}+\frac{3}{10}\left(3\Phi^i_z-4\right)\alpha_{z_3}l^{i^4}\\
-\frac{1}{5}\left(5\Phi^i_z-7\right)\alpha_{z_2}l^{i^3}+\left(\Phi^i_z-2\right)\alpha_{z_1}l^{i^2}+6\alpha_{z_0}l^i
\end{array}\right\}\\
&- \Gamma_{zz}\left\{\begin{array}{l}
-\frac{2}{35}\left(14\Phi^i_z-19\right)l^{i^5}+\frac{3}{10}\left(3\Phi^i_z-4\right)\alpha_{y_3}l^{i^4}\\
-\frac{1}{5}\left(5\Phi^i_z-7\right)\alpha_{y_2}l^{i^3}+\left(\Phi^i_z-2\right)\alpha_{y_1}l^{i^2}+6\alpha_{y_0}l^i
\end{array}\right\}
\end{aligned}
$$

$$
\begin{aligned}
k^{vw}_{12,3} = -k^{vw}_{12,9} &= \Gamma_{yy}\left\{\begin{array}{l}
\frac{2}{35}\left(14\Phi^i_z+47\right)l^{i^5}-\frac{3}{10}\left(3\Phi^i_z+10\right)\alpha_{z_3}l^{i^4}\\
+\frac{1}{5}\left(5\Phi^i_z+17\right)\alpha_{z_2}l^{i^3}-\left(\Phi^i_z+4\right)\alpha_{z_1}l^{i^2}+6\alpha_{z_0}l^i
\end{array}\right\}\\
&- \Gamma_{zz}\left\{\begin{array}{l}
\frac{2}{35}\left(14\Phi^i_z+47\right)l^{i^5}-\frac{3}{10}\left(3\Phi^i_z+10\right)\alpha_{y_3}l^{i^4}\\
+\frac{1}{5}\left(5\Phi^i_z+17\right)\alpha_{y_2}l^{i^3}-\left(\Phi^i_z+4\right)\alpha_{y_1}l^{i^2}+6\alpha_{y_0}l^i
\end{array}\right\}
\end{aligned}
$$

$$
\begin{aligned}
k^{vw}_{6,5} &= \Gamma_{yy}\left\{\begin{array}{l}
-\frac{1}{35}\left(7\Phi^i_y\Phi^i_z-7\Phi^i_y-7\Phi^i_z+12\right)l^{i^6}+\frac{1}{20}\left(5\Phi^i_y\Phi^i_z-4\Phi^i_y-4\Phi^i_z+8\right)\alpha_{z_3}l^{i^5}\\
-\frac{1}{30}\left(10\Phi^i_y\Phi^i_z-5\Phi^i_y-5\Phi^i_z+16\right)\alpha_{z_2}l^{i^4}+\frac{1}{2}\left(\Phi^i_y\Phi^i_z+2\right)\alpha_{z_1}l^{i^3}\\
-\left(\Phi^i_y\Phi^i_z+\Phi^i_y+\Phi^i_z+4\right)\alpha_{z_0}l^{i^2}
\end{array}\right\}\\
&- \Gamma_{zz}\left\{\begin{array}{l}
-\frac{1}{35}\left(7\Phi^i_y\Phi^i_z-7\Phi^i_y-7\Phi^i_z+12\right)l^{i^6}+\frac{1}{20}\left(5\Phi^i_y\Phi^i_z-4\Phi^i_y-4\Phi^i_z+8\right)\alpha_{y_3}l^{i^5}\\
-\frac{1}{30}\left(10\Phi^i_y\Phi_z-5\Phi^i_y-5\Phi^i_z+16\right)\alpha_{y_2}l^{i^4}+\frac{1}{2}\left(\Phi^i_y\Phi^i_z+2\right)\alpha_{y_1}l^{i^3}\\
-\left(\Phi^i_y\Phi^i_z+\Phi^i_y+\Phi^i_z+4\right)\alpha_{y_0}l^{i^2}
\end{array}\right\}
\end{aligned}
$$

$$
\begin{aligned}
k^{vw}_{12,5} &= \Gamma_{yy}\left\{\begin{array}{l}
\frac{1}{35}\left(7\Phi^i_y\Phi^i_z+21\Phi^i_y-7\Phi^i_z-26\right)l^{i^6}-\frac{1}{20}\left(5\Phi^i_y\Phi^i_z+14\Phi^i_y-4\Phi^i_z-16\right)\alpha_{z_3}l^{i^5}\\
+\frac{1}{30}\left(10\Phi^i_y\Phi^i_z+25\Phi^i_y-5\Phi^i_z-26\right)\alpha_{z_2}l^{i^4}-\frac{1}{2}\left(\Phi^i_y\Phi^i_z+2\Phi^i_y-2\right)\alpha_{z_1}l^{i^3}\\
+\left(\Phi^i_y\Phi^i_z+\Phi^i_y+\Phi^i_z-2\right)\alpha_{z_0}l^{i^2}
\end{array}\right\}\\
&- \Gamma_{zz}\left\{\begin{array}{l}
\frac{1}{35}\left(7\Phi^i_y\Phi^i_z+21\Phi^i_y-7\Phi^i_z-26\right)l^{i^6}-\frac{1}{20}\left(5\Phi^i_y\Phi^i_z+14\Phi^i_y-4\Phi^i_z-16\right)\alpha_{y_3}l^{i^5}\\
+\frac{1}{30}\left(10\Phi^i_y\Phi^i_z+25\Phi^i_y-5\Phi^i_z-26\right)\alpha_{y_2}l^{i^4}-\frac{1}{2}\left(\Phi^i_y\Phi^i_z+2\Phi_y-2\right)\alpha_{y_1}l^{i^3}\\
+\left(\Phi^i_y\Phi^i_z+\Phi^i_y+\Phi^i_z-2\right)\alpha_{y_0}l^{i^2}
\end{array}\right\}
\end{aligned}
$$

$$
\begin{aligned}
k^{vw}_{11,6} \;=\;& \Gamma_{yy}\left\{\begin{array}{l}
\frac{1}{35}\left(7\Phi^i_y\Phi^i_z-7\Phi^i_y+21\Phi^i_z-26\right)l^{i^6}-\frac{1}{20}\left(5\Phi^i_y\Phi^i_z-4\Phi^i_y+14\Phi^i_z-16\right)\alpha_{z_3}l^{i^5}\\
+\frac{1}{30}\left(10\Phi^i_y\Phi^i_z-5\Phi^i_y+25\Phi^i_z-26\right)\alpha_{z_2}l^{i^4}-\frac{1}{2}\left(\Phi^i_y\Phi^i_z+2\Phi^i_z-2\right)\alpha_{z_1}l^{i^3}\\
+\left(\Phi^i_y\Phi^i_z+\Phi^i_y+\Phi^i_z-2\right)\alpha_{z_0}l^{i^2}
\end{array}\right\}\\
-\;& \Gamma_{zz}\left\{\begin{array}{l}
\frac{1}{35}\left(7\Phi^i_y\Phi^i_z-7\Phi^i_y+21\Phi^i_z-26\right)l^{i^6}-\frac{1}{20}\left(5\Phi^i_y\Phi^i_z-4\Phi^i_y+14\Phi^i_z-16\right)\alpha_{y_3}l^{i^5}\\
+\frac{1}{30}\left(10\Phi^i_y\Phi^i_z-5\Phi^i_y+25\Phi^i_z-26\right)\alpha_{y_2}l^{i^4}-\frac{1}{2}\left(\Phi^i_y\Phi^i_z+2\Phi^i_z-2\right)\alpha_{y_1}l^{i^3}\\
+\left(\Phi^i_y\Phi^i_z+\Phi^i_y+\Phi^i_z-2\right)\alpha_{y_0}l^{i^2}
\end{array}\right\}
\end{aligned}
$$

$$
\begin{aligned}
k^{vw}_{12,11} \;=\;& \Gamma_{yy}\left\{\begin{array}{l}
-\frac{1}{35}\left(7\Phi^i_y\Phi^i_z+21\Phi^i_y+21\Phi^i_z+68\right)l^{i^6}+\frac{1}{20}\left(5\Phi^i_y\Phi^i_z+14\Phi^i_y+14\Phi^i_z+44\right)\alpha_{z_3}l^{i^5}\\
-\frac{1}{30}\left(10\Phi^i_y\Phi^i_z+25\Phi^i_y+25\Phi^i_z+76\right)\alpha_{z_2}l^{i^4}+\frac{1}{2}\left(\Phi^i_y\Phi^i_z+2\Phi^i_y+2\Phi^i_z+6\right)\alpha_{z_1}l^{i^3}\\
-\left(\Phi^i_y\Phi^i_z+\Phi^i_y+\Phi^i_z+4\right)\alpha_{z_0}l^{i^2}
\end{array}\right\}\\
-\;& \Gamma_{zz}\left\{\begin{array}{l}
-\frac{1}{35}\left(7\Phi^i_y\Phi^i_z+21\Phi^i_y+21\Phi^i_z+68\right)l^{i^6}+\frac{1}{20}\left(5\Phi^i_y\Phi^i_z+14\Phi^i_y+14\Phi^i_z+44\right)\alpha_{y_3}l^{i^5}\\
-\frac{1}{30}\left(10\Phi^i_y\Phi^i_z+25\Phi^i_y+25\Phi^i_z+76\right)\alpha_{y_2}l^{i^4}+\frac{1}{2}\left(\Phi^i_y\Phi^i_z+2\Phi^i_y+2\Phi^i_z+6\right)\alpha_{y_1}l^{i^3}\\
-\left(\Phi^i_y\Phi^i_z+\Phi^i_y+\Phi^i_z+4\right)\alpha_{y_0}l^{i^2}
\end{array}\right\}
\end{aligned}
$$

Table C.6: Elemental shear stiffness matrix due to shear in the (xy)-plane

$$
\left[k^i_{s,v}\right]_{12\times 12}=\frac{A_o\kappa_y\;G\Phi^{i^2}_z\overline{\Phi}^{i^2}_z}{L_{oy}L_{oz}}\left[k^{s,v}_{p,q}\right],\qquad p,q=1,2,...,12
$$

where the nonzero entries of the lower triangular part of $[k^{s,v}_{p,q}]$ are given by

$$
\begin{aligned}
k^{s,v}_{2,2} &= -k^{s,v}_{8,2} = k^{s,v}_{8,8} &&= \mu_1 l^{i^{-1}}-\mu_2+\frac{1}{3}l^i\\
k^{s,v}_{6,2} &= -k^{s,v}_{8,6} = -k^{s,v}_{12,8}=k^{s,v}_{12,2} &&= \frac{1}{2}\mu_1-\frac{1}{2}\mu_2 l^i+\frac{1}{6}l^{i^2}\\
k^{s,v}_{6,6} &= k^{s,v}_{12,6} = k^{s,v}_{12,12} &&= \frac{1}{4}\mu_1 l^i-\frac{1}{4}\mu_2 l^{i^2}+\frac{1}{12}l^{i^3}
\end{aligned}
$$

Table C.7: Elemental shear stiffness matrix due to shear in the (xz)-plane

$$
\left[k^i_{s,w}\right]_{12\times 12}=\frac{A_o\kappa_z\;G\Phi^{i^2}_y\overline{\Phi}^{i^2}_y}{L_{oy}L_{oz}}\left[k^{s,w}_{p,q}\right],\qquad p,q=1,2,...,12
$$

where the nonzero entries of the lower triangular part of $[k^{s,w}_{p,q}]$ are given by

$$
\begin{aligned}
k^{s,w}_{33} &= -k^{s,w}_{93} = k^{s,w}_{99} &&= \mu_1 l^{i^{-1}}-\mu_2+\frac{1}{3}l^i\\
k^{s,w}_{53} &= -k^{s,w}_{95} = k^{s,w}_{11,3}=k^{s,w}_{11,9} &&= -\frac{1}{2}\mu_1+\frac{1}{2}\mu_2 l^i-\frac{1}{6}l^{i^2}\\
k^{s,w}_{55} &= k^{s,w}_{11,5} = k^{s,w}_{11,11} &&= \frac{1}{4}\mu_1 l^i-\frac{1}{4}\mu_2 l^{i^2}+\frac{1}{12}l^{i^3}
\end{aligned}
$$

Table C.8: Elemental centrifugal stiffness matrix in the (xy)-plane

$$\left[k^i_{c,v}\right]_{12\times 12} = \frac{\rho\Omega^2 A_\circ \overline{\Phi}_z^{i^2}}{l^i L_{oy} L_{oz}} \left[k^{c,v}_{p,q}\right], \qquad p,q = 1,2,...,12$$

where the nonzero entries of the lower triangular part of $[k^{c,v}_{p,q}]$ are given by:

$$\begin{aligned}
k^{c,v}_{2,2} = -k^{c,v}_{8,2} = k^{c,v}_{8,8} &= -\frac{1}{35}\left(7\Phi_z^{i^2} + 10\Phi_z^i + 5\right)\beta_4 l^{i^4} - \frac{1}{140}\left(35\Phi_z^{i^2} + 56\Phi_z^i + 30\right)\beta_3 l^{i^3} \\
&- \frac{1}{105}\left(35\Phi_z^{i^2} + 63\Phi_z^i + 36\right)\beta_2 l^{i^2} - \frac{1}{10}\left(5\Phi_z^{i^2} + 10\Phi_z^i + 6\right)\beta_1 l^i \\
&+ \frac{1}{5}\left(5\Phi_z^{i^2} + 10\Phi_z^i + 6\right)\beta_0
\end{aligned}$$

$$\begin{aligned}
k^{c,v}_{6,2} = -k^{c,v}_{8,6} &= -\frac{1}{420}\left(28\Phi_z^{i^2} + 31\Phi_z^i + 15\right)\beta_4 l^{i^5} - \frac{1}{280}\left(21\Phi_z^{i^2} + 26\Phi_z^i + 14\right)\beta_3 l^{i^4} \\
&- \frac{1}{420}\left(35\Phi_z^{i^2} + 49\Phi_z^i + 30\right)\beta_2 l^{i^3} - \frac{1}{60}\left(5\Phi_z^{i^2} + 8\Phi_z^i + 6\right)\beta_1 l^{i^2} + \frac{1}{10}\beta_0 l^i
\end{aligned}$$

$$\begin{aligned}
k^{c,v}_{12,2} = -k^{c,v}_{12,8} &= \frac{1}{420}\left(28\Phi_z^{i^2} + 55\Phi_z^i + 15\right)\beta_4 l^{i^5} + \frac{1}{280}\left(21\Phi_z^{i^2} + 40\Phi_z^i + 10\right)\beta_3 l^{i^4} \\
&+ \frac{1}{420}\left(35\Phi_z^{i^2} + 63\Phi_z^i + 12\right)\beta_2 l^{i^3} + \frac{1}{60}\left(5\Phi_z^{i^2} + 8\Phi_z^i\right)\beta_1 l^{i^2} + \frac{1}{10}\beta_0 l^i
\end{aligned}$$

$$\begin{aligned}
k^{c,v}_{6,6} &= -\frac{1}{420}\left(11\Phi_z^{i^2} + 9\Phi_z^i + 4\right)\beta_4 l^{i^6} - \frac{1}{1680}\left(49\Phi_z^{i^2} + 44\Phi_z^i + 22\right)\beta_3 l^{i^5} \\
&- \frac{1}{210}\left(7\Phi_z^{i^2} + 7\Phi_z^i + 4\right)\beta_2 l^{i^4} - \frac{1}{120}\left(5\Phi_z^{i^2} + 6\Phi_z^i + 4\right)\beta_1 l^{i^3} \\
&+ \frac{1}{60}\left(5\Phi_z^{i^2} + 10\Phi_z^i + 8\right)\beta_0 l^{i^2}
\end{aligned}$$

$$\begin{aligned}
k^{c,v}_{12,6} &= \frac{1}{420}\left(11\Phi_z^{i^2} + 22\Phi_z^i + 5\right)\beta_4 l^{i^6} + \frac{1}{1680}\left(49\Phi_z^{i^2} + 98\Phi_z^i + 22\right)\beta_3 l^{i^5} \\
&+ \frac{1}{210}\left(7\Phi_z^{i^2} + 14\Phi_z^i + 3\right)\beta_2 l^{i^4} + \frac{1}{120}\left(5\Phi_z^{i^2} + 10\Phi_z^i + 2\right)\beta_1 l^{i^3} \\
&- \frac{1}{60}\left(5\Phi_z^{i^2} + 10\Phi_z^i + 2\right)\beta_0 l^{i^2}
\end{aligned}$$

$$\begin{aligned}
k^{c,v}_{12,12} &= -\frac{1}{420}\left(11\Phi_z^{i^2} + 35\Phi_z^i + 30\right)\beta_4 l^{i^6} - \frac{1}{1680}\left(49\Phi_z^{i^2} + 152\Phi_z^i + 130\right)\beta_3 l^{i^5} \\
&- \frac{1}{210}\left(7\Phi_z^{i^2} + 21\Phi_z^i + 18\right)\beta_2 l^{i^4} - \frac{1}{120}\left(5\Phi_z^{i^2} + 14\Phi_z^i + 12\right)\beta_1 l^{i^3} \\
&+ \frac{1}{60}\left(5\Phi_z^{i^2} + 10\Phi_z^i + 8\right)\beta_0 l^{i^2}
\end{aligned}$$

Table C.9: Elemental centrifugal stiffness matrix in the (xz)-plane

$$\left[k^i_{c,w}\right]_{12\times 12} = \frac{\rho\Omega^2 A_\circ \overline{\Phi}_y^{i^2}}{l^i L_{oy} L_{oz}} \left[k^{c,w}_{p,q}\right], \qquad p,q = 1,2,...,12$$

where the nonzero entries of the lower triangular part of $[k^{c,w}_{p,q}]$ are given by:

$$\begin{aligned}
k^{c,w}_{3,3} = -k^{c,w}_{9,3} = k^{c,w}_{9,9} &= -\frac{1}{35}\left(7\Phi_y^{i^2}+10\Phi_y^i+5\right)\beta_4 l^{i^4} - \frac{1}{140}\left(35\Phi_y^{i^2}+56\Phi_y^i+30\right)\beta_3 l^{i^3} \\
&- \frac{1}{105}\left(35\Phi_y^{i^2}+63\Phi_y^i+36\right)\beta_2 l^{i^2} - \frac{1}{10}\left(5\Phi_y^{i^2}+10\Phi_y^i+6\right)\beta_1 l^i \\
&+ \frac{1}{5}\left(5\Phi_y^{i^2}+10\Phi_y^i+6\right)\beta_0
\end{aligned}$$

$$\begin{aligned}
k^{c,w}_{5,3} = -k^{c,w}_{9,5} &= \frac{1}{420}\left(28\Phi_y^{i^2}+31\Phi_y^i+15\right)\beta_4 l^{i^5} + \frac{1}{280}\left(21\Phi_y^{i^2}+26\Phi_y^i+14\right)\beta_3 l^{i^4} \\
&+ \frac{1}{420}\left(35\Phi_y^{i^2}+49\Phi_y^i+30\right)\beta_2 l^{i^3} + \frac{1}{60}\left(5\Phi_y^{i^2}+8\Phi_y^i+6\right)\beta_1 l^{i^2} - \frac{1}{10}\beta_0 l^i
\end{aligned}$$

$$\begin{aligned}
k^{c,v}_{11,3} = -k^{c,w}_{11,9} &= -\frac{1}{420}\left(28\Phi_y^{i^2}+55\Phi_y^i+15\right)\beta_4 l^{i^5} - \frac{1}{280}\left(21\Phi_y^{i^2}+40\Phi_y^i+10\right)\beta_3 l^{i^4} \\
&- \frac{1}{420}\left(35\Phi_y^{i^2}+63\Phi_y^i+12\right)\beta_2 l^{i^3} - \frac{1}{60}\left(5\Phi_y^{i^2}+8\Phi_y^i\right)\beta_1 l^{i^2} - \frac{1}{10}\beta_0 l^i
\end{aligned}$$

$$\begin{aligned}
k^{c,w}_{5,5} &= -\frac{1}{420}\left(11\Phi_y^{i^2}+9\Phi_y^i+4\right)\beta_4 l^{i^6} - \frac{1}{1680}\left(49\Phi_y^{i^2}+44\Phi_y^i+22\right)\beta_3 l^{i^5} \\
&- \frac{1}{210}\left(7\Phi_y^{i^2}+7\Phi_y^i+4\right)\beta_2 l^{i^4} - \frac{1}{120}\left(5\Phi_y^{i^2}+6\Phi_y^i+4\right)\beta_1 l^{i^3} \\
&+ \frac{1}{60}\left(5\Phi_y^{i^2}+10\Phi_y^i+8\right)\beta_0 l^{i^2}
\end{aligned}$$

$$\begin{aligned}
k^{c,w}_{11,5} &= \frac{1}{420}\left(11\Phi_y^{i^2}+22\Phi_y^i+5\right)\beta_4 l^{i^6} + \frac{1}{1680}\left(49\Phi_y^{i^2}+98\Phi_y^i+22\right)\beta_3 l^{i^5} \\
&+ \frac{1}{210}\left(7\Phi_y^{i^2}+14\Phi_y^i+3\right)\beta_2 l^{i^4} + \frac{1}{120}\left(5\Phi_y^{i^2}+10\Phi_y^i+2\right)\beta_1 l^{i^3} \\
&- \frac{1}{60}\left(5\Phi_y^{i^2}+10\Phi_y^i+2\right)\beta_0 l^{i^2}
\end{aligned}$$

$$\begin{aligned}
k^{c,w}_{11,11} &= -\frac{1}{420}\left(11\Phi_y^{i^2}+35\Phi_y^i+30\right)\beta_4 l^{i^6} - \frac{1}{1680}\left(49\Phi_y^{i^2}+152\Phi_y^i+130\right)\beta_3 l^{i^5} \\
&- \frac{1}{210}\left(7\Phi_y^{i^2}+21\Phi_y^i+18\right)\beta_2 l^{i^4} - \frac{1}{120}\left(5\Phi_y^{i^2}+14\Phi_y^i+12\right)\beta_1 l^{i^3} \\
&+ \frac{1}{60}\left(5\Phi_y^{i^2}+10\Phi_y^i+8\right)\beta_0 l^{i^2}
\end{aligned}$$

Table C.10: Elemental axial mass matrix

$$\left[\overline{m}_a^i\right]_{12\times 12} = \frac{\rho A_o l^i}{60 L_{oy} L_{oz}} \left[m_{p,q}^a\right] \qquad p,q = 1,2,...,12$$

where the nonzero entries of the lower triangular part of $\left[m_{p,q}^a\right]$ are given by:

$$\begin{aligned}
m_{1,1}^a &= 2\left(10\mu_1 - 5\mu_2 l^i + {l^i}^2\right) \\
m_{7,1}^a &= 10\mu_1 - 10\mu_2 l^i + 3{l^i}^2 \\
m_{7,7}^a &= 2\left(10\mu_1 - 15\mu_2 l^i + 6{l^i}^2\right)
\end{aligned}$$

Table C.11: Elemental torsional mass matrix

$$\left[\overline{m}_{\theta_x}^i\right]_{12\times 12} = \frac{\rho l^i}{420} \left[m_{p,q}^{\theta_x}\right] \qquad p,q = 1,2,...,12$$

where the nonzero entries of the lower triangular part of $\left[m_{p,q}^{\theta_x}\right]$ are given by:

$$\begin{aligned}
m_{4,4}^{\theta_x} &= \Gamma_{zz}\left(4{l^i}^4 - 7\alpha_{y_3}{l^i}^3 + 14\alpha_{y_2}{l^i}^2 - 35\alpha_{y_1} l^i + 140\alpha_{y_0}\right) \\
&+ \Gamma_{yy}\left(4{l^i}^4 - 7\alpha_{z_3}{l^i}^3 + 14\alpha_{z_2}{l^i}^2 - 35\alpha_{z_1} l^i + 140\alpha_{z_0}\right) \\
m_{10,4}^{\theta_x} &= \Gamma_{zz}\left(10{l^i}^4 - 14\alpha_{y_3}{l^i}^3 + 21\alpha_{y_2}{l^i}^2 - 35\alpha_{y_1} l^i + 70\alpha_{y_0}\right) \\
&+ \Gamma_{yy}\left(10{l^i}^4 - 14\alpha_{z_3}{l^i}^3 + 21\alpha_{z_2}{l^i}^2 - 35\alpha_{z_1} l^i + 70\alpha_{z_0}\right) \\
m_{10,10}^{\theta_x} &= \Gamma_{zz}\left(60{l^i}^4 - 70\alpha_{y_3}{l^i}^3 + 84\alpha_{y_2}{l^i}^2 - 105\alpha_{y_1} l^i + 140\alpha_{y_0}\right) \\
&+ \Gamma_{yy}\left(60{l^i}^4 - 70\alpha_{z_3}{l^i}^3 + 84\alpha_{z_2}{l^i}^2 - 105\alpha_{z_1} l^i + 140\alpha_{z_0}\right)
\end{aligned}$$

Table C.12: Elemental translational mass matrix in the (xy)-plane

$$\left[\overline{m}^i_{t,v}\right] = \frac{\rho A_o l^i \overline{\Phi}_z^{i^2}}{L_{oy} L_{oz}} \left[m^{t,v}_{p,q}\right], \qquad p,q = 1,2,...,12$$

where the lower triangular part of the translational mass matrix $\left[m^{t,v}_{p,q}\right]$ in (xy)-plane is given by:

$$\begin{aligned}
m^{t,v}_{2,2} &= \frac{1}{630}\left(21\Phi_z^{i^2} + 39\Phi_z^i + 19\right) l^{i^2} - \frac{1}{210}\left(35\Phi_z^{i^2} + 70\Phi_z^i + 36\right)\mu_2 l^i \\
&+ \frac{1}{210}\left(70\Phi_z^{i^2} + 147\Phi_z^i + 78\right)\mu_1
\end{aligned}$$

$$\begin{aligned}
m^{t,v}_{6,2} &= \frac{1}{2520}\left(21\Phi_z^{i^2} + 36\Phi_z^i + 17\right) l^{i^3} - \frac{1}{420}\left(14\Phi_z^{i^2} + 27\Phi_z^i + 14\right)\mu_2 l^{i^2} \\
&+ \frac{1}{840}\left(35\Phi_z^{i^2} + 77\Phi_z^i + 44\right)\mu_1 l^i
\end{aligned}$$

$$\begin{aligned}
m^{t,v}_{8,2} &= \frac{1}{1260}\left(63\Phi_z^{i^2} + 111\Phi_z^i + 46\right) l^{i^2} - \frac{1}{210}\left(35\Phi_z^{i^2} + 63\Phi_z^i + 27\right)\mu_2 l^i \\
&+ \frac{1}{210}\left(35\Phi_z^{i^2} + 63\Phi_z^i + 27\right)\mu_1
\end{aligned}$$

$$\begin{aligned}
m^{t,v}_{12,2} &= -\frac{1}{2520}\left(21\Phi_z^{i^2} + 42\Phi_z^i + 19\right) l^{i^3} + \frac{1}{420}\left(14\Phi_z^{i^2} + 27\Phi_z^i + 12\right)\mu_2 l^{i^2} \\
&- \frac{1}{840}\left(35\Phi_z^{i^2} + 63\Phi_z^i + 26\right)\mu_1 l^i
\end{aligned}$$

$$\begin{aligned}
m^{t,v}_{6,6} &= \frac{1}{2520}\left(6\Phi_z^{i^2} + 9\Phi_z^i + 4\right) l^{i^4} - \frac{1}{840}\left(7\Phi_z^{i^2} + 12\Phi_z^i + 6\right)\mu_2 l^{i^3} \\
&+ \frac{1}{840}\left(7\Phi_z^{i^2} + 14\Phi_z^i + 8\right)\mu_1 l^{i^2}
\end{aligned}$$

$$\begin{aligned}
m^{t,v}_{8,6} &= \frac{1}{2520}\left(42\Phi_z^{i^2} + 69\Phi_z^i + 25\right) l^{i^3} - \frac{1}{420}\left(21\Phi_z^{i^2} + 36\Phi_z^i + 14\right)\mu_2 l^{i^2} \\
&+ \frac{1}{840}\left(35\Phi_z^{i^2} + 63\Phi_z^i + 26\right)\mu_1 l^i
\end{aligned}$$

$$\begin{aligned}
m^{t,v}_{12,6} &= -\frac{1}{2520}\left(6\Phi_z^{i^2} + 12\Phi_z^i + 5\right) l^{i^4} + \frac{1}{840}\left(7\Phi_z^{i^2} + 14\Phi_z^i + 6\right)\mu_2 l^{i^3} \\
&- \frac{1}{840}\left(7\Phi_z^{i^2} + 14\Phi_z^i + 6\right)\mu_1 l^{i^2}
\end{aligned}$$

$$\begin{aligned}
m^{t,v}_{8,8} &= \frac{1}{630}\left(126\Phi_z^{i^2} + 270\Phi_z^i + 145\right) l^{i^2} - \frac{1}{210}\left(105\Phi_z^{i^2} + 224\Phi_z^i + 120\right)\mu_2 l^i \\
&+ \frac{1}{210}\left(70\Phi_z^{i^2} + 147\Phi_z^i + 78\right)\mu_1
\end{aligned}$$

$$\begin{aligned}
m^{t,v}_{12,8} &= -\frac{1}{2520}\left(42\Phi_z^{i^2} + 105\Phi_z^i + 65\right) l^{i^3} + \frac{1}{420}\left(21\Phi_z^{i^2} + 50\Phi_z^i + 30\right)\mu_2 l^{i^2} \\
&- \frac{1}{840}\left(35\Phi_z^{i^2} + 77\Phi_z^i + 44\right)\mu_1 l^i
\end{aligned}$$

$$\begin{aligned}
m^{t,v}_{12,12} &= \frac{1}{2520}\left(6\Phi_z^{i^2} + 15\Phi_z^i + 10\right) l^{i^4} - \frac{1}{840}\left(7\Phi_z^{i^2} + 16\Phi_z^i + 10\right)\mu_2 l^{i^3} \\
&+ \frac{1}{840}\left(7\Phi_z^{i^2} + 14\Phi_z^i + 8\right)\mu_1 l^{i^2}
\end{aligned}$$

Table C.13: Elemental translational mass matrix in the (xz)-plane

$$\left[\overline{m}^i_{t,w}\right] = \frac{\rho^i A_o l^i \overline{\Phi}_y^{i^2}}{L_{oy} L_{oz}} \left[m^{t,w}_{p,q}\right], \qquad p,q = 1,2,...,12$$

where the lower triangular part of the translational mass matrix $\left[m^{t,w}_{p,q}\right]$ in (xz)-plane is given by:

$$\begin{aligned}
m^{t,w}_{3,3} &= \frac{1}{630}\left(21\Phi_y^{i^2} + 39\Phi_y^i + 19\right) l^{i^2} - \frac{1}{210}\left(35\Phi_z^{i^2} + 70\Phi_y^i + 36\right)\mu_2 l^i \\
&+ \frac{1}{210}\left(70\Phi_y^{i^2} + 147\Phi_y^i + 78\right)\mu_1 \\
m^{t,w}_{5,3} &= -\frac{1}{2520}\left(21\Phi_y^{i^2} + 36\Phi_y^i + 17\right) l^{i^3} + \frac{1}{420}\left(14\Phi_y^{i^2} + 27\Phi_y^i + 14\right)\mu_2 l^{i^2} \\
&- \frac{1}{840}\left(35\Phi_y^{i^2} + 77\Phi_z^i + 44\right)\mu_1 l^i \\
m^{t,w}_{9,3} &= \frac{1}{1260}\left(63\Phi_y^{i^2} + 111\Phi_y^i + 46\right) l^{i^2} - \frac{1}{210}\left(35\Phi_y^{i^2} + 63\Phi_y^i + 27\right)\mu_2 l^i \\
&+ \frac{1}{210}\left(35\Phi_y^{i^2} + 63\Phi_y^i + 27\right)\mu_1 \\
m^{t,w}_{11,3} &= \frac{1}{2520}\left(21\Phi_y^{i^2} + 42\Phi_y^i + 19\right) l^{i^3} - \frac{1}{420}\left(14\Phi_y^{i^2} + 27\Phi_y^i + 12\right)\mu_2 l^{i^2} \\
&+ \frac{1}{840}\left(35\Phi_y^{i^2} + 63\Phi_y^i + 26\right)\mu_1 l^i \\
m^{t,w}_{5,5} &= \frac{1}{2520}\left(6\Phi_y^{i^2} + 9\Phi_y^i + 4\right) l^{i^4} - \frac{1}{840}\left(7\Phi_y^{i^2} + 12\Phi_y^i + 6\right)\mu_2 l^{i^3} \\
&+ \frac{1}{840}\left(7\Phi_y^{i^2} + 14\Phi_y^i + 8\right)\mu_1 l^{i^2} \\
m^{t,w}_{9,5} &= -\frac{1}{2520}\left(42\Phi_y^{i^2} + 69\Phi_y^i + 25\right) l^{i^3} + \frac{1}{420}\left(21\Phi_y^{i^2} + 36\Phi_y^i + 14\right)\mu_2 l^{i^2} \\
&- \frac{1}{840}\left(35\Phi_y^{i^2} + 63\Phi_y^i + 26\right)\mu_1 l^i \\
m^{t,w}_{11,5} &= -\frac{1}{2520}\left(6\Phi_y^{i^2} + 12\Phi_y^i + 5\right) l^{i^4} + \frac{1}{840}\left(7\Phi_y^{i^2} + 14\Phi_y^i + 6\right)\mu_2 l^{i^3} \\
&- \frac{1}{840}\left(7\Phi_y^{i^2} + 14\Phi_y^i + 6\right)\mu_1 l^{i^2} \\
m^{t,w}_{9,9} &= \frac{1}{630}\left(126\Phi_y^{i^2} + 270\Phi_y^i + 145\right) l^{i^2} - \frac{1}{210}\left(105\Phi_y^{i^2} + 224\Phi_y^i + 120\right)\mu_2 l^i \\
&+ \frac{1}{210}\left(70\Phi_y^{i^2} + 147\Phi_z^i + 78\right)\mu_1 \\
m^{t,w}_{11,9} &= \frac{1}{2520}\left(42\Phi_y^{i^2} + 105\Phi_y^i + 65\right) l^{i^3} - \frac{1}{420}\left(21\Phi_y^{i^2} + 50\Phi_y^i + 30\right)\mu_2 l^{i^2} \\
&+ \frac{1}{840}\left(35\Phi_y^{i^2} + 77\Phi_y^i + 44\right)\mu_1 l^i \\
m^{t,w}_{11,11} &= \frac{1}{2520}\left(6\Phi_y^{i^2} + 15\Phi_y^i + 10\right) l^{i^4} - \frac{1}{840}\left(7\Phi_y^{i^2} + 16\Phi_y^i + 10\right)\mu_2 l^{i^3} \\
&+ \frac{1}{840}\left(7\Phi_y^{i^2} + 14\Phi_y^i + 8\right)\mu_1 l^{i^2}
\end{aligned}$$

Table C.14: Elemental rotary inertia mass matrix in the (xy)-plane

$$\left[\overline{m}^{i}_{r,v}\right] = \frac{\rho^{i} A_{\circ} l^{i^3} \overline{\Phi}_{z}^{i^2}}{L_{oy} L_{oz}} \left[m^{r,v}_{p,q}\right], \qquad p,q = 1,2,...,12$$

where the lower triangular part of the rotary inertia mass matrix $[m^{r,v}_{p,q}]$ in (xy)-plane is given by

$$\begin{aligned} m^{r,v}_{2,2} = \; -m^{r,v}_{8,2} = \; m^{r,v}_{8,8} \; &= \; \Xi_{yy} \left(\frac{1}{7} l^{i^2} - \frac{3}{14} \alpha_{z_3} l^{i} + \frac{12}{35} \alpha_{z_2} - \frac{3}{5} \alpha_{z_1} l^{i^{-1}} + \frac{6}{5} \alpha_{z_0} l^{i^{-2}} \right) \sin^2 \psi \\ &+ \; \Xi_{zz} \left(\frac{1}{7} l^{i^2} - \frac{3}{14} \alpha_{y_3} l^{i} + \frac{12}{35} \alpha_{y_2} - \frac{3}{5} \alpha_{y_1} l^{i^{-1}} + \frac{6}{5} \alpha_{y_0} l^{i^{-2}} \right) \cos^2 \psi \end{aligned}$$

$$\begin{aligned} m^{r,v}_{6,2} = \; -m^{r,v}_{8,6} \; &= \; \Xi_{yy} \left\{ \begin{array}{l} -\frac{1}{28} \left(\Phi^{i}_{z} - 1 \right) l^{i^3} + \frac{1}{140} \left(8\Phi^{i}_{z} - 7 \right) \alpha_{z_3} l^{i^2} \\ -\frac{1}{70} \left(7\Phi^{i}_{z} - 5 \right) \alpha_{z_2} l^{i} + \frac{1}{10} \left(2\Phi^{i}_{z} - 1 \right) \alpha_{z_1} \\ -\frac{1}{10} \left(5\Phi^{i}_{z} - 1 \right) \alpha_{z_0} l^{i^{-1}} \end{array} \right\} \sin^2 \psi \\ &+ \; \Xi_{zz} \left\{ \begin{array}{l} -\frac{1}{28} \left(\Phi^{i}_{z} - 1 \right) l^{i^3} + \frac{1}{140} \left(8\Phi^{i}_{z} - 7 \right) \alpha_{y_3} l^{i^2} \\ -\frac{1}{70} \left(7\Phi^{i}_{z} - 5 \right) \alpha_{y_2} l^{i} + \frac{1}{10} \left(2\Phi^{i}_{z} - 1 \right) \alpha_{y_1} \\ -\frac{1}{10} \left(5\Phi^{i}_{z} - 1 \right) \alpha_{y_0} l^{i^{-1}} \end{array} \right\} \cos^2 \psi \end{aligned}$$

$$\begin{aligned} m^{r,v}_{12,2} = \; -m^{r,v}_{12,8} \; &= \; \Xi_{yy} \left\{ \begin{array}{l} -\frac{1}{28} \left(3\Phi^{i}_{z} + 1 \right) l^{i^3} + \frac{1}{28} \left(4\Phi^{i}_{z} + 1 \right) \alpha_{z_3} l^{i^2} \\ -\frac{1}{35} \left(7\Phi^{i}_{z} + 1 \right) \alpha_{z_2} l^{i} + \frac{3}{10} \alpha_{z_1} \Phi^{i}_{z} - \frac{1}{10} \left(5\Phi^{i}_{z} - 1 \right) \alpha_{z_0} l^{i^{-1}} \end{array} \right\} \sin^2 \psi \\ &+ \; \Xi_{zz} \left\{ \begin{array}{l} -\frac{1}{28} \left(3\Phi^{i}_{z} + 1 \right) l^{i3} + \frac{1}{28} \left(4\Phi^{i}_{z} + 1 \right) \alpha_{y_3} l^{i2} \\ -\frac{1}{35} \left(7\Phi^{i}_{z} + 1 \right) \alpha_{y_2} l^{i} + \frac{3}{10} \alpha_{y_1} \Phi^{i}_{z} - \frac{1}{10} \left(5\Phi^{i}_{z} - 1 \right) \alpha_{y_0} l^{i^{-1}} \end{array} \right\} \cos^2 \psi \end{aligned}$$

$$\begin{aligned} m^{r,v}_{6,6} \; &= \; \Xi_{yy} \left\{ \begin{array}{l} \frac{1}{420} \left(4\Phi^{i^2}_{z} - 7\Phi^{i}_{z} + 4 \right) l^{i^4} - \frac{1}{840} \left(14\Phi^{i^2}_{z} - 20\Phi^{i}_{z} + 11 \right) \alpha_{z_3} l^{i3} \\ +\frac{1}{210} \left(7\Phi^{i^2}_{z} - 7\Phi^{i}_{z} + 4 \right) \alpha_{z_2} l^{i2} - \frac{1}{60} \left(5\Phi^{i^2}_{z} - 2\Phi^{i}_{z} + 2 \right) \alpha_{z_1} l^{i} \\ +\frac{1}{30} \left(10\Phi^{i^2}_{z} + 5\Phi^{i}_{z} + 4 \right) \alpha_{z_0} \end{array} \right\} \sin^2 \psi \\ &+ \; \Xi_{zz} \left\{ \begin{array}{l} \frac{1}{420} \left(4\Phi^{i^2}_{z} - 7\Phi^{i}_{z} + 4 \right) l^{i4} - \frac{1}{840} \left(14\Phi^{i^2}_{z} - 20\Phi^{i}_{z} + 11 \right) \alpha_{y_3} l^{i3} \\ +\frac{1}{210} \left(7\Phi^{i^2}_{z} - 7\Phi^{i}_{z} + 4 \right) \alpha_{y_2} l^{i^2} - \frac{1}{60} \left(5\Phi^{i^2}_{z} - 2\Phi^{i}_{z} + 2 \right) \alpha_{y_1} l^{i} \\ +\frac{1}{30} \left(10\Phi^{i^2}_{z} + 5\Phi^{i}_{z} + 4 \right) \alpha_{y_0} \end{array} \right\} \cos^2 \psi \end{aligned}$$

$$
\begin{aligned}
m^{r,v}_{12,6} &= \Xi_{yy}\left\{\begin{array}{l}
\frac{1}{84}\left(2\Phi_z^{i^2}-2\Phi_z^i-1\right)l^{i^4}-\frac{1}{840}\left(28\Phi_z^{i^2}-28\Phi_z^i-11\right)\alpha_{z_3}l^{i^3}\\
+\frac{1}{140}\left(7\Phi_z^{i^2}-7\Phi_z^i-2\right)\alpha_{z_2}l^{i^2}-\frac{1}{60}\left(5\Phi_z^{i^2}-5\Phi_z^i-1\right)\alpha_{z_1}l^i\\
+\frac{1}{30}\left(5\Phi_z^{i^2}-5\Phi_z^i-1\right)\alpha_{z_0}
\end{array}\right\}\sin^2\psi\\
&+ \Xi_{zz}\left\{\begin{array}{l}
\frac{1}{84}\left(2\Phi_z^{i^2}-2\Phi_z^i-1\right)l^{i^4}-\frac{1}{840}\left(28\Phi_z^{i^2}-28\Phi_z^i-11\right)\alpha_{y_3}l^{i^3}\\
+\frac{1}{140}\left(7\Phi_z^{i^2}-7\Phi_z^i-2\right)\alpha_{y_2}l^{i^2}-\frac{1}{60}\left(5\Phi_z^{i^2}-5\Phi_z^i-1\right)\alpha_{y_1}l^i\\
+\frac{1}{30}\left(5\Phi_z^{i^2}-5\Phi_z^i-1\right)\alpha_{y_0}
\end{array}\right\}\cos^2\psi
\end{aligned}
$$

$$
\begin{aligned}
m^{r,v}_{12,12} &= \Xi_{yy}\left\{\begin{array}{l}
\frac{1}{28}\left(4\Phi_z^{i^2}+5\Phi_z^i+2\right)l^{i^4}-\frac{1}{168}\left(28\Phi_z^{i^2}+32\Phi_z^i+13\right)\alpha_{z_3}l^{i^3}\\
+\frac{1}{35}\left(7\Phi_z^{i^2}+7\Phi_z^i+3\right)\alpha_{z_2}l^{i^2}-\frac{1}{20}\left(5\Phi_z^{i^2}+4\Phi_z^i+2\right)\alpha_{z_1}l^i\\
+\frac{1}{30}\left(10\Phi_z^{i^2}+5\Phi_z^i+4\right)\alpha_{z_0}
\end{array}\right\}\sin^2\psi\\
&+ \Xi_{zz}\left\{\begin{array}{l}
\frac{1}{28}\left(4\Phi_z^{i^2}+5\Phi_z^i+2\right)l^{i^4}-\frac{1}{168}\left(28\Phi_z^{i^2}+32\Phi_z^i+13\right)\alpha_{y_3}l^{i^3}\\
+\frac{1}{35}\left(7\Phi_z^{i^2}+7\Phi_z^i+3\right)\alpha_{y_2}l^{i^2}-\frac{1}{20}\left(5\Phi_z^{i^2}+4\Phi_z^i+2\right)\alpha_{y_1}l^i\\
+\frac{1}{30}\left(10\Phi_z^{i^2}+5\Phi_z^i+4\right)\alpha_{y_0}
\end{array}\right\}\cos^2\psi
\end{aligned}
$$

where

$$
\Xi_{yy}=\frac{1}{L_{oz}^2}\left(\frac{r_{g_y}}{l^i}\right)^2 \qquad \text{and} \qquad \Xi_{zz}=\frac{1}{L_{oy}^2}\left(\frac{r_{g_z}}{l^i}\right)^2
$$

and r_{g_y} and r_{g_z} are radii of gyration about y and z-axes, respectively.

Table C.15: Elemental rotary inertia mass matrix in the (xz)-plane

$$
\left[\overline{m}^i_{r,w}\right]=\frac{\rho A_o l^{i^3}\overline{\Phi}_y^{i^2}}{L_{oy}L_{oz}}\left[m^{r,w}_{p,q}\right], \quad p,q=1,2,...,12
$$

where the lower triangular part of the rotary inertia mass matrix $[m^{r,w}_{p,q}]$ in (xy)-plane is given by

$$
\begin{aligned}
m^{r,w}_{3,3} = -m^{r,w}_{9,3} = m^{r,w}_{9,9} &= \Xi_{yy}\left(\frac{1}{7}l^{i^2}-\frac{3}{14}\alpha_{z_3}l^i+\frac{12}{35}\alpha_{z_2}-\frac{3}{5}\alpha_{z_1}l^{i^{-1}}+\frac{6}{5}\alpha_{z_0}l^{i^{-2}}\right)\cos^2\psi\\
&+ \Xi_{zz}\left(\frac{1}{7}l^{i^2}-\frac{3}{14}\alpha_{y_3}l^i+\frac{12}{35}\alpha_{y_2}-\frac{3}{5}\alpha_{y_1}l^{i^{-1}}+\frac{6}{5}\alpha_{y_0}l^{i^{-2}}\right)\sin^2\psi
\end{aligned}
$$

$$
\begin{aligned}
m^{r,w}_{5,3} = \; -m^{r,w}_{9,5} \;=\; & \Xi_{yy}\left(\begin{array}{l}
\frac{1}{28}\left(\Phi^i_y-1\right)l^{i^3}-\frac{1}{140}\left(8\Phi^i_y-7\right)\alpha_{z_3}l^{i^2}\\
+\frac{1}{70}\left(7\Phi^i_y-5\right)\alpha_{z_2}l^i-\frac{1}{10}\left(2\Phi^i_y-1\right)\alpha_{z_1}\\
+\frac{1}{10}\left(5\Phi^i_y-1\right)\alpha_{z_0}l^{i^{-1}}
\end{array}\right)\cos^2\psi\\
+\; & \Xi_{zz}\left(\begin{array}{l}
\frac{1}{28}\left(\Phi^i_y-1\right)l^{i^3}-\frac{1}{140}\left(8\Phi^i_y-7\right)\alpha_{y_3}l^{i^2}\\
+\frac{1}{70}\left(7\Phi^i_y-5\right)\alpha_{y_2}l^i-\frac{1}{10}\left(2\Phi^i_y-1\right)\alpha_{y_1}\\
+\frac{1}{10}\left(5\Phi^i_y-1\right)\alpha_{y_0}l^{i^{-1}}
\end{array}\right)\sin^2\psi
\end{aligned}
$$

$$
\begin{aligned}
m^{r,w}_{11,3} = \; -m^{r,w}_{11,9} \;=\; & \Xi_{yy}\left(\begin{array}{l}
\frac{1}{28}\left(3\Phi^i_y+1\right)l^{i^3}-\frac{1}{28}\left(4\Phi^i_y+1\right)\alpha_{z_3}l^{i^2}\\
+\frac{1}{35}\left(7\Phi^i_y+1\right)\alpha_{z_2}l^i-\frac{3}{10}\alpha_{z_1}\Phi^i_y+\frac{1}{10}\left(5\Phi^i_y-1\right)\alpha_{z_0}l^{i^{-1}}
\end{array}\right)\cos^2\psi\\
+\; & \Xi_{zz}\left(\begin{array}{l}
\frac{1}{28}\left(3\Phi^i_y+1\right)l^{i3}-\frac{1}{28}\left(4\Phi^i_y+1\right)\alpha_{y_3}l^{i2}\\
+\frac{1}{35}\left(7\Phi^i_y+1\right)\alpha_{y_2}l^i-\frac{3}{10}\alpha_{y_1}\Phi^i_y+\frac{1}{10}\left(5\Phi^i_y-1\right)\alpha_{y_0}l^{i^{-1}}
\end{array}\right)\sin^2\psi
\end{aligned}
$$

$$
\begin{aligned}
m^{r,w}_{5,5} \;=\; & \Xi_{yy}\left(\begin{array}{l}
\frac{1}{420}\left(4\Phi^{i^2}_y-7\Phi^i_y+4\right)l^{i^4}-\frac{1}{840}\left(14\Phi^{i^2}_y-20\Phi^i_y+11\right)\alpha_{z_3}l^{i3}\\
+\frac{1}{210}\left(7\Phi^{i^2}_y-7\Phi^i_y+4\right)\alpha_{z_2}l^{i2}-\frac{1}{60}\left(5\Phi^{i^2}_y-2\Phi^i_y+2\right)\alpha_{z_1}l^i\\
+\frac{1}{30}\left(10\Phi^{i^2}_y+5\Phi^i_y+4\right)\alpha_{z_0}
\end{array}\right)\cos^2\psi\\
+\; & \Xi_{zz}\left(\begin{array}{l}
\frac{1}{420}\left(4\Phi^{i^2}_y-7\Phi^i_y+4\right)l^{i4}-\frac{1}{840}\left(14\Phi^{i^2}_y-20\Phi^i_y+11\right)\alpha_{y_3}l^{i^3}\\
+\frac{1}{210}\left(7\Phi^{i^2}_y-7\Phi^i_y+4\right)\alpha_{y_2}l^{i^2}-\frac{1}{60}\left(5\Phi^{i^2}_y-2\Phi^i_y+2\right)\alpha_{y_1}l^i\\
+\frac{1}{30}\left(10\Phi^{i^2}_y+5\Phi^i_y+4\right)\alpha_{y_0}
\end{array}\right)\sin^2\psi
\end{aligned}
$$

$$
\begin{aligned}
m^{r,w}_{11,5} \;=\; & \Xi_{yy}\left(\begin{array}{l}
\frac{1}{84}\left(2\Phi^{i^2}_y-2\Phi^i_y-1\right)l^{i^4}-\frac{1}{840}\left(28\Phi^{i^2}_y-28\Phi^i_y-11\right)\alpha_{z_3}l^{i^3}\\
+\frac{1}{140}\left(7\Phi^{i^2}_y-7\Phi^i_y-2\right)\alpha_{z_2}l^{i^2}-\frac{1}{60}\left(5\Phi^{i^2}_y-5\Phi^i_y-1\right)\alpha_{z_1}l^i\\
+\frac{1}{30}\left(5\Phi^{i^2}_y-5\Phi^i_y-1\right)\alpha_{z_0}
\end{array}\right)\cos^2\psi\\
+\; & \Xi_{zz}\left(\begin{array}{l}
\frac{1}{84}\left(2\Phi^{i^2}_y-2\Phi^i_y-1\right)l^{i^4}-\frac{1}{840}\left(28\Phi^{i^2}_y-28\Phi^i_y-11\right)\alpha_{y_3}l^{i^3}\\
+\frac{1}{140}\left(7\Phi^{i^2}_y-7\Phi^i_y-2\right)\alpha_{y_2}l^{i^2}-\frac{1}{60}\left(5\Phi^{i^2}_y-5\Phi^i_y-1\right)\alpha_{y_1}l^i\\
+\frac{1}{30}\left(5\Phi^{i^2}_y-5\Phi^i_y-1\right)\alpha_{y_0}
\end{array}\right)\sin^2\psi
\end{aligned}
$$

$$
\begin{aligned}
m^{r,w}_{11,11} \;=\; & \Xi_{yy}\left(\begin{array}{l}
\frac{1}{28}\left(4\Phi^{i^2}_y+5\Phi^i_y+2\right)l^{i^4}-\frac{1}{168}\left(28\Phi^{i^2}_y+32\Phi^i_y+13\right)\alpha_{z_3}l^{i^3}\\
+\frac{1}{35}\left(7\Phi^{i^2}_y+7\Phi^i_y+3\right)\alpha_{z_2}l^{i^2}-\frac{1}{20}\left(5\Phi^{i^2}_y+4\Phi^i_y+2\right)\alpha_{z_1}l^i\\
+\frac{1}{30}\left(10\Phi^{i^2}_y+5\Phi^i_y+4\right)\alpha_{z_0}
\end{array}\right)\cos^2\psi\\
+\; & \Xi_{zz}\left(\begin{array}{l}
\frac{1}{28}\left(4\Phi^{i^2}_y+5\Phi^i_y+2\right)l^{i^4}-\frac{1}{168}\left(28\Phi^{i^2}_y+32\Phi^i_y+13\right)\alpha_{y_3}l^{i^3}\\
+\frac{1}{35}\left(7\Phi^{i^2}_y+7\Phi^i_y+3\right)\alpha_{y_2}l^{i^2}-\frac{1}{20}\left(5\Phi^{i^2}_y+4\Phi^i_y+2\right)\alpha_{y_1}l^i\\
+\frac{1}{30}\left(10\Phi^{i^2}_y+5\Phi^i_y+4\right)\alpha_{y_0}
\end{array}\right)\sin^2\psi
\end{aligned}
$$

Table C.16: Elemental rotary inertia mass matrix due to coupling in bending

$$\left[\overline{m}^{i}_{r,vw}\right] = \frac{\rho A_o l^{i^3} \overline{\Phi}^{i}_{y} \overline{\Phi}^{i}_{z} \sin 2\psi}{2 L_{oy} L_{oz}} \left[m^{r,vw}_{p,q}\right], \qquad p,q = 1,2,...,12$$

where the lower triangular part of the rotary inertia mass matrix $[m^{r,vw}_{p,q}]$ in (xz)-plane is given by

$$\begin{aligned}
m^{r,vw}_{3,2} &= -m^{r,vw}_{9,2} = -m^{r,vw}_{8,3} = m^{r,vw}_{9,8} = \Xi_{yy} \left\{ \begin{array}{l} \frac{1}{7} l^{i^2} - \frac{3}{14} \alpha_{z_3} l^i + \frac{12}{35} \alpha_{z_2} \\ -\frac{3}{5} \alpha_{z_1} l^{i-1} + \frac{6}{5} \alpha_{z_0} l^{i-2} \end{array} \right\} \\
&\quad - \Xi_{zz} \left\{ \begin{array}{l} \frac{1}{7} l^{i^2} - \frac{3}{14} \alpha_{y_3} l^i + \frac{12}{35} \alpha_{y_2} \\ -\frac{3}{5} \alpha_{y_1} l^{i-1} + \frac{6}{5} \alpha_{y_0} l^{i-2} \end{array} \right\} \\
m^{r,vw}_{5,2} &= -m^{r,vw}_{8,5} = \Xi_{yy} \left\{ \begin{array}{l} \frac{1}{28} \left(\Phi^i_y - 1\right) l^{i^3} - \frac{1}{140} \left(8\Phi^i_y - 7\right) \alpha_{z_3} l^{i^2} + \frac{1}{70} \left(7\Phi^i_y - 5\right) \alpha_{z_2} l^i \\ -\frac{1}{10} \left(2\Phi^i_y - 1\right) \alpha_{z_1} + \frac{1}{10} \left(5\Phi^i_y - 1\right) \alpha_{z_0} l^{i-1} \end{array} \right\} \\
&\quad - \Xi_{zz} \left\{ \begin{array}{l} \frac{1}{28} \left(\Phi^i_y - 1\right) l^{i^3} - \frac{1}{140} \left(8\Phi^i_y - 7\right) \alpha_{y_3} l^{i^2} + \frac{1}{70} \left(7\Phi^i_y - 5\right) \alpha_{y_2} l^i \\ -\frac{1}{10} \left(2\Phi^i_y - 1\right) \alpha_{y_1} + \frac{1}{10} \left(5\Phi^i_y - 1\right) \alpha_{y_0} l^{i-1} \end{array} \right\} \\
m^{r,vw}_{11,2} &= -m^{r,vw}_{11,8} = \Xi_{yy} \left\{ \begin{array}{l} \frac{1}{28} \left(3\Phi^i_y + 1\right) l^{i^3} - \frac{1}{28} \left(4\Phi^i_y + 1\right) \alpha_{z_3} l^{i^2} + \frac{1}{35} \left(7\Phi^i_y + 1\right) \alpha_{z_2} l^i \\ -\frac{3}{10} \alpha_{z_1} \Phi^i_y + \frac{1}{10} \left(5\Phi^i_y - 1\right) \alpha_{z_0} l^{i-1} \end{array} \right\} \\
&\quad - \Xi_{zz} \left\{ \begin{array}{l} \frac{1}{28} \left(3\Phi^i_y + 1\right) l^{i^3} - \frac{1}{28} \left(4\Phi^i_y + 1\right) \alpha_{y_3} l^{i^2} + \frac{1}{35} \left(7\Phi^i_y + 1\right) \alpha_{y_2} l^i \\ -\frac{3}{10} \alpha_{y_1} \Phi^i_y + \frac{1}{10} \left(5\Phi^i_y - 1\right) \alpha_{y_0} l^{i-1} \end{array} \right\} \\
m^{r,vw}_{6,3} &= -m^{r,vw}_{9,6} = \Xi_{yy} \left\{ \begin{array}{l} -\frac{1}{28} \left(\Phi^i_z - 1\right) l^{i^3} + \frac{1}{140} \left(8\Phi^i_z - 7\right) \alpha_{z_3} l^{i^2} - \frac{1}{70} \left(7\Phi^i_z - 5\right) \alpha_{z_2} l^i \\ +\frac{1}{10} \left(2\Phi^i_z - 1\right) \alpha_{z_1} - \frac{1}{10} \left(5\Phi^i_z - 1\right) \alpha_{z_0} l^{i-1} \end{array} \right\} \\
&\quad - \Xi_{zz} \left\{ \begin{array}{l} -\frac{1}{28} \left(\Phi^i_z - 1\right) l^{i^3} + \frac{1}{140} \left(8\Phi^i_z - 7\right) \alpha_{y_3} l^{i^2} - \frac{1}{70} \left(7\Phi^i_z - 5\right) \alpha_{y_2} l^i \\ +\frac{1}{10} \left(2\Phi^i_z - 1\right) \alpha_{y_1} - \frac{1}{10} \left(5\Phi^i_z - 1\right) \alpha_{y_0} l^{i-1} \end{array} \right\} \\
m^{r,vw}_{12,3} &= -m^{r,vw}_{12,9} = \Xi_{yy} \left\{ \begin{array}{l} -\frac{1}{28} \left(3\Phi^i_z + 1\right) l^{i^3} + \frac{1}{28} \left(4\Phi^i_z + 1\right) \alpha_{z_3} l^{i^2} - \frac{1}{35} \left(7\Phi^i_z + 1\right) \alpha_{z_2} l^i \\ +\frac{3}{10} \alpha_{z_1} \Phi^i_z - \frac{1}{10} \left(5\Phi^i_z - 1\right) \alpha_{z_0} l^{i-1} \end{array} \right\} \\
&\quad - \Xi_{zz} \left\{ \begin{array}{l} -\frac{1}{28} \left(3\Phi^i_z + 1\right) l^{i^3} + \frac{1}{28} \left(4\Phi^i_z + 1\right) \alpha_{y_3} l^{i^2} - \frac{1}{35} \left(7\Phi^i_z + 1\right) \alpha_{y_2} l^i \\ +\frac{3}{10} \alpha_{y_1} \Phi^i_z - \frac{1}{10} \left(5\Phi^i_z - 1\right) \alpha_{y_0} l^{i-1} \end{array} \right\}
\end{aligned}$$

$$
\begin{aligned}
m_{6,5}^{r,vw} &= \Xi_{yy}\left(\begin{array}{l}
-\frac{1}{840}\left(8\Phi_y^i\Phi_z^i-7\Phi_y^i-7\Phi_z^i+8\right)l^{i^4}+\frac{1}{840}\left(14\Phi_y^i\Phi_z^i-10\Phi_y^i-10\Phi_z^i+11\right)\alpha_{z_3}l^{i^3}\\
-\frac{1}{420}\left(14\Phi_y^i\Phi_z^i-7\Phi_y^i-7\Phi_z^i+8\right)\alpha_{z_2}l^{i^2}+\frac{1}{60}\left(5\Phi_y^i\Phi_z^i-\Phi_y^i-\Phi_z^i+2\right)\alpha_{z_1}l^i\\
-\frac{1}{60}\left(20\Phi_y^i\Phi_z^i+5\Phi_y^i+5\Phi_z^i+8\right)\alpha_{z_0}
\end{array}\right)\\
&- \Xi_{yy}\left(\begin{array}{l}
-\frac{1}{840}\left(8\Phi_y^i\Phi_z^i-7\Phi_y^i-7\Phi_z^i+8\right)l^{i^4}+\frac{1}{840}\left(14\Phi_y^i\Phi_z^i-10\Phi_y^i-10\Phi_z^i+11\right)\alpha_{y_3}l^{i^3}\\
-\frac{1}{420}\left(14\Phi_y^i\Phi_z^i-7\Phi_y^i-7\Phi_z^i+8\right)\alpha_{y_2}l^{i^2}+\frac{1}{60}\left(5\Phi_y^i\Phi_z^i-\Phi_y^i-\Phi_z^i+2\right)\alpha_{y_1}l^i\\
-\frac{1}{60}\left(20\Phi_y^i\Phi_z^i+5\Phi_y^i+5\Phi_z^i+8\right)\alpha_{y_0}
\end{array}\right)
\end{aligned}
$$

$$
\begin{aligned}
m_{12,5}^{r,vw} &= \Xi_{yy}\left(\begin{array}{l}
-\frac{1}{168}\left(4\Phi_y^i\Phi_z^i+\Phi_y^i-5\Phi_z^i-2\right)l^{i^4}+\frac{1}{840}\left(28\Phi_y^i\Phi_z^i+4\Phi_y^i-32\Phi_z^i-11\right)\alpha_{z_3}l^{i^3}\\
-\frac{1}{140}\left(7\Phi_y^i\Phi_z^i-7\Phi_z^i-2\right)\alpha_{z_2}l^{i^2}+\frac{1}{60}\left(5\Phi_y^i\Phi_z^i-\Phi_y^i-4\Phi_z^i-1\right)\alpha_{z_1}l^i\\
-\frac{1}{60}\left(10\Phi_y^i\Phi_z^i-5\Phi_y^i-5\Phi_z^i-2\right)\alpha_{z_0}
\end{array}\right)\\
&- \Xi_{zz}\left(\begin{array}{l}
-\frac{1}{168}\left(4\Phi_y^i\Phi_z^i+\Phi_y^i-5\Phi_z^i-2\right)l^{i^4}+\frac{1}{840}\left(28\Phi_y^i\Phi_z^i+4\Phi_y^i-32\Phi_z^i-11\right)\alpha_{y_3}l^{i^3}\\
-\frac{1}{140}\left(7\Phi_y^i\Phi_z^i-7\Phi_z^i-2\right)\alpha_{y_2}l^{i^2}+\frac{1}{60}\left(5\Phi_y^i\Phi_z^i-\Phi_y^i-4\Phi_z^i-1\right)\alpha_{y_1}l^i\\
-\frac{1}{60}\left(10\Phi_y^i\Phi_z^i-5\Phi_y^i-5\Phi_z^i-2\right)\alpha_{y_0}
\end{array}\right)
\end{aligned}
$$

$$
\begin{aligned}
m_{11,6}^{r,vw} &= \Xi_{yy}\left(\begin{array}{l}
-\frac{1}{168}\left(4\Phi_y^i\Phi_z^i-5\Phi_y^i+\Phi_z^i-2\right)l^{i^4}+\frac{1}{840}\left(28\Phi_y^i\Phi_z^i-32\Phi_y^i+4\Phi_z^i-11\right)\alpha_{z_3}l^{i^3}\\
-\frac{1}{140}\left(7\Phi_y^i\Phi_z^i-7\Phi_y^i-2\right)\alpha_{z_2}l^{i^2}+\frac{1}{60}\left(5\Phi_y^i\Phi_z^i-4\Phi_y^i-\Phi_z^i-1\right)\alpha_{z_1}l^i\\
-\frac{1}{60}\left(10\Phi_y^i\Phi_z^i-5\Phi_y^i-5\Phi_z^i-2\right)\alpha_{z_0}
\end{array}\right)\\
&- \Xi_{zz}\left(\begin{array}{l}
-\frac{1}{168}\left(4\Phi_y^i\Phi_z^i-5\Phi_y^i+\Phi_z^i-2\right)l^{i^4}+\frac{1}{840}\left(28\Phi_y^i\Phi_z^i-32\Phi_y^i+4\Phi_z^i-11\right)\alpha_{y_3}l^{i^3}\\
-\frac{1}{140}\left(7\Phi_y^i\Phi_z^i-7\Phi_y^i-2\right)\alpha_{y_2}l^{i^2}+\frac{1}{60}\left(5\Phi_y^i\Phi_z^i-4\Phi_y^i-\Phi_z^i-1\right)\alpha_{y_1}l^i\\
-\frac{1}{60}\left(10\Phi_y^i\Phi_z^i-5\Phi_y^i-5\Phi_z^i-2\right)\alpha_{y_0}
\end{array}\right)
\end{aligned}
$$

$$
\begin{aligned}
m_{12,11}^{r,vw} &= \Xi_{yy}\left(\begin{array}{l}
-\frac{1}{56}\left(8\Phi_y^i\Phi_z^i+5\Phi_y^i+5\Phi_z^i+4\right)l^{i^4}+\frac{1}{168}\left(28\Phi_y^i\Phi_z^i+16\Phi_y^i+16\Phi_z^i+13\right)\alpha_{z_3}l^{i^3}\\
-\frac{1}{70}\left(14\Phi_y^i\Phi_z^i+7\Phi_y^i+7\Phi_z^i+6\right)\alpha_{z_2}l^{i^2}+\frac{1}{20}\left(5\Phi_y^i\Phi_z^i+2\Phi_y^i+2\Phi_z^i+2\right)\alpha_{z_1}l^i\\
-\frac{1}{60}\left(20\Phi_y^i\Phi_z^i+5\Phi_y^i+5\Phi_z^i+8\right)\alpha_{z_0}
\end{array}\right)\\
&- \Xi_{zz}\left(\begin{array}{l}
-\frac{1}{56}\left(8\Phi_y^i\Phi_z^i+5\Phi_y^i+5\Phi_z^i+4\right)l^{i^4}+\frac{1}{168}\left(28\Phi_y^i\Phi_z^i+16\Phi_y^i+16\Phi_z^i+13\right)\alpha_{y_3}l^{i^3}\\
-\frac{1}{70}\left(14\Phi_y^i\Phi_z^i+7\Phi_y^i+7\Phi_z^i+6\right)\alpha_{y_2}l^{i^2}+\frac{1}{20}\left(5\Phi_y^i\Phi_z^i+2\Phi_y^i+2\Phi_z^i+2\right)\alpha_{y_1}l^i\\
-\frac{1}{60}\left(20\Phi_y^i\Phi_z^i+5\Phi_y^i+5\Phi_z^i+8\right)\alpha_{y_0}
\end{array}\right)
\end{aligned}
$$

Table C.17: Elemental Coriolis matrix

$$\boxed{\left[\widetilde{C_1^i}\right] = \frac{2\Omega\rho A_o l^i \overline{\Phi}_z^i}{L_{oy}L_{oz}}\left[c_{p,q}^1\right], \qquad p,q = 1,2,...,12}$$

where the lower triangular part of the matrix $\left[c_{p,q}^1\right]$ is given by

$$\begin{aligned}
c_{2,1}^1 &= -\frac{1}{420}\left(14\Phi_z^i + 13\right) l^{i^2} + \frac{1}{6}\left(\Phi_z^i + 1\right)\mu_2 l^i - \frac{1}{60}\left(20\Phi_z^i + 21\right)\mu_1 \\
c_{6,1}^1 &= -\frac{1}{840}\left(7\Phi_z^i + 6\right) l^{i^3} + \frac{1}{30}\left(\Phi_z^i + 1\right)\mu_2 l^{i^2} - \frac{1}{120}\left(5\Phi_z^i + 6\right)\mu_1 l^i \\
c_{8,1}^1 &= -\frac{1}{420}\left(21\Phi_z^i + 22\right) l^{i^2} + \frac{1}{6}\left(\Phi_z^i + 1\right)\mu_2 l^i - \frac{1}{60}\left(10\Phi_z^i + 9\right)\mu_1 \\
c_{12,1}^1 &= \frac{1}{840}\left(7\Phi_z^i + 8\right) l^{i^3} - \frac{1}{30}\left(\Phi_z^i + 1\right)\mu_2 l^{i^2} + \frac{1}{120}\left(5\Phi_z^i + 4\right)\mu_1 l^i \\
c_{7,2}^1 &= \frac{1}{140}\left(7\Phi_z^i + 5\right) l^{i^2} - \frac{1}{30}\left(5\Phi_z^i + 4\right)\mu_2 l^i + \frac{1}{60}\left(10\Phi_z^i + 9\right)\mu_1 \\
c_{7,6}^1 &= \frac{1}{420}\left(7\Phi_z^i + 4\right) l^{i^3} - \frac{1}{60}\left(3\Phi_z^i + 2\right)\mu_2 l^{i^2} + \frac{1}{120}\left(5\Phi_z^i + 4\right)\mu_1 l^i \\
c_{8,7}^1 &= -\frac{1}{70}\left(14\Phi_z^i + 15\right) l^{i^2} + \frac{1}{30}\left(15\Phi_z^i + 16\right)\mu_2 l^i - \frac{1}{60}\left(20\Phi_z^i + 21\right)\mu_1 \\
c_{12,7}^1 &= \frac{1}{420}\left(7\Phi_z^i + 10\right) l^{i^3} - \frac{1}{60}\left(3\Phi_z^i + 4\right)\mu_2 l^{i^2} + \frac{1}{120}\left(5\Phi_z^i + 6\right)\mu_1 l^i
\end{aligned}$$

$$\boxed{\left[\widetilde{C_2^i}\right] = 2\Omega\rho\overline{\Phi}_z^i \sin\psi\cos\psi\left[c_{p,q}^2\right], \qquad p,q = 1,2,...,12}$$

where the lower triangular part of the matrix $\left[c_{p,q}^2\right]$ is given by

$$\begin{aligned}
c_{4,2}^2 = c_{8,4}^2 &= \Gamma_{yy}\left(\frac{1}{28}l^{i^4} - \frac{2}{35}\alpha_{z_3}l^{i^3} + \frac{1}{10}\alpha_{z_2}l^{i^2} - \frac{1}{5}\alpha_{z_1}l^i + \frac{1}{2}\alpha_{z_0}\right) \\
&- \Gamma_{zz}\left(\frac{1}{28}l^{i^4} - \frac{2}{35}\alpha_{y_3}l^{i^3} + \frac{1}{10}\alpha_{y_2}l^{i^2} - \frac{1}{5}\alpha_{y_1}l^i + \frac{1}{2}\alpha_{y_0}\right) \\
c_{10,2}^2 &= \Gamma_{yy}\left(\frac{3}{28}l^{i^4} - \frac{1}{7}\alpha_{z_3}l^{i^3} + \frac{1}{5}\alpha_{z_2}l^{i^2} - \frac{3}{10}\alpha_{z_1}l^i + \frac{1}{2}\alpha_{z_0}\right) \\
&- \Gamma_{zz}\left(\frac{3}{28}l^{i^4} - \frac{1}{7}\alpha_{y_3}l^{i^3} + \tfrac{1}{5}\alpha_{y_2}l^{i^2} - \frac{3}{10}\alpha_{y_1}l^i + \frac{1}{2}\alpha_{y_0}\right) \\
c_{6,4}^2 &= \Gamma_{yy}\left(\begin{array}{l}\frac{1}{840}\left(8\Phi_z^i - 7\right) l^{i^5} - \frac{1}{420}\left(7\Phi_z^i - 5\right)\alpha_{z_3}l^{i^4} + \frac{1}{60}\left(2\Phi_z^i - 1\right)\alpha_{z_2}l^{i^3} \\ -\frac{1}{60}\left(5\Phi_z^i - 1\right)\alpha_{z_1}l^{i^2} + \frac{1}{12}\left(4\Phi_z^i + 1\right)\alpha_{z_0}l^i\end{array}\right) \\
&- \Gamma_{zz}\left(\begin{array}{l}\frac{1}{840}\left(8\Phi_z^i - 7\right) l^{i^5} - \frac{1}{420}\left(7\Phi_z^i - 5\right)\alpha_{y_3}l^{i^4} + \frac{1}{60}\left(2\Phi_z^i - 1\right)\alpha_{y_2}l^{i^3} \\ -\frac{1}{60}\left(5\Phi_z^i - 1\right)\alpha_{y_1}l^{i^2} + \frac{1}{12}\left(4\Phi_z^i + 1\right)\alpha_{yz_0}l^i\end{array}\right)
\end{aligned}$$

$$
\begin{aligned}
c^2_{12,4} &= \Gamma_{yy}\left(\begin{array}{l}\frac{1}{168}\left(4\Phi^i_z+1\right)l^{i^5}-\frac{1}{210}\left(7\Phi^i_z+1\right)\alpha_{z_3}l^{i^4}+\frac{1}{20}\alpha_{z_2}\Phi^i_z l^{i^3}\\ -\frac{1}{60}\left(5\Phi^i_z-1\right)\alpha_{z_1}l^{i^2}+\frac{1}{12}\left(2\Phi^i_z-1\right)\alpha_{z_0}l^i\end{array}\right)\\
&- \Gamma_{zz}\left(\begin{array}{l}\frac{1}{168}\left(4\Phi^i_z+1\right)l^{i^5}-\frac{1}{210}\left(7\Phi^i_z+1\right)\alpha_{y_3}l^{i^4}+\frac{1}{20}\alpha_{y_2}\Phi^i_z l^{i^3}\\ -\frac{1}{60}\left(5\Phi^i_z-1\right)\alpha_{y_1}l^{i^2}+\frac{1}{12}\left(2\Phi^i_z-1\right)\alpha_{y_0}l^i\end{array}\right)
\end{aligned}
$$

$$
\begin{aligned}
c^2_{10,6} &= \Gamma_{yy}\left(\begin{array}{l}-\frac{1}{168}\left(4\Phi^i_z-5\right)l^{i^5}+\frac{1}{210}\left(7\Phi^i_z-8\right)\alpha_{z_3}l^{i^4}-\frac{1}{20}\left(\Phi^i_z-1\right)\alpha_{z_2}l^{i^3}\\ +\frac{1}{60}\left(5\Phi^i_z-4\right)\alpha_{z_1}l^{i^2}-\frac{1}{12}\left(2\Phi^i_z-1\right)\alpha_{z_0}l^i\end{array}\right)\\
&- \Gamma_{zz}\left(\begin{array}{l}-\frac{1}{168}\left(4\Phi^i_z-5\right)l^{i^5}+\frac{1}{210}\left(7\Phi^i_z-8\right)\alpha_{y_3}l^{i^4}-\frac{1}{20}\left(\Phi^i_z-1\right)\alpha_{y_2}l^{i^3}\\ +\frac{1}{60}\left(5\Phi^i_z-4\right)\alpha_{y_1}l^{i^2}-\frac{1}{12}\left(2\Phi^i_z-1\right)\alpha_{y_0}l^i\end{array}\right)
\end{aligned}
$$

$$
\begin{aligned}
c^2_{10,8} &= \Gamma_{yy}\left(-\frac{3}{28}l^{i^4}+\frac{1}{7}\alpha_{z_3}l^{i^3}-\frac{1}{5}\alpha_{z_2}l^{i^2}+\frac{3}{10}\alpha_{z_1}l^i-\frac{1}{2}\alpha_{z_0}\right)\\
&- \Gamma_{zz}\left(-\frac{3}{28}l^{i^4}+\frac{1}{7}\alpha_{y_3}l^{i^3}-\frac{1}{5}\alpha_{y_2}l^{i^2}+\frac{3}{10}\alpha_{y_1}l^i-\frac{1}{2}\alpha_{y_0}\right)
\end{aligned}
$$

$$
\begin{aligned}
c^2_{12,10} &= \Gamma_{yy}\left(\begin{array}{l}\frac{1}{56}\left(8\Phi^i_z+5\right)l^{i^5}-\frac{1}{42}\left(7\Phi^i_z+4\right)\alpha_{z_3}l^{i^4}+\frac{1}{10}\left(2\Phi^i_z+1\right)\alpha_{z_2}l^{i^3}\\ -\frac{1}{20}\left(5\Phi^i_z+2\right)\alpha_{z_1}l^{i^2}+\frac{1}{12}\left(4\Phi^i_z+1\right)\alpha_{z_0}l^i\end{array}\right)\\
&- \Gamma_{zz}\left(\begin{array}{l}\frac{1}{56}\left(8\Phi^i_z+5\right)l^{i^5}-\frac{1}{42}\left(7\Phi^i_z+4\right)\alpha_{y_3}l^{i^4}+\frac{1}{10}\left(2\Phi^i_z+1\right)\alpha_{y_2}l^{i^3}\\ -\frac{1}{20}\left(5\Phi^i_z+2\right)\alpha_{y_1}l^{i^2}+\frac{1}{12}\left(4\Phi^i_z+1\right)\alpha_{y_0}l^i\end{array}\right)
\end{aligned}
$$

$$
\boxed{\left[\widetilde{\overline{C}^i_3}\right]=2\Omega\rho\overline{\Phi}^i_y\left[c^3_{p,q}\right],\qquad p,q=1,2,...,12}
$$

where the lower triangular part of the matrix $\left[c^3_{p,q}\right]$ is given by

$$
\begin{aligned}
c^3_{4,3}=c^3_{9,4} &= \Gamma_{yy}\left(\frac{1}{28}l^{i^4}-\frac{2}{35}\alpha_{z_3}l^{i^3}+\frac{1}{10}\alpha_{z_2}l^{i^2}-\frac{1}{5}\alpha_{z_1}l^i+\frac{1}{2}\alpha_{z_0}\right)\cos^2\psi\\
&+ \Gamma_{yy}\left(\frac{1}{28}l^{i^4}-\frac{2}{35}\alpha_{y_3}l^{i^3}+\frac{1}{10}\alpha_{y_2}l^{i^2}-\frac{1}{5}\alpha_{y_1}l^i+\frac{1}{2}\alpha_{y_0}\right)\sin^2\psi
\end{aligned}
$$

$$
\begin{aligned}
c^3_{10,3}=-c^3_{10,9} &= \Gamma_{yy}\left(\frac{3}{28}l^{i^4}-\frac{1}{7}\alpha_{z_3}l^{i^3}+\frac{1}{5}\alpha_{z_2}l^{i^2}-\frac{3}{10}\alpha_{z_1}l^i+\frac{1}{2}\alpha_{z_0}\right)\cos^2\psi\\
&+ \Gamma_{zz}\left(\frac{3}{28}l^{i^4}-\frac{1}{7}\alpha_{y_3}l^{i^3}+\frac{1}{5}\alpha_{y_2}l^{i^2}-\frac{3}{10}\alpha_{y_1}l^i+\frac{1}{2}\alpha_{y_0}\right)\sin^2\psi
\end{aligned}
$$

$$
\begin{aligned}
c^3_{5,4} &= \Gamma_{yy}\left(\begin{array}{l}-\frac{1}{840}\left(8\Phi^i_y-7\right)l^{i^5}+\frac{1}{420}\left(7\Phi^i_y-5\right)\alpha_{z_3}l^{i^4}-\frac{1}{60}\left(2\Phi^i_y-1\right)\alpha_{z_2}l^{i^3}\\ +\frac{1}{60}\left(5\Phi^i_y-1\right)\alpha_{z_1}l^{i^2}-\frac{1}{12}\left(4\Phi^i_y+1\right)\alpha_{z_0}l^i\end{array}\right)\cos^2\psi\\
&+ \Gamma_{zz}\left(\begin{array}{l}-\frac{1}{840}\left(8\Phi^i_y-7\right)l^{i^5}+\frac{1}{420}\left(7\Phi^i_y-5\right)\alpha_{y_3}l^{i^4}-\frac{1}{60}\left(2\Phi^i_y-1\right)\alpha_{y_2}l^{i^3}\\ +\frac{1}{60}\left(5\Phi^i_y-1\right)\alpha_{y_1}l^{i^2}-\frac{1}{12}\left(4\Phi^i_y+1\right)\alpha_{y_0}l^i\end{array}\right)\sin^2\psi
\end{aligned}
$$

$$
\begin{aligned}
c^3_{11,4} &= \Gamma_{yy}\left(\begin{array}{l} -\frac{1}{168}\left(4\Phi^i_y+1\right)l^{i^5}+\frac{1}{210}\left(7\Phi^i_y+1\right)\alpha_{z_3}l^{i^4}-\frac{1}{20}\alpha_{z_2}\Phi^i_y l^{i^3} \\ +\frac{1}{60}\left(5\Phi^i_y-1\right)\alpha_{z_1}l^{i^2}-\frac{1}{12}\left(2\Phi^i_y-1\right)\alpha_{z_0}l^i \end{array}\right)\cos^2\psi \\
&+ \Gamma_{zz}\left(\begin{array}{l} -\frac{1}{168}\left(4\Phi^i_y+1\right)l^{i^5}+\frac{1}{210}\left(7\Phi^i_y+1\right)\alpha_{y_3}l^{i^4}-\frac{1}{20}\alpha_{y_2}\Phi^i_y l^{i^3} \\ +\frac{1}{60}\left(5\Phi^i_y-1\right)\alpha_{y_1}l^{i^2}-\frac{1}{12}\left(2\Phi^i_y-1\right)\alpha_{y_0}l^i \end{array}\right)\sin^2\psi
\end{aligned}
$$

$$
\begin{aligned}
c^3_{10,5} &= \Gamma_{yy}\left(\begin{array}{l} \frac{1}{168}\left(4\Phi^i_y-5\right)l^{i^5}-\frac{1}{210}\left(7\Phi^i_y-8\right)\alpha_{z_3}l^{i^4}+\frac{1}{20}\left(\Phi^i_y-1\right)\alpha_{z_2}l^{i^3} \\ -\frac{1}{60}\left(5\Phi^i_y-4\right)\alpha_{z_1}l^{i^2}+\frac{1}{12}\left(2\Phi^i_y-1\right)\alpha_{z_0}l^i \end{array}\right)\cos^2\psi \\
&+ \Gamma_{zz}\left(\begin{array}{l} \frac{1}{168}\left(4\Phi^i_y-5\right)l^{i^5}-\frac{1}{210}\left(7\Phi^i_y-8\right)\alpha_{y_3}l^{i^4}+\frac{1}{20}\left(\Phi^i_y-1\right)\alpha_{y_2}l^{i^3} \\ -\frac{1}{60}\left(5\Phi^i_y-4\right)\alpha_{y_1}l^{i^2}+\frac{1}{12}\left(2\Phi^i_y-1\right)\alpha_{y_0}l^i \end{array}\right)\sin^2\psi
\end{aligned}
$$

$$
\begin{aligned}
c^3_{11,10} &= \Gamma_{yy}\left(\begin{array}{l} -\frac{1}{56}\left(8\Phi^i_y+5\right)l^{i^5}+\frac{1}{42}\left(7\Phi^i_y+4\right)\alpha_{z_3}l^{i^4}-\frac{1}{10}\left(2\Phi^i_y+1\right)\alpha_{z_2}l^{i^3} \\ +\frac{1}{20}\left(5\Phi^i_y+2\right)\alpha_{z_1}l^{i^2}-\frac{1}{12}\left(4\Phi^i_y+1\right)\alpha_{z_0}l^i \end{array}\right)\cos^2\psi \\
&+ \Gamma_{zz}\left(\begin{array}{l} -\frac{1}{56}\left(8\Phi^i_y+5\right)l^{i^5}+\frac{1}{42}\left(7\Phi^i_y+4\right)\alpha_{y_3}l^{i^4}-\frac{1}{10}\left(2\Phi^i_y+1\right)\alpha_{y_2}l^{i^3} \\ +\frac{1}{20}\left(5\Phi^i_y+2\right)\alpha_{y_1}l^{i^2}-\frac{1}{12}\left(4\Phi^i_y+1\right)\alpha_{y_0}l^i \end{array}\right)\sin^2\psi
\end{aligned}
$$

Table C.18: Elemental centrifugal inertia term (quadratic velocity term) $\left[m^i_{\mathcal{R}_o e}\right]$

$$
\left[m^i_{\mathcal{R}_o e}\right] = \frac{\rho X_0 A_o l^i \overline{\Phi}^i_z}{120 L_{oy} L_{oz}}\left[m^{\mathcal{R}_o e}_{p,q}\right], \quad p,q = 1,2,...,12
$$

where the nonzero entries of the lower triangular part of $\left[m^{\mathcal{R}_o e}_{p,q}\right]$ are given by

$$m^{\mathcal{R}_o e}_{1,1} = 10\left(1+\Phi^i_z\right)\left(l^{i^2}-4\mu_2 l^i+6\mu_1\right)\cos\Omega t$$

$$m^{\mathcal{R}_o e}_{2,1} = -2\left(\left(5\Phi^i_z+4\right)l^{i^2}-2\left(10\Phi^i_z+9\right)\mu_2 l^i+30\left(\Phi^i_z+1\right)\mu_1\right)\sin\Omega t$$

$$m^{\mathcal{R}_o e}_{6,1} = -\left(\left(3\Phi^i_z+2\right)l^{i^3}-2\left(5\Phi^i_z+4\right)\mu_2 l^{i^2}+10\left(\Phi^i_z+1\right)\mu_1 l^i\right)\sin\Omega t$$

$$m^{\mathcal{R}_o e}_{7,1} = 10\left(1+\Phi^i_z\right)\left(3l^{i^2}-8\mu_2 l^i+6\mu_1\right)\cos\Omega t$$

$$m^{\mathcal{R}_o e}_{8,1} = -2\left(\left(15\Phi^i_z+16\right)l^{i^2}-2\left(20\Phi^i_z+21\right)\mu_2 l^i+30\left(\Phi^i_z+1\right)\mu_1\right)\sin\Omega t$$

$$m^{\mathcal{R}_o e}_{12,1} = \left(\left(3\Phi^i_z+4\right)l^{i^3}-2\left(5\Phi^i_z+6\right)\mu_2 l^{i^2}+10\left(\Phi^i_z+1\right)\mu_1 l^i\right)\sin\Omega t$$

where $\left[\begin{array}{ccc} X_0, & 0, & 0 \end{array}\right]^T$ are the co-ordinates of $\{\mathcal{R}_o\}$.

Table C.19: Elemental centrifugal inertia term (quadratic velocity term) $\left[m^i_{r_{P_o e}}\right]$

$$\left[m^i_{r_{P_o e}}\right] = \frac{\rho x^i_p A_o l^i \overline{\Phi}^i_z \cos\phi}{120 L_{oy} L_{oz}} \left[m^{r_{P_o e}}_{p,q}\right], \quad p,q = 1,2,...,12$$

where the nonzero entries of the lower triangular part of $\left[m^{r_{P_o e}}_{p,q}\right]$ are given by

$$m^{r_{P_o e}}_{1,1} = 10\left(1+\Phi^i_z\right)\left(l^{i^2} - 4\mu_2 l^i + 6\mu_1\right)$$

$$m^{r_{P_o e}}_{7,1} = 10\left(1+\Phi^i_z\right)\left(3l^{i^2} - 8\mu_2 l^i + 6\mu_1\right)$$

where $\left[\begin{array}{ccc} x^i_o, & 0, & 0 \end{array}\right]^T$ are the co-ordinates of $\left\{r^i_{P_o}\right\}$.